Graphene Inkjet Integrated Intelligent Sensors and Systems

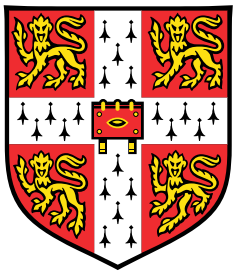

Tien-Chun Wu

Department of Engineering
University of Cambridge

This dissertation is submitted for the degree of
Doctor of Philosophy

Sidney Sussex College

September 2019

Declaration

I hereby declare that except where specific reference is made to the work of others, the contents of this dissertation are original and have not been submitted in whole or in part for consideration for any other degree or qualification in this, or any other university. This dissertation is my own work and contains nothing which is the outcome of work done in collaboration with others, except as specified in the text and Acknowledgements. This dissertation contains fewer than 65,000 words including appendices, bibliography, footnotes, tables and equations and has fewer than 150 figures.

Tien-Chun Wu
September 2019

Acknowledgements

I would like to take this opportunity to express my gratitude to those who offered me support. Foremost, I am grateful to my supervisor Dr. Tawfique Hasan. The project started from scratch. Under his supervision, it has expanded so far than what we initially planned. Now different aspects of new technologies have been developed in a cross-disciplinary manner, and the project can be passed down to new students for further development. Tawfique values autonomy in solving challenging tasks, developing my ability to search for feasible solutions. As inspired by his results-driven mindset, my project management skills such as preparation for Plan B are reinforced during the course of my doctoral work, especially the 2-year InnovateUK project involved where practical multi-sensory hubs are developed collaboratively. Tawfique's high standards drive me for delivering high quality publications in peer-reviewed journals and presentations in conferences. Moreover, during the volunteering full-year supervision of Master's student and the lab demonstrator job, I gained valuable teaching experiences as well as new perspectives for my our research.

I am grateful for my major collaborators Dr. Andrea De Luca and Prof. Florin Udrea. They are both great scientists and entrepreneurs who provide insightful technical supports towards my research. I would also like to thank my advisor Dr. Luigi Occhipinti who is both an experienced engineer and manager. I also wish to thank my main collaborators in InnovateUK – Dr. Abdul Alzahrani and Prof. Xiao Huang, along with other industrial and academic partners. I also thank the supports from CAPA Acorn Award and Prof. Daping Chu for a 3-month project. Moreover, I thank my cohort members in Tawfique's group who offer different skillsets for establishing great collaborations. Their individual contributions have been acknowledged in my publications. Finally, I am grateful for my dearest family for your invaluable support.

Abstract

Increasing awareness of personal health conditions has emerged as a key driver in point-of-care breath analysis for early diagnosis. This also demands real-time monitoring of air pollution based on internet of things (IoT) networks. Both systems rely on the development of scalable mobile-embeddable devices. Conventional devices face challenges like high power consumption, severe baseline drifts, and cross-analyte interferences, compromising the detection accuracies. Recently, 2D nanomaterials and their functionalization with metal oxides (MOx) have become attractive for high performing sensors. Solution processing of these materials coupled with inkjet printing can be promising for fabricating low-cost devices.

I have addressed the abovementioned challenges from the perspectives of materials, device fabrication, and algorithmic approaches. I develop an inkjet-printed array of graphene-ZnO and graphene-WO_3 system integrated onto miniaturized CMOS platforms to detect NH_3 and acetone for potential diagnosis of diseases. I also develop a machine-intelligent classification system based on inkjet-integrated α-Fe_2O_3-rGO CMOS devices to selectively measure NO_2 air pollutants.

The ink formulation and the theoretical model I develop facilitate uniform printed morphology, achieving excellent device reproducibility. Coupled with temperature modulation (TM) algorithms I develop, the devices achieve high responsivity, eliminated baseline drift, reduced response/recovery time, high SNR, and extraordinary repeatability. Moreover, a sensor array is established for compensation of cross-analyte interference. The influences of interferents are addressed by machine learning (ML) approaches. The predictive system quantifies NO_2 concentrations under different humidity conditions, with excellent separation between classes. Furthermore, the fully inkjet-printed room temperature NO_2 sensors assembled within the developed multi-sensory hub have performed reliable measurements in a real-world environment.

My strategy to combine the sensing material, inkjet printing onto the CMOS platform, and TM/ML algorithms promises a robust system that outperforms conventional devices. The versatile technologies enable reliable multi-material array for potential multi-disease diagnostics. The systems developed also pave the way for ubiquitous implementation of adaptive wireless-connected monitoring systems.

Publications

Peer-reviewed journal articles

(1) **Tien-Chun Wu**, Andrea De Luca, Qinyu Zhong, Xiaoxi Zhu, Osarenkhoe Ogbeide, Doo-Seung Um, Guohua Hu, Tom Albrow-Owen, Florin Udrea, and Tawfique Hasan. Inkjet-printed CMOS-Integrated Graphene-Metal Oxide Sensors for Breath Analysis. ***npj 2D Materials and Applications***, 3(42), 2019.

(2) Zongyin Yang, Tom Albrow-Owen, Hanxiao Cui, Jack Alexander-Webber, Fuxing Gu, Xiaomu Wang, **Tien-Chun Wu**, Minghua Zhuge, Calum Williams, Pan Wang, Anatoly V. Zayats, Weiwei Cai, Lun Dai, Stephan Hofmann, Mauro Overend, Limin Tong, Qing Yang, Zhipei Sun, and Tawfique Hasan. Single-nanowire spectrometers. ***Science***, 365(6457):1017–1020, 2019.

(3) Leonard Wei Tat Ng, Xiaoxi Zhu, Guohua Hu, Nasiruddin Macadam, Dooseung Um, **Tien-Chun Wu**, Frederic Le Moal, Chris Jones, and Tawfique Hasan. Conformal Printing of Graphene for Single- and Multilayered Devices onto Arbitrarily Shaped 3D Surfaces. ***Advanced Functional Materials***, 29(36):1807933, 2019.

(4) Guohua Hu, Tom Albrow-Owen, Xinxin Jin, Ayaz Ali, Yuwei Hu, Richard C T Howe, Khurram Shehzad, Zongyin Yang, Xuekun Zhu, Robert I Woodward, **Tien-Chun Wu**, Henri Jussila, Jiang-Bin Wu, Peng Peng, Ping-Heng Tan, Zhipei Sun, Edmund J R Kelleher, Meng Zhang, Yang Xu, and Tawfique Hasan. Black phosphorus ink formulation for inkjet printing of optoelectronics and photonics. ***Nature Communications***, 8(1):278, 2017.

(5) Xinxin Jin, Guohua Hu, Meng Zhang, Yuwei Hu, Tom Albrow-Owen, Richard C. T. Howe, **Tien-Chun Wu**, Qing Wu, Zheng Zheng, and Tawfique Hasan. 102 fs pulse generation from a long-term stable, inkjet-printed black phosphorus-mode-locked fiber laser. ***Optics Express***, 26(10):12506, 2018.

Submitted/Under review

(1) **Tien-Chun Wu**, Jie Dai, Guohua Hu, Wen-Bei Yu, Osarenkhone Ogbeide, Andrea De Luca, Xiao Huang, Bao-Lian Su, Yu Li, Florin Udrea, and Tawfique Hasan. Machine-intelligent inkjet-printed α-Fe_2O_3/rGO towards NO_2 detection in ambient humidity. ***Sensors and Actuators B: Chemical (under review)***, 2020.

(2) Xiaoxi Zhu, Leonard Ng, Guohua Hu, **Tien-Chun Wu**, Doo-Seung Um, Nasiruddin Macadam, and Tawfique Hasan. Hexagonal boron nitride enhanced optically transparent polymer dielectric inks for printable electronics. ***ACS Nano (under review)***, 2019.

(3) Guohua Hu, Lisong Yang, Zongyin Yang, Yubo Wang, Xinxin Jin, Jie Dai, Qing Wu, Shouhu Liu, Xiaoxi Zhu, Xiaoshan Wang, **Tien-Chun Wu**, Richard Howe, Tom Albrow-Owen, Leonard Ng, Qing Yang, Luigi Occhipinti, Robert Woodward, Edmund Kelleher, Zhipei Sun, Xiao Huang, Meng Zhang, Colin Bain, and Tawfique Hasan. A general ink formulation of 2d crystals for wafer-scale inkjet printing. ***Science Advances (under review)***, 2019.

(4) Wen-Bei Yu, Wen-Da Dong, Chao-Fan Li, Nasiruddin Macadam, Guo-Bin Zhang, Jiu-Xiang Yang, **Tien-Chun Wu**, Yu Li, Tawfique Hasan, Hong-En Wang, Li-Hua Chen, Li-Qiang Mai, and Bao-Lian Su. Interwoven scaffolded titanium oxide/carbon nanotubes framework for high-performance sodium-ion battery. *Submitted*, 2019.

Conference presentations

(1) **Tien-Chun Wu**, Andrea De Luca, Tom Albrow-Owen, Guohua Hu, Florin Udrea, and Tawfique Hasan. Inkjet-Printed Graphene/ZnO Ammonia Sensor for Personal Healthcare Monitoring. In ***Materials Research Society Symposium***, Boston, USA, 2018.

(2) **Tien-Chun Wu**, Guohua Hu, Jie Dai, Andrea De Luca, Xiao Huang, Florin Udrea, and Hasan Tawfique. Printed graphene-based sensors for air quality monitoring. In ***The Nanotube Conference***, Beijing, China, 2018.

(3) Guohua Hu, **Tien-Chun Wu**, Jie Dai, Leonard Ng, Xiaoxi Zhu, Xiao Huang, and Tawfique Hasan. Functional inkjet printing inks of graphene/oxide for gas sensors. In ***The Nanotube Conference***, Beijing, China, 2018.

(4) **Tien-Chun Wu**, Andrea De Luca, Tom Albrow-Owen, Florin Udrea, and Tawfique Hasan. Inkjet-printed graphene zinc oxide ammonia sensor for personal healthcare monitoring. In ***Cyber Physical Systems***, Cambridge, UK, 2017.

(5) Zongyin Yang, Guohua Hu, Richard Howe, Tom Albrow-Owen, Shouhu Liu, **Tien-Chun Wu**, Leonard Ng, Yubo Wang, Qing Yang, and Tawfique Hasan. High Device-Device Uniformity Using Inkjet-Printable Transition Metal Dichalcogenide Functional Inks. In ***Materials Research Society Symposium***, Boston, USA, 2017.

Conference proceedings

(1) Xinxin Jin, Guohua Hu, Meng Zhang, Yuwei Hu, Qianchao Wu, Tom Albrow-Owen, Richard Howe, **Tien-Chun Wu**, Zheng Zheng, and Tawfique Hasan. Stable, inkjet printed temperature- and humidity-resistant black phosphorus for ultrafast lasers. In *Conference on Lasers and Electro-Optics*, page JTh2A.82, Washington, D.C., 2018. OSA.

(2) Qianchao Wu, Guohua Hu, Meng Zhang, Xinxin Jin, Yuwei Hu, Ting Li, Tom Albrow-Owen, Richard Howe, **Tien-Chun Wu**, Zheng Zheng, and Tawfique Hasan. Inkjet-printed optically uniform transition metal dichalcogenide saturable absorbers. In *Conference on Lasers and Electro-Optics*, page JTh2A.83, Washington, D.C., 2018. OSA.

(3) Xinxin Jin, Guohua Hu, Meng Zhang, Yuwei Hu, Qianchao Wu, Tom Albrow-Owen, Richard Howe, **Tien-Chun Wu**, Zheng Zheng, and Tawfique Hasan. Ultrafast dispersion-managed fiber laser mode-locked by black phosphorus saturable absorber. In *Conference on Lasers and Electro-Optics*, page SF3K.2, Washington, D.C., 2018. OSA.

(4) Xinxin Jin, Guohua Hu, Meng Zhang, Yuwei Hu, Tom Albrow-Owen, Richard Howe, **Tien-Chun Wu**, Xuekun Zhu, Zheng Zheng, and Tawfique Hasan. Observation of tunable dual-wavelength in a fiber laser mode-locked by black phosphorus. In *Opto-Electronics and Communications Conference and Photonics Global Conference*, pages 1–2. IEEE, 2017.

(5) Xinxin Jin, Guohua Hu, Meng Zhang, Yuwei Hu, Tom Albrow-Owen, Richard Howe, **Tien-Chun Wu**, Xuekun Zhu, Zheng Zheng, and Tawfique Hasan. Wideband tunable ultrafast fiber laser using blackphosphorus saturable absorber. In *Opto-Electronics and Communications Conference and Photonics Global Conference*, pages 1–3. IEEE, 2017.

(6) Xinxin Jin, Guohua Hu, Meng Zhang, Yuwei Hu, Tom Albrow-Owen, Richard Howe, **Tien-Chun Wu**, Xuekun Zhu, Zheng Zheng, and Tawfique Hasan. Long term stable black phosphorus saturable absorber for mode-locked fiber laser. In *Conference on Lasers and Electro-Optics*, page SW4K.1, Washington, D.C., 2017. OSA.

Table of contents

List of figures

List of tables

List of abbreviations and symbols

Roman Symbols

A_{recov}	Area under recovery signal
A_{resp}	Area under response signal
C	Capacitance
c_{surf}	Analyte concentration at the surface
D	Nozzle diameter
D_k	Diffusion rate
E_a	Activation energy
$f(\theta)$	Volume correction factor for cylindrical-cap
$f_{n,m,k}$	Feature element with indices m,n,k
$g(r')$	Volume correction function for spherical-cap
H	Height of peak
h	Peak-to-peak interval at baseline
I	Current
I_D	Drain current
k	Chemical reaction rate
k_B	Boltzmann constant ($1.38064852 \times 10^{-23}\ \mathrm{m^2\,kg\,s^{-2}\,K^{-1}}$)
m	Proportion of analyte reaching distance L

P_i Fitting parameters of Lorentz equation

R Resistance

r Distance between the particles

R' Radius of droplet with cylindrical-cap geometry

R_g Ideal gas constant (8.31 J mol^{-1} K^{-1})

r' Radius of droplet with spherical-cap geometry

R_s Resistance of the sensor

S Responsivity

SD Standard deviation

S_t Output curve of processed sensor response

T Temperature

U Potential energy

ΔV Change in potential barrier

V_{drop} Volume of droplet

V_{GS} Gate voltage

V Voltage

W_g Depletion width in air

Greek Symbols

ϵ Depth of potential well

ϵ_r Permittivity

η Viscosity

γ Surface tension

Φ_{bg} Potential barrier in air

Φ_s Work function of a semiconductor

Φ_m Work function of a metal

ρ Density

ρ' Resistivity

σ Conductivity

τ Shear stree

τ_{recov} Recovery time constant

τ_{res} Response time constant

Other Symbols

Ag_2WO_4 Silver tungstate

Ag Silver

Au Gold

BP Black phosphorus

C_3H_6O Acetone

C_3H_8 Propane

CH_4 Methane

CO_2 Carbon dioxide

CO Carbon monoxide

-COOH Carboxyl group

Cu_2O Copper(I) oxide

Cu_3HHTP_2 Copper-2,3,6,7,10,11-hexahydroxytriphenylene

Cu Copper

CuO Copper(II) oxide

DFM N,N-dimethylformamide

EC Ethyl cellulose

Fe_2O_3 Iron(III) oxide

$FeCl_3$ Iron(III) chloride

GaN Gallium nitride

GO Graphene oxide

H_2 Hydrogen

In_2O_3 Indium(III) oxide

InN Indium nitride

IPA Isopropyl alcohol

ITO Indium tin oxide

MoS_2 Molybdenum disulfide

N_2 Nitrogen

$Na_2C_4H_4O_6$ Sodium tartrate

NH_3 Ammonia

Ni Nickel

NMP N-Methyl-2-pyrrolidone

NO_2 Nitrogen dioxide

O_2 Oxygen

-OH Hydroxyl group

Pd Palladium

PEN Polyethylene naphthalate

PET Polyethylene terephthalate

PTFE Polytetrafluoroethylene

Pt Platinum

PVP Polyvinylpyrrolidone

rGO Reduced graphene oxide

Si_3N_4 Silicon nitride

SiO_2 Silicon dioxide

Si Silicon

$SnCl_2$ Tin(II) chloride

SnS_2 Tin(IV) sulfide

TiO_2 Titanium dioxide

TMD Transition metal dichalcogenides

WO_3 Tungsten oxide

WS_2 Tungsten disulfide

ZnO Zinc oxide

Acronyms / Abbreviations

ADC Analog-to-digital converter

AFE Analog front-end

AFM Atomic force microscopy

AP Access point

API Application programming interface

AQM Air quality monitoring

CDF Cumulative distribution functions

CIJ Continuous inkjet

CMOS Complementary metal oxide semiconductor

CNW Carbon nanowall

CVD Chemical vapor deposition

DI Deionized

DoD Drop-on-demand inkjet

DRIE Deep reactive ion etching

ESRD End-state renal disease

FET Field-effect transistor

FOM Figure of merit

GPS Global positioning system

GRM Graphene and related materials

HRG Highly reduced suspensions of graphene

HSP Hansen solubility parameter

I^2C Inter-integrated circuit

IA Instrumentation amplifier

IDE Interdigitated electrode

IoT Internet of things

IR Infrared

ISFET Ion-sensitive field-effect transistor

ISO Isothermal

kNN k-nearest neighbors

LbL Layer-by-layer

LDA Linear discriminant analysis

LOD Limit of detection

MCU Microcontroller unit

MFC Mass flow controller

ML Machine learning

MOF Metal-organic frameworks

MOx	Metal oxides
M-S	Metal-semiconducting
NN	Neural network
NP	Nanoparticles
PCA	Principal component analysis
PCB	Printed circuit board
PCR	Principal component regression
PDF	Probability distribution functions
PLS	Partial least squares
PM	Particle matter
PWM	Pulse width modulation
RF	Random forest
RH	Relative humidity
SAED	Selected area diffraction
SA	Synthetic air
SAW	Surface acoustic wave
SBS	Sedimentation based separation
SEM	Scanning electron microscope
SNR	Signal-to-noise ratio
SOI	Silicon on insulator
SPDT	Single-pole double-throw switch
SVM	Support vector machine
TEM	Transmission electron microscopy
TGA	Thermogravimetric analysis

TM Temperature modulation

UALPE Ultrasonic-assisted liquid phase exfoliation

UART Universal Asynchronous Receiver/Transmitter

μHP Microhotplate

UV-Vis Ultraviolet–visible spectroscopy

vdW van der Waals

VOC Volatile organic compounds

Chapter 1

Introduction

1.1 Background and motivations

The emerging fifth generation cellular network (5G) technologies enable low power and low latency data transmission, boosting the development of portable internet of things (IoT) devices and distributed networks to establish cloud-based analytical systems for personal healthcare and environmental monitoring.

The increasing awareness of personal health conditions arising from the pursuit for well-being in an aging society has promoted the development of technologies for early diagnosis in cancers and diseases. Early diagnosis of cancers will prevent patients from unnecessary suffering and early death. For instance, 5-year survival rate increases from 5% to 31% (244,000 patients) for liver cancer and to 67% (505,000 patients) for stomach cancer when diagnosed in stage 1 compared to stage 4. However, only 46% of cancers are diagnosed at the advanced stage. It is estimated to save £150 million of medical treatments and loss in workforces in UK [2] if diagnosed early.

Among various disease detection technologies, breath analysis is a promising candidate as a non-invasive and harmless approach where rapid responses can be generated from the unique signatures, produced by metabolic processes, which are highly correlated with the diseases of interest. Fig. 1.1 illustrates the process of breath analysis technology with the focus on ammonia (NH_3). It is a critical biomarker associated with hepatitis (related to liver cancer), kidney failure, and *Helicobacter pylori* (related to stomach cancer) [3, 4]. Acetone (C_3H_6O) is another critical component in human breath and could be a biomarker for diabetes [5] which is one of four major lingering diseases in the world recognized by the United Nations [6]. Patients with diabetes are unable to make or effectively use insulin. As a result, their body burns fat instead of glucose for energy leading to higher acetone concentrations in blood [7]. Analysis of exhaled breath provides a more efficient approach than blood and

urine test as an early-stage diagnosis. Therefore, detecting acetone level in exhaled breath has become a desirable alternative to monitor health condition and a marker for effective treatments.

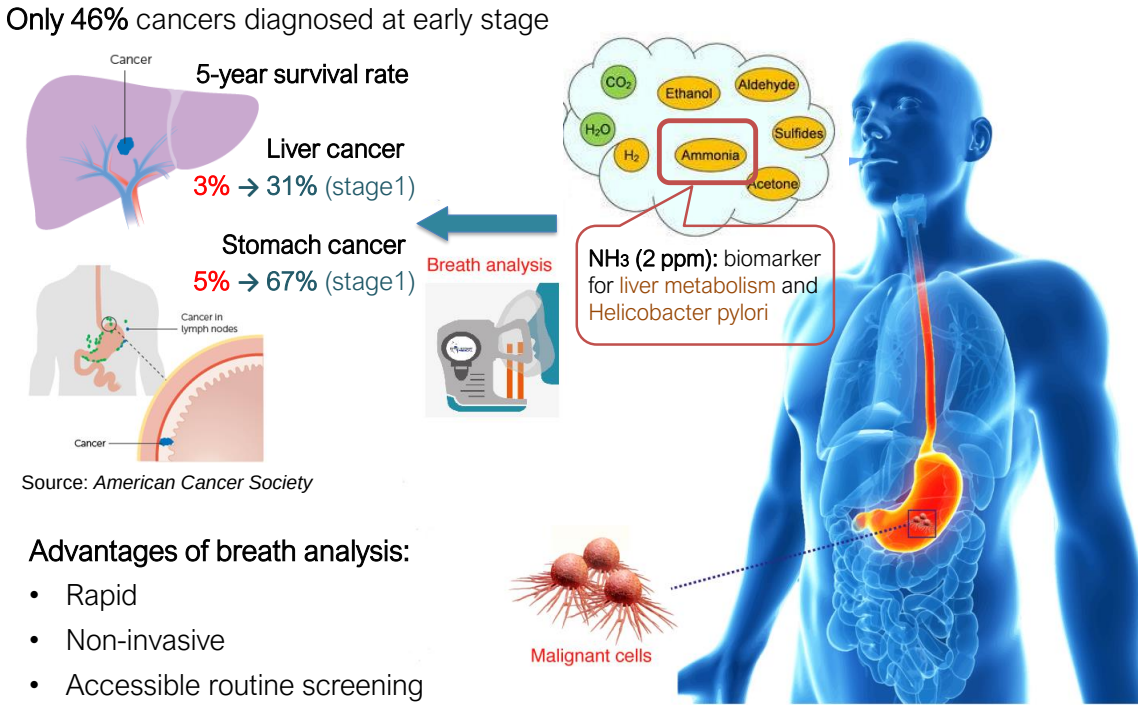

Fig. 1.1 Illustration of breath analysis using detection of NH_3 as an example.

Many analytical techniques have been developed to measure the concentration, such as gas chromatography [7], liquid chromatography [8], mass spectroscopy [9] and portable gas sensors [10]. Recently, the ubiquitous IoT devices and booming cloud-based analytical technologies accelerate the development of personal healthcare monitoring, exploring the potentials for routine screening at home based on professional diagnosis. The evolution of point-of-care diagnostic thus opens up the widespread access for the public and reduces loading for specialized diagnostics instruments in hospitals. It is hence beneficial to develop scalable and miniaturized lab-on-chip technologies for IoT integration.

On the other hand, rapidly increasing environmental pollution has been recognized as a major concern for human health. Mobile-embeddable gas sensors promote the evolution from the current spatial environmental monitoring, to people as the center of the environmental monitoring. Ubiquitous deployment of sensor networks in mobile configurations could effectively increase coverage of existing static stations and the capability to generate real-time high-resolution air quality map, which enhances residences' awareness of urban pollutant level of their surrounding environment. This information is useful for both public

and the authorities to monitor whether the air pollution level has met environmental regulations or not, and allow stakeholders to take appropriate mitigation actions. The decision support system could quantify the major sources of emission from the pollution distribution and has potential to realize automatic emissions control in smart cities. Moreover, deployment of sensor nodes on vehicles enables monitoring emissions on the road and support traffic control. In particular, nitrogen dioxide (NO_2) is a critical risk factor for asthma and respiratory infections.

1.2 Aims of the project

The ultimate goals for this project are to establish low-powered, printable, and mobile-embeddable devices as well as intelligent sensory systems as an integral part of personal healthcare and air quality monitoring systems. The goals will be achieved through the development of novel sensing nanomaterials, scalable fabrication and device integration technologies, and signal processing and machine learning algorithms for intelligent systems.

Metal oxides (MOx)-based chemiresistive sensing materials are scalable and sensitive and can be utilized on the miniaturized platform. Conventional MOx sensors face critical challenges such as high power consumption, insufficient detection accuracies, low reproducibility, baseline drifts, and cross-analyte interferences, limiting applicability for real-world implementations. Recently, 2D nanomaterials have proven to be attractive for high performing chemical sensors due to their remarkable electronic and physical properties originating from their 2D structure. In my PhD, I will exploit the synergistic advantages offered by 2D graphene and related materials (GRM)-MOx nanocomposites to develop high performing low-cost and scalable sensing devices.

Moreover, the production and deposition methods for the nanomaterials hybrid should be compatible with both the high performing materials and the device platform. Solution processing of the nanomaterials coupled with inkjet printing technology could be a promising route for high yield and cost-effective manufacture approach for batch fabrication of multiple materials on the miniaturized device. However, non-uniform material deposition remains a critical challenge for inkjet technology. The challenges will be addressed through the comprehensive studies of the dynamics in the ink system.

To further address the challenges presented for device applicability in healthcare diagnostics and air quality monitoring systems, signal processing and control algorithms will be developed to further improve power consumption, sensitivity, and reproducibility. Furthermore, cross-analyte interference will be compensated with a multi-material sensor array and the development of specialized machine learning algorithms. The developed devices along

with the electronic configurations will then be assembled in a wireless hub containing multiple of different sensory components. Field trials will be carried out for the sensory hub to monitor real-time air quality of an ambient environment.

1.3 Structure of the thesis

Chapter 1 introduces the background motivations and aims of this thesis. Chapters 2-4 mainly review the current literature from the perspectives of sensor architecture, sensing materials and their properties, and the ink system for device fabrication.

In Chapter 2, I first introduce various types of sensor architectures and focus on chemiresistive devices. Next, comprehensive mechanisms involved in chemiresistors during sensing events are reviewed. The sensing mechanisms comprising analyte-material interactions, transduction process, and signal transformation are explained in Section 2.2. Then, performance parameters are defined. Finally, the computational approaches for discriminating analytes in a multi-component environment will be reviewed in Section 2.4.

In Chapter 3, I introduce the fundamental sensing mechanisms of graphene-MOx composites and the state-of-art materials for our target sensing applications. Next, I explain the common material synthesis methods with a focus on the hydrothermal method which will be used in our device fabrication. In addition, Section 3.3 details the practical materials characterization techniques used throughout the project. Section 3.3.1 is my original work that features the program I develop for automatic Raman mapping.

In Chapter 4, I review the literature on functional ink systems, introducing the fundamental attributes of different ink systems. Next, I focus on the inkjet deposition technique employed throughout the project, focusing on studies on ink formulation, and the properties that govern the uniformity of printed morphologies: jetting properties, droplet spreading dynamics, and coffee-ring effect and the suppression approaches. Section 4.3.6 is my original work in which I develop a model to simulate the printed morphology based on experimental printing parameters. The final section details the architecture of our CMOS device platform.

In Chapter 5 is my original work where I detail the measurement protocols, signal processing and machine learning algorithms that are employed throughout the project. First, I introduce the electronics and measurement setups for gas characterization. Next, I discuss a more advanced temperature modulation (TM) technique (Section 6.3) I developed to optimize the sensing performances. In this section, the mechanisms on temperature dependent sensing is analyzed, and the associated signal processing algorithm is developed. In the analyte classification section (Section 5.3), I discuss the machine learning approaches

including signal pre-processing and cluster analysis techniques to address the common issue of cross-analyte interference. Finally, Section 5.4 presents an IoT implementation.

Chapters 6-8 describe my original work on the development of inkjet-printed graphene-MOx sensors and intelligent systems for personal healthcare diagnostics (Chapter 6, 7) and air quality monitoring (Chapter 8) applications. In Chapter 6 and 7, I present graphene-MOx hybrid sensors that are integrated onto a CMOS microhotplate (μHP) to detect NH_3 (Chapter 6) and acetone (Chapter 7) levels in simulated breath for diagnostics of diseases. I develop graphene-zinc oxide (ZnO) ink for the ammonia sensor. I address the shortcomings on high power consumption, long recovery time and baseline drifts by optimizing the sensing material along with the temperature modulation strategy I develop. The strategy focuses on the control of interplays between surface-analyte adsorption/desorption, carrier transport, and analyte diffusion taking place at different temperature conditions. The development of algorithms, as well as the optimization of ink formulation lead to enhanced sensing performances and reproducibility. In Chapter 7, graphene-tungsten oxide (WO_3) ink is developed for the acetone sensor. I investigate the effect of different graphene concentrations and different operational mode on the gas sensor performance with respect to sensitivity and response time. Cross-selectivity, as pointed out in Chapter 6, is further addressed by the parallel sensor. My dual graphene-MOx strategy, therefore, allows tentative mapping of disease probability being constructed.

In Chapter 8, I will establish an intelligent system for NO_2 air quality monitoring. In addition to the optimization of the ink system and TM schemes, my solution focuses on the development of machine learning (ML) approaches, including PCA and clustering, on a single inkjet-printed α-Fe_2O_3/rGO nanocomposite platform to establish a prediction system that allows discrimination of relative humidity (RH) level in a mixture of NO_2 and RH in an ambient environment. Furthermore, in Section 8.6, I implement fully inkjet-printed room temperature NO_2 sensors integrated within the co-developed multi-sensory hub to carry out field trials in a real-world environment.

Chapter 2

Electrically-transduced Sensors

Chemical sensors have become an integral part of the infrastructure in our society. They have been widely used in different fields of applications, including industrial monitoring, environmental protection, public safety, medical and healthcare, home automation, and so on. For industrial process monitoring, applications include flue gases, emission, and heavy metals monitoring. For environmental protection, applications include urban air and water pollution monitoring, and waste management. For public safety, applications include monitoring of toxins, explosives, and abuse of drugs. For medical and healthcare, applications include bedside/home diagnostics, hygiene test, wearable biosensors, and breath biomarkers. My target applications in this thesis focus on two different applications: air pollution monitoring and personal healthcare diagnostics with breath analysis.

Fig. 2.1 illustrates the logical structure of a chemical sensor which associates the physical device with the different sensing mechanisms. A sensor typically consists of sensing material and transducer. When the analytes in the environment interact with the sensing material, some of its properties such as conductivity σ, work function Φ_{wf}, and permittivity ϵ_r may change. The transducer converts these properties into fundamental electric parameters: capacitance C, inductance L, and resistance R. The circuitry configurations connected to the sensor transform these parameters into electrical signals, such as current I, voltage V, frequency f, and phase ϕ.

In this Chapter, the structural components of chemical sensors and the underlying operating principles of different types of architectures are first discussed. Next, I focus on the chemiresistive-type sensors that are used throughout this project. I detail their sensing mechanisms which are decomposed into analyte-material interaction and transduction process, in accordance with Fig. 2.1. Then, performance measures used throughout this thesis are defined. Finally, the computational approaches for discriminating different analytes are reviewed in Section 2.4.

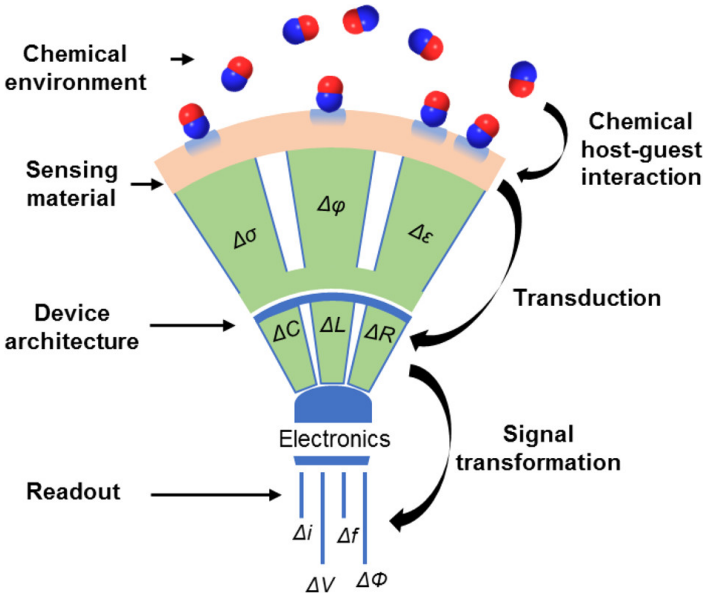

Fig. 2.1 Logical structure of a chemical sensor. Adapted from [11]

2.1 Overview of sensing architectures

Gas sensors can be categorized into conductometric, potentiometric, capacitive, amperometric, gravimetric, optical, resonant, and fluorescent types according to their signal transduction principles. Table 2.1 summarizes these different classes of gas sensors.

Principle	Mesurand	Type of sensor
Conductometric	Resistance/conductivity	Metal oxide sensor
Potentiometric	Tension	ISFET for pH
Capacitive	Capacity	Polymer humidity sensor
Amperometric	Current	Electrochemical cell
Gravimetric	Mass	Piezoelectric or SAW sensor
Optical	Frequency/absorption	IR methane detector
Resonant	Frequency	Surface plasmon
Fluorescent	Intensity	Fibre optics

Table 2.1 Classes of gas sensors according to detection principles.

Fig. 2.2 provides an overview of the commonly available commercial sensors for the application of disease diagnosis. The detection accuracy, size, and cost increase from top right to bottom left. Gas chromatography and spectrometry are accurate yet expensive; whereas portable MOx sensors, including field-effect transistor (FET) and chemiresistor types, are compact, economical, and simple to fabricate and operate. These advantages make them

effective in situations where advanced equipment is constrained by access to qualified personnel and calibration procedures. However, MOx sensors generally have the disadvantages of slow recovery time, low reproducibility, low selectivity, and insufficient detection limit which restrict their applications for mobile healthcare diagnostics. In the following sections, I will discuss the different types of economical portable sensors.

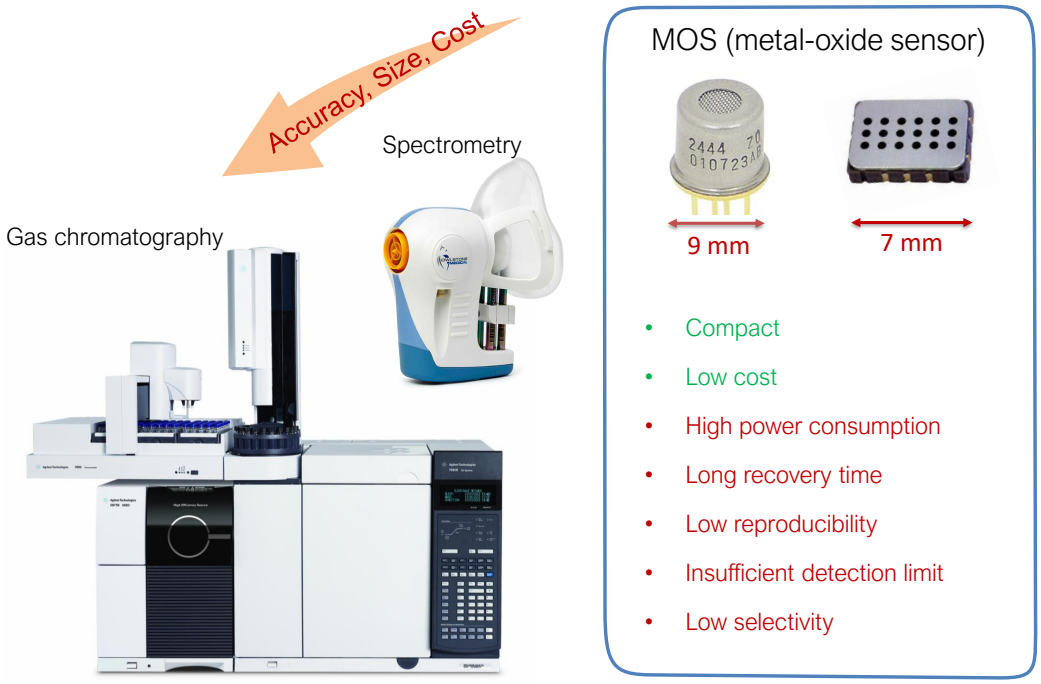

Fig. 2.2 Common types of commercial gas sensors, with the focus on MOx sensors showing their pros and cons.

2.1.1 Electrochemical sensors

Electrochemical gas sensors involve an ion conductor which allows ions to move freely within itself. It ionises the gas molecules at a three-phase boundary layer (atmosphere, electrode of a catalytically active material, electrolyte) [12]. The material used for acetone detection is sodium tartrate ($Na_2C_4H_4O_6$) electrolyte with electrodeposited platinum (Pt) electrode [10]. When acetone molecules make contacts with the ions, chemical reactions take place. Current is generated due to reactions, the magnitude of which is dependent on the concentration of acetone present in the air. However, since this design involves an ion conductor, the sensors are usually quite bulky. The power consumption is also high (hundreds of mW) [13].

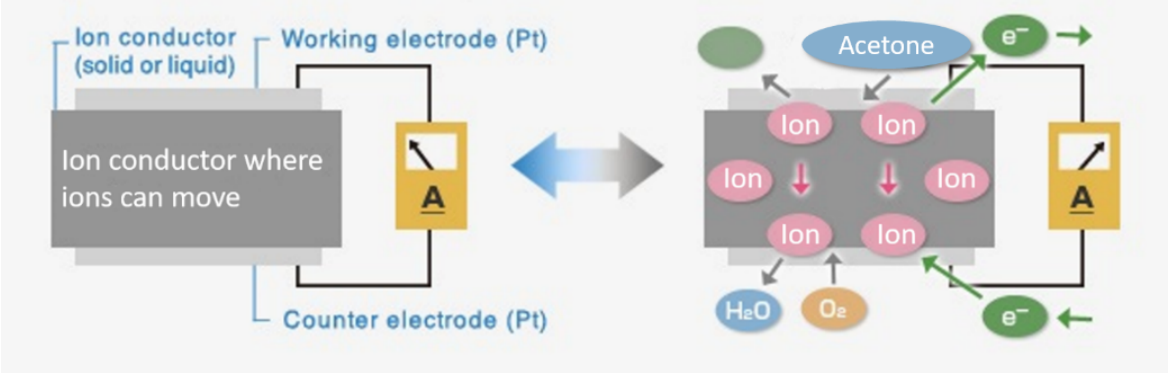

Fig. 2.3 Illustration of working principles of electrochemical gas sensors for detection of acetone.

2.1.2 Field effect transistors (FET)

Another commonly used architecture for electronic sensors is FET [14]. An FET consists of a gate, a channel connecting source and drain electrodes, and a gate oxide separating the gate from the channel. Back gate configuration (Fig. 2.4) are typically used to simplify the device structure for gas sensing. The field effect operation relies on the control of channel conductance, and thus the drain current I_D, by a gate voltage V_{GS} and/or by the surface potential. There are different materials used for the FET channel. In a graphene-based FET, the applied V_{GS} modulates the Fermi level of graphene and thereby changes in charge carrier densities, in turn, influences the conductivity of the channel [15]. The adsorption or desorption of molecules on the surface of the graphene channel changes the Dirac point voltage (V_{Dirac}) of the devices, leading to horizontal shifts of the I_D-V_{GS} transfer curves [14]. In the cases of solution-gated FETs [16], a nanometer-thick ionic double layer is formed in contact with the graphene layer, acting as a strong double-layer capacitance and thus producing large trans-conductance [16].

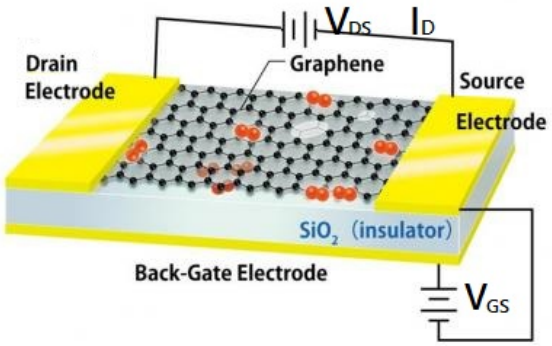

Fig. 2.4 Schematics of a graphene-based FET gas sensor. Adapted from [17].

Apart from field effects, doping effect can also change the channel conductance by altering its carrier mobility [14]. Doping effects arise from the direct charge transfer between the open-shell adsorbents (like NO_2) and graphene [18]. However, closed-shell molecules cannot exchange charge directly with graphene. Despite this, indirect doping effects may still be utilized by manipulation of charge distribution through existing doping or impurities of graphene.

An FET-based sensor could serve as both a sensor and an amplifier. A small variation of gate voltage could induce a pronounced response of the channel current [19]. This makes the FET a promising sensing device with easily adaptable configuration, high sensitivity, and real-time capability [20].

2.1.3 Chemiresistors

Chemiresistive gas sensors use a semiconductor sensing layer which is commonly deposited between electrodes. Traditionally, there are two main categories of materials used: organic conducting polymers and semiconducting MOx [21]. However, polymer sensors are generally unstable and have relatively poor sensitivity [22]. Alternatively, the most common type of semiconductors used is MOx. This class of materials generally give better responses due to the oxygen stoichiometry and electrically active surface charge [23]. Therefore, I focus on this material family in my thesis.

Most chemiresistive gas sensors detect the analyte concentration by measuring the change in resistivity of the MOx film upon exposure to certain gas analytes. This change arises from the band bending due to the electron transfer between the semiconductor and the gas molecules. The resistance of the device can be mainly divided into two components:

$$R = R_{\text{mat}} + R_{\text{contact}} \tag{2.1}$$

where R, R_{mat}, and R_{contact} are the total resistance of the device, the resistance of the sensing material, and the sum of contact resistance arising from the junctions at electrode/sensing material, and the junctions between the grains of nanomaterials, respectively.

Device structure

A simple chemiresistor is realized by either (Type 1) depositing two conductive electrodes (source and drain, respectively) of noble metal on top of the film or (Type 2) in reverse order. Type 1 refers to top contact and is often found in 1D nanostructured MOx devices [24]. Type 2 refers to side contact and is found in other MOx nanostructures [25]. Their structures are

shown in Fig. 2.5. Beyond that, an array of source and drain electrodes constructed in the form of Type 1 or Type 2 can be implemented to form an interdigitated electrode (IDE) structure.

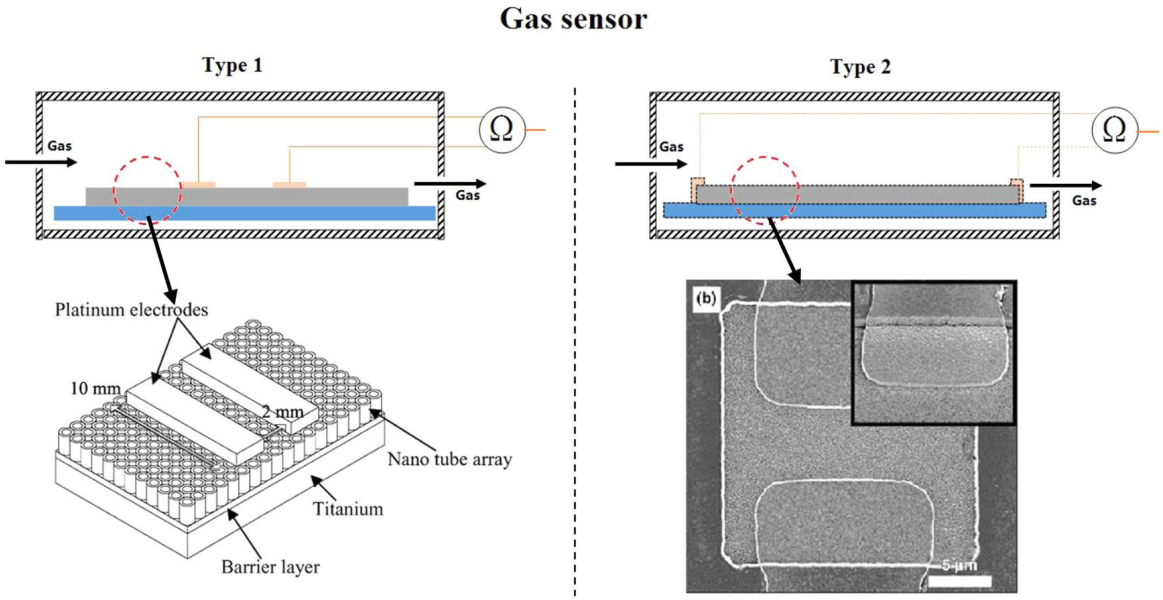

Fig. 2.5 Schematics of the device architecture for gas sensing. Type 1: top contact. Adapted from [24] Type 2: side contact. Adapted from [25].

IDEs are used mainly to overcome the issue of high resistance of the sensing materials. IDEs reduce the total resistance by splitting it into n components of individual resistors in parallel. This reduces the effective length of total resistance by n, resulting in resistance reduction by n^2. Moreover, IDE permits a larger contact area with the film's surface. Therefore, this configuration typically enhances sensitivity and detection limits [26]. In addition, micrometer-scale IDE offers improved SNR and reduced RC time constant [27], which improve resolution and reduce latency respectively.

Advantage of chemiresistive gas sensors. Compared to electrochemical sensors, chemiresistive devices can be compact in size and mass. The power consumption is typically lower than electrochemical sensors [28]. The ease of device manufacture also makes them economical. Once their fabrication can be integrated with large-scale CMOS-compatible processes, they can be further miniaturized and integrated into the existing electronic systems [29]. Comparing to FET devices which require the supply of bias voltage, chemiresistive devices have the potential for further reduction in power consumption. Considering the above advantages, I focus my studies on chemiresistive devices.

2.2 Sensing mechanisms of MOx chemiresistive sensors

I explain the sensing mechanisms based on semiconducting transition-metal oxides which are widely used for gas sensing. The active sensing materials possess a receptor and transducer function (Fig. 2.6). The receptor represents the interaction of the sensing surface with the target gas molecules, whereas the transducer function refers to an effective transduction of this molecular information into a macroscopically accessible signal, which is in the form of the change in electrical resistance [30]. The sensor works by adsorption and desorption of gas molecules on the surface of the active material and the electron transfer process.

Gas molecules interacting with the MOx either act as a donor or acceptor of charge carriers (electrons), inducing band-bending and altering the resistance of the material [31]. As shown in Fig. 2.6, when electrons are transferred away during gas molecules come into contact with MOx, the width of the depletion region of MOx NP will increase and the potential barrier becomes higher, making it harder for electrons to overcome. For molecules which give electrons to the metal oxide, the barrier will be lowered and hence the conductance will increase. The electron transfer process of the MOx is dependent on many factors such as the grain size of the nanoparticles and morphology of the sensing materials as well as the microstructures of the sensing layers [32].

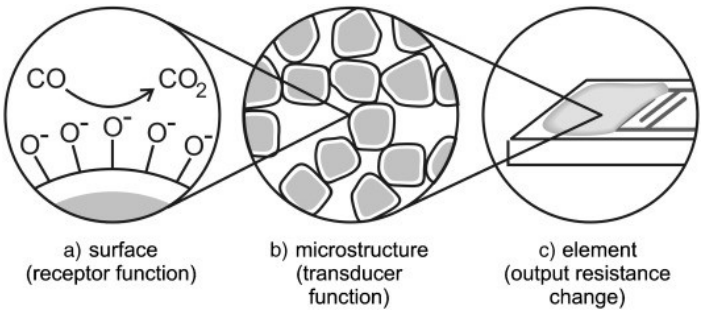

Fig. 2.6 Schematics of receptor and transducer functions decomposed into (a) receptor function occurred at the material surface (b) transducer function occurred at within the microstructure of material (c) translating to output resistance change. Adapted from [33].

2.2.1 Analyte-material interactions

The sensing processes can be further analyzed with analyte-material surface interaction, analyte diffusion, and transduction mechanisms (discussed in Section 2.2.2). First, the target gas is adsorbed on oxide's surface via physisorption followed by chemisorption processes. A gas molecule is first attracted by van der Waals and dipole interactions during physisorption. Next, it forms a strong chemical bond with the surface atoms of the semiconducting

MOx. The increase in temperature could enhance the rate of chemisorption but will reduce physisorption [34]. The adsorption process will lead to variation in the space charge which transforms into change in electrical resistance via electron transport in semiconducting materials. In this manner, gas recognition can be realized by the surface chemical reactions occurred at the adsorption sites.

I introduce the following relations to support the temperature-dependent sensing mechanisms of the MOx. Surface adsorption involves an interplay between physisorption and chemisorption processes [34]. Physisorption typically occurs first and can be modelled by Lennard-Jones potential:

$$U(r,T) \propto \frac{\epsilon(T)}{n}(\frac{r_{max}(T)}{r})^n \tag{2.2}$$

where U is potential energy, ϵ is depth of the potential well, r is the distance between the particles, and r_{max} is the distance at which the potential reaches its minimum. The relationship of physisorption with temperature is such that as temperature increases, the Lennard-Jones potential becomes more positive. The repulsive forces caused by the electron clouds of the adsorbate therefore dominate, resulting in less physisorption at high temperatures [35, 36]. On the other hand, Chemisorption follows Arrhenius' law [37]:

$$k \propto \exp(\frac{-E_a}{R_g T}) \tag{2.3}$$

where k is chemical reaction rate, E_a is activation energy, R_g is ideal gas constant (8.31 $\mathrm{J\,mol^{-1}\,K^{-1}}$). Once the activation temperature is reached, a marginal increase in temperature leads to a dramatic increase in the reaction rate.

Further, the diffusion rate and gas analyte concentration diffused to the deepest layer of the active material can be described in the following equations based on Knudsen diffusion model [38].

$$c(x = L) = c_{\mathrm{surf}}\frac{m}{\cosh(m)} \tag{2.4}$$

$$m = L(\frac{k}{D_k})^{1/2}, D_k \propto T^{1/2} \tag{2.5}$$

where D_k is diffusion rate, c_{surf} is analyte concentration at the surface, m indicates the proportion of analyte reaching distance L.

2.2.2 Transduction mechanisms

The next phase in the sensing processes (as illustrated in Fig. 2.1) is the transduction process. This process is induced by the analyte-material interactions and contributes to change in resistivity for chemireistive sensors.

Grain-controlled model

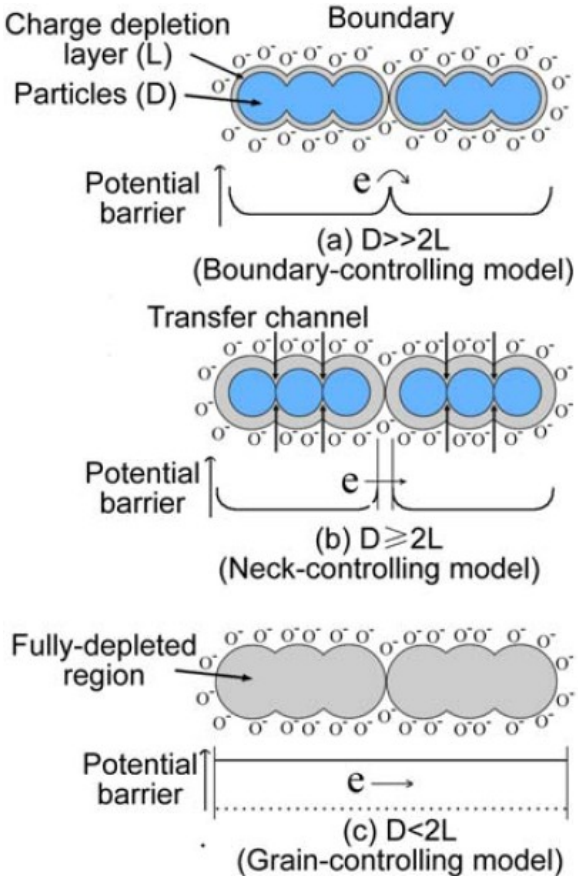

Fig. 2.7 Schematic model of the effect of the crystallite size on the sensitivity of MOx sensors (a) boundary-controlled model (b) neck-controlled model (c) grain-controlled model. Adapted from [39].

The electron transportation pattern is classified into surface-, neck-, and grain-controlled modes which depend on particle size r and width of space charge layer L as defined in Fig. 2.7. The surface- (or boundary-) controlled mode ($r >> 2L$) associates with compact layer structures and it is not sensitive to gas reactions. In neck-controlled mode ($r \geq 2L$), the depletion layer around each neck of particle forms a constricted conduction channel within each aggregate [39]. In grain-controlled mode ($r < 2L$), the whole grain is fully depleted

of mobile charge carriers, resulting in a nearly flat energy band throughout interconnected grains. In this case, the entire grain can be harnessed for carrier transport, therefore smaller particle size is preferable.

Overall, the sensitivity is influenced by the layer thickness, pore size, and diffusion length of the carriers. In summary, nanostructured oxides such as nanowires demonstrate superior sensitivity over nanoparticle agglomerates because of increased surface-to-volume ratio with more activated sites and improved electron transport which is attributed to the absence of necks [40].

Modulation of Schottky barrier

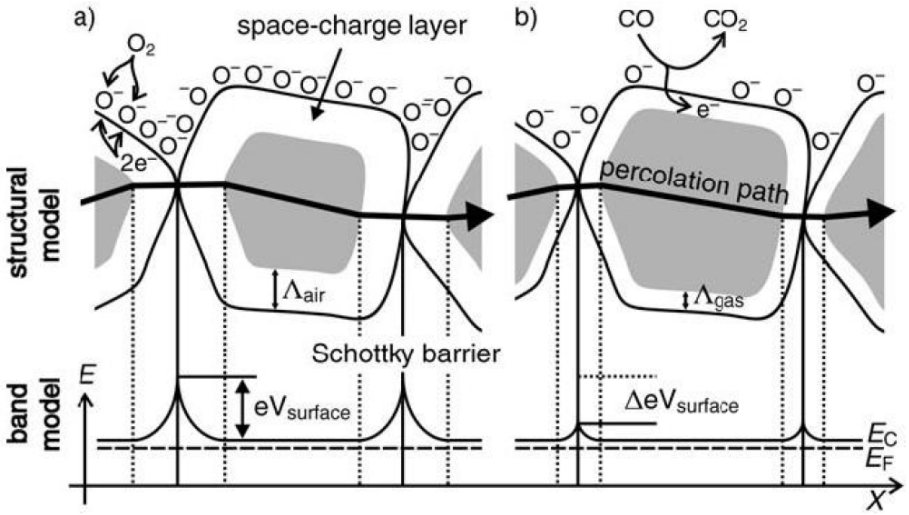

Fig. 2.8 Structural and band diagrams of electron transport upon exposure to gases. (a) with O_2 (b) with CO. Adapted from [30].

When oxygen (O_2) molecules are adsorbed on the surface of MOx nanoparticles (NP), with their high electron affinity, they attract free electrons from the conduction band and trap them in form of O^- ions. This results in band-bending and creates a Schottky barrier at the grain boundaries (Fig. 2.8). The potential barrier prevents electron flow, leading an to increase in electrical resistance.

When MOx is exposed to a reducing gas (which has low oxidation number and usually is hydrogen-rich) such as carbon monoxide (CO) or NH_3, the gas is oxidized by the adsorbed O^- and releases electrons. This reduces the density of adsorbed O^-, thereby reducing the width of the depletion layer. Thus, the inter-granular Schottky barrier is lowered and electrons conduct more easily in-between grains, reducing the electrical resistance. The resistivity for an electron to overcome a potential barrier can be associated with the following relationship

[37]:

$$\rho \propto \exp(\frac{\Delta V}{k_B T}) \tag{2.6}$$

where ρ' is the resistivity, ΔV is the change in potential barrier, k_B is the Boltzmann constant. Further details regarding the mechanisms on metal-semiconductor (graphene-MOx) sensing are detailed in Section 3.2.2.

2.3 Performance measures

After the transduction process, the signal can be transformed by the electronics that is configured for the sensor. The performance measures are the statistical signatures that convey the performances of a sensor. The significance of individual parameters depends on the target application for which it is desired, and should be optimized accordingly. Fig. 2.9 illustrates the common performance measures in a sensor under successive exposure to the analyte.

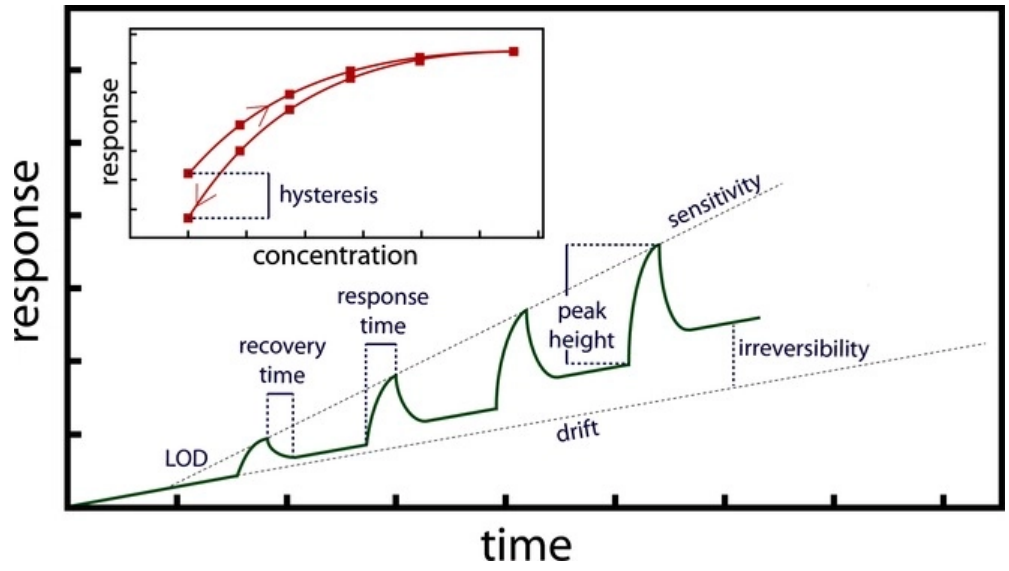

Fig. 2.9 Graphical representation of selected performance measures in a device successively exposed to increasing concentrations of analyte. Adapted from [41]

2.3.1 Characteristic measures

Responsivity: The resistance of a chemiresistive material can be altered by exposure to gaseous analytes. By measuring the change in resistance or current of the sensor device, the

concentration of analytes can be measured. The responsivity S is defined by Equation 2.7.

$$S = \frac{|\Delta R|}{R_0} = \frac{|R_{\text{analyte}} - R_0|}{R_0} \tag{2.7}$$

where R_0 and R_{analyte} are the resistances of the device without and upon exposure to analyte, respectively.

Sensitivity: Sensitivity is defined as the slope of the characteristic responsivity curve [42]. Sensitivity can be enhanced by the promotion of analyte-material interactions through the enlarged surface area and abundant active sites on sensing material surface [11].

Response/recovery time: Response time is the time consumed to reach 90% of the equilibrium value in response to a step change of analyte exposure [43]. Recovery time is the converse of the response time, and it is defined as the time required for the signal to return to its initial value after a step release of the analyte.

Limit of detection (LOD): LOD is the smallest concentration of an analyte that can be distinguished from its absence with 99% confidence interval [44]. The most widely used analytical specification defines LOD as the concentration at the signal that is 3 times of noise level [44]. As the LOD depends on sensitivity and resolution of the sensor, it can be improved through the promotion of analyte-material interactions as well as through signal amplifications [45].

Selectivity: Selectivity describes the extent to which the target analyte can be distinguished among a multi-analyte mixture [46]. It is measured as the ratios of the responsivity of the target analyte to that of the interferents [41]. Selectivity is commonly enhanced by functionalization of analyte-specific receptors upon the sensing material. Another strategy is to construct cross-reactive arrays and process with computational approaches. This strategy will be discussed in Section 2.4.

2.3.2 Sustainability measures

Stability: Stability is a measure that describes the capability that the same output signal can be generated when the same measurement is carried out over time [47]. The parameter is quantified by the percentage changes (including the abovementioned measures like responsivity, sensitivity, selectivity, response/recovery time) in the responses over a different period of time from the same device.

Drift: Drift is the analyte-independent change of a response over a period. This quantity can induce uncertainties in measurements, false alarms, the need for recalibration [41]. Drift may be attributed to a static electric field applied to the device, as well as contamination or

degradation of sensing materials. One approach to mitigate drift due to the electric field is to operate under AC voltage [41]. Drift can also be minimized through the application of computational processing approaches [48].

Hysteresis: Hysteresis measures the difference between outputs at a specific concentration of analyte when the device is approached from increasing and decreasing concentrations. Hysteresis is related to the reversibility of the sensor, where reversibility is the extent to which the signal is restored to its initial state prior to analyte exposure [49]. Full recovery of the sensor is essential for continuous sample monitoring.

Device-to-device reproducibility: Reproducibility is the extent to which a fabricated device can produce the same output signal generated by an alternative device that is fabricated with the identical production method. Device-to-device reproducibility is associated with the capability to synthesize materials and integrate them into sensors in a controllable manner.

The constraints in current technologies for chemiresistive sensors have long restricted their performances in selectivity, drift, and reproducibility. In this thesis, much emphasis has been put on addressing these challenges through the development and optimization of fabrication technologies, as well as signal processing and machine learning algorithms.

2.4 Computational approaches for analyte classification

Due to poor discrimination accuracies in single chemiresitive sensors [50, 51], analyte classification in a mixture of analytes in a real-world environment is traditionally achieved by computational analysis of responses from cross-reactive arrays consisting of a variety of MOx materials [52]. Fig. 2.10 illustrates signal processing procedures to discriminate analyte classes from a multi-analyte sensor array. The sensor array consists of sensors made up of different sensing materials. Depending on the gas and its reaction, every sensor has different conductivity pattern.

Signal pre-processing is essential to generate clean dataset that is useful for analysis. This step involves data manipulation and dimensionality reduction. Data manipulation is useful to eliminate noisy information and normalize data to allow for computation. Common data manipulation techniques include relative scaling, background subtraction, signal averaging, linearization, mean-center, autoscale, range scale, baseline subtraction, etc [52]. Whereas, dimensionality reduction is useful to eliminate duplicate information in the multivariate system to enable extraction of insightful information. Common dimensionality reduction methods include linear discriminant analysis (LDA), principal component analysis (PCA), principal component regression (PCR), and partial least squares (PLS) [52]. PCA is a signal representation technique that generates projections along the directions of max-

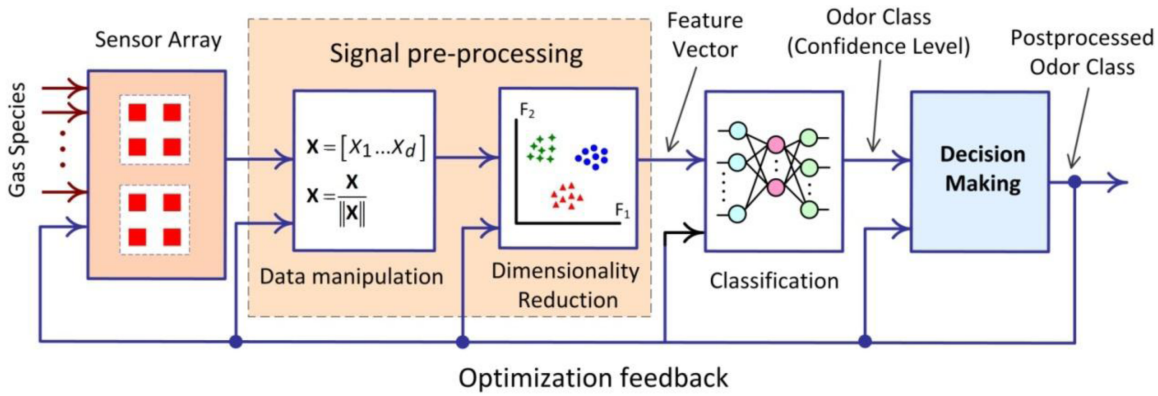

Fig. 2.10 Block diagram for signal processing of multi-analyte sensor array.

imum variance, which are defined by the eigenvectors of the covariance matrix. LDA is a signal classification technique that directly maximizes class separability, generating projections where the examples of each class form compact clusters and the different clusters are far from each other. The LDA algorithm selects features that are most effective for class separability, while PCA selects features important for class representation. In particular, PCA provides an efficient approach for reducing the dimensionality of a dataset and visualization of the clusters formed in low-dimensional projections. Often two or three principal components provide an adequate representation of the data, which is convenient for graphical output. Typically, the calibration data is collected in a feature matrix, M, with m samples and n sensors.

After feature matrix is extracted from the dataset, we can classify the analyte species with cluster analysis. The predictive accuracy is obtained through cross-validation of all the data sets. Prediction model improves the correlation of the data sets and infers a pattern. Common classification techniques comprises k-nearest neighbors (kNN), support vector machine (SVM), random forest (RF), linear discrimination analysis (LDA), neural network (NN) classifiers. Depending on the distribution of dataset in projected dimension and computational complexity, one can evaluate the most suitable classifier.

2.5 Summary

In this Chapter, the comprehensive mechanisms involved in an analytical device in the course of sensing events are reviewed. Various types of sensor architectures are first introduced. The overall sensing mechanisms comprising analyte-material interactions, transduction process, and signal transformation are explained both quantitatively and qualitatively in detail. In particular, interactions at material interfaces involving physisorption, chemisorption, and

diffusion processes are modelled. I explain the transduction mechanisms based on grain-controlled model and thereby the modulation of Schottky barrier. The analysis of these mechanisms offer useful tools for developing new models and algorithms throughout the thesis.

Next, performance parameters are defined and it is noted that the current challenges arise from the restrictions in selectivity, drift, and reproducibility. Finally, the computational approaches for discriminating analytes in a multi-component environment have been reviewed. These approaches are critical for selectivity improvement.

Chapter 3

Materials for Sensing

Semiconducting MOx nanomaterials have been long exploited for the detection of small reactive gases due to their strong responsivity. However, one of the major limitations of MOx materials is that they require fairly high operating temperatures to attain effective sensing performance. These materials also suffer from long recovery time [53–55], severe baseline drift [56, 55, 57], and reproducibility issues [56, 55, 57]. Recently, 2D nanomaterials have proven to be attractive for high performing chemical sensors due to their remarkable electronic and physical properties originating from their 2D structure. Exploiting the synergistic advantages offered by 2D graphene and related material (GRM)-MOx nanocomposites attracts current interest in fabricating high performing low-cost and scalable sensing devices.

This chapter reviews the advances in electrically-transduced chemical sensors that rely on 2D materials (Section 3.1) and their hybrids with MOx (Section 3.2). The material structure and its sensing properties, the mainstream production methods, comprehensive literature on sensing applications, and its limitations are discussed in detail in both sections. For graphene and 2D materials, I focus on the production methods of chemical vapor deposition (CVD) and solution processing techniques which have been employed to date for the demonstration of sensors. The sensing applications focus on the detection of small reactive gases, including the reducing gas NH_3, the oxidizing gas NO_2, and volatile organic compounds (VOCs). These gases have been the target analytes that I sense for which the devices have been fabricated in the experimental chapters.

For GRM-MOx composites materials, I first introduce the sensing properties of MOx. Then I discuss the underlying sensing mechanisms of graphene-MOx composites which build the fundamentals for all the sensors I develop. Next, I explain the mainstream material synthesis methods including hydro/solvothermal method, thermal method, and alternative techniques. The focus will be on the hydrothermal method which will be used in my device fabrication. Finally, this section concludes with the limitations on the materials perspective

and will lead to more advanced techniques for addressing these shortcomings, as discussed in Chapter 5.

Furthermore, to facilitate the fundamental understandings on sensing mechanisms, it is useful to carry out material characterizations. Section 3.3 discusses the principles and practical methods of the common materials characterization techniques I have used throughout the project, including Raman spectroscopy, UV-Vis spectroscopy, AFM, and SEM.

The program I develop for automatic Raman mapping for solution-processed materials in Section 3.3.1 has been employed in my publications [58, 59]. The Raman section (Section 3.3.1) is my original work and does not form part of the literature review.

3.1 Graphene and 2D materials

3.1.1 Material and sensing properties

Graphene and related 2D materials have become attractive candidates for sensing applications. Graphene is a two-dimensional surface material. This structure (Fig. 3.1) enables individual carbon atoms in the graphene film to be in contact with the ambient environment, which makes it sensitive to local chemical and electrical perturbations [60]. Graphene offers greater surface area per unit volume as compared to 1D nanostructures [61]. Moreover, the material exhibits high carrier mobility (CVD: 3×10^4 $cm^2\ V^{-1}\ s^{-1}$ [62], LPE: 100 $cm^2\ V^{-1}\ s^{-1}$ [63]) and high carrier density which generate fast and strong electrical response as a result of efficient electron transport when molecules are adsorbed [64]. Graphene also exhibits low intrinsic noise which allows for high signal-to-noise ratio in sensing [64]. The ambipolar property (i.e. the charge carriers can be either electrons or holes) along with its zero-bandgap permit easy setting of desired operating point by modulating the gate voltage. These properties make it preferable for FET sensing devices. Furthermore, pristine graphene has no dangling bonds on its surface. The target gas molecules cannot therefore easily adsorb onto graphene [65]. Surface modification is often desirable to promote binding of specific analytes which allows discrimination of analytes and optimization of sensor performance. Graphene offers many venues to conduct surface modifications, attachments may include metal nanoparticles [66], organic groups [67], polymers [68], etc. The capability for selectivity enhancement is essential to applications for broadly responsive cross-reactive arrays such as electronic noses.

Related 2D materials such as black phosphorus (BP) [70] and transition metal dichalcogenides (TMDs) including tungsten disulfide (WS_2) [71], molybdenum disulfide (MoS_2) [72] have emerged as gas sensing materials. In addition to the surface area offered by the layered

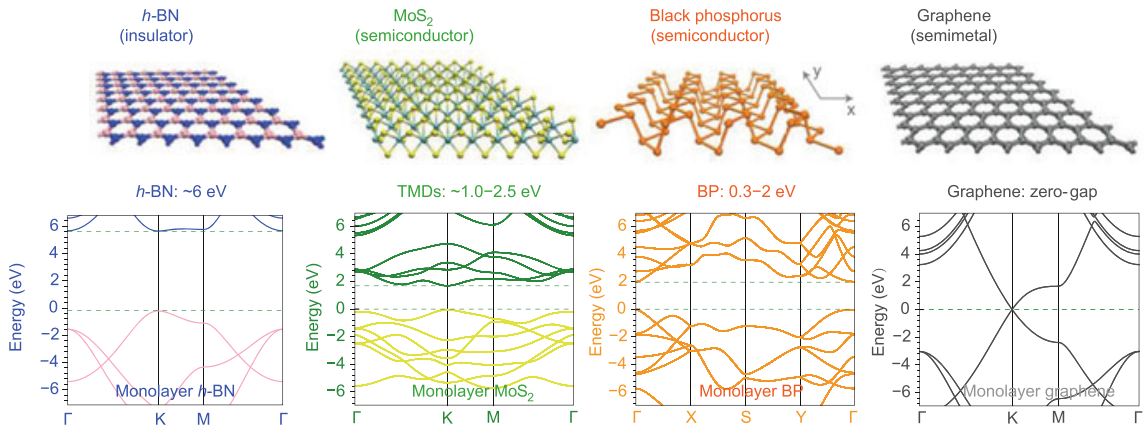

Fig. 3.1 Molecular and band structure of common 2D materials. Adapted from [69].

structure, the semiconducting properties of these materials lead to the formation of Schottky barriers at the electrode contacts [73]. The barrier can then be modulated through the change of doping levels during adsorption/desorption of analytes, translating to change in electrical conductance.

3.1.2 Production methods

Chemical vapor deposition (CVD)

CVD has become one of the most promising techniques for mass production of mono- and multilayer graphene films. CVD produces polycrystalline graphene film with large crystallites up to 50 mm size [62], offering large detection area for sensing applications. Also, the uniform film produced by CVD enables reproducible production of sensors with reliable sensing performance. The large sample size (up to 1 m) of CVD-grown graphene allows large-scale production of miniaturized multi-sensor arrays manufactured by microfabrication technologies [74]. Another advantage of CVD growth is the feasibility of substitutional doping by introducing heteroatoms into the carbon lattice [75].

The CVD method grows graphene film typically on transition metal substrates (e.g., nickel (Ni), copper (Cu)) by exposing carbon precursors in the quartz chamber at low pressure [76]. Fig. 3.2(a) shows a typical CVD setup. Cu is a cheap and weakly interacting catalyst often used as the growth substrate. The growth process involves catalyst pretreatment, carbon precursor exposure, and precipitation [77]. During catalyst pretreatment, Cu nanocrystal is obtained in 1000 °C [77]. Next, during carbon precursor exposure, precursor gas dissociates at Cu sites and carbon is dissolved in Cu. After isothermal growth and pre-

cipitation, monolayer graphene is formed as a self-limiting process [76]. Fig. 3.2(b) shows a sample of graphene crystalline grown on Cu.

Nevertheless, there are still many shortcomings. Since the film is grown on metallic foils, it requires additional transfer process (as illustrated in Fig. 3.2(c)) which introduces additional complexity to the quality such as contaminations from the use of polymethyl methacrylate (PMMA) in wet transfer [78], cracking, and irreversible damages. These complications lead to deterioration of the electronic properties and variations between fabricated devices.

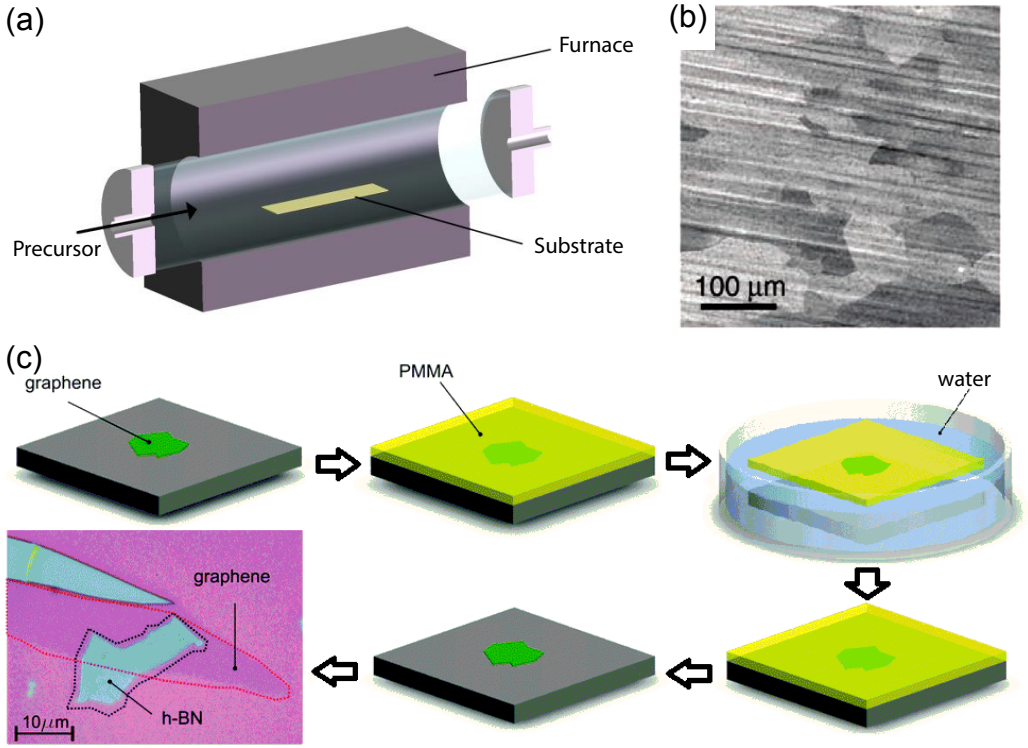

Fig. 3.2 (a) Schematics of a typical CVD set-up. (b) SEM image of graphene grown on a copper foil, scale bar 100 μm [76]. (c) Schematic of a typical wet-transfer process: A graphene sample is deposited onto the silicon (Si)/ silicon dioxide (SiO_2) substrate. A PMMA film is deposited by spin coating. The PMMA film is detached from the substrate via intercalation, and graphene is removed from substrate along with PMMA. Once the sample is fished, PMMA is dissolved by acetone releasing the graphene on the target substrate. A graphene flake deposited onto BN by wet transfer. Adapted from [60].

Solution processing

The solution processing technique is a top-down approach that isolates individual flakes from bulk layered materials via ion intercalation [79], ion exchange [79] or pure sonication.

Solution-processed exfoliation of graphite into graphene oxide (GO), reduced graphene oxide (rGO), or pristine graphene enables up-scalable production of large volume (> kg) of materials at low cost [17]. However, the shortcoming of this method is that the small flake size (tens of μm) produced exhibits poor electrical conductance.

Liquid phase exfoliation (LPE) is a physical approach employing shear forces to weaken the interlayer van der Waals (vdW) forces. Unlike ion intercalation or exchange, LPE does not induce alteration of the properties of the as-produced 2D materials [80, 81]. Pristine graphene can be exfoliated by the LPE technique. LPE involves two processes: ultrasonication and centrifugation or filtration. Ultrasonication first generates cavitation bubbles between the crystal layers. The bubbles then collapse into high-energy jets which weakens the interlayer forces, yielding isolated flakes dispersing in the solution. Sonication method offers the most facile method for mass production [80]. The typical sonication setup is shown in Fig. 3.3. Once the exfoliation is completed, centrifugation is then employed to remove the un-exfoliated pieces of graphite in the dispersion. Further details of this method will be explained in Chapter 4.

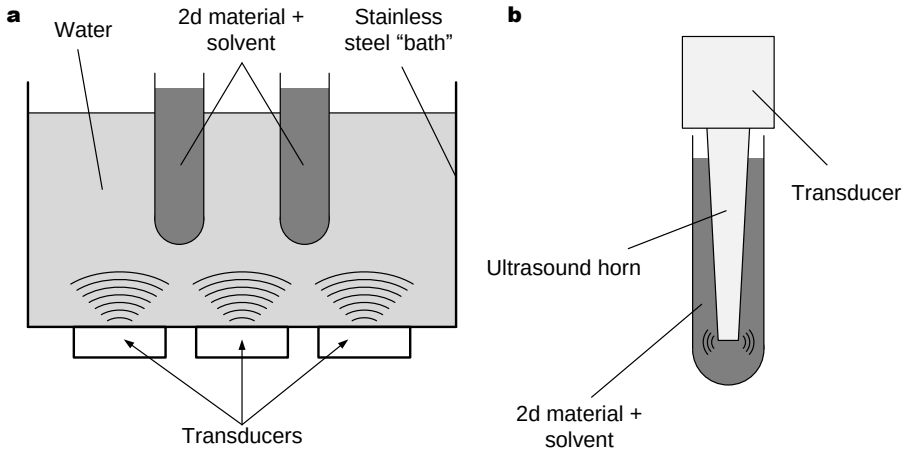

Fig. 3.3 Commonly used LPE techniques: (a) bath sonication, (b) tip sonication.

The structure of GO contains functional groups including epoxy, hydroxyl groups, and pairwise carboxyl groups. Typically, a stable and homogeneous GO suspension is produced by modified Hummers method [82, 83]. However, the defects in GO scatter the charge carriers and create significant noise and reduction in carrier mobility. Many reduction methods [84] have been developed to remove functional groups on GO to produce rGO to restore electrical conductivity. rGO offers rich sites for functionalization which may benefit the sensor performance by augmenting interactions between the target molecules and the functional groups. However, its conductivity is still inferior to pristine graphene.

3.1.3 Sensing applications

The sensing of small molecules with GRM operates through orbital hybridization [11] which creates a charge transfer during the physisorption process. In this thesis, I focus on the review on NO_2, NH_3, VOC, and humidity applications. Note that VOCs are organic chemicals that have low boiling points at the ambient environment. Acetone in exhaled breath is an example of VOCs to be detected in my thesis.

Ref [64] demonstrates a pioneer few-layer graphene chemiresistor device, where the material is produced by mechanical cleavage. Its detection resolves adsorption and desorption of individual gas molecules in step-like changes in resistance (Fig. 3.4), achieving NO_2 detection limit of 1 ppb at room temperature (RT). The level of sensitivity obtained is attributed to the defect-free material which is exceptionally sensitive to tiny chemical perturbation, as well as the low-noise Hall bar structure.

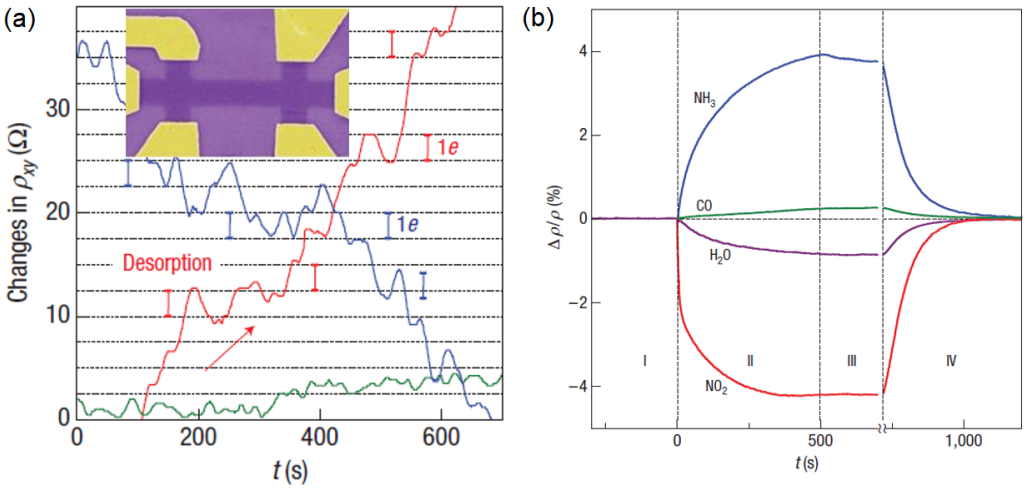

Fig. 3.4 (a) The adsorbed molecules change the local carrier concentration in graphene one by one electron. (Inset) Microscopic image of the device. (b) Changes in resistivity, ρ, while exposure to various gases diluted in concentration to 1 ppm. Adapted from [64].

NO_2 sensors

It is suggested that open-shell adsorbates such as NO_2 can perform direct charge transfers, leading to strong doping effects [18]. NO_2 is an electron acceptor. Upon adsorption of NO_2, the hole density of p-type graphene increases and thus the resistance decreases.

The sensing performance of graphene could also be improved either by doping or by the incorporation of defects. Calculations have shown enhanced interactions with NO_2 with defective graphene [85]. One approach with nanopatterning using colloidal lithography

has shown sensitivity enhancement of pristine graphene gas sensors [86]. The graphene nanomesh (Fig. 3.5) exhibits sensitivities of 4.32%/ppm in NO_2 with limits of detection of 15 ppb [86]. The superior response is attributed to a large number of edges in the nanomesh structure where gas molecules can readily attach to the edges of narrow neck regions which effectively control the charge transport.

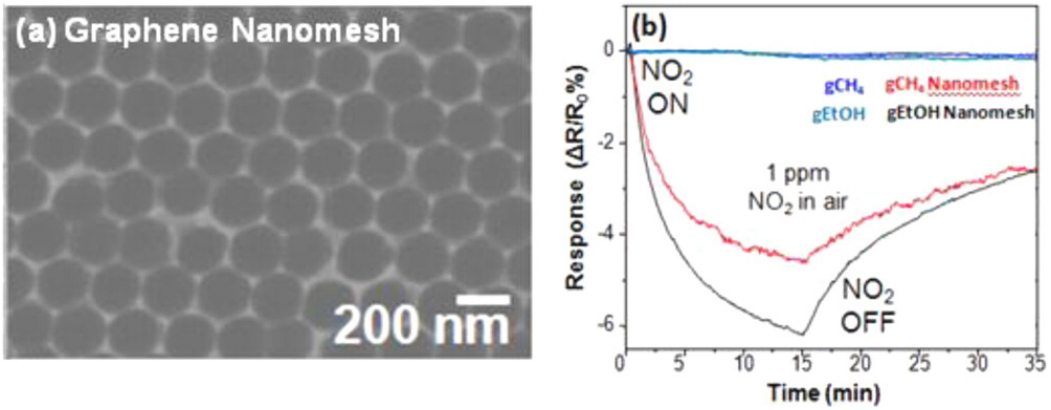

Fig. 3.5 (a) Microscopic image of graphene nanomesh. (b) NO_2 response for gCH_4 and gEtOH nanomesh. Adapted from [86].

LPE-processed GRM sensors have also demonstrated good sensing performances. Ref [87] demonstrates a representative example of NO_2 sensing with inkjet-printed rGO prepared by reduction of exfoliated GO. Uniform film and low detection limit of 400 ppt are obtained [87]. The reduction method (by using Vitamin C) produces rGO film with high electrical conductivity ($\sigma \approx 15\ \mathrm{S\,cm^{-1}}$) and fewer defects [87]. However, with the LPE route, it is essential to balance the trade-offs between edge defects (in favor of sensitivity) and conductivity (promotes carrier transport) in designing sensory devices.

NH_3 sensors

NH_3 is an electron donor. Upon adsorption of NH_3, the holes of p-type graphene deplete during electron transfer and thus the overall resistance increases. Nevertheless, n-type graphene with positive gate bias in a FET device (Fig. 3.6(a)) has been shown to sense NH_3 with improved sensitivity [88]. Additionally, vertically oriented graphene sheets (Fig. 3.6(b)) offers large surface area for detection of low-concentration NH_3 [89].

Volatile organic compounds (VOC) sensors

An attractive chemiresistive vapor sensor constructed by monolayer pristine CVD graphene on Au interdigitated electrode has been reported in Ref [90] (Fig. 3.7). The sensor exhibits

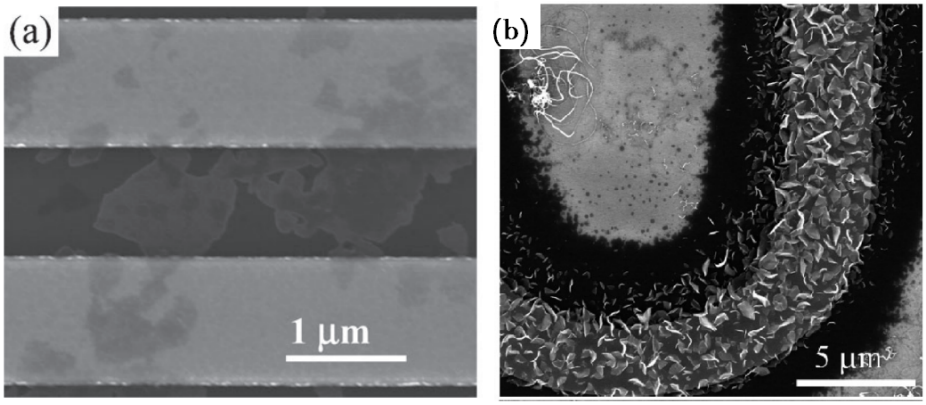

Fig. 3.6 (a) A network of rGO bridging a pair of Au fingers [88]. (b) CNWs grown on letter U, the clear boundaries distinguish gold from SiO_2. Adapted from [89].

excellent selectivity towards both chemically diverse and chemically similar compounds. As classified by machine learning algorithms, the sensor is capable of classifying 11 chemically diverse compounds and 9 monosubstituted benzene compounds with an accuracy of 96% and 92%, respectively [90]. The sensor possesses rapid response and recovery, and reproducibility at RT. Despite excellent prediction capability with the computational technique, the magnitudes of responses for most of the VOCs are rather low due to lack of available binding sites at the pristine graphene.

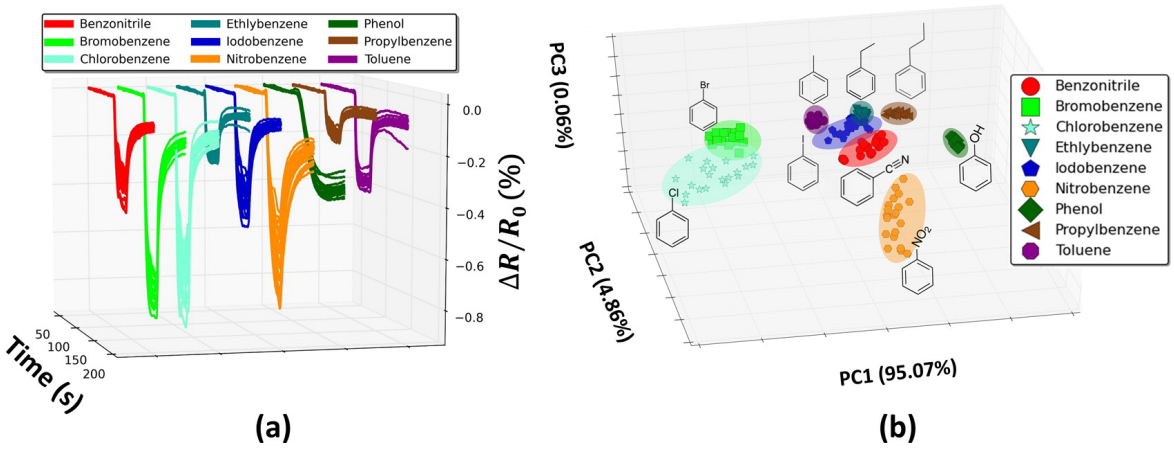

Fig. 3.7 (a) Normalized sensor response to a chemically diverse set of compounds and (b) corresponding PCA transform. Adapted from [90].

Humidity sensors

A representative humidity sensor is fabricated by deposition of GO films by either drop casting or spray coating on top of silver screen-printed interdigitated electrodes on a polyethy-

lene naphthalate (PEN) substrate (Fig. 3.8) [91]. The humidity sensor is operated based on GO's super-permeability to water molecules. The protons generated via the reaction of water molecules with the GO surface functional groups produce a decrease in the electrical impedance [92]. The sensor exhibits unprecedented response and recovery times of 30 ms.

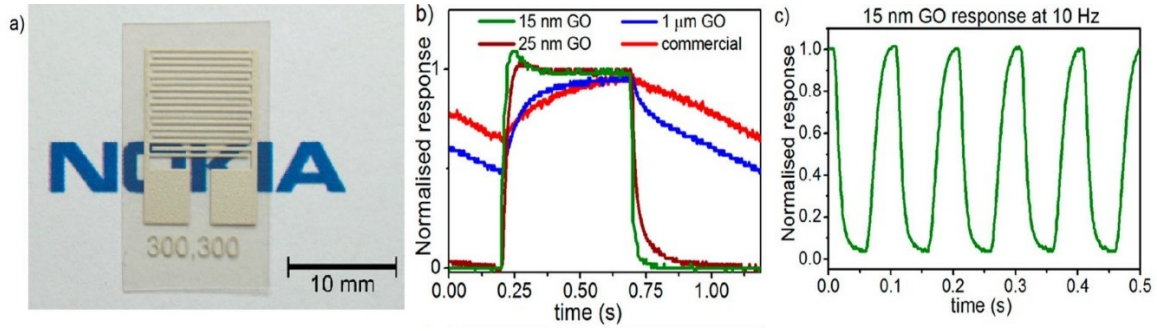

Fig. 3.8 (a) Sprayed GO (transparent) sensing element. (b) Normalized response of the different sensors (c) Normalized response of a 15 nm-thick GO sensor to a modulated humid air flow at 10 Hz. Adapted from [91].

In addition, Ref [93] presents an inkjet-printed graphene-PVP composite onto CMOS device. PVP is used as an active material (without undergoing annealing process) in a PVP-graphene matrix for humidity sensing based on its hygroscopic nature. As moisture adsorbs on the electrically insulating PVP, it causes PVP to swell which leads to a reduction in electrically percolating pathways established by the graphene flakes, resulting in a conductivity change.

Limitations

Despite some reports of demonstrated performance, most devices are far from practical applications due to lack of reproducible, scalable, and controllable fabrication techniques. While employing scalable solution processing techniques, it is essential to balance the trade-offs between edge defects and conductivity in designing sensory devices. These techniques are required to be refined to achieve uniformity in graphene production, to improve stability of measurements and device-to-device reproducibilities.

Furthermore, the selectivity of the sensors requires to be optimized. Discrimination approaches based on the response characteristics of different substances in either time [64], as a function of gate voltage, or by performing classification techniques have been taken to resolve the challenge. Another feasible approach is to combine individual surface-modified sensors as multi-sensor arrays which are known as electronic noses. In this case, miniaturization and functionalization are important to the realization of multifunctional microchips.

3.2 Graphene-metal oxide (MOx) hybrid

3.2.1 Functionalization with MOx

Surface functionalization of graphene or rGO with MOx has proven to be an effective method for improving responsivity and selectivity [60] due to the formation of metal-semiconducting heterojunctions [94]. On the other hand, incorporation of graphene has the capability to offer lowered operating temperatures [95, 96] to conventional MOx sensors.

Applicable MOx materials for gas sensing are transition-metal oxides with d^0 and d^{10} electronic configurations [97]. The d^0 configuration is found in binary transition-metal oxides such as titanium dioxide (TiO_2), WO_3 [97]. Whereas, the d^{10} configuration is found in post-transition-metal oxides, such as ZnO, tin(IV) oxide (SnO_2).

Sensing properties of MOx

The oxygen ions formed within MOx structure dominates the sensing properties including molecular adsorption [98], charge transfer [99], and catalytic performances [100]. The high polarizability of O_2^- causes MOx to exert large and nonlinear distributions of charges within their lattices, creating an electrostatic screening zone that induces significant Coulombic interactions with adjacent ions [101]. A built-in potential will then arise when MOx surfaces are in contact [102]. Due to the strong ionic characteristics of transition MOx, the surfaces of MOx become electronically activated [103], and they become ordered arrays of Lewis acid-base centers, which allow adsorption of small molecules.

Sensing applications of MOx

Taking acetone detection (as studied in experimental Chapter 7) as an example, the materials commonly used are ZnO [104], SnO_2 [105], iron(III) oxide (Fe_2O_3) [106], and WO_3 [33]. A typical performance metrics of common gas sensors in the literature is presented in Table 3.1.

Material	Sensitivity	LoD (ppm)	Resp time	Temp (°C)	Ref
In_2O_3 nanowire	0.6	25	10 s	400	[107]
WO_3 NP	1.5	0.2	3.5 min	400	[33]
ZnO film	5.71	100	30 s	200	[108]
$LaFeO_3$ film	0.7	500	33 s	275	[109]
TiO_2 film	< 4	1	10 s	500	[110]

Table 3.1 Selected literature survey for acetone sensing

Among those, WO_3 is particularly useful for acetone sensing. For example, Si:WO_3 could measure concentration down to 20 ppb of acetone [111]. The mechanism behind the selectivity of WO_3-based sensing materials is believed to be attributed to the spontaneous electric dipole moment of WO_3. It increases the interaction with gas molecules with high dipole moment [111]. The dipole moment of acetone is 2.88, which is larger than most of the other gases (NH_3, H_2O, and ethanol) presented in breath. NH_3, H_2O, and ethanol has a dipole moment of 1.46, 1.85 and 1.69 [112], respectively. Therefore, the sensor exhibits a higher response to acetone.

One of the limitations of WO_3 semiconductor, however, is that since the depletion region can be too wide, and thus the barrier can be too high for electrons to overcome, resulting in low conductivity at ambient temperature. In order to compensate for this effect, high operating temperature (300-500 ℃) [107, 33, 110, 113] is used for sensing.

Furthermore, a single MOx sensor is unable to distinguish different analytes and its response is easily affected by the presence of other gases. A feasible solution is to construct a multi-sensor array. For example, Hwang et al. made a sensor array consisting of TiO_2, indium tin oxide (ITO), SnO_2, and WO_3 to sense hydrogen (H_2), CO, and NO_2 [114].

Limitations

One of the major limitations of MOx materials is that they require fairly high operating temperatures to attain effective sensing performance due to the threshold of activation energy in chemisorption processes [11]. High temperature is also an essential condition for the desorption of some gas molecules, allowing for electrical resistance recovery back to baseline. The constraint on temperature not only poses an obstacle for reduction of power consumption but also deteriorates material's structural stability, leading to shortened lifetime and compromised responses [97]. It also limits potential applications based on textile or flexible polymer substrates e.g. PET which cannot sustain above 150 ℃.

Moreover, due to the wide depletion layer induced around the MOx NPs, it imposes a large energy barrier for electrons to transfer between grains, and thus slows down the response of the device [115]. Another limitation is the low selectivity of most MOx sensors. A feasible solution is to construct a multi-sensor array. The pattern of distributed response may be classified using machine learning classifiers.

3.2.2 Sensing mechanisms of graphene-MOx hybrid

The graphene-MOx hybrids reported to date exhibit improved responsivity [56] which is attributed to the formation of local metal-semiconducting (M-S) heterojunctions [94, 116], as well as the enhanced gas adsorption capacity at the active graphene sites [94, 57].

The sensing principle of graphene-semiconducting MOx NPs is described as follows. When gas molecules are adsorbed or desorbed at the interface, the modulation of potential barriers between grain boundaries will result in exponential increase or decrease in resistivity. Nevertheless, the variation in resistance will be amplified when loaded with a small concentration of graphene [94].

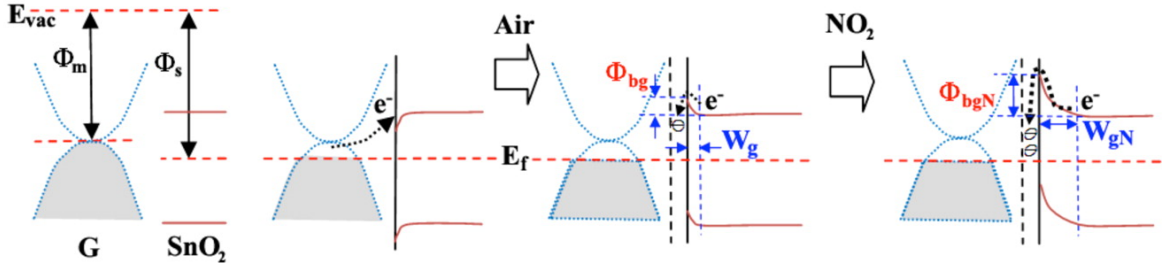

Fig. 3.9 Band diagram for NO_2 sensing at graphene-SnO_2 interface. W_g: depletion width in air; Φ_{bg}: potential barrier in air; W_{gN}: depletion width in NO_2; Φ_{bgN}: potential barrier in NO_2. Adapted from [94].

When graphene is uniformly distributed in MOx matrix, M-S junctions are formed at the interfaces. Taking SnO_2 as an example, because the work function of SnO_2 $\Phi_s > 4.7$ eV is greater than graphene $\Phi_m \approx 4.5$ eV, the interfaces form Ohmic contacts in vacuum, as depicted in Fig. 3.9. Upon exposure to air, the potential barrier Φ_{bg} at M-S contact is smaller compared with that of pure SnO_2 NPs because electrons near the interfaces have been acquired. The reduction in the barrier is represented as receded depletion region in Fig. 3.10(a). Upon NO_2 exposure, the interfaces act as active sites [117] which improves gas adsorption. The improved gas adsorption results in greater expansion of depletion width and a greater increase in potential barrier compared with those of pure SnO_2 [94]. Since the resistance has exponential relationships with the increased potential barrier, the sensitivity of the sensor enhances dramatically [118].

As graphene loading increases, since graphene has high conductivity, the majority of electrons transports via the interconnected graphene flakes, bypassing the path through MOx NPs (as indicated in Fig. 3.10(b)), resulting in a dramatic reduction in sensitivity.

In summary, the amplification of resistance variation is contributed by two effects: (1) the expansion of conduction channel in air due to Ohmic contact; and (2) the enlarged change in resistance upon gas exposure due to improved gas adsorption at the interface.

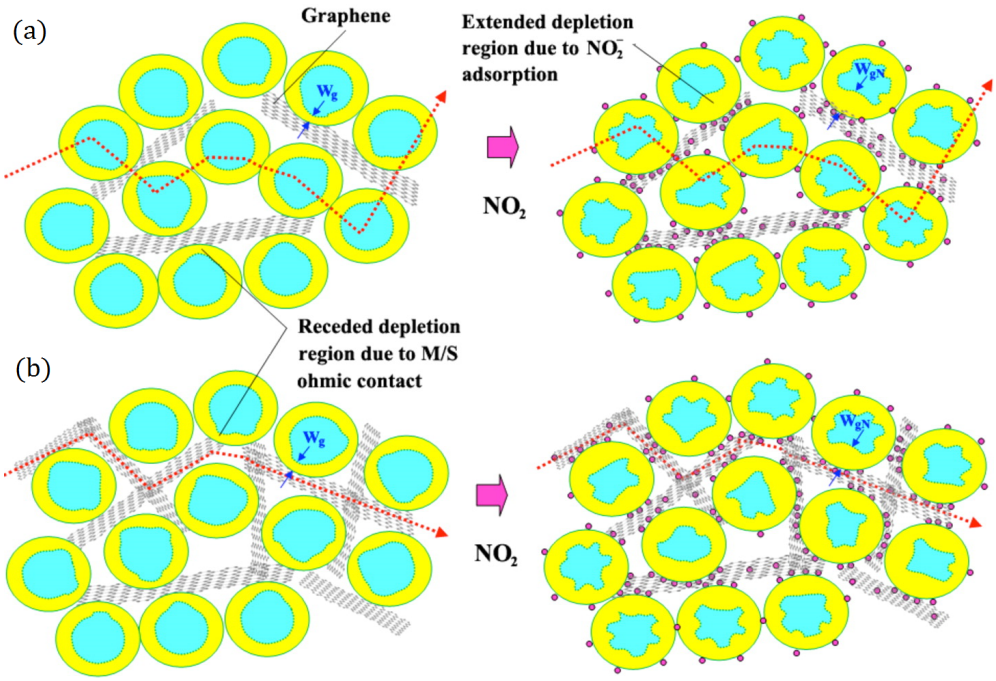

Fig. 3.10 Representative physical models for NO_2 sensing mechanisms of SnO_2 nanoparticles loaded with graphene at (a) moderately low and (b) high graphene loadings. Adapted from [94].

3.2.3 Approaches for performance improvement

In this section, the approaches for improvements for sensitivity, selectivity, and lowered temperature operation in sensor performances are further analyzed with respects to the control of their material, structural, and electronic properties.

For sensitivity improvement

Apart from the effect of M-S material interfaces discussed in the previous section, the surface morphology of the sensing material plays a key role in sensitivity. It has been proven that graphene with edge defects is able to enhance interactions with small molecules like NO_2 in particular [85]. This property is especially useful for LPE-produced materials in which defects have been created during production processes. In such sensing devices, deposition of graphene/MOx hybrid in multiple layers would maximize the total area of gas exposure to these heterojunctions (as opposed to exposure to single interfacial layer) and thus enhancements in sensitivity. The argument is practically supported by the literature on thin-film MOx/graphene hybrid composite sensors demonstrating profound sensitivities [11].

High porosity surfaces in other low-dimensional structures are also proven to improve sensitivity. Ref [110] reports porous TiO_2 nanoparticles made by flame spray pyrolysis. The

sensor showes a sensitivity of 8 under exposure of acetone with a detection limit of 1 ppm. Ref [119] reports porous TiO_2 nanotube made by hydrothermal synthesis, achieving a sensitivity of 50 for toluene detection. The sensitivity enhances when the size of nanowires is decremented such that the depletion layer is greater than their diameters [120]. Furthermore, Ref [121] reports sensitive NO_2 detection using NiO sheets with large degree of mesoporosity. The hybrid of those mesoporous materials with graphene offers great potential for further sensitivity improvements.

For selectivity improvement

Sensing properties of nanostructure greatly rely on the crystal defect structure in the material [11]. Taking ZnO (which is extensively employed in the thesis) as an example, its intrinsic defects including oxygen vacancy and zinc interstitial sites, lead to adsorption of nitrate and nitrite anions species onto its surface [122] and exhibits excellent selectivity at a particular operating temperature. Additionally, creating local polarized covalent centers [123] or p/n heterostructures [124] may also improve selectivity. For example, selective adsorption of NH_3 may be contributed by the cancelation of the opposite responses of n- and p-type MOx nanomaterials [124].

For operating temperature reduction

MOx often require high operating temperature to overcome the activation energy threshold in order to trigger the reaction between the analyte and surface-adsorbed oxygen [125]. Control over structure and surface chemistry can offer a route for room temperature sensing [126]. Ref [96, 127] have shown the elimination of oxygen activation layer through blending of Cu_2O with rGO, to achieve room temperature operation.

3.2.4 Production methods

Low-dimensional MOx-based composites nanostructures are favorably produced by bottom-up approaches due to the advantages of easy controllability, cost-effectiveness, fewer defects, and homogeneity in composition [37]. Among MOx and GRM hybrids, MOx-rGO presents a stable form of composite due to the established bondings between the two. The most common approaches in the literature for synthesizing these composites include solvo/hydrothermal method [117, 96, 128–131], and thermal reduction [132, 133] techniques.

Hydro/solvothermal synthesis

Hydro/solvothermal synthesis is the most widely used method for production of MOx-rGO composites, in which MOx including SnO_2 [117, 130], copper(I) oxide (Cu_2O) [96], indium(III) oxide (In_2O_3) [128], Fe_2O_3 [129], WO_3 [131], etc have been synthesized for sensing applications. This method allows synthesis of high purity and single crystalline samples with convenient and easily controllable reaction based on temperature [134]. Fig. 3.11(a) shows the hydro/solvothermal setup. The method offers a tool of using solvents in a tefflon-lined steel vessel and conducting reactions at a temperature well above boiling points. Pressure is built-up in the vessel by the solvent vapor, promoting crystal growth due to the elevation in boiling points [37].

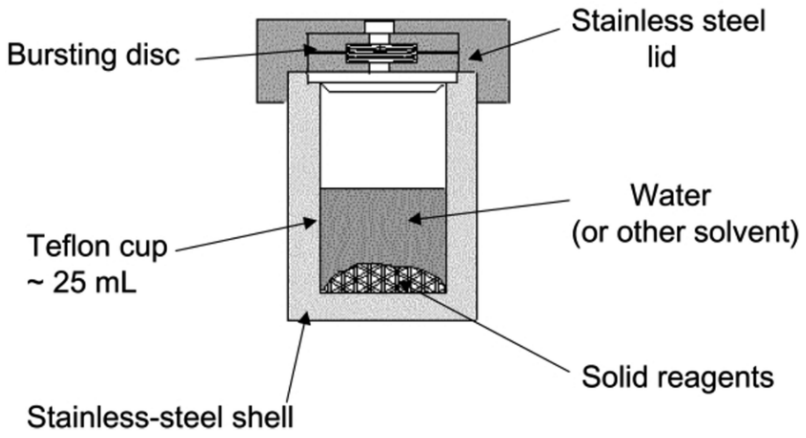

Fig. 3.11 Setup for hydro/solvothermal synthesis. Adapted from [134].

The supercritical water formed in the pressurized aqueous solution can act as a reducing agent for the reduction of GO [135]. Supercritical water not only partly removes the oxygen-containing functional groups, but also restores the aromatic structure [136], producing highly reduced graphene (HRG) suspensions. On the other hand, the method is effective in yielding nanowire-like MOx nanostructures. The growth of nanocrystal is via the oriented attachment mechanism which results in particular shape due to preferential attachment of the crystal planes [137].

The MOx NP/rGO composite is produced by the nucleation of NPs grown on GO in the high temperature and pressure environment. The existing hydroxyl (-OH) and carboxyl (-COOH) functional groups on GO serve as nucleation sites for NP growth and form covalent metal-O-C bonds [138]. Moreover, GO acts as a template to promote preferential growth of MOx nanocrystals and to prevent the agglomeration of MOx NP [117].

The factors that affect the growth process include the precursors, solvents, pH, temperature, and reaction time [37]. These factors contribute to the morphology, size, and level of impurities/defects of the nanomaterials and affect their physical and chemical properties [37]. Higher pH value tends to yield stable HRG dispersions, while HRG aggregates in an acidic dispersion [135]. HRG/MOx is commonly yielded in solvents such as ethanol-water mixture [139] and glycol [138] due to their reducing capabilities. Furthermore, the morphology of NPs on HRG sheets can be controlled by the ionic liquids. Ref [140] shows that ionic liquids facilitate the production of TiO_2 NPs.

In summary, the hydrothermal method allows control of the crystal defect structure or oxygen vacancies in the material, which may translate to sensitivity and selectivity [122]. The method can also produce mesoporosity in nanostructures to enhance sensitivity [141] and to reduce response time [142]. However, the main drawbacks of this method are the slow reaction kinetics [134] and a poor control of the grain morphology and size [134] that affect the conductance of materials.

Thermal reduction

MOx-rGO composites can also be prepared through thermal treatment of deposited GO in a matrix of pre-deposited MOx layers. HRG can be prepared by the thermal exfoliation and reduction of GO through rapid heating of GO under inert gas and high temperature (1050 ˚C) [143]. The heating led to the decomposition of oxygen-containing functional groups attached on the carbon plane of GO [143]. However, the release of CO and CO_2 during the thermal exfoliation process causes significant structural damage to the platelets [143], leading to adverse effects on their electronic properties [144]. Moreover, the high temperature processing used in this method is not compatible with industrial fabrication techniques.

Alternative methods

Alternative methods are developed to construct MOx nanostructures with high porosity and surface area, as introduced as follows. 2D MOx nanosheets can be exfoliated by surfactant self-assembly using lamellar reverse micelles [145]. 2D metal oxides without the intrinsically layered structures (e.g. ZnO) is obtained via morphological transformations [145], self-assembly from its oligomers [145], and salt-template methods [146]. Whereas 3D mesoporous single-crystal can be made by growing inside a mesoporous template immersed in dilute reaction solution [147]. The produced MOx nanostructures are then grown, deposited, or mixed with GRM to establish hybrid interfaces for high sensing performances.

Device fabrication. After synthesis using any of the abovementioned methods, the as-prepared nanostructure can be dispersed in a solution containing binders. The functional materials are often deposited by drop- or spray- coating onto micro-fabricated contact pads. After deposition, the coated substrate requires high temperature annealing. With strong oxidizing power, good chemical inertness, low cost, non-toxic, and high surface-to-volume ratio, nanostructured MOx/GRM is promising for gas sensing [37].

3.2.5 Sensing applications

In this section, I focus on sensing applications for the detection of NH_3, NO_2, and VOCs which have been developed in this thesis.

NH_3 sensors

The comprehensive literature survey (Table 3.1) shows the comparison between different representative nanomaterial-based sensors to date. The commonly studied nanomaterial-based sensors are classified into 2D materials [148, 149, 71, 70, 72], pure MOx [150–154], 2D/MOx hybrids [117, 132, 123, 155, 156, 133, 157], and organic materials, including polymer [149] and metal–organic frameworks (MOF) [158–160].

In Table 3.1, responsivity is compared at the concentration of desired application (10 ppm of NH_3) if applicable. Baseline drift/sensitivity shows the average drift in one cycle, represented as the percentage of sensitivity computed. Selectivity is quantified by the ratio of sensitivity of NH_3 to the next sensitive interfering gas presented. The text in brown indicates poor performance, whereas the text in green indicates excellent performance.

For pure MOx, the adsorption of NH_3 on the surfaces reduces the Schottky barriers, resulting in decrease in resistance. Commonly used MOx for NH_3 sensors include WO_3 [150], SnO_2 [151, 161], In_2O_3 [151], copper(II) oxide (CuO) [152], ZnO [153], and TiO_2 [154]; with nanostructures ranging from nanoparticle, nanorod, to nanofibre.

In particular, ZnO is a chemically stable n-type semiconductor with high electron mobility and conductivity. It has been long exploited for NH_3 detection due to its strong response [162, 117] attributed to its oxygen vacancy and Zn interstitial sites [122].

Table 3.1 Literature table of performance matrix of selected sensors based on nanomaterials and their hybrid composites

Type	Material	Responsivity	Baseline Drift/Sensitivity	Selectivity (coefficient to interfering gas)	LOD	SNR; Stability	Ref
2D	Gr (pristine)	~1.9% @ 10 ppm	53%	Very poor (0.12 - NO)	83.7 ppb	3	Chen2012
	rGO	~21% @ 10 ppm	Not recoverable	Good (1.9 - VOCs)	1 ppb	Noisy	Hu2014
	WS_2	~900% @ 10 ppm	11%	Good (2.2 - ethanol)	1 ppm	Noisy	Li2017
	BP	~30% @ 10 ppm	47%	Poor (1.3 - NO_2)	1 ppm	4.8	Donarelli2016
	MoS_2	~3% @ 10 ppm	67%	Very Poor	0.3 ppm	38	Lee2013
MOx	WO_3 nanofibre	44% @ 10 ppm	3.6%	Good (4.6 - NO_2)	N/A	OK	Leng2011
	SnO_2 nanorod	25% @ 10 ppm	N/A	N/A	N/A	Noisy; Unstable	Rout2007
	In_2O_3 nanorod	10% @ 10 ppm	N/A	N/A	N/A	Noisy; Unstable	Rout2007
	CuO nanofibre	10% @ 10 ppm	N/A	Very Poor (0.25 - H_2S)	3 ppm	Noisy; Unstable	Zhou2018
	ZnO	27% @100 ppm	56%	N/A	50 ppm	Noisy	Li2014
	TiO_2	8% @ 10 ppm	Negligible	N/A	5 ppm	-	Dhivya2014
2D/Mox	Gr/SnO_2	6% @ 10 ppm	28%	N/A	10 ppm	-	Lin2012
	rGO/ZnO	1.2% @ 10 ppm	8.30%	Good (2 - NO_2)	N/A	Unstable	Zhang2017
	rGO/Co_3O_4 nanofibre	27% @ 10 ppm	N/A	Good (6.7 - VOC)	5 ppm	Noisy	Zhang2017
	MoS_2/ZnO	37.5% @ 10 ppm	0.37%	Good (6.3 - CO)	12 ppb	Noisy; Unstable	Tai2016
	MoS_2/Co_3O_4	65% @ 5 ppm	17%	Good (2.6 - ethanol)	0.1 ppm	Noisy; Unstable	Feng2016
	WS_2/WO_3	80% @ 10 ppm	N/A	Poor(1.25-H_2)	1 ppm	OK	Perrozzi2017
	SnS_2/SnO_2	16% @ 10 ppm	20%	N/A	10 ppm	Noisy; Unstable	Xu2015
Organic	Polypyrrole	8% @ 50 ppm	25%	N/A	N/A	Very Noisy	Hu2014
	Cu_3HHTP_2	25% @ 10ppm	10%	Good (3.25-acetone)	0.5 ppm	-	Yao2017
	$Cu_3(HIIP)_2$	2.5% @ 10ppm	16%	N/A	0.5 ppm	Unrepeatable	Campbell2015
	Cu_3HHTP_2 and Ni_3HHTP_2	0.3% @ 10ppm	Profound	Very Poor (0.6-NO)	2.5 ppm	Very Noisy	Smith2016

For organic materials, although the best performing Cu-2,3,6,7,10,11- hexahydroxytriphenylene (Cu_3HHTP_2) sensor [158] shows good selectivity, it is produced by a layer-by-layer (LbL) liquid phase epitaxial method which is not scalable, and it has high baseline drift and low sensitivity, making it unsuitable for practical applications.

Selectivity in the ambient environment is a critial criteria for applications. The works like rGO/cobalt(II,III) oxide (Co_3O_4) nanofibre [123], MoS_2/ZnO [155], WO_3 nanofibre [150] perform superior selectivity over others. On the other hand, scalability and miniaturization are also important for practical implementation. The reports to date are not fabricated with scalable methods (e.g. electrospinning and LbL self-assembly). The reliability of sensing performances is also crucial for applications. Most sensors reported to date have not demonstrated stable responses, sufficient SNR (signal-to-noise ratio), and device-to-device consistancy; in most reports, only single devices are studied.

Fig. 3.12 summarizes the selected literature on MOx/graphene NH_3 sensors. Ref [117] synthesized SnO_2/graphene composite via a simple one-pot hydrothermal method with tin(II) chloride ($SnCl_2$) as the precursor and GO as template. It exhibits 3D nanostructure of flower-like SnO_2 nanoflakes distributed among the graphene layers. It shows 6% responsivity at 10 ppm, response and recovery time < 1 min. However, the baseline drift of 28% is severe. Ref [132] produced ZnO NP/rGO thin film by spray-coating ZnO colloids and subsequent thermal reduction of GO. Although the production method is very simple, the performances are poor with low sensitivity and unstable responses. Ref [123] synthesized encapsulated Co_3O_4-rGO nanofibres using electrospinning. It shows 27% responsivity at 10 ppm and excellent selectivity (best at 6.7) against VOC interferents. The selective NH_3 adsorption is attributed to the polarized C-Co_3^+ covalent centers within the nanofibers, and the hierarchical wrapping microstructure. [123] However, it shows a long recovery time of 5 min.

More recently, transition metal dichalcogenides (TMDs) 2D materials such as MoS_2 [155, 156], WS_2 [133], tin(IV) sulfide (SnS_2) [157] have been synthesized with MOx to study the sensing properties of those composites. Apart from the layered nanostructures, these TMDs possess semiconduing properties [11] which are harnessed to create p-n junctions with semiconducting MOx to improve sensing performances [156, 157].

Ref [155, 156] reports multi-layered MoS_2/MOx composite film fabricated by an LbL self-assembly technique. The MoS_2/Co_3O_4 sensor [156] exhibits sensitivity of 65% at 5 ppm. The sensing property is ascribed to the heterojunction created at the interface of n-type MoS_2 and p-type Co_3O_4. However, the production method is not scalable and the SNR is low, preventing them from practical applications. Ref [133] presented WS_2/WO_3 composite produced by drop-casting WS_2 dispersion and subsequent thermal treatment in air. It exhibits

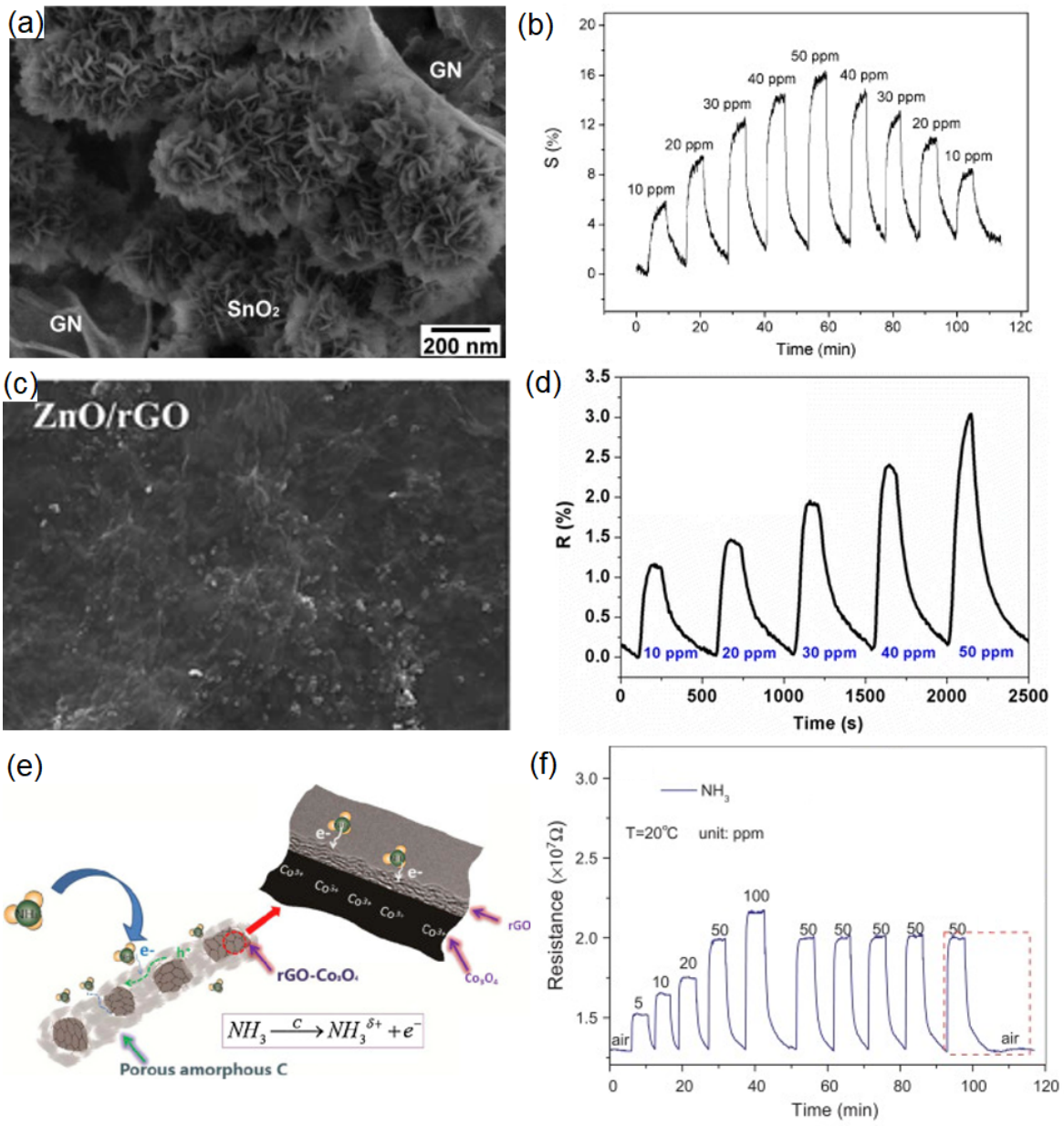

Fig. 3.12 (a) SEM of SnO_2/graphene [117]. (b) Response of SnO_2/graphene device [117]. (c) SEM of ZnO NP/rGO [132]. (d) Response of ZnO NP/rGO devices [132]. (e) Illustration of Co_3O_4 nanofibre /rGO [123]. (f) Response of Co_3O_4 nanofibre /rGO [123].

80% responsivity at 10 ppm NH_3 with 1 ppm detection limit. However, the selectivity of this composite is poor, as it is also sensitive to H_2 and NO_2 due to physisorption mechanism [133].

NO_2 sensors

rGO functionalized with MOx including ZnO [55, 163], Cu_2O [96], In_2O_3 [128], Fe_2O_3 [129], SnO_2 [164, 165, 130, 166], WO_3 [131], NiO [141] have been studied extensively for NO_2 detection. Due to oxygen vacancies presented in these oxides, oxidative NO_2 gas with high electron affinity can capture electrons from conduction bands of the oxides, resulting in an increase in resistance. The rationale for using rGO is that its high porosity not only provides sufficient active sites for gas adsorption, but also supplies channels for gas diffusion [167].

Table 3.2 summarizes the sensor performances in literatures using MOx-rGO hybrids.

Material	Conc(ppm)	Resp(@ppm)	Resp/Recov	Temp(°C)	Select	Fab	Ref
ZnO-rGO	1-25	0.26@5	165/499s	RT	poor	easy	[55]
Cu_2O-rGO	0.4-2	0.68@2	400/600s	RT	N/A	easy	[96]
Cu_xO-rGO	0.1-97	0.7@4.8	20.6/-s	RT	N/A	easy	[127]
In_2O_3-rGO	5-100	8.25@30	4/24min	RT	good	easy	[128]
Fe_2O_3-rGO	0.18-90	0.4@9	100/800s	RT	good	easy	[129]
In-SnO_2-rGO	0.3-100	0.7@5	500/1000s	RT	good	easy	[164]
SnO_2 NF-rGO	1-5	100@5	100/100s	50-250	good	hard	[165]
SnO_2 NP-rGO	0.5-500	3.31@5	75/300s	30-60	poor	easy	[130]
SnO_2-rGO	2-8	10@8	50/500s	50-350	N/A	hard	[166]
ZnO-rGO	0.5-5	6.8@5	45/65 min	250	poor	hard	[163]
WO_3-rGO	0.025-20	61@1	50/50s	300	good	easy	[131]
NiO-rGO	1-15	4.7@5	200/400s	200	good	hard	[141]

Table 3.2 Literature survey for NO_2 sensing

The following reports (as summarized in Fig. 3.13) show NO_2 sensors operating at room temperature. Ref [96] synthesized rGO-conjugated Cu_2O nanowire mesocrystals by crystallization under hydrothermal conditions. The sensors are fabricated by drop-casting rGO/Cu_2O onto pre-patterned electrodes. The LoD is 0.4 ppm and sensitivity is 0.68 (at 2 ppm), while the detection range is narrow and the response/recovery time are very long (400/600 s). Ref [127] demonstrates a novel 3D nanoflower-like Cu_xO/multilayer graphene composite. It shows a high sensitivity of 27% at RT, LOD of 97 ppb, a response time of 58 s, and good linearity. However, the preparation method is very complex. These reports show that blending of Cu_2O with graphene or rGO can eliminate the need for oxygen activation layer [168], achieving RT operation.

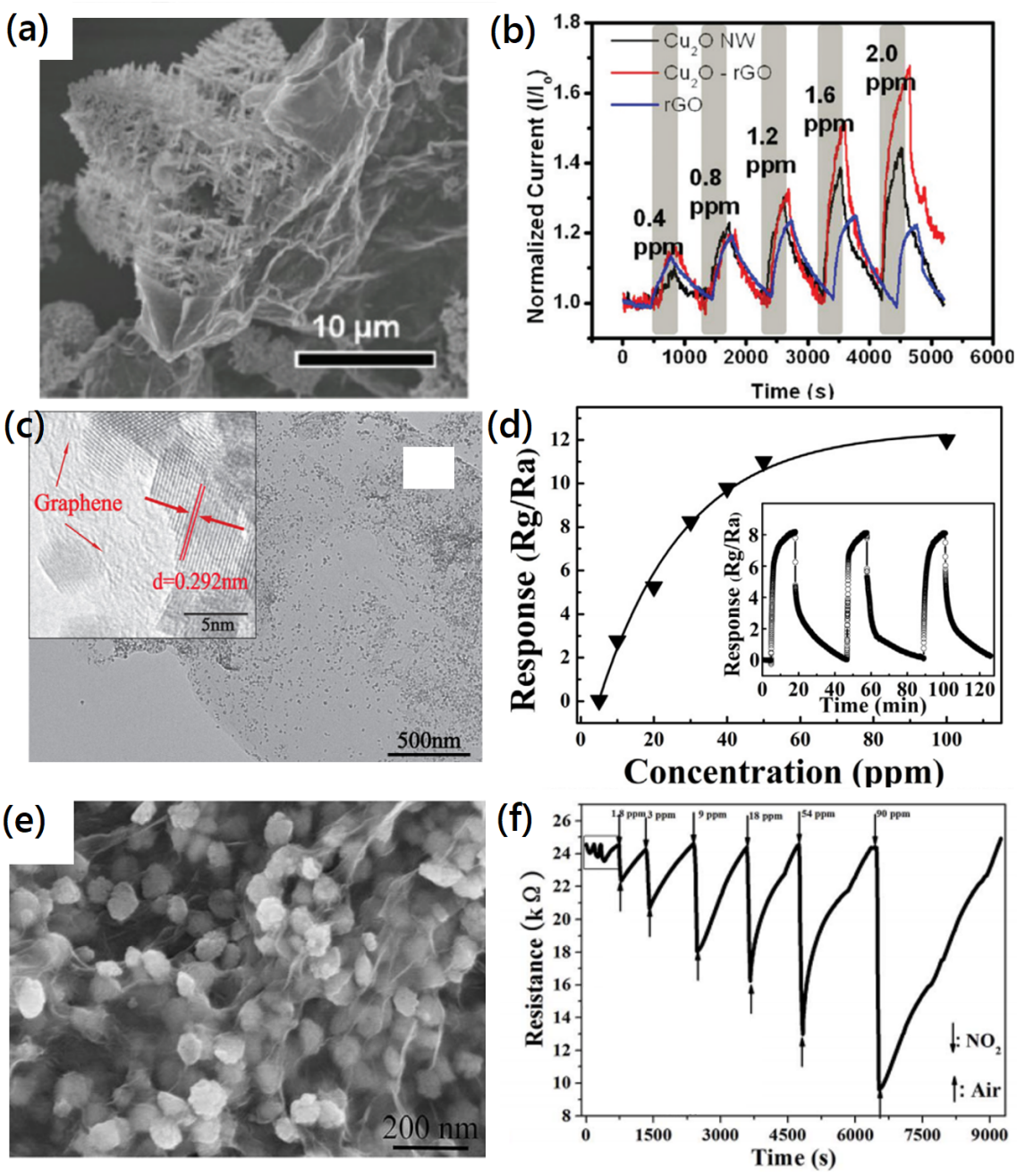

Fig. 3.13 (a) SEM of Cu_2O/rGO nanowire mesocrystals [96] (b) Response comparison of Cu_2O/rGO, Cu_2O nanowire, and rGO devices [96] (c) TEM and (inset) HRTEM of In_2O_3/rGO [128] (d) Response of In_2O_3/rGO device [128] (e) TEM of α-Fe_2O_3/rGO [129] (f) Response of α-Fe_2O_3/rGO device [129]

The following reports show the capability of fabricating sensitive and selective NO_2 sensors using facile hydrothermal process. Ref [128] synthesized In_2O_3/rGO composite by a simple hydrothermal method, using GO and $In(NO_3)_3$ precursor at 200 ˚C for 24 h. The suspension is coated followed by aging. The sensor shows sensitivity of 8.25 at 30 ppm, good linearity within 5-60 ppm, and good selectivity. However, the response/recovery time are extremely long (4 / 24 min). Additionally, Ref [129] synthesized α-Fe_2O_3/rGO using facile hydrothermal process followed by spin-coating deposition. It is capable of RT operation with 180 ppb detection limit. It exhibits good linearity and selectivity to NO_2.

The following reports show improved sensitivity and selectivity using more complex production methods. Ref [169] develops In_2O_3 cube/rGO sensor and shows excellent sensitivity and selectivity against interferrants. The author attributes this to the effective electronic interaction between n-type In_2O_3 and p-type rGO via the hybrid architectures [169]. Additionally, Ref [165] synthesized SnO_2 nanofibre with rGO using electrospinning. The interface creates local p–n heterojunctions, providing a potential barrier and a local electron absorption reservoir [165]. It exhibits excellent sensitivity of 100 at 5 ppm and 200 ˚C with rGO loading of 0.44 wt%. It shows good selectivity. However, it experienced long response/recovery time and is difficult to prepare.

Limitations

Despite of improved sensitivity, selectivity, and lowered operating temperatures that can be realized with MOx/GRM nanostructure hybrids, critical issues common to chemiresistive sensors such as long response/recovery time [53–55, 96, 128, 164, 163], severe baseline drift [56, 55, 57], low SNR and unstable responses [56, 55, 57], poor device-to-device consistency [170], selectivity issues [55, 130, 163] including interference with VOCs [171] and water vapor [117], require to be further improved.

Based on existing literature on other material platform, I hypothesize that dynamic control of operating temperature could be applied to improve detection limit [38], baseline drift [172], cross-selectivity [173, 174], and power consumption of MOx and 2D material gas sensors. This approach is further developed in Chapter 5.

3.3 Material characterization techniques

To facilitate the fundamental understandings on sensing mechanisms, it is useful to carry out material characterizations. Here, I introduce the common spectroscopic and microscopic techniques used throughout this thesis.

3.3.1 Spectroscopy

Raman

Raman spectroscopy is the most widely used non-destructive techniques for studying the interatomic vibrations (phonons) of 2D materials [175, 176]. Raman spectroscopy uses a monochromatic laser to interact with molecular vibrational modes and phonons in a sample, shifting the laser energy down (Stokes) or up (anti-Stokes) through inelastic scattering [177]. Identifying vibrational modes using only laser excitation, Raman spectroscopy has become the most powerful method to characterize 2D materials [178]. The characterization is conducted on the samples deposited on a Si/SiO_2 wafer or device to assess the composition of the printed film.

I develop a MATLAB program that automatically analyses raw Raman data to evaluate characteristics Raman peaks of printed graphene sensing film, as well as to generate mappings of oxidation level of printed BP film. The data is fitted to the Lorentz equation:

$$Y'(X) = \frac{P_1}{(X - P_2)^2 + P_3} + Const \tag{3.1}$$

where X and Y are the independent and dependent variables; P_i are the fitting parameters; and the baseline constant $Const$ is computed by $Y_{fit} = \frac{P_{1,fit}}{P_{3,fit}}$.

Each file of raw data contains the intensity data corresponding to the Raman shift, carried out at one measurement point. Often non-linear baseline (background) appears in the Raman plot due to interference with the substrate or other materials. To perform background suppression, I first estimate the locations where the characteristics peaks occurred in the curves. Next, the Lorenz curves of characteristics peaks are extracted. Then, I cover the locations where the curves are. Finally, apply polynomial fit and subtract the entire curve by the fitted polynomial. The fitted Lorenz curves of characteristics peaks are displayed in Fig. 3.14.

The Raman spectrum of few-layer graphene has three main peaks: the G peak (at ≈1,580 cm^{-1}, yellow fitted curve), a primary in-plane vibrational mode; and the D peak (at ≈1,350 cm^{-1}, orange fitted curve) and the $2D_{Gr}$ peak (at ≈2,700 cm^{-1}, purple fitted curve), a second-order overtone of another in-plane vibration mode [176].

To examine the oxidation level of the printed BP film as presented in my work [58] (in collaboration with Dr. Hu), I scan through the entire surface of the sample to create a spatial mapping based on the intensity ratio $I(A_g^1)/I(A_g^2)$ (Fig. 3.15(a)) where A_g^1 is out-of-plane peak and A_g^2 is in-plane peak. Generally, A_g^1 is at ≈363 cm^{-1}, A_g^2 is at ≈467 cm^{-1}. $I(A_g^1)/I(A_g^2) = 0.6$ is the threshold for oxidation level. In the program, the oxidation level at each point can be associated with the characteristic peaks fittings. Fig. 3.15(b) shows

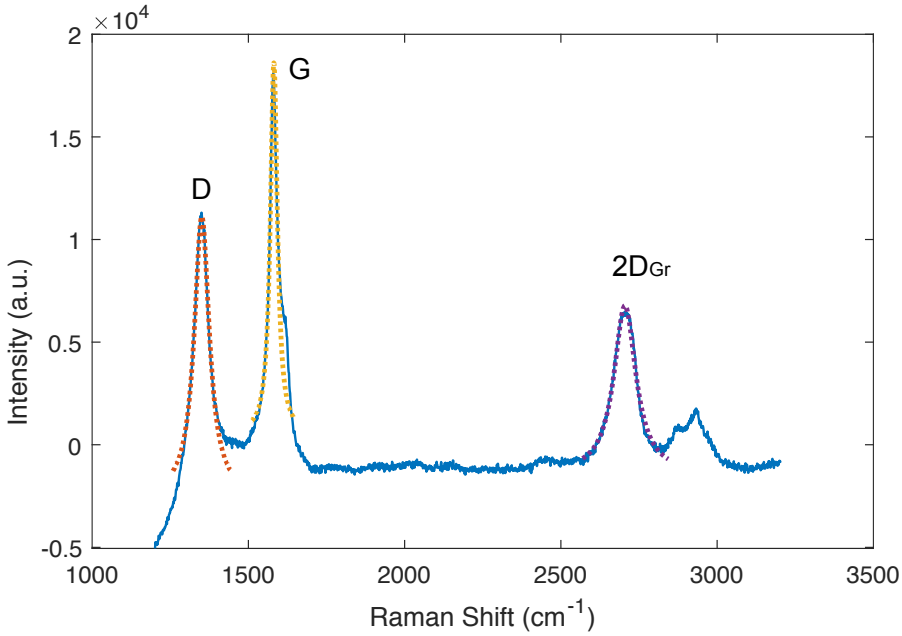

Fig. 3.14 Raman fitted with peaks of interest: D, G, and $2D_{Gr}$ peaks are indicated by orange, yellow, and purple dotted curves, respectively.

the selected Raman curves corresponding to the locations labelled in Fig. 3.15(a), where #1 presents a null data point; #2 (0.38) presents a data point with low oxidation level; #3 (0.74) presents a data point with high oxidation level.

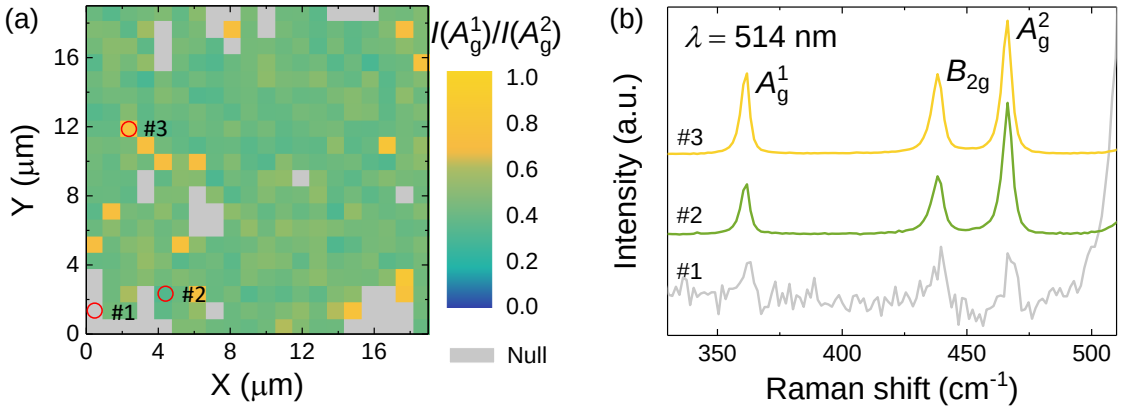

Fig. 3.15 (a) Raman map of the intensity ratio $I(A_g^1)/I(A_g^2)$ with 1 μm spatial step. The grey squares correspond to regions where the Raman intensity is too low for accurate interpretation. (b) Raman curves corresponding to the locations labelled in (a).

Ultraviolet–visible spectroscopy (UV-Vis)

UV-Vis is an instrument used to estimate the concentration of flake dispersion of the inks. UV-Vis measures the optical absorbance of a compound in solution. The apparatus usually consists of the light source, a monochromator, sample and reference holders, and detectors. A filtered monochrome beam is split and passed through a sample and a reference, respectively, allowing the collection of an absorbance spectrum spanning a wide wavelength.

The concentration c is obtained by using Beer-Lambert Law:

$$A = \alpha c l \tag{3.2}$$

where A is absorbance obtained from UV-Vis; l is the length of the optical path; α is the absorption coefficient. The dispersion is diluted to 20% to avoid scattering losses. The experimentally determined absorption coefficient of graphene $\alpha = 360\ \mathrm{L\,g^{-1}\,m^{-1}}$ at wavelength of 660 nm [179].

3.3.2 Microscopy

Atomic force microscopy (AFM)

AFM is a microscopic technique used to study the thickness and morphology of the samples [180]. AFM consists of a cantilever with a sharp tip in nanometers size, that scans across the surface of the sample. The scanning mode of AFM may be either static, whereby the tip and the surface contact, or dynamic, whereby the cantilever vibrates. During operation, the tip is driven close to the surface, such that the repulsive force against the tip is collected to represent the thickness and the surface morphology.

The sample is prepared by drop-casting diluted ink (20×) onto Si/SiO_2 wafer and dry on top of 120 ℃ hotplate. To blow off dust, the sample is then blown with nitrogen (N_2) gun before carrying out AFM measurements. The AFM samples are characterized with a Bruker Dimension Icon AFM in ScanAsyst^{TM} mode, using a silicon cantilever with a silicon nitride tip. Fig. 3.16 shows the AFM images with graphene flakes and the cross-sectional thickness of the flakes.

Scanning electron microscope (SEM)

SEM is utilized to visualize the surface morphology of the printed films produced from the inks I prepared. The operating principle of SEM is described as follows. The samples are placed in a chamber pumped into a high vacuum. Primary electrons generated by the strong electric field between thermionic cathode and anode are focused by electromagnetic lens to

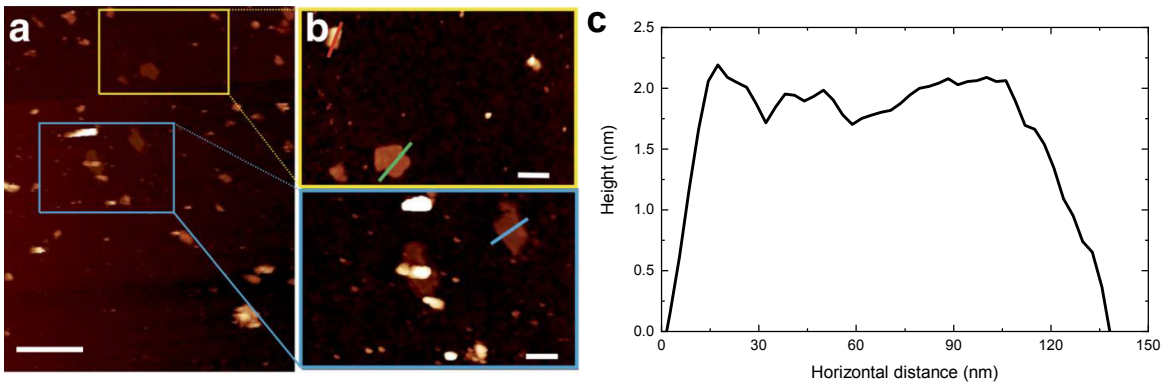

Fig. 3.16 (a) Representative AFM images of UALPE exfoliated graphene flakes. (b) Zoomed-in image of (a). (c) An example of measured cross-sectional thickness of individual flake from the green line in (b). Adapted from [81].

strike the specimens. These electrons knock out the electrons of the sample material and generate secondary electrons. These secondary electrons are led by a positively biased grid to the detector which is connected to a computer for processing. The principle is that many recorded secondary electrons lead to a bright point; fewer electrons lead to a grey point; none at all leads to a black one. After scanning over the sample, the final image is generated. To eliminate electron charging which distorts the scanning images, I sputter-coated a nanometer-thick Au/Pd layer prior to conducting SEM. During the SEM process, specimens are placed in a chamber under vacuum environment. The electron beam of 3eV energy is applied.

3.4 Summary

In this chapter, the key advances in the sensing application of 2D nanomaterials and their composites with MOx nanomaterials, are summarized for different groups of analytes including NH_3, NO_2, VOCs, and humidity. The graphene-MOx hybrids reported to date exhibit improved responsivity which is attributed to the formation of local M-S heterojunctions and enhancement in gas adsorption capability at the active graphene sites. The production of such nanocomposite in literature is mostly based on the hydrothermal synthesis, as it allows low-cost and solution-processable synthesis of high purity materials. Despite the improved material system, the challenges of recovery time, baseline drift, reproducibility, device-to-device consistency, and so on need to be further addressed through measurement protocols and fabrication techniques. In addition, the insights of the 2D-MOx material characteristics are discussed and the program I develop for automatic Raman mapping is highlighted in the material characterization techniques section.

Chapter 4

Ink Systems for Device Fabrication

In the previous chapter, I discussed about the current literature on 2D, MOx, and hybrid materials for sensing applications. My target applications of point-of-care diagnostics and air quality monitoring rely on the development of material production and deposition technologies tailored for compatible integration with low-powered mobile-embeddable CMOS chips. The deposition method should be compatible with both the high performing 2D/MOx materials and the device platform. Solution processing of 2D materials coupled with printing technologies is regarded as a promising route for high yield and cost-effective manufacturing approach for printed devices.

The common industrial printing methods comprise flexographic, gravure, screen, and inkjet printing. Each method has its own tailored applications and limitations. Among these methods, inkjet is the most suitable technique for my application, because it is a high-precision, material-efficient and scalable technique that is capable of producing thin sensing layers suitable for the miniaturized CMOS platform. Furthermore, this process enables automated fabrication of multiple materials on the same platform, allowing batch production of multi-sensor array. However, the non-uniform material deposition attributed to the coffee-ring effect remains a critical challenge for inkjet technology.

In this chapter, I review the current literature on the functional ink systems, starting with the comparison of printing technologies (Section 4.1), proceeding with the understandings on the fundamental rheological properties in different ink systems (Section 4.2). Next, I focus on the inkjet deposition technique employed throughout the project (Section 4.3), introducing its principle and processes; the ink production technique including the requirements for ink formulation; the properties and processes that govern the uniformity of printed morphologies, including jetting properties, droplet spreading dynamics, and coffee-ring effect. In particular, I develop a model to simulate the printed morphology based on experimental printing parameters.

The contents in Section 4.3.5 have been submitted and are under review [181]. Guohua Hu has contributed to Section 4.3.5. The modeling of inkjet morphology in Section 4.3.6 is my original work and does not form part of the literature review.

4.1 Overview of printing technologies

The common industrial printing methods comprise flexographic, gravure, screen, and inkjet printing. Table 4.1 summarizes the key output parameters of these printing techniques.

Method	Ink viscosity(cP)	Linewidth(μm)	Thickness(μm)	Speed(m min^{-1})	Contact
Inkjet	4-30 (Very low)	30-50	$\approx$1	1 (Slow)	No
Gravure	100-1000 (Low)	10-50	$\approx$1	250 (Fast)	Yes
Flexo	1,000-2,000	45-100	$<$ 1	200	Yes
Screen	1,000-10,000 (High)	30-50	5-100	$\approx$70 (Medium)	Yes

Table 4.1 Comparison of print parameters across common printing methods. Adapted from [182–184].

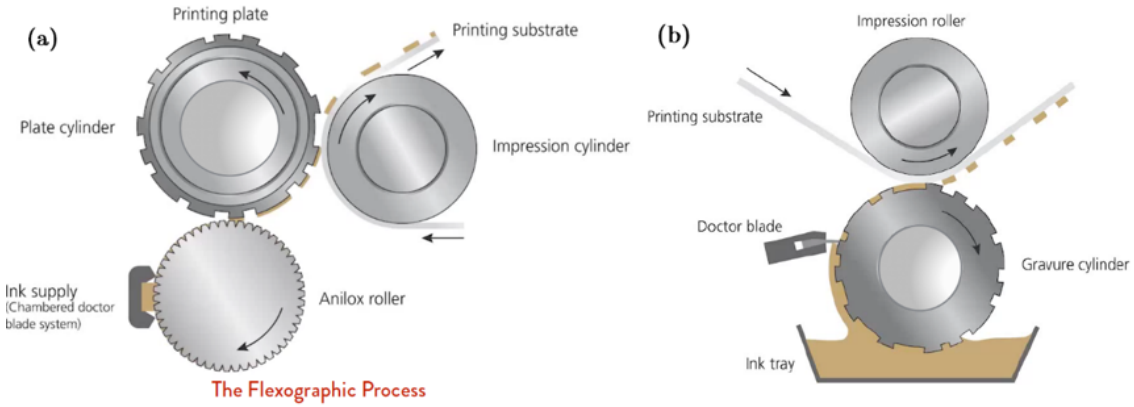

Fig. 4.1 Schematics of printing techniques (a) flexographic (b) gravure. Adapted from [183].

4.1.1 Flexographic printing

As shown in Fig. 4.1(a), the ink is supplied from an ink reservoir to an anilox roller, which then delivers a metered amount of ink to the plate cylinder. The plate cylinder consists of raised plastic or rubber blocks which allows transfer of desired patterns. The technique is capable of printing at a fast rate of up to 200 m min^{-1} [183]. However, it produces comparatively low film thickness ($<$ 1 μm) [184] which may result in discontinuities in printed pattern.

4.1.2 Gravure printing

The setup is shown in Fig. 4.1(b). The gravure cylinder is made of metal, with the pattern taking in the form of engraved cells. The depth of engraved cells controls the amount of ink to be transferred to the substrate. During print press, ink is transferred directly from the ink reservoir to the gravure cylinder. Because the ink is stored within these engraved cells, it eliminates the need for anilox roller. This reduces the complexity of the printing process. Print speed as fast as 250 m min^{-1} is hence attainable [183].

4.1.3 Screen printing

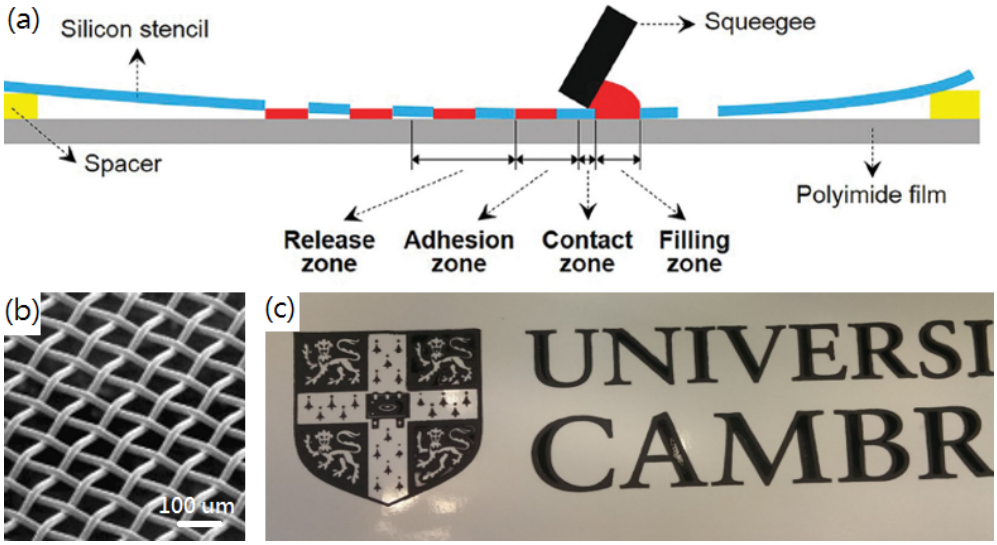

Fig. 4.2 (a) Illustration of the screen printing method. Adapted from [185]. (b) Microscopic image of the screen mesh. The scale bar is 100 μm. (c) My demonstration of screen-printed Cambridge University crest using graphene paste.

The main advantages of this technique are: it produces the thickest film for best substrate coverage; high materials loading is possible; the film thickness and definition of printed patterns are controllable via thread diameters, mesh thickness, and mesh openings [184]. Along with the inexpensive mesh, this technique is suitable for customized designs. Furthermore, the ink viscosity as high as 10,000 cP [183] is achievable thanks to the possibility of the application of high shear rates to shear-thinning pastes during printing. However, this process is a relatively slow production process, with capacity of 70 m min^{-1} when automated in flat bed systems [183].

The screen-printing technique uses a woven mesh to support an ink-blocking stencil. The operating process is illustrated in Fig. 4.2(a). The screen consists of a finely woven mesh

of stainless steel, nylon or polyester, mounted under tension on a metal frame. Fig. 4.2(b) shows a microscopic image of the mesh.

During printing, the substrate is held at a distance from one side of the screen, while the ink is loaded on the opposite side of the screen. A squeegee traverses the screen under pressure. The screen is thereby brought into contact with the substrate and also the ink is forced through the open threads of the woven mesh. The required device pattern from the screen is thus left on the substrate. The next step is to dry the paste by evaporating the solvent. After drying, the film may be subjected to thermal treatment. During this stage, the organic carrier is evaporated, and other chemical and physical processes impart adhesion. Fig. 4.2(c) demonstrates the screen-printed Cambridge University logo with graphene ink on a photo paper substrate. It shows high print definition with high material loading.

4.2 Rheological properties of ink systems

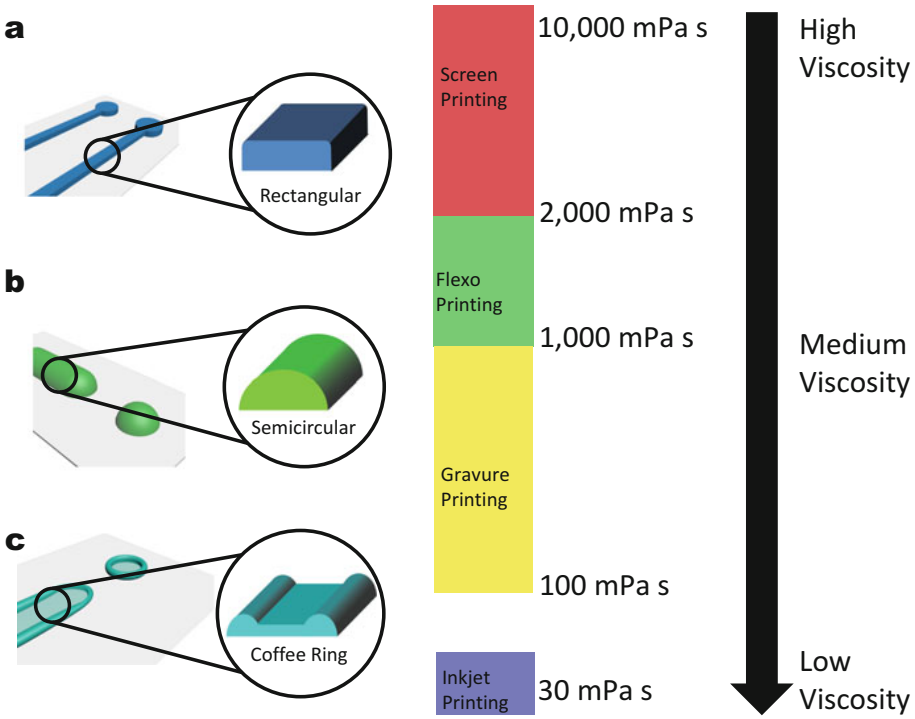

Fig. 4.3 Typical profiles of printed lines of (a) high and (b) medium and (c) low viscosity inks. Adapted from [182].

As mentioned earlier, the ink viscosity specification across different techniques vary vastly, descending from screen-, flexo-, gravure, inkjet printing. This is illustrated in Fig. 4.3.

The ink viscosity can transform to different printed morphology: high viscosity inks produce rectangular printed lines; medium viscosity produce semi-circular feature; low viscosity can produce printed films with coffee rings.

Printing techniques rely on shear-thinning behaviors (Fig. 4.4(a)) i.e. to become less viscous at higher shear rates. This property is crucial especially when the inks contain high pigment contents. Shear-thinning allows high loading inks to transform into a printable form when a high shear rate is applied during the printing press. These inks normally contain rheology modifiers which are polymers that are endowed with shear-thinning properties. Such property derives from the tendency of the long-chain molecules to orient themselves in the direction of flow.

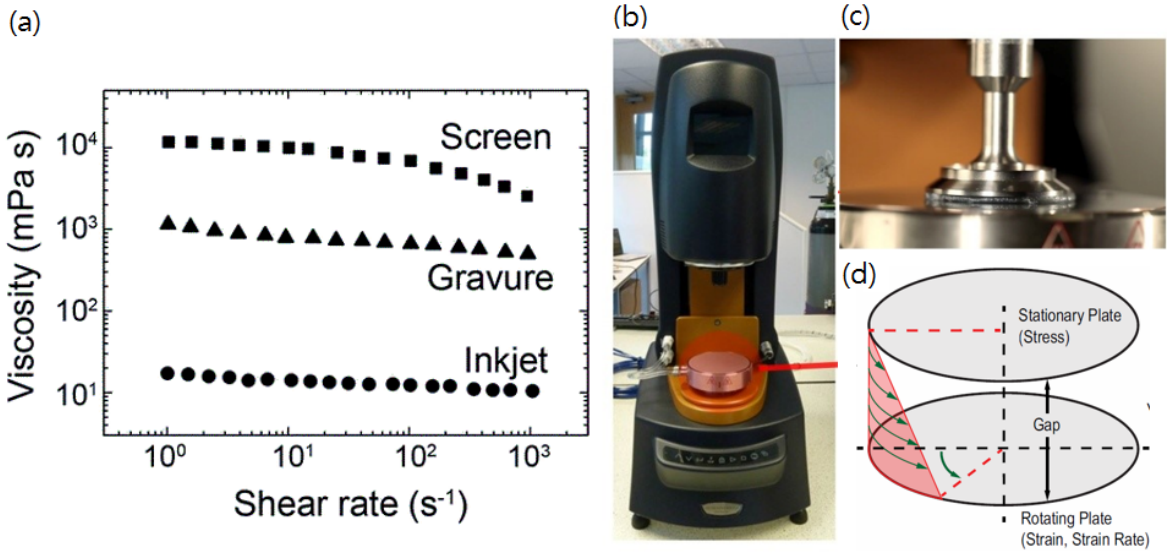

Fig. 4.4 (a) Rheological profile of various printing techniques. Adapted from [186]. (b) Image of a rheometer. (c) Zoomed in of parallel plates. (d) Schematics of parallel plates.

Rheological properties of the ink can be characterized by a rheometer (Fig. 4.4(b)). One of its function is to measure viscosity of the ink at different shear rate applied. It is thus a useful tool to stimulate rheological behaviors during printing press and at storage conditions. The parallel plate rheometer consists of a stationary plate and a rotating plate (Fig. 4.4(c,d)) which controls the velocity. Shear rate $\dot{\gamma}$ is determined by the velocity v of fluid dropping across plate separation h (or gap) to $v = 0$ at the stationary plate.

$$\dot{\gamma} = \frac{v}{h} \tag{4.1}$$

Viscosity η is then defined as shear stress τ that resists the deformation over shear rate $\dot{\gamma}$.

$$\eta = \frac{\tau}{\dot{\gamma}} \tag{4.2}$$

The shear stress of sample is measured by the torque transducer.

4.3 Inkjet printing

Inkjet printing is a direct-write and contactless digital printing technique where desired patterns are deposited by the ink droplets which are propelled from an ink chamber [187]. Unlike analog printing techniques, inkjet printing enables computer-assisted layout design and production which not only can be automated but also offers flexibility in prototyping [188]. Moreover, it achieves high resolution with a minimum feature size of 20 μm [189]. Besides, the low volume (10 pL) of ink consumption makes it attractive for deposition of high-cost materials. However, disadvantages include issues such as nozzle clogging, the temperature dependence of dispensing reagents, slow print rate, and costly printers [187].

The main challenges for inkjet printing are to produce stable ink at high concentrations and uniformly deposited film which is influenced by coffee ring effect and wettability of solvent used. The coffee ring effect results in materials deposited towards the edges [190], whereas wettability influences the adhesion of the film [184].

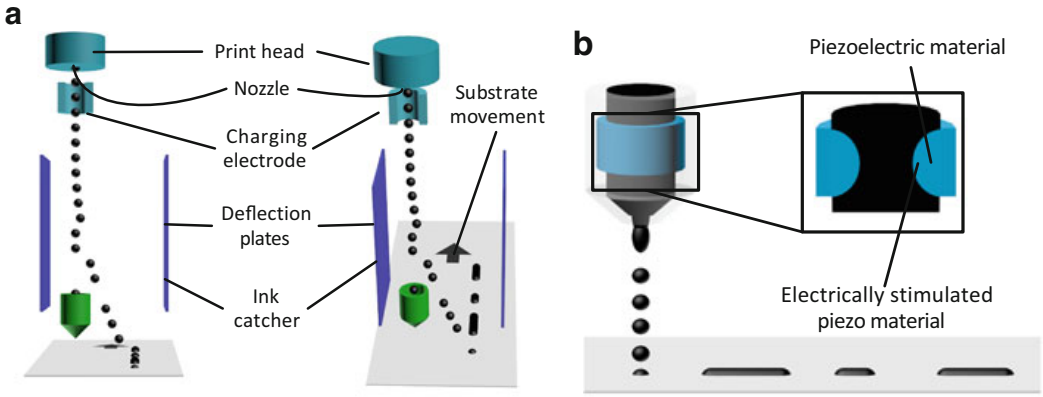

Fig. 4.5 Inkjet printing principles: schematics of (a) CIJ, and (b) DoD inkjet printing with piezoelectric printhead. Adapted from [182].

4.3.1 Principle and processes

Fig. 4.5 presents the schematics of the two popular jetting strategies: continuous inkjet (CIJ) and drop-on-demand inkjet (DoD). CIJ printer (Fig. 4.5(a)) jets the droplet continuously,

and the frequency of jetting is controlled by the pressure applied to the ink reservoir. The deposition of droplets is controlled by the deflection plates which apply an electrostatic field to charge the droplets that are to be printed onto the substrate.

Whereas DoD (Fig. 4.5(b)) only jets droplets on demand. The droplets are jetted through the control of the shape of a piezoelectric material via passing a voltage waveform. This change in shape leads to a change in pressure of the reservoir and force the ink out of the printhead. Printing parameters including voltage waveform, inter-drop distance, and printing repetitions can be tuned to obtain optimal jetting properties and printed morphology. DoD inkjet is the most widely used instrument in academia and thus I also use a commercial DoD printer in my research. Fig. 4.6 shows a single printed droplet of graphene ink using Dimatrix DMP-2831.

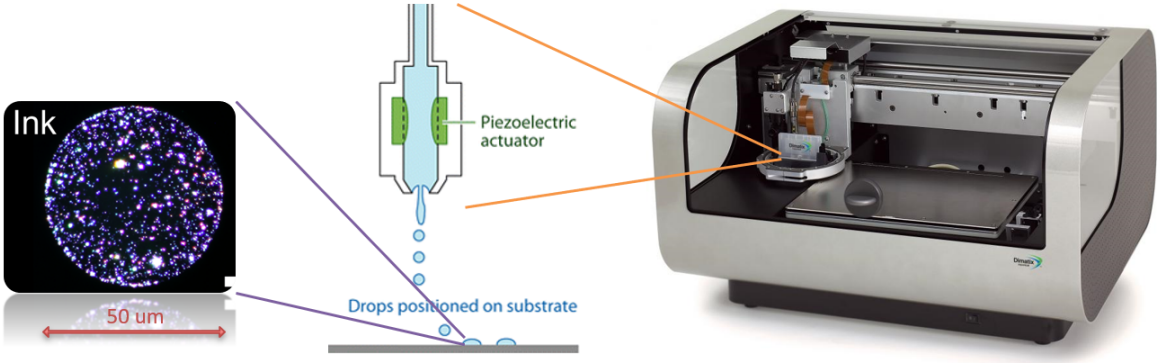

Fig. 4.6 Dark field microscopic image of a single droplet (left) printed with Dimatix materials printer (right).

4.3.2 Ink preparation: Ultrasonic Assisted Liquid Phase Exfoliation (UALPE)

UALPE is a scalable and controllable approach to yield high quality flakes [179, 191], through the processes of overcoming the interlayer van der Waals forces and balancing nanosheet-solvent interactions [192]. UALPE involves the following processes: ultrasonication, centrifugation, and redispersing in a solvent mixture (optional). Fig. 4.7 illustrates the overall process commonly carried out for the preparation of graphene inks. First, ultrasonication generates cavitation bubbles between the crystal layers. The bubbles then collapse into high energy jets which weaken the interlayer forces, yielding isolated flakes dispersed in the solution. Bath sonicator is selected for exfoliation as it offers evenly distributed power which prevents defects of basal planes. I note that after low power bath sonication for 12 hr, much of the starting graphite material typically remains unexfoliated.

Purification of the resultant mixture is carried out using centrifugation to sediment these unexfoliated flakes [81]. Sedimentation based separation (SBS) is the most commonly used method to separate various particles on the basis of their sedimentation rate in response to centrifugal force acting [193]. Convenient control of the average flake size of 2D materials through the control of the centrifugation speed is therefore attainable [194]. The supernatant (top $\geq$ 70 %) after centrifugation is collected as the graphene dispersion. After filtration, the dispersion can be re-dispersed in a solvent mixture for better rheological properties and printed morphologies [58]. The inks are then ready to be loaded into an inkjet printer.

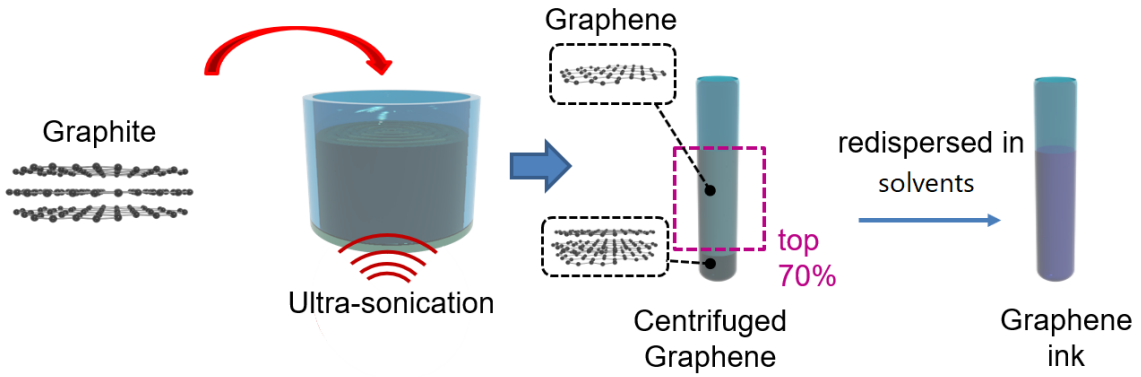

Fig. 4.7 Illustration of graphene ink formulation process.

The UALPE method allows production of dispersions with flake dimension < 1 μm and viscosity of ≈ 2 mPa s [195, 63, 196], which satisfy the requirements for inkjet printing. This approach has since been successfully extended to a wide range of 2D materials, including TMDCs [81], BP [58], and *h*-BN [81], as shown in Fig. 4.8(a,b).

The following targets are considered in the process of formulating high-performing inks tailored for the sensing applications: (1) to facilitate high quality exfoliation of graphite; (2) to produce stable and homogeneous dispersion consisting of two sensing material classes (graphene and MOx) at high concentrations; and (3) to optimize jetting and wetting properties for producing uniformly-printed films.

Selection of solvents

Selection of suitable solvents and stabilization agents plays crucial roles in minimizing enthalpy of mixing [179, 81], preventing re-stacking of the exfoliated flakes [197] and facilitating stable dispersions [198].

The dispersion of flakes in a general solvent occurs when the Gibbs free energy of mixing has a negative value or is close to zero. Successful solvents for graphene dispersibility are

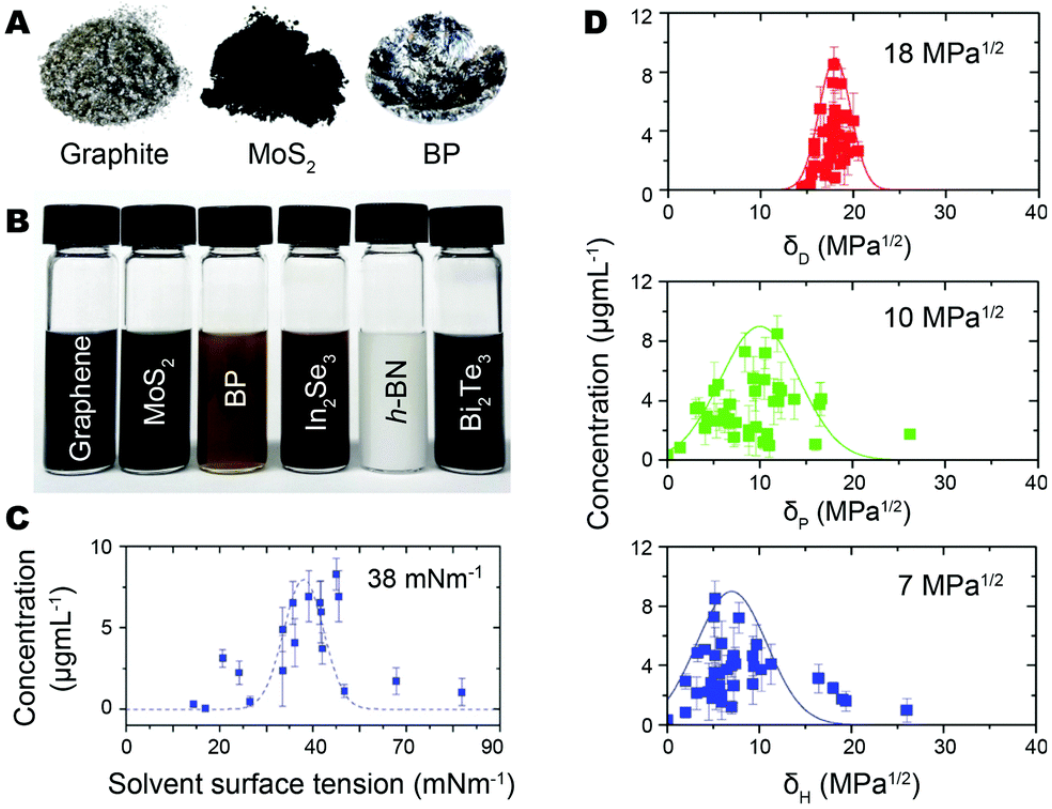

Fig. 4.8 Liquid phase exfoliation: photographs of (a) selected bulk materials before exfoliation, and (b) 2D material dispersions. The concentration of graphene dispersions with respect to (c) solvent surface tension (adapted from [191]) and (d) Hansen solubility parameters with fitted curves. (adapted from [199])

generally those with surface tension of 38 mN m^{-1} (Fig. 4.8(c)) [191]. The characteristics of dispersibility is further analysed with a more realistic Hansen solubility parameter (HSP) [200]. Dispersibility is optimal when the change in enthalpy of mixing, ΔH_{mix}, is minimal. ΔH_{mix} is determined by the intermolecular interactions between the 2D material flakes and the solvent(s) in the dispersion. The interactions can be decomposed into contributions of three HSP components: the dispersion δ_D, polar δ_P and hydrogen-bonding δ_H which arise from nonpolar/dispersion forces in atomic level, permanent dipole-permanent dipole, and hydrogen bonding in molecular level, respectively. Equation 4.3 associates ΔH_{mix} with the HSP components.

$$\Delta H_{mix} \propto (\delta_{D,solvent} - \delta_{D,flake})^2 + \frac{(\delta_{P,solvent} - \delta_{P,flake})^2}{4} + \frac{(\delta_{H,solvent} - \delta_{H,flake})^2}{4} \quad (4.3)$$

Good solvents for graphene are found to have HSPs of $\delta_D \approx 18$ MPa$^{\frac{1}{2}}$, $\delta_P \approx 9.3$ MPa$^{\frac{1}{2}}$, and $\delta_H \approx 7.7$ MPa$^{\frac{1}{2}}$ (Fig. 4.8(d)) [199]. Solvents matching surface tension and Hansen solubility parameters [200] like N-Methyl-2-pyrrolidone (NMP), N,N-dimethylformamide (DFM), cyclohexanone can suspend graphite without stabilization agents [199]. Despite commonly used NMP satisfies this selection criteria, NMP is toxic and has a high boiling point (204 ℃), additionally its high surface tensions (40.79 mN m^{-1}) hinder adhesion on Si/SiO_2 and Si_3N_4 substrates used for the CMOS-fabricated devices. Cyclohexanone (with $\delta_D \approx 19.6$ MPa$^{\frac{1}{2}}$, $\delta_P \approx 17.8$ MPa$^{\frac{1}{2}}$, $\delta_H \approx 6.3$ MPa$^{\frac{1}{2}}$) is more advantageous than NMP, due to its lower boiling point (155.7 ℃) which offers faster evaporation, as well as its low surface tension (34.4 mN m^{-1}) which leads to better wetting.

Ref [63] has demonstrated the first printed graphene transistor with an electron mobility of 95 cm^2 V^{-1} s^{-1} using graphene inks in a pure NMP solvent. The printed morphologies on different substrates are displayed in Fig. 4.9(a).

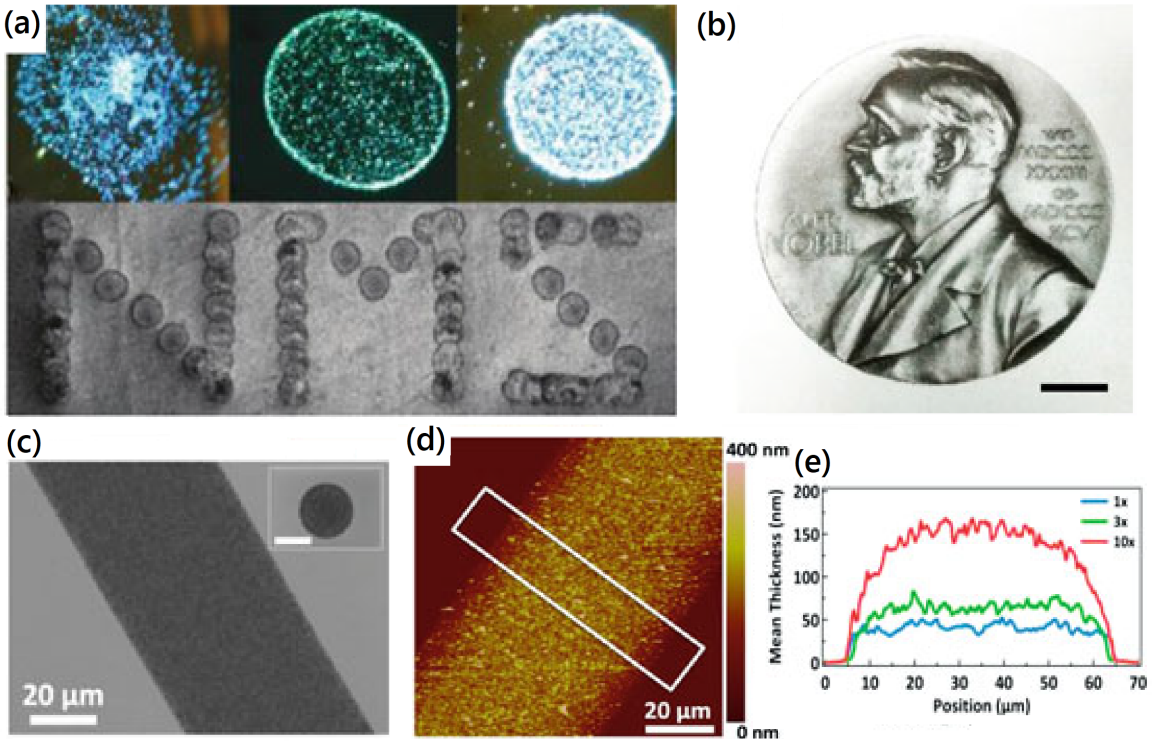

Fig. 4.9 Inkjet printing of 2D material inks: (a) Inkjet-printed droplets of graphene NMP ink on (top row) Si/SiO_2 treated with O_2 plasma, untreated Si/SiO_2, Si/SiO_2 treated with HMDS, and (bottom row) paper, respectively. Adapted from [63]. (b) Inkjet-printed graphene pattern on paper, scale bar 5 cm. Adapted from [201]. (c) A single inkjet-printed graphene/EC line (inset) droplet of graphene; scale bar 10 μm. Adapted from [202]. (d) An AFM image of a single line after 10 printing passes. (e) Cross-sectional profiles of printed lines after 1, 3 and 10 passes.

On the other hand, alcoholic solvents are demanding due to their environmental friendliness, rapid drying, and excellent substrate wetting properties due to their low surface tension ($\gamma \approx 20$ mN m^{-1}). These properties make them favorable for manufacture processes [182]. However, they are unable to exfoliate and stabilize pristine graphene and other 2D crystals due to strong mismatch of Hansen solubility parameters [198].

Addition of polymers

Vehicle of pure alcoholic solvents is insufficient for maintaining stable graphene-MOx dispersions for inkjet printing. Incorporating surfactants or stabilization agents is a widely used approach to formulating high concentration functional inks [203, 197] while improving their wetting and jetting properties [204, 205]. Stabilizing polymers have been shown to contribute significant enhancements in exfoliation of graphite in alcoholic solvents [203] or water [201]. Fig. 4.9(b) demonstrates an inkjet-printed graphene pattern on paper using water-based inks with a water soluble polymer [201].

Ethylcellulose (EC) is a commonly used polymer that is suitable for printing. First of all, it is a highly effective polymer stabilizer that prevents dispersed pigments from sedimentation and re-aggregation. It produces a stable and viscous solution in a variety of solvent. It has been used as a stabilizer which sustains graphene dispersions at concentrations up to 80 mg mL^{-1} [202]. Moreover, EC serves as a binder that mitigates the coffee-ring effect, as well as to adhere substrate with metal electrodes which is essential to the functioning of the device [202]. Fig. 4.9(c) demonstrates the uniformity of the printed features using graphene-EC formulation. Fig. 4.9(d,e) further support a spatially uniform deposition of graphene, with a reliable increase in thickness after multiple printing passes.

In Chapter 6, 7, I incorporate polyvinylpyrrolidone (PVP) into graphite suspension during UALPE. PVP is a commonly used polymer containing N-substituted pyrrolidone rings similar to NMP structure. PVP can readily adsorb onto graphite surface [206, 207], subsequently stabilize exfoliated flakes through steric hindrance [208, 209], forming nanosheet-polymer composite dispersions [210]. PVP is also used for the production of stable and homogeneous dispersion of MOx NPs [211, 212]. In addition, it can act as an ink binder and a rheology modifier [213, 204] to improve wetting and jetting properties of the inkjet inks [63].

Although PVP improves exfoliation and stabilization of the ink, it is an insulating polymer and is detrimental to the functionality of the graphene-MOx sensing layer. PVP is therefore suggested to be decomposed through annealing at 400 °C for 30 min [214, 215] in Ar atmosphere.

4.3.3 Jetting properties

Stable ink droplets generation during inkjet printing is crucial for high quality printed films. The printability of the ink can be predicted with inverse Ohnesorge number

$$Z = \sqrt{\gamma_{ink}\rho D}/\eta \tag{4.4}$$

where η is viscosity, ρ is density, and D is nozzle diameter. This figure of merit (FOM) is a measure of the conditions of the droplet formation process after ejection from the nozzle. The terminating conditions are associated with the reproducibility and reliability of printed patterns. Therefore, FOM serves as a guideline to the optimization of ink formulation. As a rule of thumb, studies [63, 216] have suggested that stable jetting (Fig. 4.10(b)) satisfies Z of 1-14 to avoid formation of long filament or secondary/satellite droplets as observed in Fig. 4.10(a,c). The printing stability is also related to the flakes' lateral size. A sufficient condition is that their dimension should be at least 1/20 of the nozzle diameter.

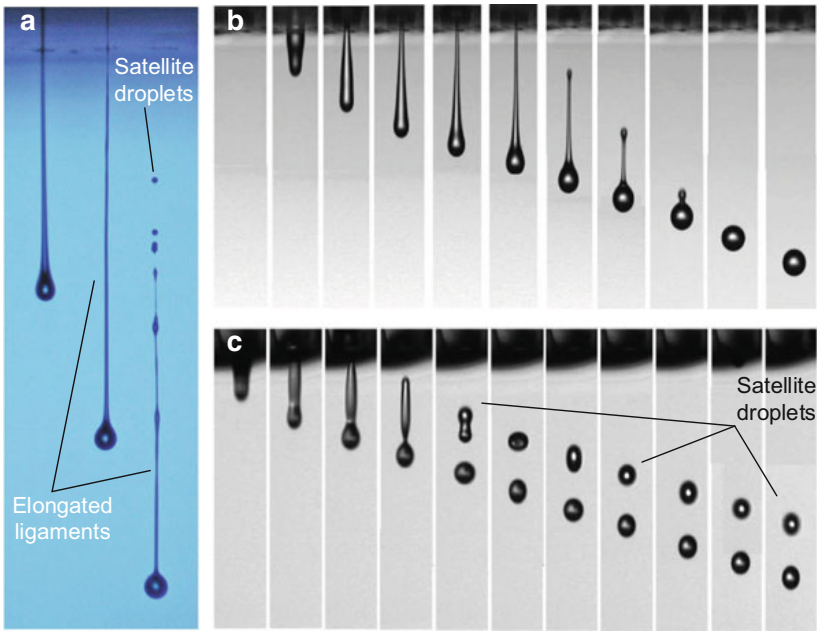

Fig. 4.10 (a) High-speed micrographs of three jetted droplets at different jetting stages, showing elongated ligaments break up into satellite droplets. High-speed micrographs of droplet jetting sequence for (b) stable jetting when Z is 2.2, and (c) jetting with satellite droplets when Z is > 14. Adapted from [217].

4.3.4 Coffee ring effect and suppression approaches

Ring-like deposition of solutes or suspended particles during drying (known as the *coffee-ring effect*) is commonly seen in many mono alcoholic solvent-based inks [190, 218]. The droplet drying process in a mono alcoholic system is illustrated in Fig. 4.11(a). As for a relatively low boiling point solvent ($\lesssim 100$ ˚C), the larger surface-area-to-volume ratio and thus faster evaporation rate at the droplet edges results in an apparent dominance of capillary edgeward flow [190, 218], carrying dispersed materials towards the edges, leaving little materials in the interior and a ring-like contact line after drying.

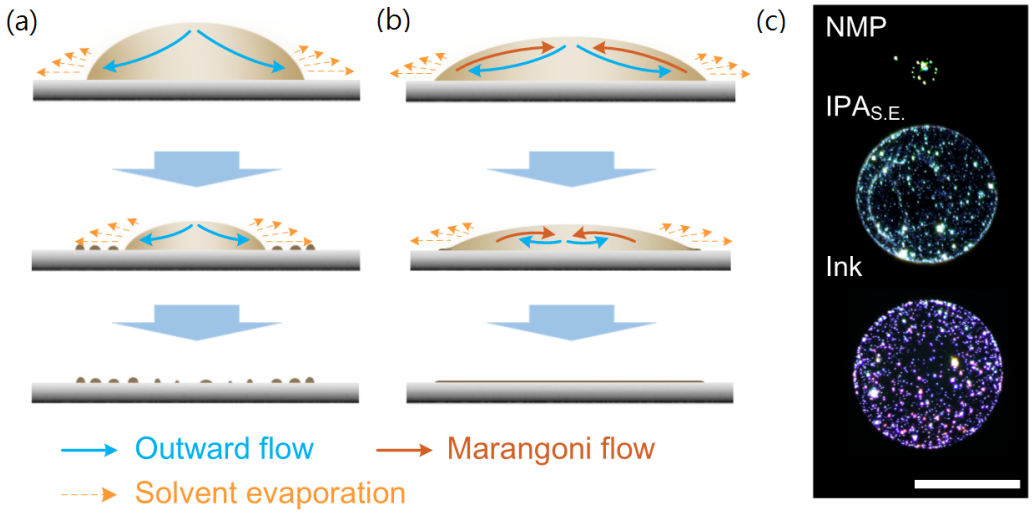

Fig. 4.11 Droplet drying process (a) without and (b) with a recirculating Marangoni flow induced to prevent coffee ring effect. (c) Microscopic images of the dried droplets: NMP dispersion, the BP-IPA (after solvent exchange), and the BP ink on Si/SiO_2, from top to bottom. Adapted from [58].

In order to suppress the coffee ring effect, there have been attempts to incorporate surfactants into the ink formulation to achieve spatially uniform printing [195]. However, surfactants are generally detrimental for electronics applications and are difficult to remove. Our work in Ref [58] presents a binary solvent strategy in the ink formulation, and demonstrates excellent spatial uniformity and consistency across inkjet printed BP flakes. The authors employ a binary alcohol mixture based ink formulation strategy with 90 vol.% isopropyl alcohol (IPA) and 10 vol.% 2-butanol composition [58, 59]. This formulation (surface tension $\gamma_{ink} = 31.12$ mN m^{-1}) allows deformation of the ink droplet and counteracts the capillary flow during drying, while keeping the surface tension low enough for good wetting of the substrate for my research: Si_3N_4 μHP membrane (surface energy $\gamma_{sub} \approx 40$ mN m^{-1} [219]).

It is suggested that the suppression of the coffee-ring effect is through the introduction of a composition variation where higher proportions of faster evaporating solvent (IPA, boiling point: 82.3 ˚C) is distributed around the center and slower evaporating solvent (2-butanol, boiling point: 100 ˚C) around the edges [220, 221]. These localized variations result in temperature gradients during vaporization and thus creating surface tension gradients within the droplet [220–223], inducing recirculating Marangoni flows which redistribute part of the dispersed materials back to the center, leading to a uniform materials coverage. The droplet drying process in a binary alcoholic solvent system is illustrated in Fig. 4.11(b) with printed droplet in Fig. 4.11(c).

The suppression of coffee-ring effect is essential to producing uniform printed morphologies which translate to consistencies in device-to-device performances in sensors. The approach using binary alcoholic solvents may serve as a practical production method that eliminates the use of surfactants which are detrimental for electrical conduction.

4.3.5 Droplet impact and spreading

The contents in this section consist of my original work [181] based on the pioneer study in Ref [224]. For the formulated inks with a typical surface tension of ≈30 mN m^{-1}, a viscosity of 2 mPa s and a density of 0.8 g cm^{-3} and thus a Z value of 10, the impingement of a droplet onto a predefined pattern needs to be controlled in a way that it does not cause neither overspreading nor insufficient merging [224]. Fig. 4.12(a) schematically illustrates a droplet impinging onto a printed line with different droplet spacing d'. The droplet radius r varies with substrate temperatures, as shown in Fig. 4.13(b). Assuming a track of ink droplets with volume V_{drop} is printed in an ideal case, the droplets then merge and form a line with uniform edges. Before solvent evaporation, the droplet has a spherical-cap geometry with a radius of r', while the line has a cylindrical-cap geometry with a radius of R'. The scenario for spherical-cap can be modelled as:

$$V_{drop} = \frac{2}{3}\pi r'^3 g(r') \tag{4.5}$$

where $g(r')$ is the volume correction function. $g(r')$ depends on several factors, including drop fluid, momentum, and size. Note that $g(r')$ is expected to be very small when the droplet wets the substrate well. On the other hand, $g(r')$ approaches 1 for contact angles close to 180^{o}. If d' is optimal, the impingement is then ideal such that the droplet extends the line by d' while the radius of the line remains R'. Whereas, the scenario for cylindrical-cap can be modelled as:

$$\frac{V_{drop}}{d'} = \frac{1}{2}\pi R'^2 f(\theta) \tag{4.6}$$

where $f(\theta)$ is the volume correction factor for cylindrical-cap. Therefore, the relationship between R' and r' is:

$$\frac{R'}{r'} = \sqrt{\frac{4}{3d'/r'}\frac{g(r')}{f(\theta)}} \tag{4.7}$$

In addition, the impinging distance from the droplet to the end of the line (defined herein as the 'bead') is:

$$D' = d' - R' \tag{4.8}$$

Therefore, the relationship between D' and r' is:

$$\frac{D'}{r'} = \frac{d'}{r'} - \sqrt{\frac{4}{3d'/r'}\frac{g(r')}{f(\theta)}} \tag{4.9}$$

The morphologies of the printed patterns are governed by the droplet impinging behavior, which is essentially defined by the above parameters. As depicted in Fig. 4.12(b), when d' is excessively small: $d' < R'$, i.e. $D' < 0$, the droplet lands on the bead of the line and expands around the bead rather than creating its own contact line, forming 'stacked coins' or 'bulged' line morphologies. However, when d' is large: $2R' < d' < 2r'$, i.e. $D' > R'$, the impinging of the droplet with the bead is restrained, forming 'scalloped' lines. For excessively large d': $d' > 2r'$, the droplet does not impinge onto the line, forming 'isolated droplets'. For d' values between the bulged and scalloped scenarios (i.e. $0 < D' < R'$), the droplet impinges onto the bead and forms contact line with uniform edges. Varying d' for the 2D ink on Si/SiO_2 produces vastly different morphologies, varying from stacked coins to uniform lines and eventually to isolated droplets, as displayed in Fig. 4.13(a).

Using the empirically obtained parameters ($r' = 34$ μm, $R' = 38$ μm, $d' = 35$ μm) and V_{drop} of 10 pL (defined by the ink cartridge), the correction factors $f(\theta)$ and $g(r')$ in Equation 4.6 and 4.5 are determined, giving $f(\theta)/g(r')$ as 0.96. The normalised R' and D' values as a function of normalized d' are therefore plotted in Fig. 4.12(c). Considering the above boundary condition for uniform line edges, $0 < D' < R'$, this suggests that the printed morphology with uniform line edges can be found when $d' = r'$ is 1.1-1.7. Fig. 4.13(a,b) present respective printed lines of the 2D ink on untreated Si/SiO_2 with single print repetition with variable d' and varied r'. I also define the edge roughness as $(L_a–L_b)/2$, where L_a and L_b are the maximum and minimum width of a printed line.

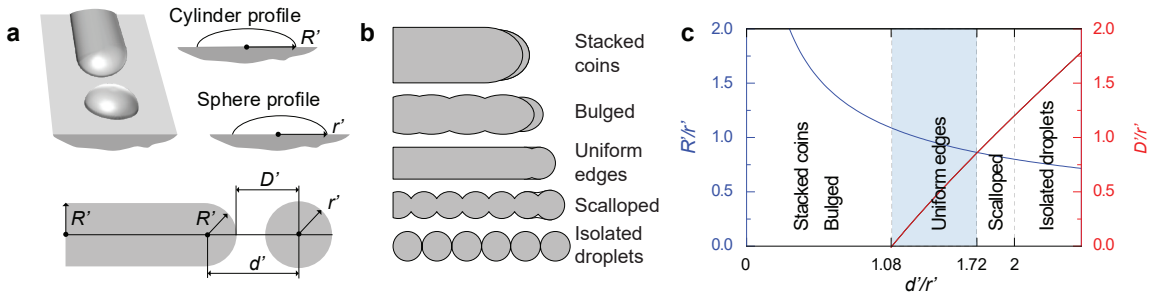

Fig. 4.12 (a) Schematic figure with top view showing a droplet deposited to a defined cylindrical-cap line of a radius of R' with a droplet spacing of d'. (b) Schematic figures showing printed morphologies defined at varied droplet spacings. (c) Dimensionless R' versus d' plot predicting that printed morphology with uniform line edges is achieved when d' is 1.1-1.7 of r'. Adapted from [181].

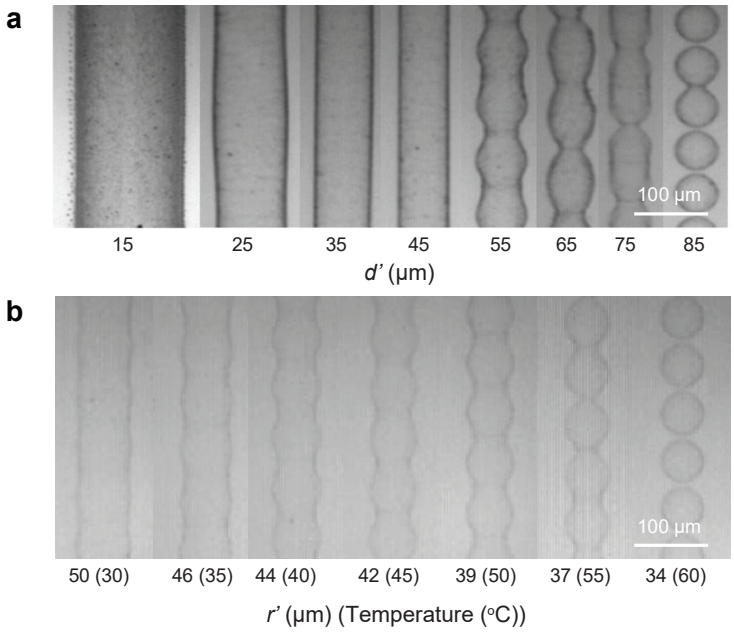

Fig. 4.13 Photographs of typical printed lines with single print repetition under (a) varied d' with fixed $r' = 34\mu$m; (b) varied r' with fixed $d' = 85\mu$m. Adapted from [181].

4.3.6 Modelling of inkjet morphology

Based on the model presented in the previous section, I have developed a MATLAB program to simulate the printed morphology (i.e. uniform, scalloping, bead separation, and isolated drops) according to the printing parameters (eg. drop spacing, diameter, and temperature) determined experimentally. The program offers a tool for predicting the printed morpholo-

gies from a set of printing parameters. This program can serve as a guideline for optimization of printing design for my experimental work.

Simulation procedures

The inputs are the average linewidths of printed patterns at different drop spacing and substrate temperature.

1. Find V_{drop} from the camera of the printer.
2. Find contact angles at different temperature based on

$$\frac{V_{drop}}{d'} = \frac{1}{2}\pi R'^2 f(\theta) \tag{4.10}$$

$$f(\theta) = \frac{2A_{cross-section}}{\pi R'^2} = \frac{2}{\pi}(\frac{\theta}{\sin^2\theta} - \cot\theta) \tag{4.11}$$

   This generates estimated contact angle matrix θ_{est} of

$$\theta_{est} = \begin{bmatrix} 4.6463 & 6.9411 & 5.7378 & 6.1881 & 7.8058 & 9.3055 & 10.6633 \\ 5.9562 & 8.8104 & 9.4127 & 11.1051 & 13.3885 & 14.3056 & 17.2568 \\ 6.9034 & 7.5446 & 9.5277 & 10.9077 & 12.5025 & 14.4685 & 17.2554 \\ 7.9333 & 9.5879 & 12.0332 & 13.7519 & 17.2833 & 16.1987 & 20.2661 \\ 7.8544 & 10.2407 & 11.2801 & 15.1871 & 16.6725 & 15.9043 & 20.3572 \\ 9.3717 & 9.9497 & 14.1526 & 15.6134 & 16.4284 & 22.9229 & 26.3356 \\ 9.7858 & 12.4397 & 14.8472 & 14.8472 & 19.0939 & 20.9081 & 29.6502 \\ 9.8806 & 9.8806 & 16.4091 & 17.6844 & 18.8117 & 20.3741 & NaN \\ 9.6086 & 12.5816 & 15.3878 & 20.5725 & NaN & NaN & NaN \\ NaN & 14.6019 & NaN & NaN & NaN & NaN & NaN \\ NaN & NaN & NaN & NaN & NaN & NaN & NaN \end{bmatrix}$$

   where each row representing d' from 15 to 115 μm with 10 μm step; each colomn representing temperature from 30 to 60 ℃ with 5 ℃ step.

3. Obtain average θ for uniform print and hence compute optimal $f(\theta)$.
4. From temperature versus diameter relationships, find $g(r')$ based on Equation 4.5.
5. Determine boundary conditions by equating D' with R' and r' combinations based on

$$\frac{D'}{r'} = y - \sqrt{\frac{4}{3y}\frac{g(r')}{f(\theta)}} \tag{4.12}$$

where $y = \frac{d'}{r'}$.

6. Compute y matrix and compare them with experimental findings y_{exp}.

The computed y that determines the boundary conditions for each printed morphology.

$$y_{uniform} = \begin{bmatrix} 1.2167 & 1.2695 & 1.3613 & 1.2640 & 1.2839 & 1.2543 & 1.3493 \end{bmatrix}$$

$$y_{scallop} = \begin{bmatrix} 1.6946 & 1.7188 & 1.7593 & 1.7163 & 1.7253 & 1.7119 & 1.7541 \end{bmatrix}$$

$$y_{isolated} = \begin{bmatrix} 2.2206 & 2.2523 & 2.3053 & 2.2490 & 2.2608 & 2.2433 & 2.2985 \end{bmatrix}$$

where y_{exp} is given as

$$y_{exp} = \begin{bmatrix} 0.3061 & 0.3125 & 0.3333 & 0.3448 & 0.3614 & 0.3750 & 0.4054 \\ 0.5102 & 0.5208 & 0.5556 & 0.5747 & 0.6024 & 0.6250 & 0.6757 \\ 0.7143 & 0.7292 & 0.7778 & 0.8046 & 0.8434 & 0.8750 & 0.9459 \\ 0.9184 & 0.9375 & 1.0000 & 1.0345 & 1.0843 & 1.1250 & 1.2162 \\ 1.1224 & 1.1458 & 1.2222 & 1.2644 & 1.3253 & 1.3750 & 1.4865 \\ 1.3265 & 1.3542 & 1.4444 & 1.4943 & 1.5663 & 1.6250 & 1.7568 \\ 1.5306 & 1.5625 & 1.6667 & 1.7241 & 1.8072 & 1.8750 & 2.0270 \\ 1.7347 & 1.7708 & 1.8889 & 1.9540 & 2.0482 & 2.1250 & 2.2973 \\ 1.9388 & 1.9792 & 2.1111 & 2.1839 & 2.2892 & 2.3750 & 2.5676 \\ 2.1429 & 2.1875 & 2.3333 & 2.4138 & 2.5301 & 2.6250 & 2.8378 \\ 2.3469 & 2.3958 & 2.5556 & 2.6437 & 2.7711 & 2.8750 & 3.1081 \end{bmatrix}$$

Fig. 4.14 shows the mapping of simulated boundaries onto the experimental data. The shaded light green, light brown, and light red regions indicate the experimental results of uniform, scalloped, and isolated printed morphologies, respectively. The green, brown, and red solid lines indicate the simulated boundaries for uniform, scalloped, isolated printed morphologies, respectively. As it can be seen, different classes of printed morphologies are predicted based on the different printing parameters.

Temp	d'	min	max	rough	Temp	d'	min	max	rough	Temp	d'	min	max	rough
	15	290	308	9		15	242	247	2.5		15	263	275	6
	25	200	209	4.5		25	160	176	8		25	155	170	7.5
	35	153	168	7.5		35	147	160	6.5		35	130	143	6.5
	45	132	132	0		45	120	120	0		45	107	107	0
	55	120	120	0		55	105	105	0		55	100	100	0
30	65	101	101	0	35	65	98	98	0	40	65	82	82	0
	75	92	92	0		75	70	93	11.5		75	67	82	7.5
	85	73	99	13		85	66	106	20		85	53	80	13.5
	95	60	105	22.5		95	50	94	22		95	44	86	21
	105	0	102	51		105	30	97	33.5		105	0	90	45
	115	0	98	49		115	0	96	48		115	0	90	45
	15	256	262	3		15	227	234	3.5		15	208	214	3
	25	143	156	6.5		25	130	142	6		25	120	143	11.5
	35	120	135	7.5		35	108	130	11		35	104	117	6.5
	45	100	100	0		45	89	89	0		45	92	92	0
	55	86	86	0		55	82	82	0		55	84	84	0
45	65	78	78	0	50	65	76	76	0	55	65	64	64	0
	75	64	85	10.5		75	54	77	11.5		75	54	71	8.5
	85	44	84	20		85	50	74	12		85	44	75	15.5
	95	27	85	29		95	0	83	41.5		95	0	80	40
	105	0	87	43.5		105	0	83	41.5		105	0	80	40
	115	0	87	43.5		115	0	83	41.5		115	0	80	40
						15	196	198	1					
						25	114	125	5.5					
						35	101	101	0					
						45	82	82	0					
						55	74	74	0					
					60	65	47	72	12.5					
						75	40	64	12					
						85	0	74	37					
						95	0	74	37					
						105	0	74	37					
						115	0	74	37					

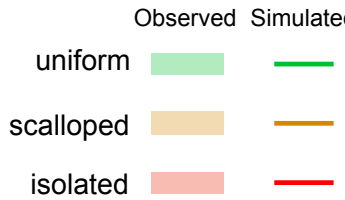

Fig. 4.14 Simulated boundary conditions mapped onto printed morphologies. Roughness (rough) is defined as (max − min)/2.

4.4 Summary

This section discusses the optimization approaches for delivering stable ink formulations that are capable of depositing spatially uniform printed morphology desirable for reproducible sensing devices. The approaches discussed focus on the optimization of solvent/polymer system which influences the dispersibility and rheological properties of inks and the dynamics during the droplet drying process. Moreover, based on droplet impact and spreading mechanisms, a model has been developed to optimize the printed morphology through tuning of the printing parameters. Furthermore, the suppresion of coffee-ring effect has been investigated to be employed in my ink formulation.

Chapter 5

Signal Transformation, Processing and Algorithmic Approaches

In the previous chapter, I discussed the methods for fabricating printed devices. Inkjet integration onto CMOS platform is considered a promising route for scalable fabrication approach. The fabricated device requires effective and reliable electrical measurement and signal processing protocols to convey the information incurred during the sensing events. In this chapter, I detail the signal transformation protocols and algorithms that are employed throughout the rest of the experimental chapters. First, I introduce the CMOS platform architecture used in my research. Next, I introduce the measurement setup including the gas characterization system, the electronics configurations, and the approaches for conducting electrical measurements. In the analyte classification section (Section 5.3), I discuss the computational approaches including signal pre-processing and cluster analysis techniques to address the common issue of cross-analyte interference. Finally, Section 5.4 presents an IoT implementation I develop using commercial sensors. This section is part of the CAPA Acorn project.

All the contents of this Chapter are my original work, apart from the measurement setup in Section 5.2 which involves collaboration with Andrea De Luca and Abdul Alzahrani. I thank Andrea for the technical support on the design of the measurement setup. I thank Abdul for the assistance on the PCB design.

5.1 CMOS device platform

The CMOS platform architecture used in my research is represented in Fig. 5.1(a). The structure consists of an embedded, 0.3 μm thick, resistive tungsten microheater, 0.3 μm thick

heat spreader plate, and a top gold layer for interdigitated sensing electrodes. I fabricate inkjet-integrated CMOS sensors by deposition of inks onto the IDEs consisting of 5 μm finger width and gap, summing to 250 μm in diameter.

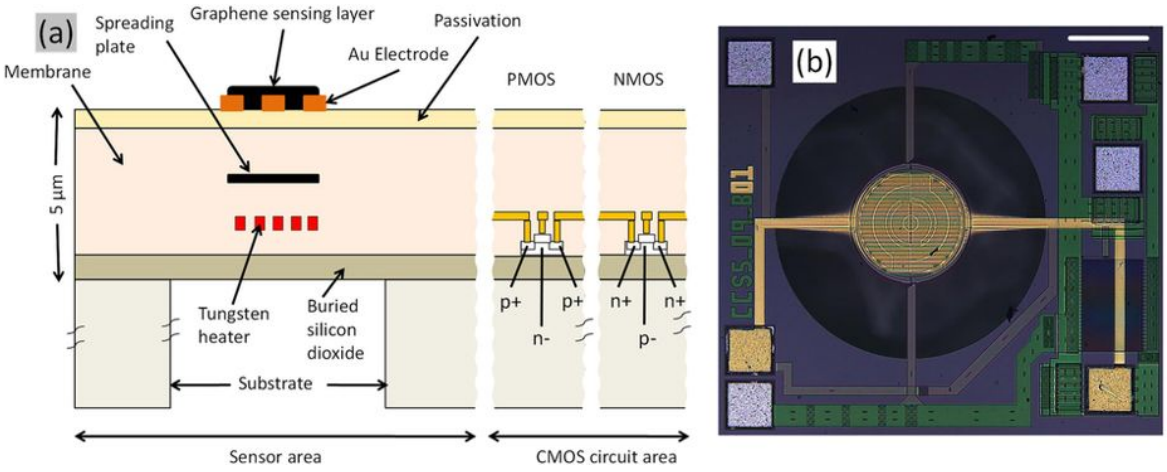

Fig. 5.1 (a) Cross sectional view of the CMOS μHP platform. (b) Optical micrograph of the CMOS device. the scale bar is 200 μm. Adapted from [93].

The microhotplate is formed from a circular dielectric SiO_2/Si_3N_4 membrane, supported on a silicon substrate onto which the microheater and electrodes are suspended. The μHP is fabricated by silicon on insulator (SOI) CMOS process, followed by deep reactive ion etching (DRIE) to etch away the silicon underneath the membrane, using dioxide layer as etch stopper. This forms a 4.5 μm SiO_2 (4 μm)/Si_3N_4 (0.5 μm) membrane structure onto which the microheater and electrodes are suspended. The use of SOI technology allows greater flexibility in the design of microhotplates and also allows the sensor interface circuitry to operate at higher temperatures [1].

The microhotplate controls the operating temperature of the sensing layer. Tungsten heater permits high temperature operation required for MOS sensing materials. By turning the heater on, it makes the electron transfer process and desorption of gas molecules from the surface of MOx easier. IDEs are used to overcome high resistance resulted from MOx materials. Au is used for the electrode due to its chemical inertness.

Suspended microhotplate allows low power consumption, rapid and accurate temperature control. The miniaturized μHP platform has an ultralow power consumption (down to 1.6 mW [1]), high thermal efficiency (0.11 mW/°C [172]) and fast thermal response (tens of ms [172]). The heating temperature is uniformly confined over the microheater region, due to the buried heat spreader. The inherently low thermal mass allows for rapid heating to high temperature (> 500 °C). The rapid thermal response enables sensing operation in dy-

namic temperature-programmed modes. Temperature control enables algorithms to enhance sensitivity, selectivity, and recovery time.

5.2 Measurement setup

5.2.1 Gas testing rig and software interface

The CMOS devices are placed in a gas testing rig which is an air-sealed stainless steel chamber, as shown in Fig. 5.2. Four devices can be tested simultaneously. The devices are wire-bonded to DIP8 test package which fits in the socket that connects to a microprocessor board.

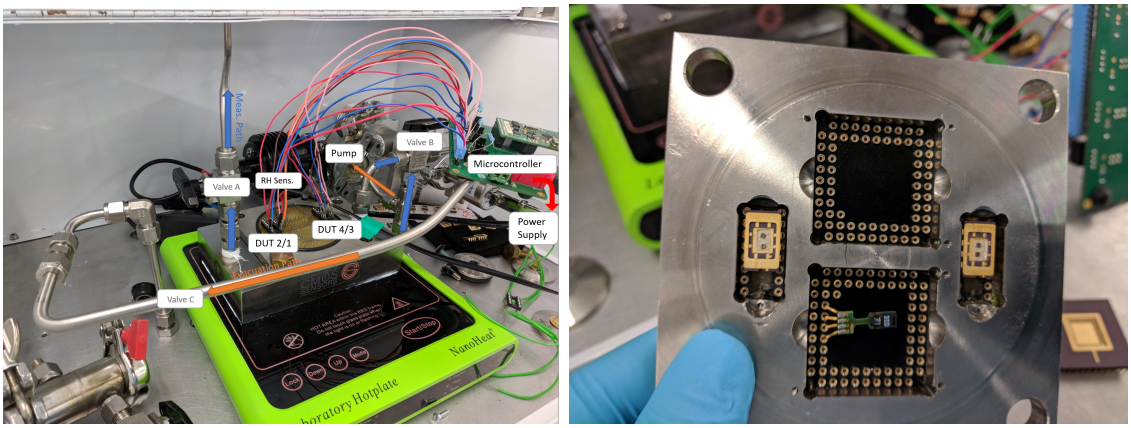

(a) Test rig (b) Test rig chamber

Fig. 5.2 Gas characterization system setup.

The testing rig is controlled by a software interface as shown in Fig. 5.3. It turns on and off the environmental gas and testing gas using mass flow controllers (MFCs). The pressure is controlled at 1 atm. For controlling the concentrations of the analyte gas, 1 ppm of analyte is produced from dilution of an analyte cylinder (BOC, 100 ppm in Ar) by balancing 5 sccm of analyte and 500 sccm of synthetic air cylinder (BOC, zero grade air).

RH level of synthetic air is controlled by balancing dry air with an according proportion of humid air. Humid air is produced by passing dry air into water bubbler. A commercial humidity sensor is used for RH characterization. Annealing can be conducted in argon (Ar), which is a noble gas. Ar annealing has shown strong evidence to reduce the concentration of defects in MOx [225].

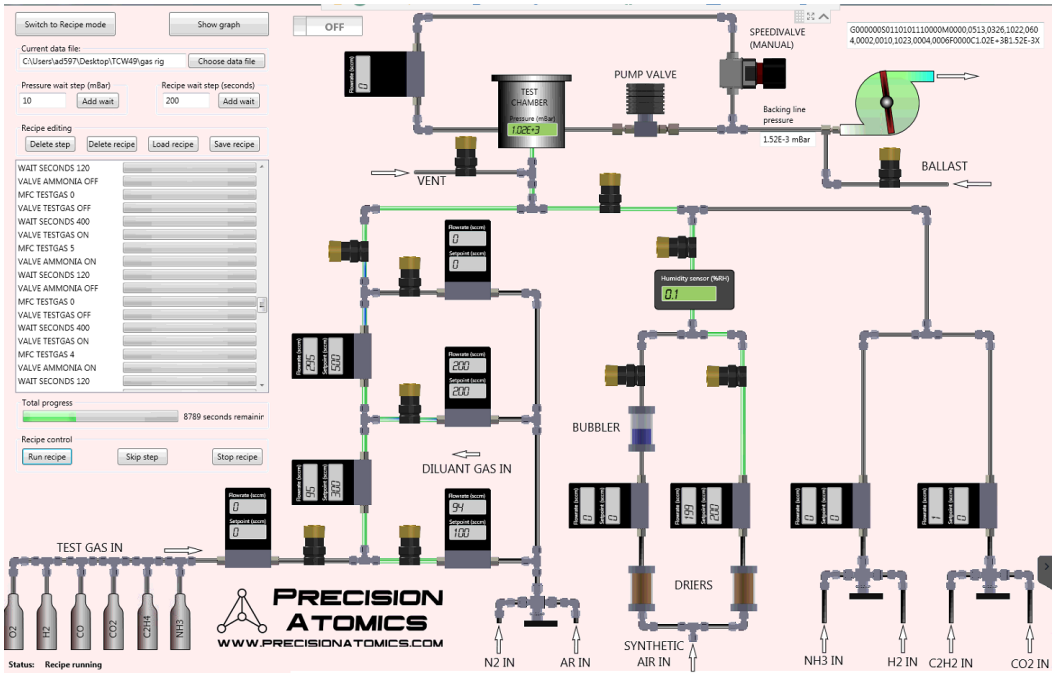

Fig. 5.3 Software interface of test rig.

5.2.2 Electrical measurement

For CMOS devices

The setup for electrical measurements carried out for CMOS devices in Chapter 6, 7, 8 are described in this section. The printed circuit board (PCB) in Fig. 5.4(b) contains a circuit controlling the voltage on the heater and hence the temperature. It also measures the change in resistance of the devices during adsorption and desorption gas molecules. The resistance of sensor is evaluated by the voltage division of a series connection of pull-up resistance and sensor, as illustrated in Fig. 5.4(a). The supply voltage is 2.5 V, $R_{pull-up}$ is selected to be comparable to R_{sensor}. Multi-device readout is realized through a multiplexer followed by A/D converter to generate output to be transmitted to PC for signal processing.

The temperature of heater embedded in CMOS device is controlled by the software interface shown in Fig. 5.5, exhibiting an example of response plots under temperature modulation mode (discussed in Section 6.3). There is a regular pattern in heater current and voltage, also in the resistance of the device.

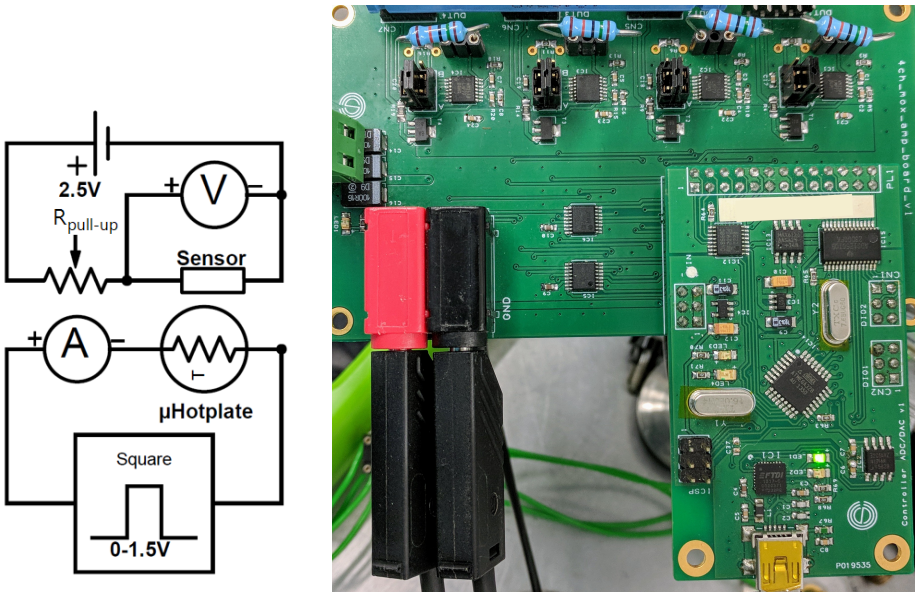

(a) Basic circuitry (b) PCB board.

Fig. 5.4 PCB board for laboratory gas characterization.

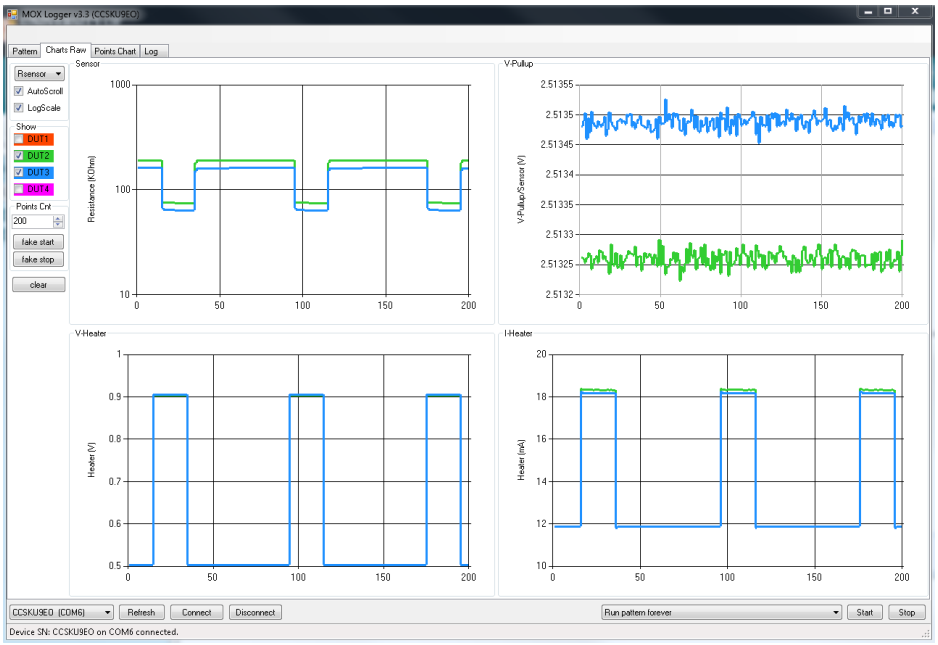

Fig. 5.5 Software interface for controlling the board.

For fully inkjet-printed devices

The setup for electrical measurements carried out for fully inkjet-printed devices in Chapter 8 Section 8.6 is described in this section. The system design uses the Wheatstone bridge circuit to calculate the unknown resistance value of the sensor and as a means of regulating measuring instrument. The bridge circuit is constructed with two serial and parallel resistances in between a voltage supply terminal and ground terminals as shown in Fig. 5.6(a).

When the bridge is balanced, the ground terminal produces a zero voltage difference between the two parallel branches. The expression illustrates the bridge sensor as follow. $R_s = \frac{R_2}{R_1} \times R_3$ Where R_s is the resistance of the sensor. The circuit is built with three known resistors and one unknown resistor (the inkjet-printed sensor) that is connected in the form of bridge. Since currents are flowing through each branch, when the value of the R_s changes, the potential difference at the terminal of the instrumentation amplifier (IA) varies, and therefore the differential output will also vary accordingly.

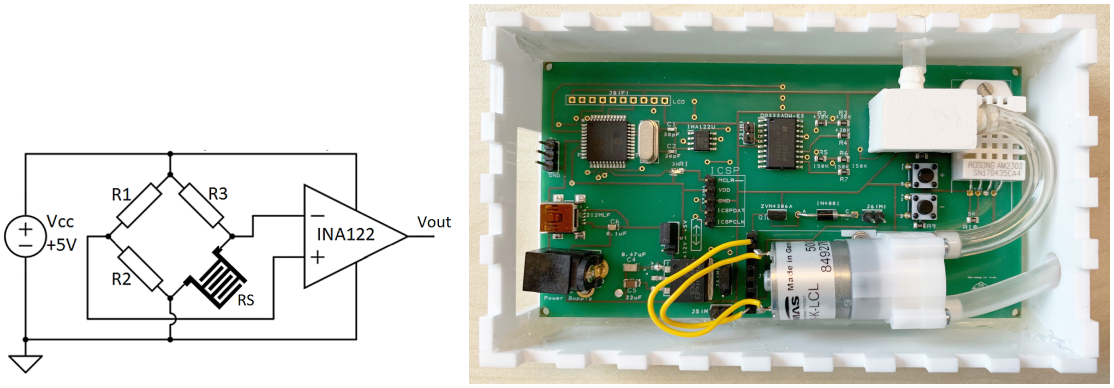

(a) Wheatsone bridge configuration. (b) PCB board.

Fig. 5.6 PCB board for real-world gas characterization.

The PCB and its main circuitry are shown in Fig. 5.6(b), 5.7, respectively. Wheatstone bridge is used with a single supply, micro-power IA (INA122, Texas Instrument, TI USA). This IA provides a low offset drift 3 μV/°C, low noise 60 nV/$\sqrt{\text{Hz}}$ and low input bias current of 25 nA. Thus this IA is capable of driving very low current, and is ideal for portable instrumentation, data acquisition systems and bridge amplifier sensor.

The output of IA is connected to an auto-select range which can be triggered by the microcontroller unit (MCU) (PIC18F) and select the specific resistance bridge range based on the value of sensor resistance R_s. The electronic configuration is selected via software detection, and can be switched through the multiplexer. The controlled single-pole double-throw switch (SPDT) minimizes measurement errors by offering a low on-resistance and low leakage (20 pA). The signal is then fed to 12-bits analog-to-digital converter (ADC) for

digitalization and further processes. The ADC of the MCU provides 12 effective number of bits (ENOB), which is equivalent to ≈1 mV resolution.

For compensating the environmental perturbations, the system design also incorporates a temperature and humidity sensor, as well as a pump to control the flow of environmental air to the sensor. The humidity sensor delivers a digital value to the MCU every 1 s through a digital pin on the MCU. The pump is driven through a CMOS transistor and altering the pulse width modulation (PWM) of changing due to cycle to adjust the flow rate of the air.

Two communications protocol have also been implemented in the MCU for interaction with the end-user by sending the processed data to the PC for real-time display and data acquisition. The first protocol is based on the universal serial bus (USB) and the second one is universal asynchronous receiver/transmitter (UART). Fig. 5.8 shows a graphical user interface (GUI) that is used for real-time display and data recording for further analysis.

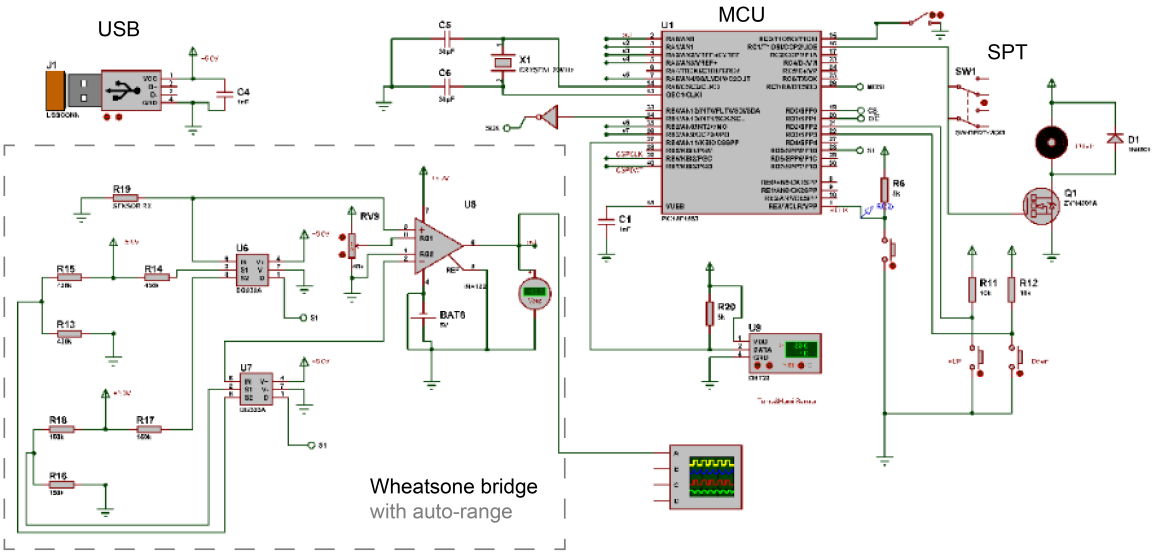

Fig. 5.7 Circuitry for the PCB. The main building blocks of the circuitry consist of Wheatstone bridge, MCU, and communications.

Fig. 5.8 Software interface for gas characterization.

5.3 Machine learning for analyte classification

In this section, I describe the machine learning techniques for discrimination of different levels of analyte, interferant combinations in an ambient environment, using a single sensor. The foundations of various machine learning techniques have been detailed in Section 2.4. This section describes the two implementation steps I employ, namely signal pre-processing and classification (with cluster analysis), according to the computation flowchart in Fig. 2.10.

5.3.1 Signal pre-processing

Signal pre-processing is essential to generate a clean dataset for analysis. Literature focusing on steady state training methods can be inaccurate in the ambient environment due to non-linear baseline drifts and variations in interfering species [226, 227]. I apply TM algorithm as pre-processing steps to suppress the effects of baseline drift and thus promote repeatability of measurements. The signals are then extracted with their transient features and trained with PCA and cluster analysis to establish a predictive system to discriminate a combination of analyte classes.

First, I obtain signatures of the pre-processed transient responses S_t to create a pattern library for the dataset. Fig. 5.9 illustrates the examples of feature extraction from a complete cycle of response under analyte exposure. The features extracted comprise (a) From exponential fitting I obtain response and recovery time constants τ_{resp}, τ_{recov}, and coefficients a_{resp}, a_{recov}. (b) Steady state information: responsivity S, and resistance change ΔR_{resp}, ΔR_{recov}. (c) Area of response and recovery signal under S_t curve A_{resp}, A_{recov}. (d) Features

from differentiated curve including timing t'_{resp}, t'_{recov} and magnitude R'_{resp}, R'_{recov} of the peaks. Note that in (a), the constants for response time τ_{resp} and recovery time τ_{recov} are evaluated with the following exponential fit of the output curve S_t:

$$S_{t,fit} = \begin{cases} S_{stab} + a_{resp} \exp(-\frac{t}{\tau_{resp}}) & [\text{analyte}] > 0 \\ S + a_{recov} \exp(-\frac{t}{\tau_{recov}}) & [\text{analyte}] = 0 \end{cases} \tag{5.1}$$

Where S_{stab} is S_t at stabilization; and responsivity S is S_t at equilibrium.

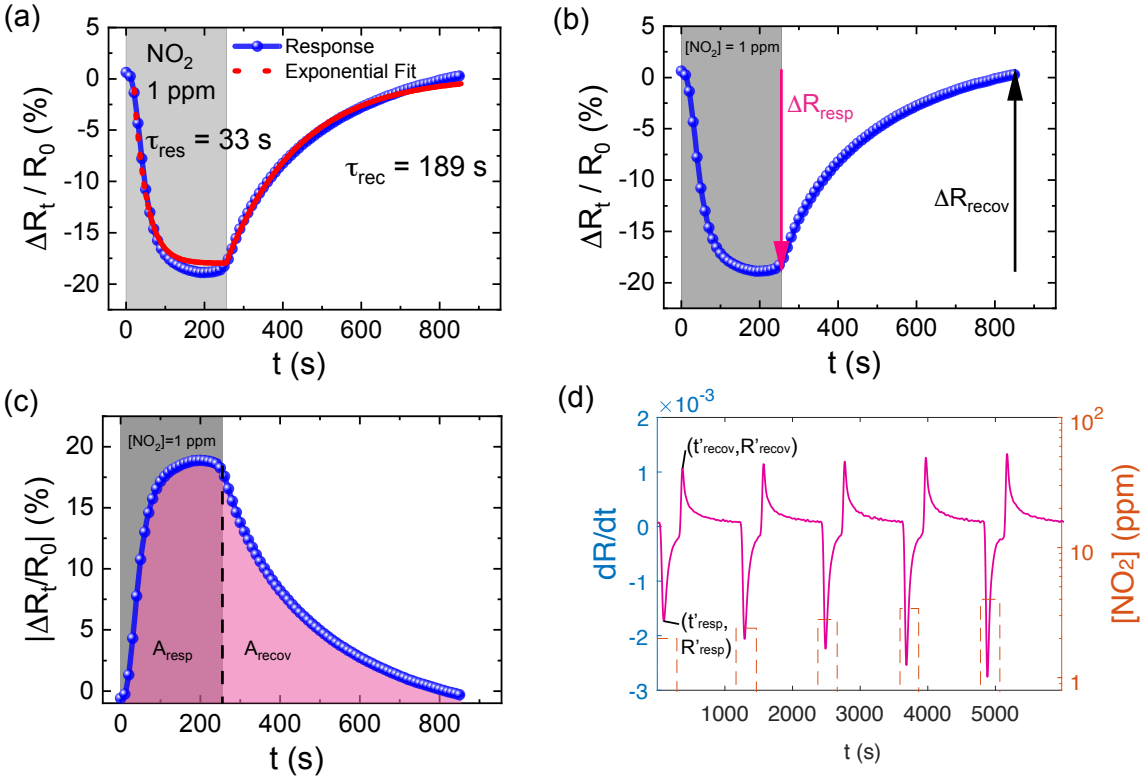

Fig. 5.9 Feature extraction methods used for computational analysis. (a) exponential fitting. (b) steady state information. (c) area under signal. (d) differentiated curve. These features are then used for cluster analysis. See Appendix Fig. A.1 for raw data.

5.3.2 Cluster analysis

Since there is often a high degree of sensor co-linearity in electronic nose data, the majority of the information held in the response can be displayed using a small number of principal components. This means that an n-dimensional problem can be described by a two- or three-dimensional plot [228]. I perform PCA for dimensionality reduction of the computed

features, and visualization of the clusters formed in low-dimensional projections. The transient feature matrix $M_{m\times n\times c,k}$ for PCA is computed as follows:

$$M = \begin{pmatrix} \left(\left(\left(\left(\frac{f_{m,n,c,k}}{\overline{f}_{m,n,c,k}}\right)_{m}^{\cdots}\right)_{n}^{\cdots}\right)_{c}^{\cdots} \\ \vdots \end{pmatrix}_{k}^{T} \tag{5.2}$$

where $f_{n,m,k}$ is the feature element with indices m: device ID, n: measurement index, c: group, k: variable. f and $\overline{f}$ denote the parameters obtained at adsorption and desorption phase, respectively.

Cluster analysis is conducted subsequent to the PCA transform. Fig. 5.10 demonstrates an example of cluster visualization using naive Bayes, decision tree, LDA, and kNN classifiers. The accuracy of the prediction can be determined by projecting untrained cross-validation dataset onto the predicted cluster and calculate the rate of misclassified data points.

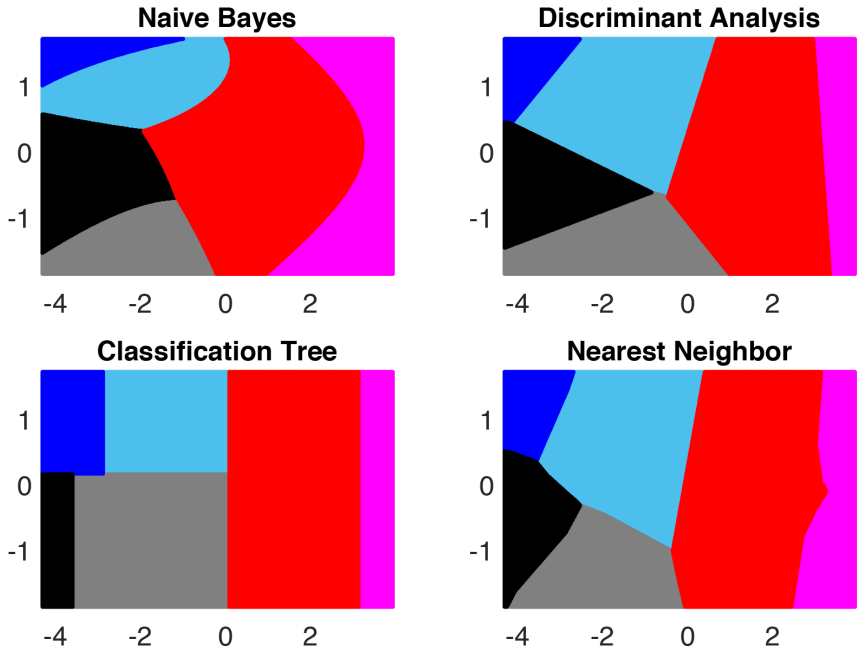

Fig. 5.10 Output of various classification algorithms.

5.4 Internet of things (IoT) implementation

In this section, I demonstrate a distributed wireless network consisting of multiple commercial sensors that could potentially be used for remote monitoring of local air quality in real-time. I developed this platform in my second year as part of the CAPA award in parallel to my research, with the aim of incorporating the sensors at the end of my PhD. Fig. 5.11 illustrates the deployment configuration of the IoT architecture consisting of sensor nodes, network layer, and the cloud. The sensor nodes deployed continuously stream the measurements using WiFi via the gateway to the server, to perform data analysis and storage. The application programming interface (API) developed then allows users to collect and manage the data from web applications.

The platform operates in such a way that multiple sensor platform networks are placed at distinct locations, and therefore the spatial mapping of different hazardous gases across certain area indoor and outdoor can be visualized with their mobile phone. Stakeholders can receive timely warnings on any toxic and combustible gases such as CO, VOC presented indoors, so they can respond accordingly. Moreover, residents in metropolitan cities can visualize the levels of urban pollutant including NO_2, CO and particle matter (PM) at different locations on the map.

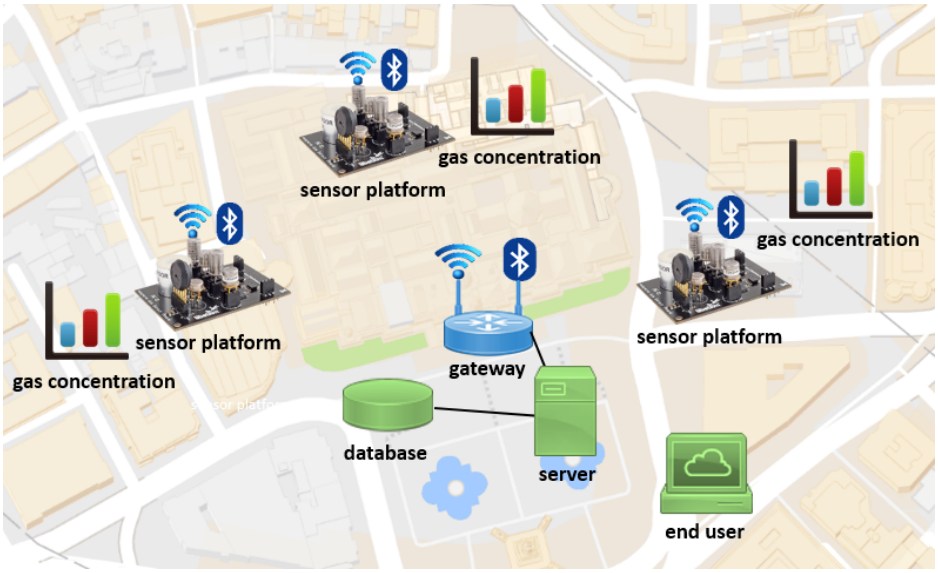

Fig. 5.11 Illustration of the spatial deployment of my IoT architecture.

The main health effects of air pollutants are summarized as follows. NO_2 will irritate our respiratory system, increasing the symptoms of those suffering from lung diseases and asthma. CO will lead to shortness of breath, dizziness, and death. Whereas the level of analyte can inflate the lining of the lungs and reduces the immunity to infections like cold,

cough, flu, and bronchitis. Furthermore, PM is a mixture of solid particles, chemicals (sulfates, nitrates, and other) and liquid droplets in the air. PM is divided into PM10 and PM2.5 depending on particle diameter. Fine particles can be carried deep into the lungs where they can cause inflammation, difficulty in breathing and even heart diseases, strokes, cancer.

5.4.1 IoT architecture

From the IoT architecture's perspective, the sensor layer is used to identify, sense and control the various state information of the end objects, and then transmit this information to the network layer through low-power, low-bandwidth sensing network communication module. Local area network (LAN) is usually used for these wireless sensors. The mainstream wireless network standards for IoT devices include RFID, ZigBee, Bluetooth, Wi-Fi, etc. The data is transmitted to the gateway via the antenna of the sensor platform then the wireless access point (AP). The signal is intervened through the gateway, and passed to the network layer. The gateway acts as a data bridge between the sensor network and the data center or cloud.

The application layer is responsible for storing and using the data received depending on the specific needs of the application. When the end object transmits the sensor information through the network to the top of the application layer, this system can connect individual data into a network of information, to perform analytical operations and automatic processing for specific events.

5.4.2 The sensor platform

The platform I develop can be decomposed into the following components.

(a) Hardware: The prototype is demonstrated in Fig. 5.12. The sensor platform is implemented on Arduino board where the sensors are connected through inter-integrated circuit (I^2C) communication. The commerical sensors used include MiCS-6814 which is capable to detect CO, NO_2, ethanol, H_2, NH_3, methane (CH_4), propane (C_3H_8); along with Grove PM sensor, and Grove global positioning system (GPS) module.

The output signal from each calibrated sensor is passed through a smoothing filter, amplifier, and then converge to a multiplexer to be processed by the microcontroller. The MCU is then interfaced with Arduino IDE programmed in C++.

Power is supplied through external battery switches to control the operations including sensor heat up, signal amplification and readout. To enable better power management for energy saving, the use of interruption control frees the MCU from having to control sensors all the time and set alarms to wake up to capture sensor values.

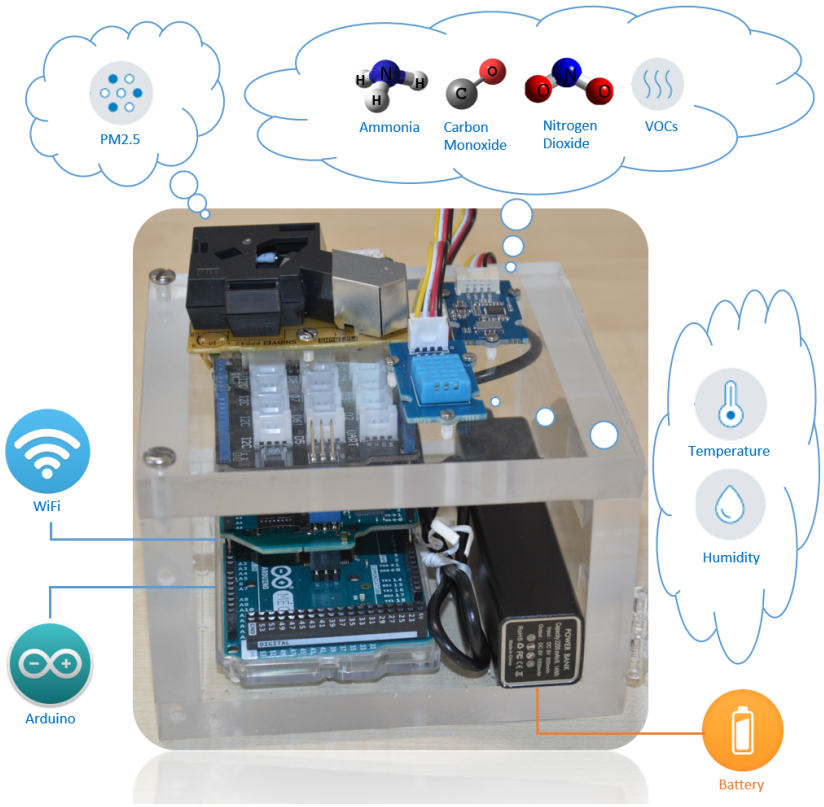

Fig. 5.12 Image of the prototype I develop. The icons indicate the functionalities of each component.

(b) Communications: The data transmission is accomplished by WiFi, Bluetooth modules which are connected through UART protocol and controlled by the multiplexer. The Raspberry Pi gateway connects the sensor network to the server via these wireless protocols. Socket programming is developed to transfer data across the network. The data received by the server is stored in the sensor memory, which can then be managed.

Realtime sensing data (including temperature, humidity, NH_3, CO, NO_2, C_3H_8) is streamed to the cloud. The live sensor data is displayed in the web server hosted at ThingSpeak^{TM}, as shown in Fig. 5.13.

(c) Analytics: The data from individual sensors is analyzed to compute air quality index (AQI). In summary, the platform delivers the following features:

- Portable: The unit can be placed both indoors and outdoors for detection.
- Wireless: Each unit is wirelessly connected with a long communication range, allowing continuous upload of sensor data.
- Traceable: The unit can be traced to display the exact location in motion.
- Reconfigurable: The unit can be readily programmed to meet specific requirements.

Fig. 5.13 Cloud-based interface showing realtime sensor data.

- Analyzable: Data collected can be sent for data analytics in cloud service.
- Accessible: Open source data that is easily accessible.

5.4.3 Field trial

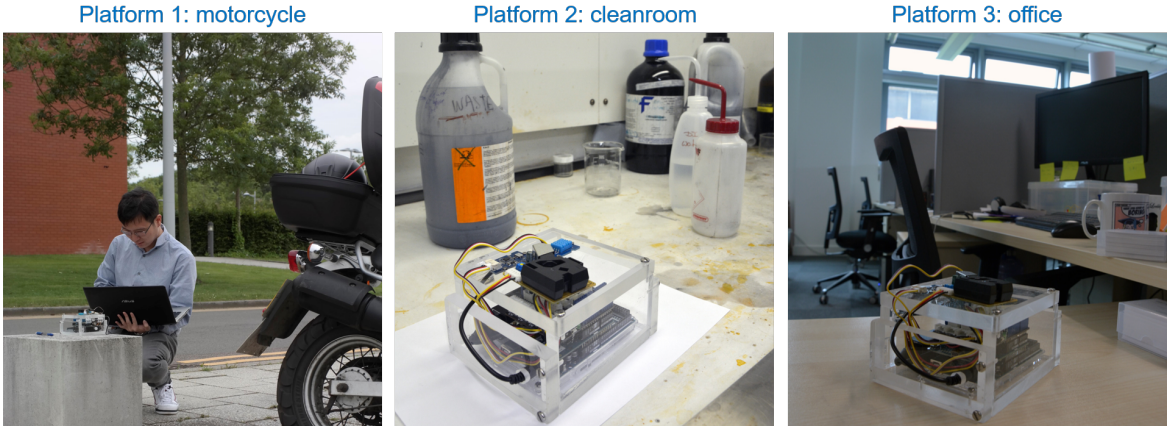

Fig. 5.14 Deployment sites: 3 platforms deployed at the road, cleanroom, and office.

Fig. 5.15 Results of the trial showing CO, NO_2, C_3H_8, NH_3 with commercial sensors.

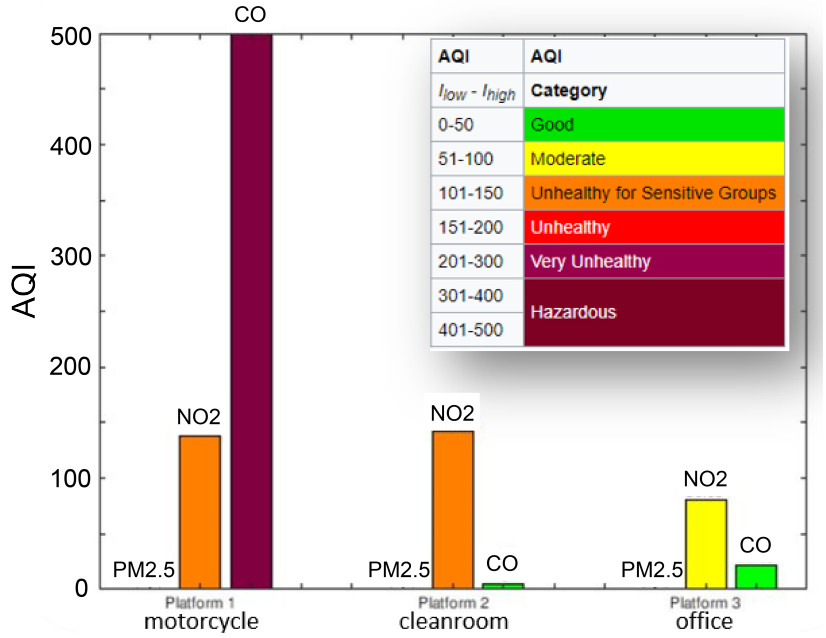

Fig. 5.16 AQI data computed from the 3 platforms.

The platforms containing commercial sensors are deployed at three different sites, as seen in Fig. 5.14. Platform 1 is deployed by the road and measured while the motorcycle is riding. Platform 2 is deployed at the cleanroom. Platform 3 is deployed at the closed office.

Fig. 5.15 displays the measurment results during a motorcycle trial carried out at the site where Platform 1 was placed. The AQI of PM2.5, analyte, and CO in each platform have been computed in Fig. 5.16. During the trial in a sunny condition, I turn the throttle for three times, then release the clutch and give it a continuous throttle, then squeeze the clutch in.

Focusing on Platform 1, I observe 3 small peaks and a huge peak at the CO level, corresponding to the action described. There is only one large peak observed for the C_3H_8 and PM2.5 levels, corresponding to the release of clutch. The response of C_3H_8 saturates after responded. It can be seen that the AQI of CO at Platform 1 reaches a hazardous level at the instance of the release of clutch. The levels of each gas at Platform 2 and 3 for the duration of testing remain constant as expected. The CO level in the office is slightly higher than in the cleanroom, as it is a closed and crowded environment. However, it is noted that the values for these low-cost commercial sensors are not accurate enough.

The monitoring system is expected to send clients Twitter alerts at the instance when the level of pollutant reaches the exposure limit. The thresholds are set to be 25 ppm for CO, 5 ppm for NO_2, and 35 ppm for NH_3. Fig. 5.17 shows a flowchart of realtime Twitter alert and verifies that alerts are sent at the instances of the peaks.

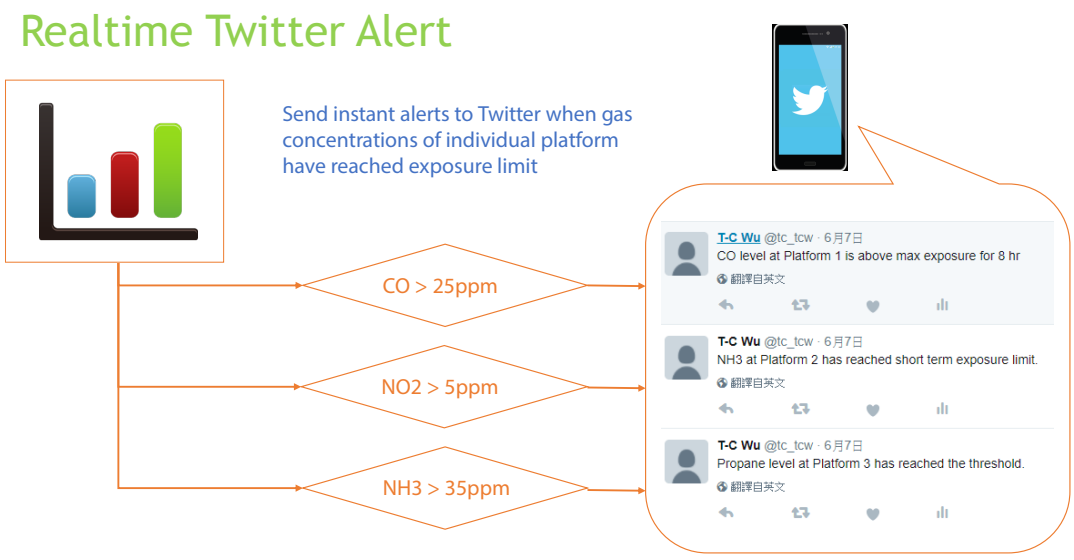

Fig. 5.17 A flowchart of realtime Twitter alert.

The cloud-based analytics I develop for recognition of pollutants and particle matters components using low-cost sensors not only has the potential for visualization of ubiquitous spatial mappings of both metropolitan and indoor AQI, but also enables transmission of

timely alerts while detection of toxic and combustible analytes. Furthermore, the multi-sensor array approach can also promote the development of algorithms to compensate for interfering effects for improvement of detection accuracy.

5.5 Summary

In this chapter, I detail the signal transformation protocols and algorithms including electronics configurations, temperature modulation technique, cluster analysis for addressing cross-analyte interference, and IoT solutions for connected sensors networks and cloud-based analytics. In the analyte classification section, I discuss the computational approaches including signal pre-processing and cluster analysis techniques to address the common issue of cross-analyte interference. Finally, I establish a distributed wireless network of sensor platforms consisting of multiple gas analyte, and generate visualization mappings of air quality index, and transmit timely alerts while the level of harzardous analyte is above threshold. The approaches discussed in each section serve as practical tools for the implementations of intelligent systems composed of sensors I fabricate in the following chapters.

Chapter 6

Detection of Ammonia

Increasing awareness of personal health conditions is rapidly promoting the development of point-of-care technologies for early diagnosis of diseases. Breath analysis is an important candidate among the various diagnostic technologies available [229, 3]. This is due to its non-invasive approach for detecting unique chemical signatures that can be correlated with specific diseases [229, 3]. Among the various species in exhaled breath, ammonia (NH_3) is a critical biomarker associated with a range of kidney and liver disorders [230, 3]. The new generation NH_3 diagnostic systems rely on the development of low-cost, miniaturized devices in which semiconducting MOx are commonly utilized as the sensing layer among chemiresistive sensors [11].

In particular, NH_3 detection using ZnO/graphene hybrids demonstrate improved responsivity [155]. Despite this, critical issues common to chemiresistive sensors such as long recovery time [53–55], severe baseline drift [56, 55, 57], poor device-to-device consistency [170], cross-analyte interference [171, 117], remain unresolved. Limited attempts based on dynamic control of operating temperature [38, 172–174] have not been sufficiently effective to resolve the issues [172], and they lack systematic and quantitative experimental support [172, 38]. This has inhibited a satisfactory understanding of the underlying mechanisms and their interplay. The aforementioned challenges all hinder diagnostic applications [3] and can not be easily addressed through the sensing material alone [229, 3]. Instead, a holistic solution is necessary to realise devices suitable for personal healthcare monitoring.

In this chapter, I present a graphene-MOx hybrid sensing material that is integrated onto a (1×1 mm) CMOS μHP platform supplied by Prof. Florin Udrea's group. The miniaturized device platform is tailored using inkjet deposition as a high-precision, material-efficient and scalable technique to produce thin and uniform sensing layers suitable for rapid and consistent detection. I address the shortcomings from previous studies on high power consumption/operating temperatures, long recovery time and baseline drifts by optimizing the

sensing material and ink formulation, together with the development of a temperature modulation strategy and measurement algorithms.

Using stage-by-stage temporal analysis, I establish comprehensive quantitative studies on temperature-dependent mechanisms for the material system to develop applicable algorithms, leading to enhanced sensing performances and reproducibility. Additionally, my approach of using inkjet deposition offers excellent device-to-device consistency, overcoming a common drawback of the majority of the other studies.

The contents of this Chapter are my original work and have been published [59]. I thank Xiaoxi Zhu for the assistance on TGA, AFM, and Raman characterizations. I thank Tom Albrow-Owen for the assistance on SEM characterizations.

6.1 Ink formulation and characterization

6.1.1 Production and formulation of graphene-MOx inks

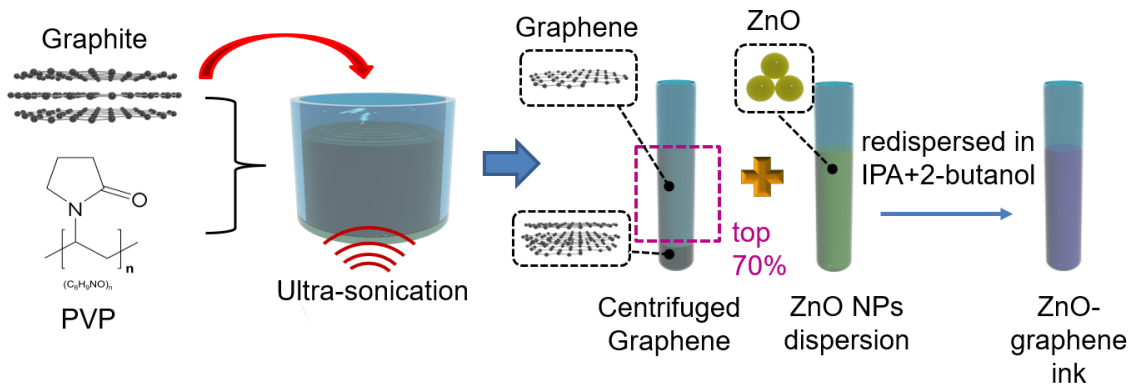

Fig. 6.1 Illustration of graphene-ZnO ink formulation process.

The ink production process is illustrated in Fig. 6.1. The process involves exfoliation of graphite crystals via ultrasonic-assisted liquid phase exfoliation (UALPE) into a stable dispersion of few-layer graphene flakes. I ultrasonicate 100 mg of graphite (Sigma-Aldrich, 100 mesh flakes) with 1.5 mg PVP (Sigma-Aldrich, average molecular weight 10,000 Da) in a mixture of 9 mL IPA and 1 mL 2-butanol for 12 h. The mixtures are sonicated for 12 h in a 20 kHz bath sonicator at 25 ˚C, centrifugated at 4030 rpm and the top 80% of resultant dispersion is collected.

ZnO nanopowder (Sigma-Aldrich 677450) is dispersed in IPA, 2-butanol, PVP, and sonicated according to the above, and subsequently filtrated. Subsequently, the graphene and ZnO dispersions are mixed according to different graphene loading and sonicated for 30 min

to produce the final ink which is then loaded into Fujifilm Dimatix DMP-2831 inkjet printer. With aid of the model developed in Chapter 4, the following printing parameters are set for the printer: inter-layer delay of 60 s; drop spacing of 30 μm at 55 ˚C which forms continuous line morphology.

To suppress such non-uniform deposition, I employ a binary alcohol mixture based ink formulation strategy with 90 vol.% IPA and 10 vol.% 2-butanol composition to the final ink [58, 186]. This formulation (surface tension $\gamma_{ink} = 31.12$ mN m^{-1}) allows deformation of the ink droplet and counteracts the capillary flow during drying, while keeping the surface tension low enough for good wetting of the silicon nitride substrate (Si_3N_4 μHP membrane, surface energy $\gamma_{sub} \approx 40$ mN m^{-1}) [219].

Ink concentrations. The effective concentrations of the inks produced can be characterized by thermogravimetric analysis (TGA). The TGA plots of ZnO ink and graphene ink, before mixing together to form ZnO-graphene hybrid ink, are shown in Fig. 6.2. These plots are used to determine the concentrations of inks, by multiplication of weight percentage by the density of the IPA/2-butanol solvent mixture ($\rho \approx 0.8$ g cm^{-3}).

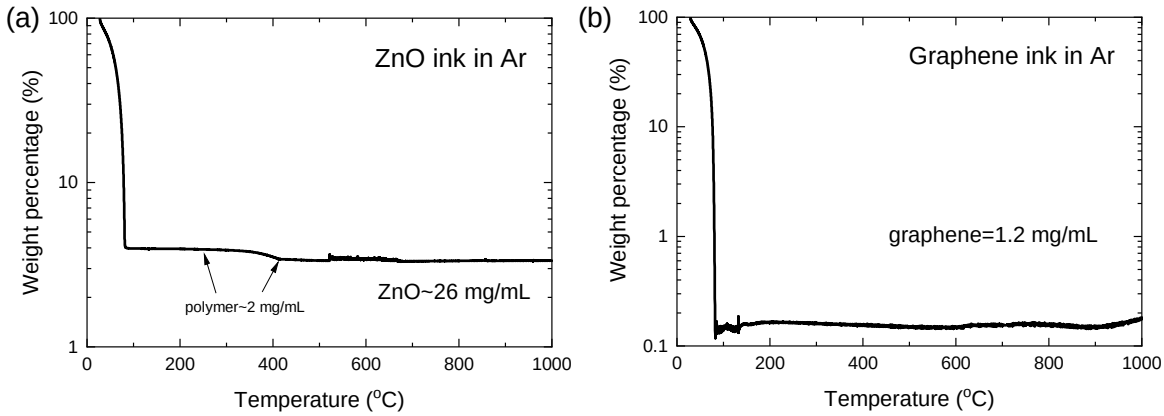

Fig. 6.2 TGA of pre-mixed (a) ZnO ink (b) graphene ink.

The solvent of both inks evaporates below 80 ˚C. In the ZnO ink, the decrease in mass in the temperature ranges between 200-400 ˚C indicates the concentration of PVP binder in the ink, estimated to be 2 mg mL^{-1}. Note that after annealing the device at above 400 ˚C, only 5 wt.% (equivalent to 0.1 mg mL^{-1}) of the initial PVP remains in the printed film. This is discussed later. The ZnO concentration is estimated to be 26 mg mL^{-1}, based on residual mass at > 600 ˚C. In the graphene ink, the effective concentration is estimated to be 1.2 mg mL^{-1}, based on residual mass at > 400 ˚C; whereas PVP content is too low to be measured. The value has been estimated to be 3.8×10^{-3} mg mL^{-1} according to Ref [93].

The prepared dispersions are sonicated together to obtain a homogeneous and stable ink. By mixing ZnO and graphene dispersions at different ratios, I formulate three graphene-ZnO inks with different graphene loadings (0%: pure ZnO, 3 wt.% graphene: ZG-3, 6 wt.% graphene: ZG-6); Fig. 6.3(a). These three formulations are all assembled onto the CMOS platform to carry out gas characterization in order to optimize the graphene loading in the composite.

6.1.2 Characterization of inks

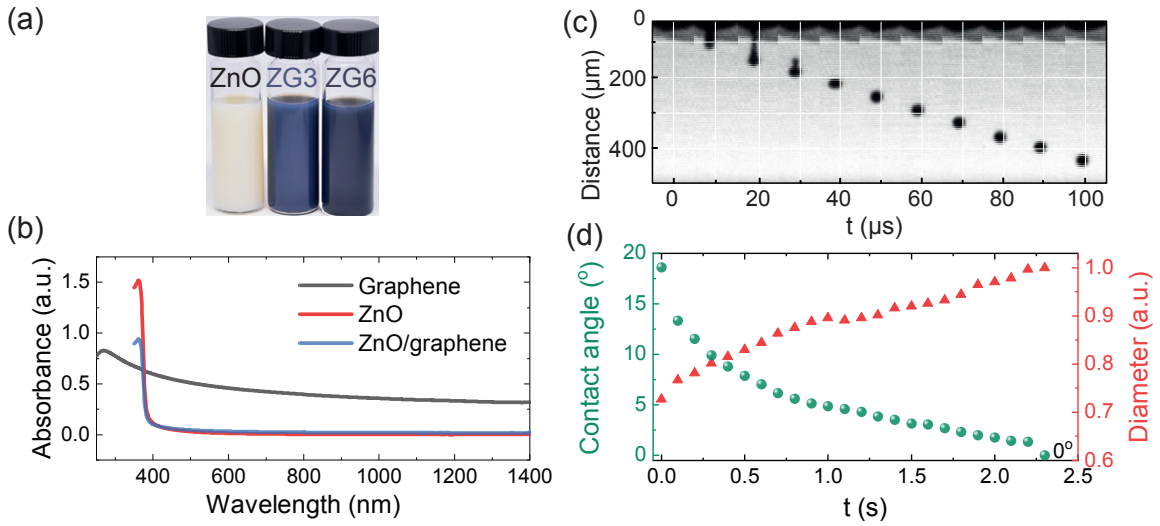

Fig. 6.3 (a) Images of formulated ZnO, ZG-3wt%, ZG-6wt% inks. (b) Optical absorption of diluted graphene, ZnO, and ZnO/graphene inks. (c) Jetting sequence of ZnO/graphene inks, showing rheological properties on the right. (d) Change in contact angle over drying process.

Absorption spectrum. Fig. 6.3(b) shows the optical absorption spectrum of diluted graphene, ZnO, and ZnO/graphene inks, respectively. The spectra identify the characteristics peaks of graphene [63] and ZnO NPs [231], where the peaks are located at 270 nm and 360 nm, respectively. The incorporation of graphene into ZnO ink does not shift the peaks in liquid phase, but lowers the concentration of dispersion, leading to a reduction in absorbance.

Jetting properties. For inkjet printing, stable ink drop generation is crucial for high quality printed films. The printability of the ink can be predicted with inverse Ohnesorge number Z from Equation 4.4 As a rule of thumb, studies [63, 216] have suggested that stable jetting satisfies Z of 1-14 to avoid the formation of long filament or secondary/satellite droplets.

The rheological properties of the formulated inks are presented in Table 6.1. Taking ZG-3 inks as an example, the rheological parameters measured are: $\gamma_{ink} = 31.12$ mN m^{-1}, $\eta = 2.14$ mPa s at 10^4 s^{-1} (shear-thinning), $\rho = 0.8$ g cm^{-3}, $D = 21.5$ μm, giving a $Z = 10.8$. The inks presented in Table 6.1 have similar surface tensions γ and viscosities η but different densities ρ, leading to slightly different Z values. Despite this, all inks lie within the optimal jetting range ($Z = 1$-14) suitable for printing.

Ink	γ (mN m^{-1})	η (mPa s)	ρ (g cm^{-3})	Z
ZnO	32.29	2.81	0.816	8.47
ZG-3	31.12	2.14	0.798	10.8
ZG-6	31.73	2.03	0.795	11.5

Table 6.1 The rheological properties of the formulated inks.

Complying with the Z estimation, all the inks exhibit similarly stable jetting and droplet formation without generation of satellite droplets, as visualized from the jetting sequence in Fig. 6.3(c).

Droplet drying dynamics. The drying dynamics of the ink is characterized by time-dependent contact angle measurement for the duration of droplet drying onto a clean Si/SiO_2 substrate (Fig. 6.3(d)). The initial angle is 18° which indicates a good wetting of the substrate. The contact angle descends as the droplet spreads due to low surface tension, dropping linearly after ≈ 0.6 s, until the angle saturates at close to 0°. At the same time, after ≈ 1 s, the diameter of the droplet increases at a reduced speed, suggesting a contribution of Marangoni flow to suppress the coffee-ring effect [58, 218]. In addition, no sudden perturbation in the contact angle is observed during the drying process. These indicate a good wetting of the substrate and uniformly deposited graphene/ZnO after ink drying.

Device fabrication. To fabricate the sensors, I use inkjet printing to deposit the ZnO-graphene functional inks directly onto the Au IDEs on to the Si_3N_4 membrane substrate (5 μm finger width and gap; 250 μm diameter) of the CMOS μHP. This process enables automated fabrication of multiple devices at once, as schematized in Fig. 6.4(a). Fig. 6.4(b) shows a typical example of an inkjet-printed graphene-ZnO device (ZG-3). The number of print repetitions (20 passes) is optimized by characterizing the morphologies of printed films with 10, 20, and 40 passes (see Appendix Section A for optimization routes). The overview image reveals a printed pattern with high print definition and uniform material distribution. The zoomed-in image further shows the evenly distributed graphene-ZnO NPs on top of and in-between the IDEs.

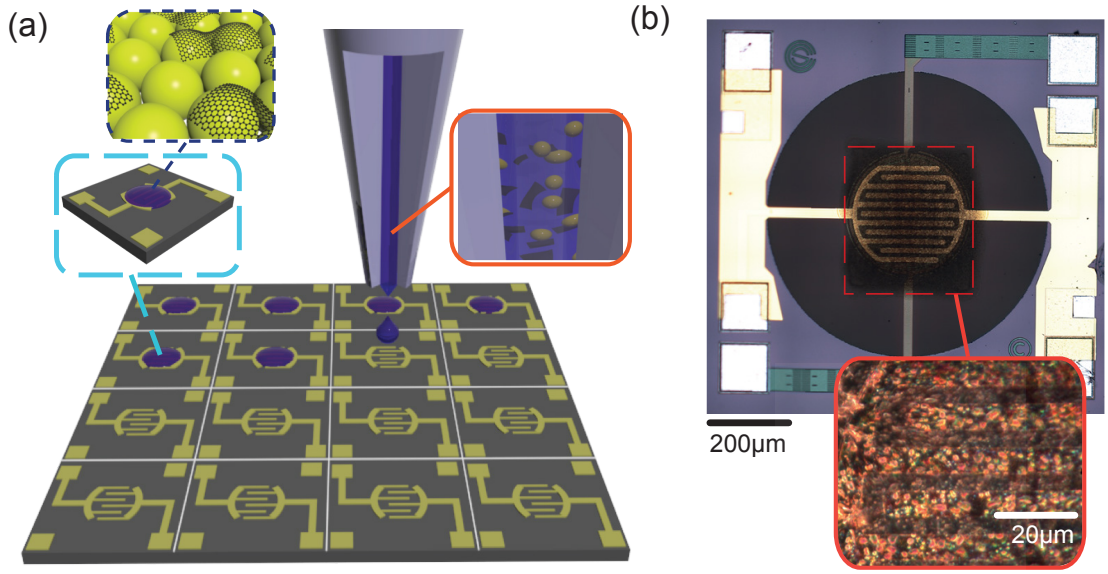

Fig. 6.4 (a) Illustration of inkjet deposition process. (b) Microscopic image of the inkjet-deposited CMOS sensory device.

6.1.3 Characterization of printed films

Decomposition characteristics of PVP. Although PVP improves exfoliation and stabilization of the ink, it is an insulating polymer and is detrimental to the functionality of the graphene-ZnO sensing layer. I therefore remove PVP by decomposing it through annealing at 400 ˚C for 30 min [214, 215] using the μHP in Ar atmosphere.

The decomposition characteristics of PVP is studied as follows. First, I verify the decomposition temperature range of PVP by TGA, as shown in Fig. 6.5(a). The temperature at which the highest rate of change occurs is ≈400 ˚C. I then apply 400 ˚C in Ar to study the decomposition profile as a function of annealing time (Fig. 6.5(b)). The weight of PVP drops significantly to ≈10% of its initial weight within 30 min. It further decomposes slowly until less than 5 wt.% (i.e. $2\text{mg mL}^{-1} \times 5\% = 0.1\text{mg mL}^{-1}$). PVP composition in the annealed film can be estimated as:

$$\frac{\text{PVP}[\text{mg mL}^{-1}]}{\text{ZnO} + \text{graphene} + \text{PVP}[\text{mg mL}^{-1}]} = \frac{0.1}{26 + 1.2 + 0.1} = 0.34\text{wt.\%}$$

As verified by the TGA data, this condition selectively decomposes PVP to less than 5 wt.% of its initial concentration, resulting in a negligible contribution (0.34 wt.% of residual) in the annealed film.

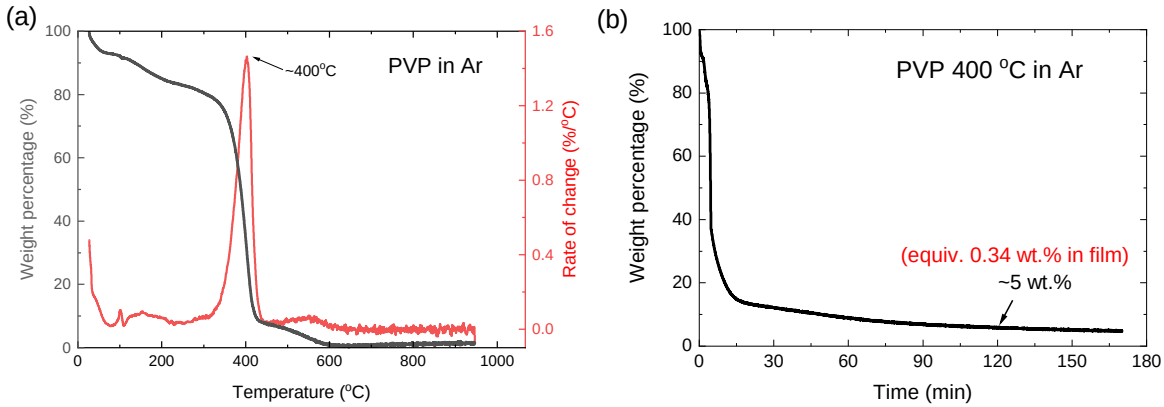

Fig. 6.5 TGA of PVP (a) as a function of temperature (b) as a function of annealing time.

AFM characterization. AFM characterization is conducted to measure the lateral size and thickenss of exfoliated graphene flakes to study the physical model governing the sensing mechanism. The dimensions of the graphene flakes is evaluated with statistics of AFM characterization. The overall procedure is described as follows. I use the ScanAsyst^{TM} software by the AFM manufacturer – Bruker, which enables flake recognition functionality with a user-definable threshold. Once the threshold is set to allow for identification of correct boundary of the flake, I scan through a 2×2 μm area for each measurement and compute the average lateral dimension and thickness counts for each flake in the field. 6 measurements were taken and the counts from each measurement are accumulated to generate the histograms shown in Fig. 6.6.

To perform statistical analysis, the histograms are fitted with a log-normal fit, as the dataset follows Poisson distribution [232]. The probability distribution functions (PDF) peak at ≈130 nm and ≈1 nm in lateral dimension and thickness, respectively. The median values are then evaluated at the positions where the corresponding cumulative distribution functions (CDF) equate to 0.5, resulting in median lateral size and thickness of ≈150 nm and ≈2 nm. My findings are supported by Ref [233, 93, 234] which produce graphene flakes by LPE and with similar formulations.

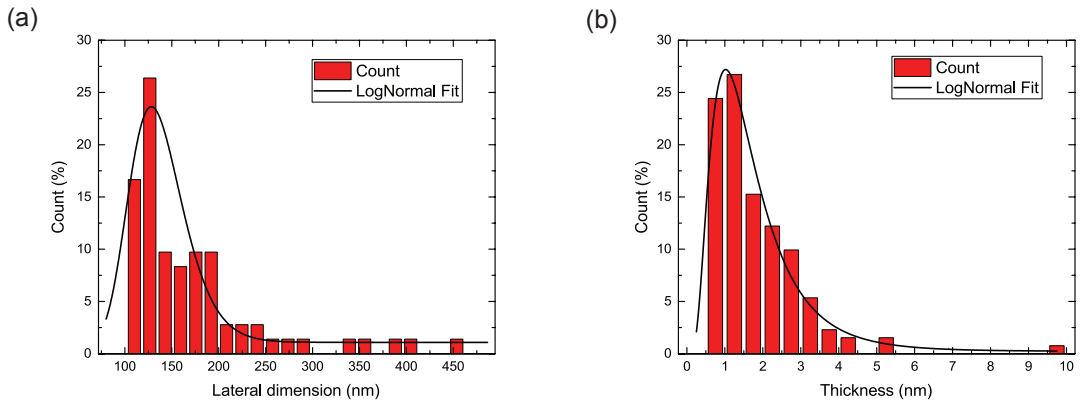

Fig. 6.6 Histogram of AFM on graphene flakes (a) lateral dimension distribution (b) thickness distribution.

SEM characterization. Fig. 6.7(a) shows a set of SEM images comparing pre- and post-annealed inkjet printed ZnO-graphene thin films. Images of graphene/ZnO films are acquired with a high resolution Magellan 400L SEM. The field emission gun is operated at 15 kV and 10 pA gun current. A 3 nm gold (Au)/Pd coating is sputtered onto the surface to reduce the build-up of electrons. The pre-annealed film above shows a matrix of ZnO NPs connected through graphene and PVP polymer; whereas the post-annealed film below shows selective decomposition of PVP. The morphology shows considerable areas of exposure to ZnO NPs. Also, I propose that the porosity of printed film, produced by the removal of PVP [233] improves gas diffusion capability. The SEM image also shows that the average diameter of the ZnO NPs is ≈ 40 nm.

Raman characterization. I also carry out Raman measurements to investigate the composition change in graphene before and after the annealing step. The measurement uses an excitation wavelength of 514 nm with a power of 16 mW and a duration of 10 s for each measurement point. Fig. 6.7(b) shows representative Raman spectra (out of 10 similar measurements taken at random locations on the samples). The existence of few layer graphene in the composite film is supported by the shape of the 2D peak which is located at 2720 cm^{-1} [175, 176]; whereas the signature of ZnO NPs is identified by the E_{2H} peak located at 438 cm^{-1} [235].

The samples are further characterized by the I_D/I_G ratios. The ratios have a small increase from 0.46 to 0.59, indicating a slight defect-generation in the graphene flakes after the annealing step. The decomposition of PVP is evident in the significant suppression of D′ peak in post-annealed film [236]. Furthermore, the tiny amount of PVP residual that could lead to electron doping of graphene [234] is reverted (hole doping restored) as seen from the

increase in the position of $2D_{Gr}$ peak [237] in Fig. 6.7(b). Therefore, PVP does not play an active role in sensing.

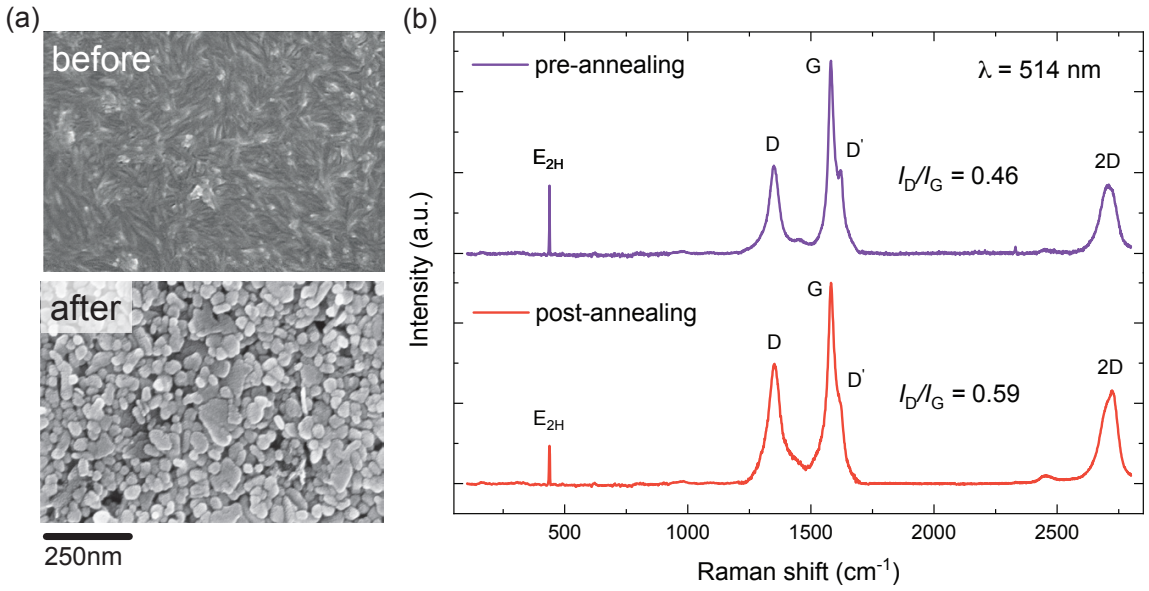

Fig. 6.7 (a) SEM images of printed ZnO-graphene composite films: pre-annealing on the top, post-annealing on the bottom. (b) Raman spectra of ZG-3wt% printed films pre- and post-annealing treatment, respectively.

6.2 Sensing mechanisms and performances

This section studies the sensing mechanisms under constant operating temperature, referred to as the isothermal (ISO) mode. Fig. 6.8(a) illustrates the sensing mechanisms for the detection of pure NH_3 with graphene-ZnO composite, with the aid of band diagram associated with the adsorption of gas at the ZnO-ZnO junction and the junction between ZnO and graphene. The bandgap alteration is established by the graphene-ZnO M-S heterojunction, where occurence of inhomogeneous electrostatic potential is created by the van der Waals interaction of graphene and MOx, allowing for the transfer of charges across the heterojunction [238, 239].

In an inert gas environment, a relatively small potential barrier is formed at the grain boundaries at the ZnO/ZnO interface [240]; whereas M-S Ohmic contacts are formed at the graphene-ZnO interface[116, 57]. The gas adsorption behavior of graphene-ZnO during NH_3 exposure can be classified as follows.

Chemisorption occurring at the ZnO surface leads to increment in the potential barrier between the ZnO NPs. The superior physisorption capability of graphene, especially at the

defect sites and ZnO interfaces [94], contributes to the increment in the potential barrier, resulting in an amplification of responsivity compared to that in pure ZnO. The amplification of bandgap alteration at graphene/ZnO interface due to the higher density of adsorbed gas molecules than at the ZnO surface is the dominating factor for responsivity enhancement [238]. The effective conduction paths consist of a combination of ZnO NPs conduction channels and graphene-ZnO heterojunctions.

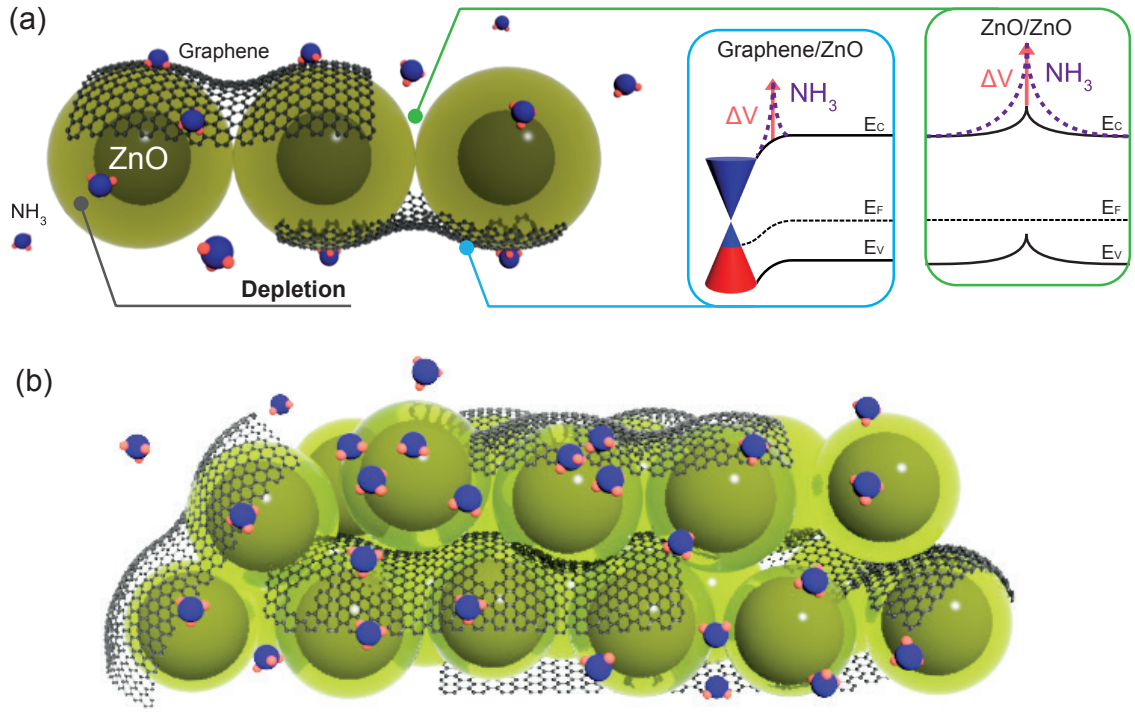

Fig. 6.8 Illustration of sensing mechanisms on detection of pure NH_3 with graphene-ZnO composite in ISO mode. (a) a simplified model with a band diagram. (b) a more realistic model.

Fig. 6.8(b) presents a more realistic physical representation that comprises multiple layers of graphene-ZnO hybrid stacking on each other, to better reflect the observed morphology and dimensions of graphene and ZnO NPs, as well as their randomness in spatial distributions. The porous structure produced by the decomposition of PVP, coupled with the edge defects on graphene [241] produced by the LPE processes, establish efficient gas diffusion channels [233] towards the graphene-ZnO heterojunctions at which bandgap alteration takes place.

As sensing in graphene/MOx system is mainly enhanced by the bandgap modulation at the graphene/MOx interfaces [94], deposition of graphene/MOx hybrid in multiple lay-

ers would maximize the total area of gas exposure to these heterojunctions (as opposed to exposure to single interfacial layer) and thus enhancements in sensitivity.

Fig. 6.9 shows the temperature dependency profile of the ZG-3 sensor in isothermal mode. When temperature increases from RT, the number of surface electrons surges due to thermal activation, which leads to more NH_3 being oxidized, and thus a surge in responsivity. Whereas the drop in responsivity at very high operating temperatures (above 325 ˚C) may be due to the favored desorption of NH_3 molecules. The profile maximizes experimentally at 300 ˚C, therefore I proceed my experiments with this condition.

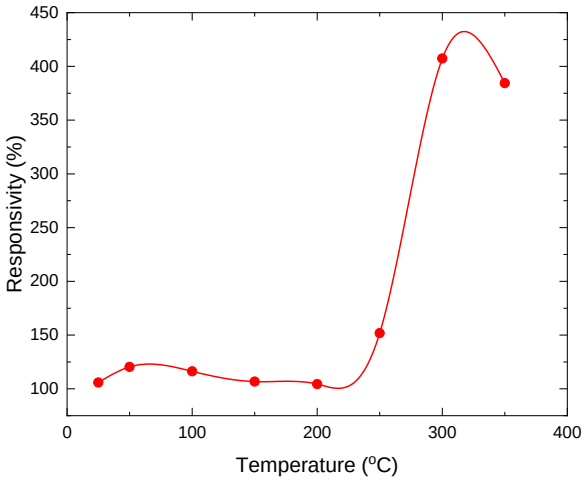

Fig. 6.9 ISO mode responsivity of ZG-3 device as a function of temperature. Curves are fitted with third order polynomial. See Appendix Fig. A.4 for raw data.

The physical model aligns with the experimental observations as follows. First, pure ZnO NPs matrix follows neck-controlling model [37] (as $d \geq 2l$, where d is diameter of NP, l is depletion width within individual NPs) where the conductivity is altered by l, and is sensitive to analyte gas concentration (Fig. 6.10(a)). Second, increasing the loading of graphene, which provides additional conduction paths between NPs, shows improvement in electron transport as revealed in the lowered resistance value in Fig. 6.10(a).

Fig. 6.10(b) shows linear responsivity of the three ink formulations on the logarithm of analyte concentration. The ZG-3 sample, corresponding to 3 wt.% graphene loading, shows maximum enhancement (60% compared to that of pure ZnO) as interconnections between graphene sheets are optimized. I note that the ZG-3 sample also presents the best repeatability over testing cycles (Fig. 6.10(c)), whereas the pure ZnO sample shows distorted and declining response. This observation indicates that graphene stabilizes the gas detection performance in my sensing material formulation. However, significant baseline drifts along with slow recovery time reveal incomplete recovery to the initial state after a sensing event.

Therefore, I attempt to establish an effective operation control algorithm to stabilize and optimize the sensing performance.

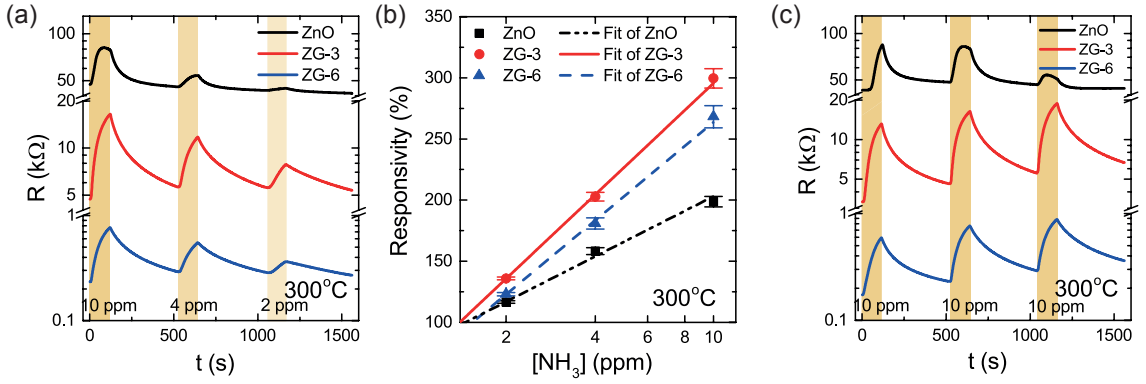

Fig. 6.10 (a) Resistance response at 10, 4, 2 ppm of NH_3 respectively. The orange region represents injection of NH_3 in ppm. (b) Responsivity as a function of NH_3 concentration with linear fits. (c) Resistance response at 10 ppm NH_3 repeated over 3 cycles.

Fig. 6.11 shows the control group using inkjet-deposited graphene devices. The mean responsivity of the devices at 10 ppm of NH_3 is 0.84% which is a negligible fraction of the responsivity observed for ZG-3 devices (≈300%). The poor responsivity of these control devices confirms that the synergistic effect of graphene and MOx is responsible for the high sensitivity of the sensors.

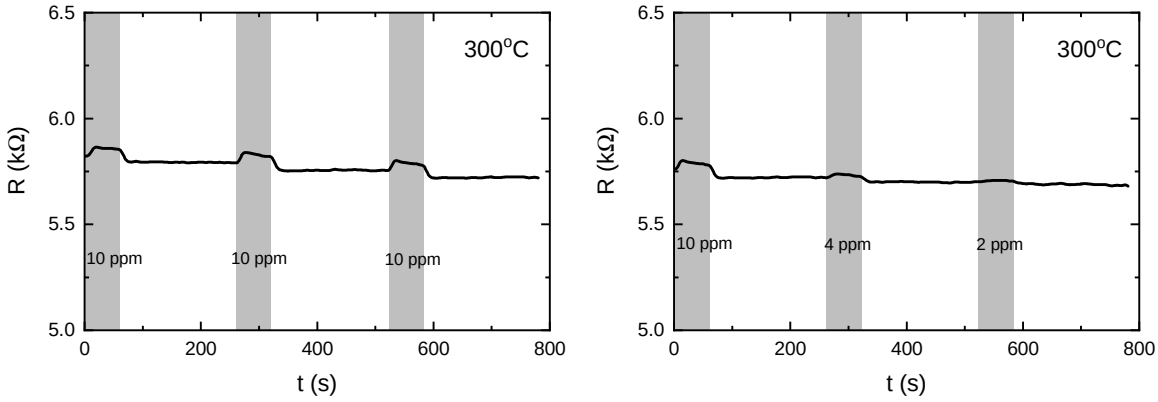

Fig. 6.11 Response curves for graphene device under exposure of NH_3 (a) at 10 ppm for 3 cycles (b) at 10, 4, 2 ppm respectively.

6.3 Temperature modulation (TM) technique

Limited attempts based on dynamic control of operating temperature have been applied in the literature to improve detection limit [38], baseline drift [172], cross-selectivity [173, 174], and power consumption of MOx and 2D material gas sensors. However, these approaches have not been sufficiently effective to resolve the issues [172], and lack systematic and quantitative experimental support [172, 38]. This has inhibited a satisfactory understanding of the underlying mechanisms and their interplay.

Harnessing the capability of rapid temperature control offered by the CMOS platform, TM can be employed in dynamic-programmed modes. There are two categories for TM: temperature cycling and thermal transients [242]. In the former, the heater voltage is periodic and the sensor is typically under a sinusoidal waveform to give a smooth temperature profile [242]. In the latter, it involves a step or pulse waveform in the heater voltage, and the discriminatory information is contained in the chemical transient induced by the fast change in temperature [243]. Thermal transient is used throughout the thesis.

6.3.1 Temperature dependency analysis

I conduct the following quantitative and qualitative analysis to establish the mechanisms on temperature-dependent sensing behaviors of graphene/MOx NP composite. Suppose the mechanisms of the operations of sensors are analyzed at RT and an opterating temperature of 300 ˚C (as seen in Ref [131, 244, 59]). At RT (25 ˚C) period (Fig. 6.12(a)), exothermic state for physisorption is maintained (Equation 2.2) while chemisorption is not activated (k in Equation 2.3 is very low at 25 ˚C). Thus, physisorption of analyte at graphene sites and graphene/MOx NP interfaces dominates chemisorption.

From the bandgap perspective, fewer electrons are energized at low temperature (as inferred from Equation 2.6) to overcome the raised barrier arising from physisorption of analyte at the junctions, leading to higher resistance. Additionally, gas diffusion is also promoted at this phase. D_k (in Equation 2.4) at 300 ˚C is 1.39 times than that at 25 ˚C, thus larger m at 25 ˚C indicates higher concentrations of analyte reaching the deepest layer at the room temperature.

As the temperature increases, gas molecules tend to desorb from the surfaces, reducing the potential barrier ΔV, as illustrated in Fig. 6.12(b). At the same time, higher concentrations of electrons (Equation 2.6) are excited to pass through the lowered barrier. The dual effects of physisorption and electron transport further lower the electrical resistance as compared to that at low temperature. As the temperature increases above a threshold, the chemisorption activity (associated with adsorbed oxygen ion) is activated and the resistance

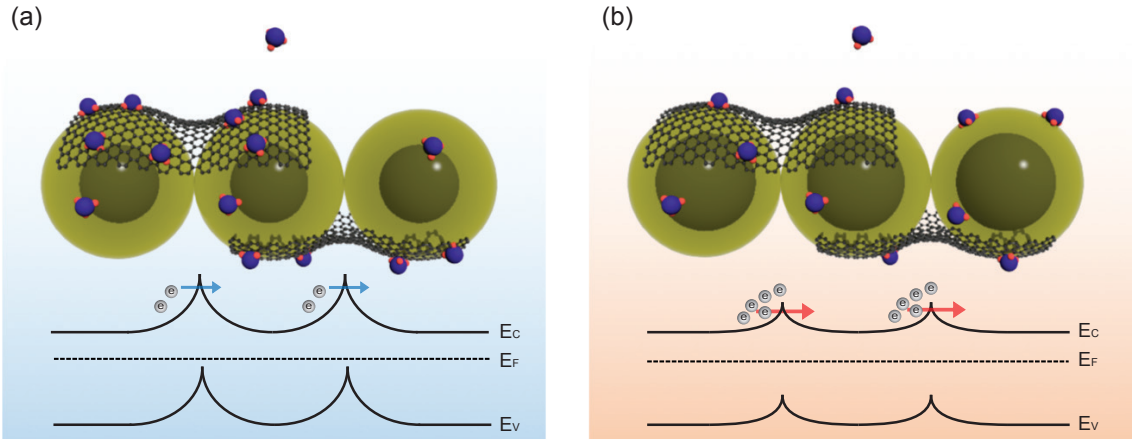

Fig. 6.12 Illustration of sensing mechanism on detection of pure analyte with graphene-MOx NP composite at (a) low temperature (b) moderate temperature.

starts to increase. From Equation 2.3, k at 300 ˚C is 10^4 times than at 25 ˚C. The chemical reaction rate (300 ˚C:25 ˚C): $\frac{k(300^oC)}{k(25^oC)} = \exp(\frac{-0.5eV}{8.31\times573}) \div \exp(\frac{-0.5eV}{8.31\times298}) = 1.15 \times 10^4$, where 1 eV = 96485 J mol^{-1}.

6.3.2 Temporal analysis of mechanisms

Next, I conduct a stage-by-stage temporal analysis which adapts the temperature dependency models I propose to develop a universal tool for the optimization process. The method for optimization is to initiate with the lowest base temperature, preferably at RT, which consumes the lowest power. The temperature of pulses applied is determined by the temperatures at which optimal responsivity occurs in ISO mode (Fig. 6.10 for instance). In cases where 25 ˚C base temperature fails to produce measurements within measurable range, the base temperature is optimized such that the lowest available base temperature within the measurable range producing reliable measurements is used.

In the following experiment, the μHP is electrically pulsed to generate a train of heating pulses consisting of high temperature pulse for 1 s (the μHP can reach that within 0.1 s) followed by 4 s of non-heating time. I use the temperature 325 ˚C (optimal responsivity as predicted from Fig. 6.10) pulse which is delivered by applying 23 mA to the heater. Temperature during non-heating period (25 ˚C) is measured by the temperature sensor in the test rig. The time series responses from measurement data can be divided into four phases: stabilization, exposure-rise, equilibrium, and release; as presented in Fig. 6.13.

During the stabilization phase (Fig. 6.13(i)), the resistance reaches a steady state corresponding to its temperature at the ambient environment. The decrease in resistance observed

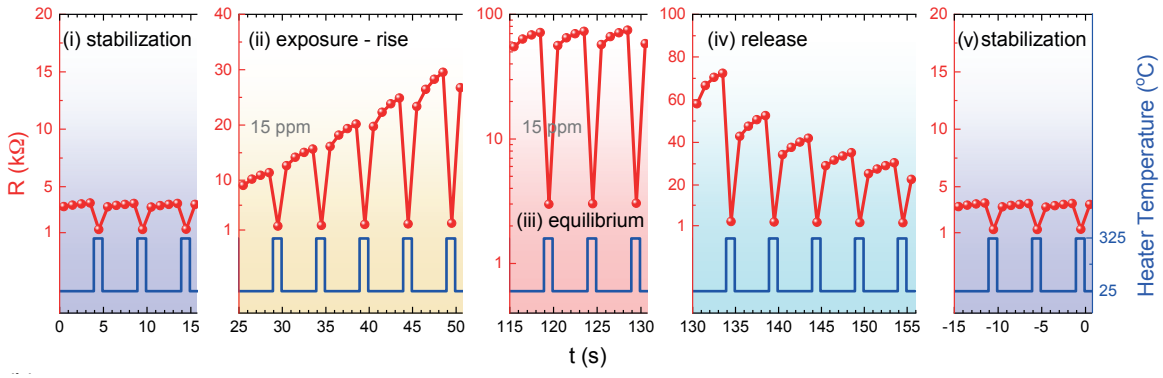

Fig. 6.13 Stage-by-stage temporal response in temperature modulation mode. The estimated heater temperature is converted from the electric current through the heater, based upon Ref [1].

at the instant of the 325 ℃ temperature pulse corresponds to the enhancement of electron transport as depicted in Equation 2.6. Note that the baseline slope, referring to the line connecting points at nominal temperature of 25 ℃ within each heating period, is attributed to cooling time for the devices.

During the exposure phase (Fig. 6.13(ii)), the devices are measured in the pure analyte. Physisorption of analyte molecules is promoted and dominates the adsorption process at 25 ℃, building up the resistance. While at 325 ℃ pulse, a sharp reduction in R is observed as the effect of T overrides that of increase due to adsorption. The surface chemical reaction is also promoted at high temperature, but the response appears at the subsequent sampling point, as the carrier transport function responses faster than the chemisorption process [34]. Overall, the increasing trends shown by both the envelopes connecting R_{25^oC} and R_{325^oC}, respectively, indicate molecule adsorption. Moreover, the slope of the envelope indicates the rate of adsorption corresponding to analyte concentration gradient which increases at first and then decreases until reaching equilibrium. Additionally, the baseline slope mentioned above also increases as the analyte is diffused to the deepest layer and being trapped at the later sampling points in each 25 ℃ period.

When equilibrium (Fig. 6.13(iii)) is reached during continuous flow of analyte, the envelopes have a slope of ≈ 0, accounting for the equal rate of adsorption and desorption. During the release phase (Fig. 6.13(iv)) in N_2 environment, desorption of analyte and byproducts are promoted by the pulses due to reduced physisorption and increased outward diffusion rate. The magnitude and slope of the envelope at low temperature transient drop dramatically until reaching a steady state (similar to Fig. 6.13(i)), indicating gas adsorbed being fully desorbed.

6.3.3 Signal processing for TM mode

The data processing procedures to generate performance curves and characteristics are depicted in Fig. 6.14(a). Considering that the analyte (NH_3) is injected for 120 s in every 520 s period. The unprocessed resistance data is shown in the shaded area. The segmented envelopes corresponding to resistances at 25 ˚C $R_{25^oC}(t)$ and 325 ˚C $R_{325^oC}(t)$ are first computed by extracting resistances at the end of cooling period $R_{25^oC}(t_i)$ and at the end of pulse $R_{325^oC}(t_i)$ respectively, for the i-th period. Subsequently, the differential readout $\Delta R_t = R_{25^oC}(t) - R_{325^oC}(t)$ is normalized by ΔR_0 (ΔR_t at stabilization) to amplify the responses between with and without exposure to analyte, generating an output curve S_t in Fig. 6.14(b). The features are extracted based on the processed output curves thereafter.

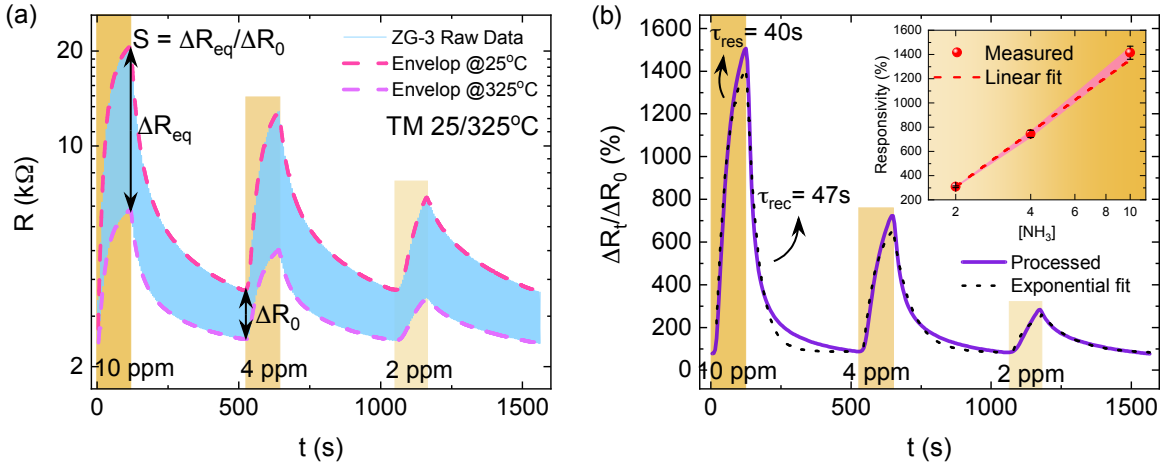

Fig. 6.14 (a) Data processing procedure; orange regions indicate injection of analyte (b) Processed response curve; (inset) responsivity as a function of concentration

6.3.4 Performances in TM mode

Fig. 6.15(a) shows a continuous S_t response consisting of 9 cycles of NH_3 injection with decreasing and increasing concentration varying at steps of 10, 4, 2 ppm. NH_3 is injected for 120 s for every 520 s period. The response curves of three devices measured simultaneously all demonstrate excellent repeatability and transient stability without hysteretic behavior. Furthermore, Fig. 6.15(b) shows a linear relationship with respect to log of concentration. An average steady state responsivity S of $\approx$ 1500% and sensitivity of 125%/ppm achieve at 10 ppm with TM mode.

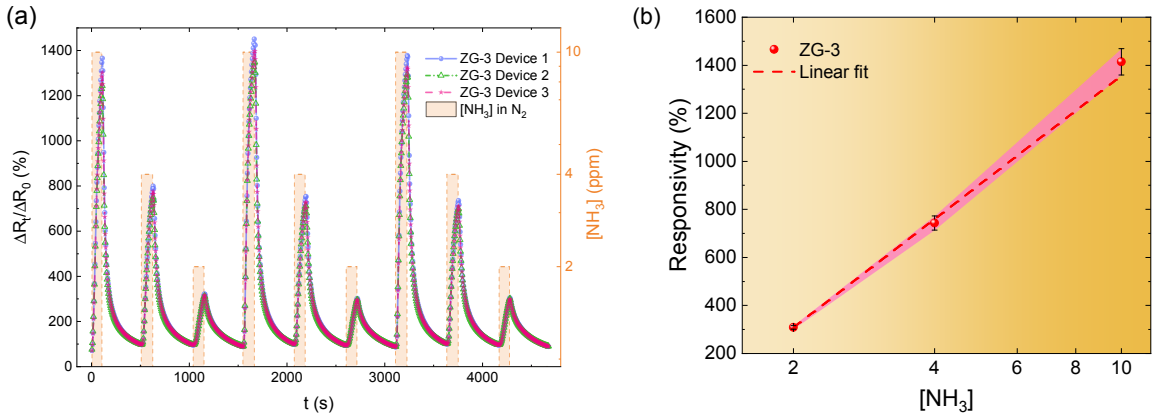

Fig. 6.15 (a) Normalized response showing repeatability at various NH_3 concentrations, exhibited with 3 devices. (b) Responsivity as a function of NH_3 concentrations under TM mode. See Appendix Fig. A.5 for raw data.

6.4 Comparisons between operating modes

Fig. 6.16 summarizes the comparison of performances between the TM (25/325 ˚C) and ISO (300 ˚C) modes. First, TM mode exhibits a responsivity improvement of 494% over ISO mode for ZG-3 at the same concentration which has a ΔR of 300%. Analysing from the raw resistance data for TM mode (Fig. A.5) at 10 ppm exposure, I observe an average responsivity of 607% extracting the envelop during the non-heating period, and that of 269% for the high-temperature pulse envelop. Comparing with ISO mode (Fig. 6.9), responsivities of 420% and 110% are observed at the corresponding estimated heater temperatures.

Second, baseline drift is significantly reduced to 0.67% per cycle (95% improvement over ISO). Third, the repeatability of responsivity in TM mode shows 1.4% $\pm$ 0.08% of average cycle variation, representing an improvement of 70% over ISO mode. The improved repeatability and minimized drift can be attributed to the effectiveness of regeneration of the sensing layer due to the effective TM scheme. The average response and recovery time constants are also shortened, where τ_{res} drops from 45 s (ISO) to 28 s (TM) while τ_{rec} drops from 98 s (ISO) to 43 s (TM). The reduction in recovery time is attributed to the short pulses that accelerate the desorption of physisorbed gas molecules. Additionally, stabilization time is reduced from 60 min (ISO) to 5 min (TM), making the re-calibration process more practical.

The device-to-device responsivity variation is within 0.5% (as shown in Fig. 6.15(a)), exhibiting good potential for mass production. The ultralow device-to-device performance variation is also attributed to the uniformity of inkjet deposition within batch. I also note that the TM technique dramatically reduces power consumption without compromising response.

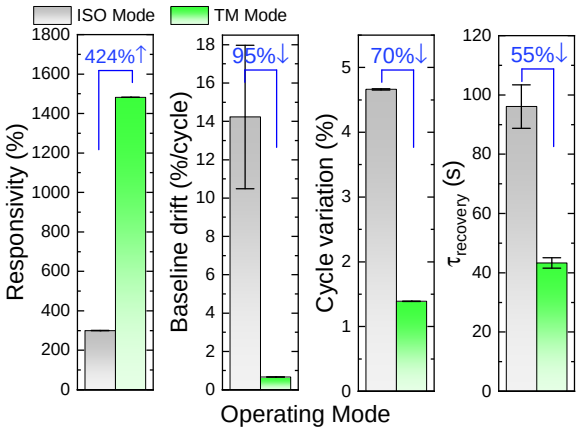

Fig. 6.16 Performance enhancement of TM over ISO mode. The statistics is derived from Fig. 6.10 and 6.15.

The device consumes 6 mW at 25/325 °C, which is 78% more energy efficient than operation in ISO mode at optimal temperature of 300 °C and 92% more energy efficient than state-of-art commercial MOS MEMS NH_3 sensor (MiCS-6814) that consumes 73 mW. Moreover, the sensors demonstrate high SNR of > 5600, with a calculated LOD down to 16 ppb.

The calculations of SNR and LOD are expressed as follows. $\text{SNR} = \frac{2\times H}{h} = \frac{2\times 1400}{0.5} = 5600$, where h is peak-to-peak interval at baseline; H is height of peak.
$\text{LOD} = \frac{3.3\times SD}{slope} = \frac{3.3\times 0.6}{125} = 15.84$ ppb, where SD is standard deviation (%), slope in %/ppm.

6.5 Performances in ambient environment

To proceed further towards the realization of breath analyzer, I next measure the device in synthetic air (SA) containing the major atmospheric composition, including nitrogen, oxygen, and carbon dioxide (CO_2). Introduction of SA results in O^-species being adsorbed onto the NP surfaces, transforming the detection of NH_3 into interactions with the adsorbed species [240]. Adsorption of NH_3, in turn, recedes the depletion region, leading to an increase in conductivity according to the concentration of NH_3 [240].

I characterize the responsivity of NH_3 in the range of 2-10 ppm which falls into the main interest of diagnosis of metabolic diseases. For instance, a mean of 4.88 ppm NH_3 may indicate that a patient has end-state renal disease (ESRD) [245], i.e. kidney failure. I assume a detection threshold of 2 ppm NH_3, provided that 0.5-2 ppm of NH_3 [246] are present in the breath of healthy adults.

Fig. 6.17(a) shows the S_t response of NH_3 in SA varying at 2 ppm decreasing steps injected for 120 s for every 520 s period. Note that employing TM 25/325 °C yields resistance

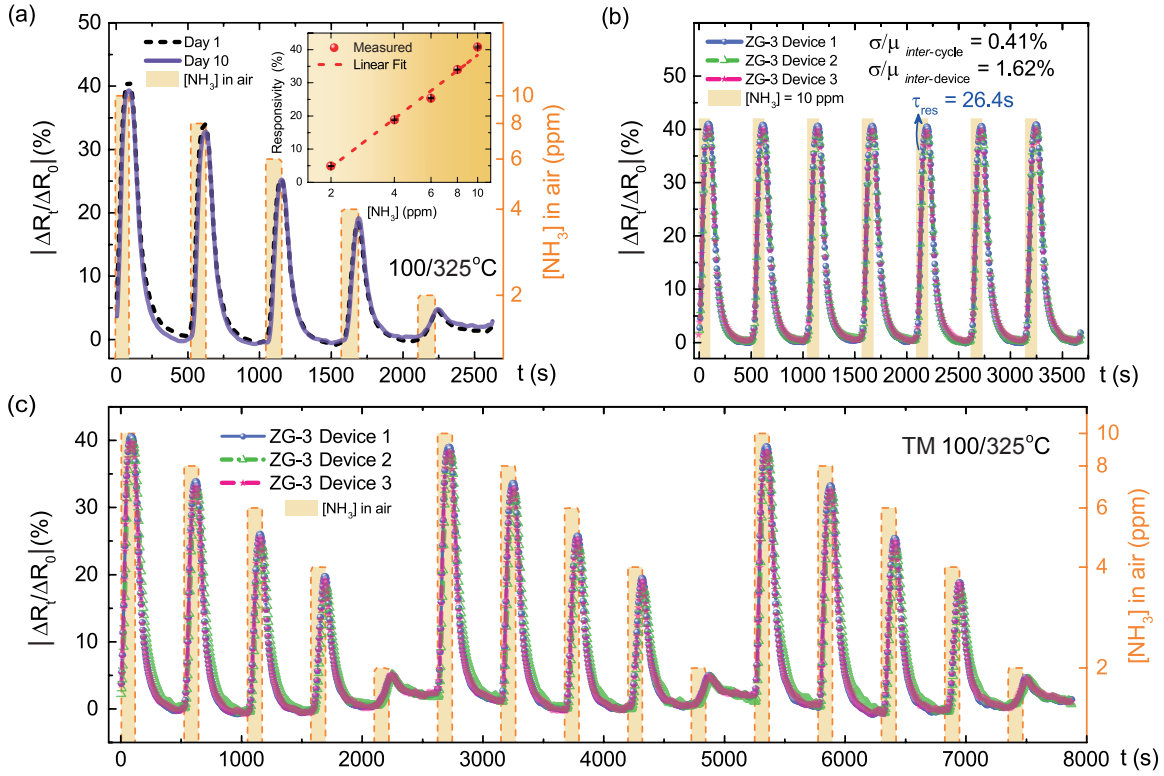

Fig. 6.17 Performance in air environment using TM mode. Plot using $|\Delta R_t/\Delta R_0|$ as y axis (a) Normalized response showing long-term stability over 10 days in air for 5 concentrations; (inset) responsivity as a function of concentration. (b) Normalized response showing repeatability (at 10 ppm) over 7 cycles, exhibited with 3 devices. (c) Repeatability at step concentration over 3 cycles. See Appendix Fig. A.6 for raw data.

values beyond the measurable range (i.e. $>$ 10 MΩ). Base temperature is raised to 100 ℃ which is the lowest temperature within the measurable range. The pulse temperature remains at 325 ℃. The responsitivity (inset of Fig. 6.17(a)) extracted from the steady state peaks of S_t at the concentration steps shows a linear relationship with log of concentrations of NH_3, with a sensitivity of 4.2%/ppm.

Moreover, the long-term stability study shows the well alignment between initial and measurements on 10^{th} day with variations within 1%. The result in the performance reflects no sign of deterioration and drifts over the period under study. Furthermore, as shown in Fig. 6.17(b), the variations of responsivity across injection cycles and across devices at 10 ppm are only 0.41% and 1.62%, respectively. Fig. 6.17(c) further showcases the robustness of the sensors with continuous S_t consisting of 15 cycles of NH_3 injection with repeated decreasing concentration varying at 2 ppm steps. The response shows no notable hysteretic behavior (max hysteresis of ±0.34%) and drift.

To analyse the hysteresis behavior of the sensor in TM mode, I cycle the sensor in air at various NH_3 concentrations within 2-10 ppm range. As presented in Fig. 6.18, the black dashed line and red solid line show the responsivities at decreasing and increasing NH_3 concentrations, respectively. The results show the maximum mean hysteresis of $\pm$0.34% occurring at 4 ppm of NH_3. Note that τ_{res} is 26.4 s and the power consumption is 12.4 mW at the optimized TM scheme (100/325 ℃) in SA environment. Despite increment of power, this still represents a 56% improvement by ISO mode.

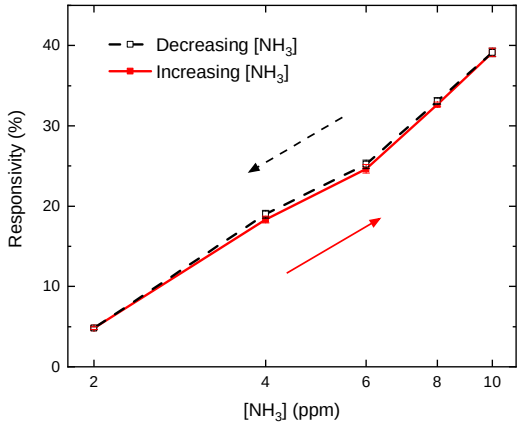

Fig. 6.18 Hysteresis characteristics of the NH_3 sensor. The characteristics is derived from Fig 6.17(c).

6.6 Cross-sensitivity and compensation

The major components of breath of a healthy person contain 4% of CO_2 [247], 0-6 ppm of CO [247], and < 1 ppm of VOCs including acetone, isoprene and ethanol [248]. However, MOx sensors often interfere with these analytes. To assess the influence of humidity on sensing performances, I characterize the response of NH_3 at 10 ppm in humidified SA at 22, 35, 45, 56, 65% RH levels, as shown in Fig. 6.19(a). Please refer to Fig. 6.17 for measurements at RH = 0%. Water vapor introduces OH^- species that can be adsorbed on the surface of sensing material, causing doping and reduction in the device responsivity.

The responsivity with respect to RH level (inset of Fig. 6.19(a)) is fitted with Boltzmann curve (Equation 6.1) as two plateaus within the ranges of RH < 20% and RH > 45% are clearly visualized.

$$S_{RH} = 21.62 + \frac{20.96}{1 + 0.1747e^{[RH]-30.42}} \tag{6.1}$$

where S_{RH} is responsivity under RH. Although humidity reduces responsivity inevitability, a common phenomenon in chemiresistive sensors, my approach allows interference to be mitigated and enables reliable characterization at high RH levels. I predict the responsivity at 80% RH (typical value in breath) to be 21.62% based on the fit from Equation 6.1, due to limitations in my measurement setup above 65% RH. The estimated value has only 0.04% variation from the measured value at 65% RH.

One approach to reconstruct the true level of NH_3 in humid breath is to compensate the readings by 190% (value as if under dry air), and then refer to the relationships deduced from the inset of Fig. 6.17(a). In addition, I note that within TM mode as long as sufficient reaction time is attained, the measurements are invariant to analyte injection/release period. This can be seen from the shortened analyte release period to 240 s from 400 s (from Fig. 6.17) without compromising the response curve. This demonstrates the algorithm's utility as a robust tool for performance optimization.

In addition to humidity, I assess the sensitivity of ethanol and acetone which are the common interfering gas species in exhaled breath. These species are measured at 2 ppm, which are above maximum levels a healthy human would exhale [247, 248]. Four repeated measurements at 2 ppm of each interferant, injected for 120 s in every 520 s period, are carried for the cross-sensitivity characterization (see Appendix Fig. A.7). The cross-selectivity data in Fig. 6.19(b) indicates relatively small amount of interference from ethanol (0.91%) while the effect of acetone is more prominent (2.12%).

To compensate for the interference effects, I introduce a complementary acetone-selective graphene-MOx sensor in Chapter 7 Section 7.4.

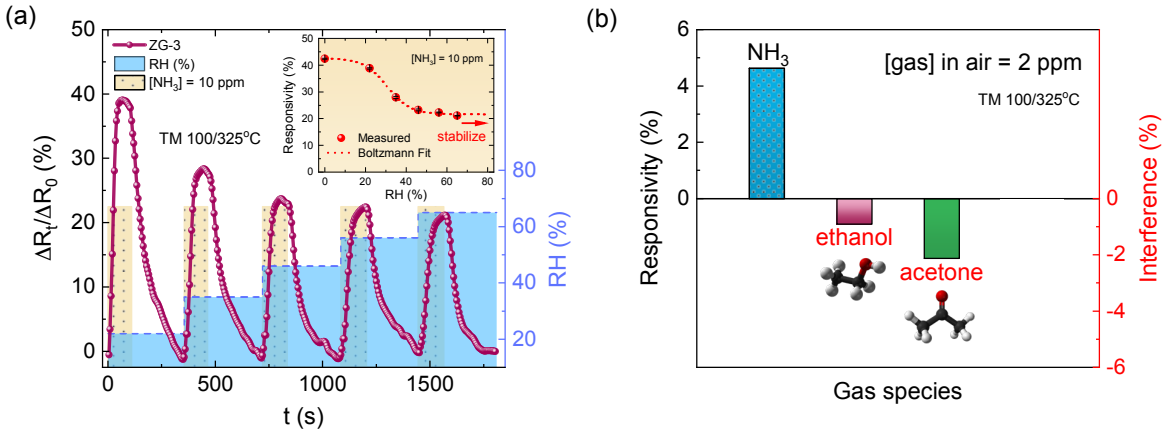

Fig. 6.19 (a) Normalized response at 120/240 s NH_3 exposure/release cycles varied at various RH levels; (inset) responsivity as a function of RH levels. (b) Cross-analyte selectivity among common interfering gas species in exhaled breath. See Appendix Fig. A.7 for raw data.

6.7 Summary of results

I have developed an inkjet-printed graphene-MOx based sensor system that has been integrated onto miniaturized CMOS compatible platforms to selectively measure ammonia, a biomarker of kidney and liver problems, with fast and accurate performance.

I have addressed the common issue of incomplete sensor regeneration faced by conventional MOx devices, through the establishment of temperature-dependent sensing mechanisms involving interplays between physisorption and chemisorption, diffusive mass transport, and electron transport processes via stage-by-stage temporal analysis.

Through the development of effective temperature modulation scheme, in pure NH_3, I achieve responsivity of 1500% at 10 ppm, sensitivity of 125%/ppm, significantly reduced baseline drift, τ_{res} of 28 s, τ_{rec} of 43 s, inter-device variation within 0.5%, SNR of 5600. In synthetic air, I achieve long-term responsivity variations within 1%, inter-cycle variations within 0.41%, showing extraordinary repeatability and device-to-device consistency with no noticeable hysteretic behavior. Considering real-world scenarios, the sensors exhibit highly stabilized responses under high RH level.

My strategy to combine the sensing material, inkjet printing onto CMOS MEMS platform and temperature-pulsed modulation promises a robust system that outperforms conventional devices in aspects of reproducibility, performance reliability, recovery time while enhancing responsivity.

Chapter 7

Detection of Acetone

Acetone (C_3H_6O) could be used as a biomarker to diagnose diabetes [5]. Detecting acetone level in breath has become a desirable alternative to monitor health condition. Patients with diabetes typically exhale acetone concentrations between 1.76 and 3.73 ppm; whereas in healthy control group, the range is between 0.22 and 0.80 ppm [7]. A variety of chemiresistive gas sensors have emerged due to its nature of being compact and inexpensive. High performing sensing materials that have been used for this include InN (LOD of 0.4 ppm [31]), α-Ag_2WO_4 nanorods (detection range of 0.5-20 ppm [249]), SnO_2 nanofibers (LOD of 100 ppb [250]), Si:WO_3 (LOD of 20 ppb [111]). Among these sensors, MOx chemiresistive sensors offer a cost-effective solution due to its facile manufacturability [33].

In this chapter, I develop a hybrid of graphene-tungsten oxide (WO_3) NP functional ink as the sensing material for acetone sensing. The composite ink is deposited onto the CMOS platform using inkjet printing. During the development of the sensing material, I investigate the effect of different graphene concentrations and different operational mode on the gas sensor performance in terms of sensitivity and response time. This chapter includes comparison between existing solutions, the working mechanisms, the method involved in fabricating the gas sensor, as well as measurement results and discussions.

Substantial contents in this Chapter have been published [59]. The contents of this Chapter are my original work. Part of the experimental work is carried out in collaboration with Qinyu Zhong (a fourth year project student) under my supervision.

7.1 Ink formulation and material characterization

The ink formulation procedure is identical to that of ZnO/graphene-PVP formulation which is presented in Section 6.1.1 except for the MOx material used in the formulation. The overall preparation of the WO_3-graphene ink involves mixing of WO_3 NP ink (Sigma, 10

mg mL^{-1}) with graphene ink in the IPA and 2-butanol solvent mixture. The inks for WO_3 and graphene are prepared separately. For the WO_3 ink, the WO_3 NP is dispersed in IPA-PVP under sonication of 12 h. After sonication, the dispersion undergoes vacuum filtration using a polytetrafluoroethylene (PTFE) membrane filter with a pore size of 0.22 μm.

To prepare the graphene ink, standard UALPE process is employed to exfoliate graphene from graphite. PVP is added as a dispersant which assists dispersing materials uniformly within the solution. The amount is minimized to avoid blocking of the percolation path and thus poor conductivity. The graphite-PVP suspension in IPA is placed in a bath sonicator where micro-bubbles are generated. During the collapsion of bubbles, the energy released breaks apart the multilayered structure of graphite. After sonication for 12 h, I obtain a solution containing large amounts of macroscopic aggregates at the bottom. These aggregates are then removed by centrifugation at 4030 rpm for 30 min [179], producing a homogenous dispersion. For the graphene ink, the effective concentration of graphene and PVP are estimated to be 1.2 mg mL^{-1} and 3.8×10^{-3} mg mL^{-1} [93], respectively. Please refer to Section 6.1.1 for the TGA data and effective concentration calculations of the graphene ink formulation. As graphene and WO_3 NPs are both dissolved in PVP-dispersed IPA solution, it is possible to directly mix the two inks.

Next, I redisperse both inks in the solvent mixture of IPA and 2-butanol according to Chapter 6. I then mix the redispersed inks at different ratios to study the sensing behaviors of composites containing graphene loadings of 0.2 wt% and 0.7 wt%, and a pure WO_3 ink as the control group. Before printing, the ink is sonicated for 0.5 h to maximize homogeneity. The drop formation process is shown in Fig. 7.1.

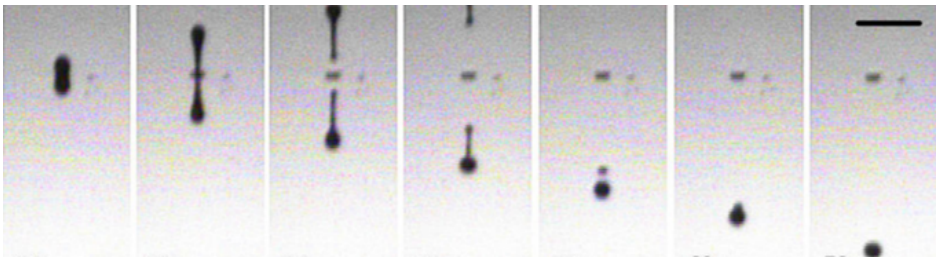

Fig. 7.1 Ink droplet generation from a nozzle.

Apart from the uniformity of the ink, the number of printing passes is trade-offs between electrical conductivity and sensing performances. Although fewer printing passes can save material cost and production time, printing too few passes can result in poor conductivity due to discontinuity of printed films. In contrast, excessive numbers of passes could extend the gas diffusion process, increasing response/recovery time [38]. In this case, 20 passes of repetitions are printed on the device. Eventually, 5 devices are made: one printed with

pure WO_3 ink, two with 0.2 wt% graphene loading and the other two with 0.7 wt% graphene loading. They are named WG0, WG0.2-Dev1, WG0.2-Dev2, WG0.7-Dev1, and WG0.7-Dev2, respectively. The baseline electrical resistances of the devices at various temperatures are shown in Table 7.1.

Temperature (°C)	Resistance (kΩ)
100	31.224 ± 4.385
150	11.118 ± 3.130
200	5.648 ± 1.419
250	2.315 ± 0.290
300	1.717 ± 0.346

Table 7.1 The electrical resistances of the WO_3/graphene devices at various temperatures.

Fig. 7.2(a) shows the inkjet-printed CMOS sensory device, where the printed film contains 0.7 wt.% graphene loading. The device undergoes annealing at 400 °C (as determined in Chapter 6) to restore device conductivity and to create porosity for gas diffusion. Raman spectrum of composite film after annealing is shown in Fig. 7.2(b). It shows characteristics of WO_3 as seen from the peak at 272 cm^{-1} due to O-W-O bending and peaks at 717 cm^{-1} and 807 cm^{-1} due to O-W-O stretching [251]. Graphene characteristics is identified by the D, G, $2D_{Gr}$ peaks.

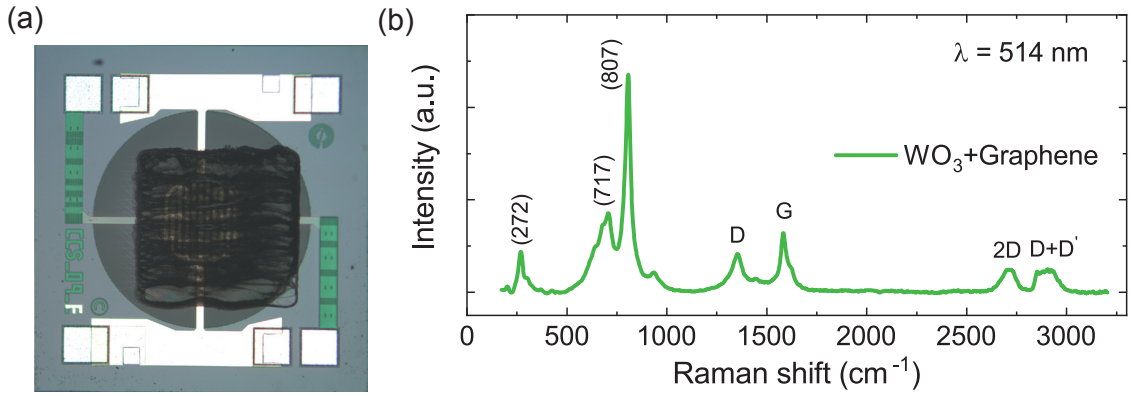

Fig. 7.2 (a) Microscopic image of inkjet-deposited WO_3-graphene CMOS sensory device. (b) Raman spectrum of WO_3-graphene printed films after annealing treatment.

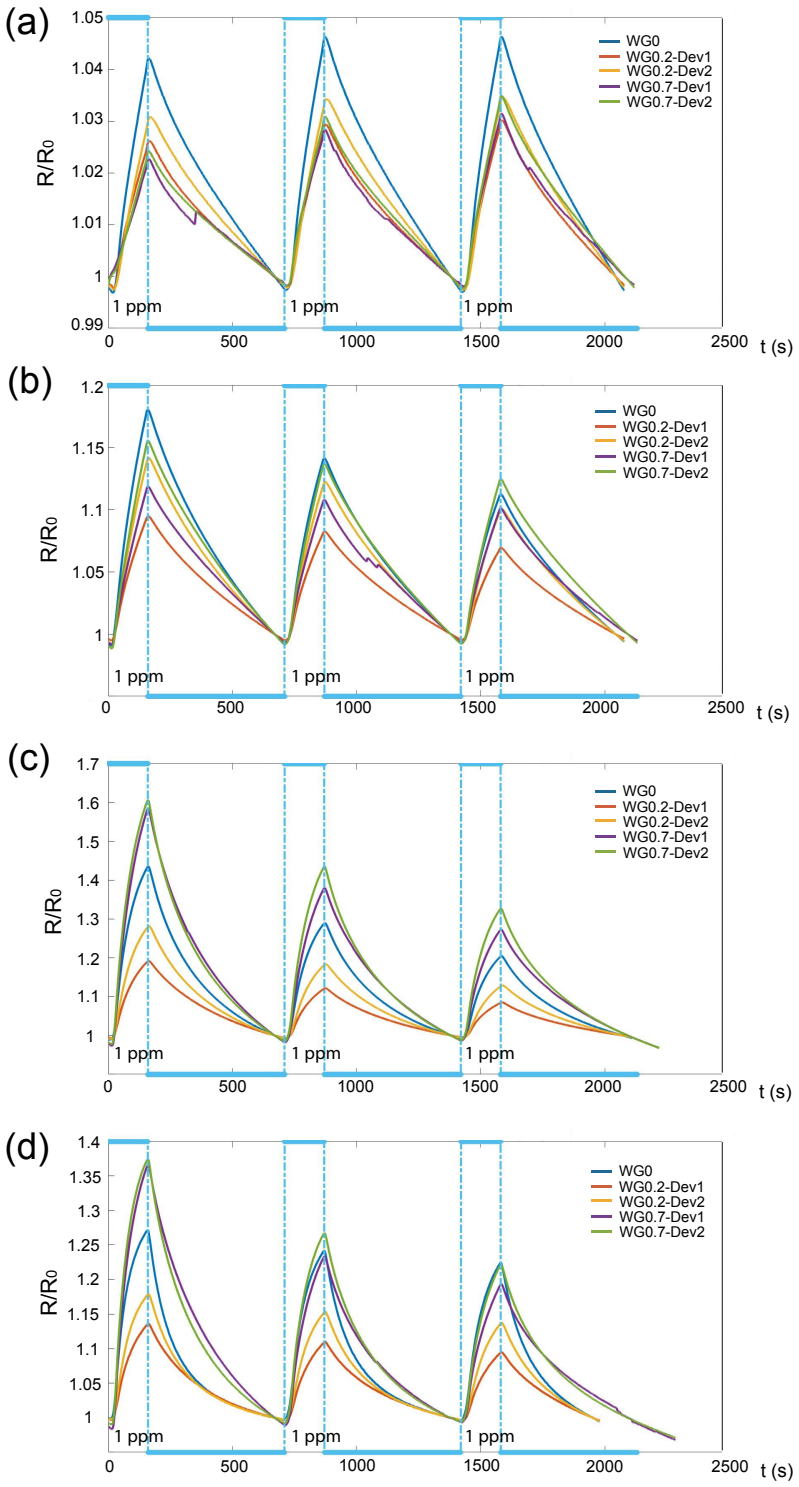

Fig. 7.3 Acetone response at constant temperature of (a) 150 ˚C (b) 200 ˚C (c) 250 ˚C (d) 300 ˚C for 3 cycles of 1 ppm acetone. See Appendix Fig. A.8 for raw data.

7.2 Sensing performances

Fig. 7.3 shows the change in resistance of 5 devices simultaneously under 3 identical cycles of acetone exposure at 1 ppm. The devices are operated at ISO mode where Fig. 7.3 (a)-(d) varies from 150-300 ℃. The exposure and release time of acetone are selected to be 160 s and 550 s, respectively. The change in resistance is translated to responsivity. Although the highest responsivity is shown at 250 ℃, the responses are more reproducible at 150 ℃.

The average responsivity of three cycles are plotted against temperature for all 5 devices in Fig. 7.4. The responsivity maximizes at 250 ℃ experimentally. For all 5 devices with different ink compositions, the responsivity increases with temperature from 100 ℃, peaks at 270 ℃ from polynominal fitting, and falls back down at 300 ℃.

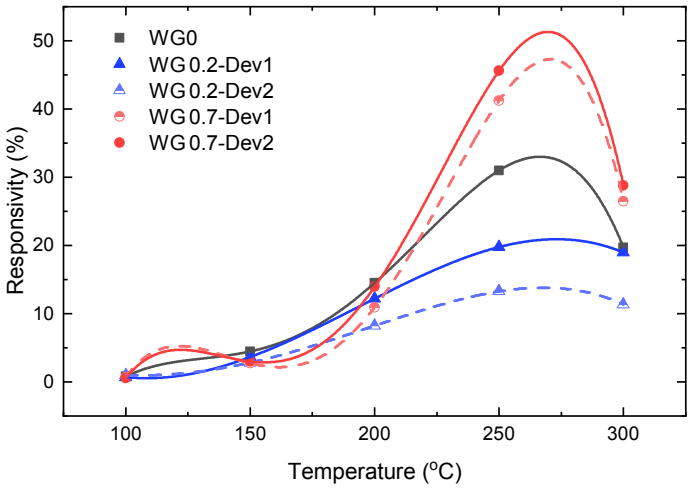

Fig. 7.4 ISO mode responsivity of all devices as a function of temperature. Curves are fitted with forth order polynomial.

The general trend in responsivities with respect to different temperatures is described as follows. When the temperature is too low: (1) The activation energy is not reached for chemisorption to take place. (2) The potential barriers between WO_3 NPs are too high, limiting the electron transfer process. Therefore the response is small. When temperature increases from RT, the number of surface electrons surge, which leads to more adsorbed O^- and therefore more adsorbed acetone, and thus a surge in responsivity.

However, if the temperature is too high, the physisorption of acetone molecules is not favored. The molecules are more likely to desorb from the surface, leading to a reduction in surface interactions. Therefore the response falls at 300 ℃. Whereas at the optimal temperature, an equilibrium between adsorption and desorption are reached, producing maximal responsivity.

Comparing the responsivities at the optimal temperature, the maximum responsivity (40-45%) is observed from WG0.7 devices; whereas WG0.2 devices have the worst responsivities (13-20%). The responsivity of pure WO_3 device (30%) lies in between. This observation is roughly consistent among different devices fabricated with the same composition. It is noted that WG0.7 devices offer superior reliability over WG0.2 devices.

The abovementioned trend in responsivities across different compositions is consistent over temperatures above 200 ˚C. The behavior of reduced responsivity of initial (0.2 wt%) loading of graphene may be attributed to the slight reduction in WO_3 receptors, leading to reduced interactions with acetone molecules. It may also be attributed to the discontinuity in the transduction path caused by the additives. As the loading of graphene increases, the edge defects of LPE graphene may start to contribute to the receptor process. The establishment of graphene/WO_3 may also facilitate transduction process. The combinational effects achieve enhanced responsivities over pure WO_3 devices. However, it is expected that if the loading of graphene continues to increase, the response will fall down again, as graphene is less sensitive to acetone than WO_3 [90].

Response/recovery time comparison

Response time and recovery time are also important parameters to measure the performance of a gas sensor. Response time, t_{Res}, is defined as the period of time from gas sensor contacting with the target gas to variation of resistance reaches 90% of $|R_a - R_g|$. Recovery time, t_{Rec}, is defined as the period of time from gas sensor being away from the target gas to variation of resistance reach to 90% of $|R_a - R_g|$. They have been calculated for all five devices and plotted against temperature in Fig. 7.5.

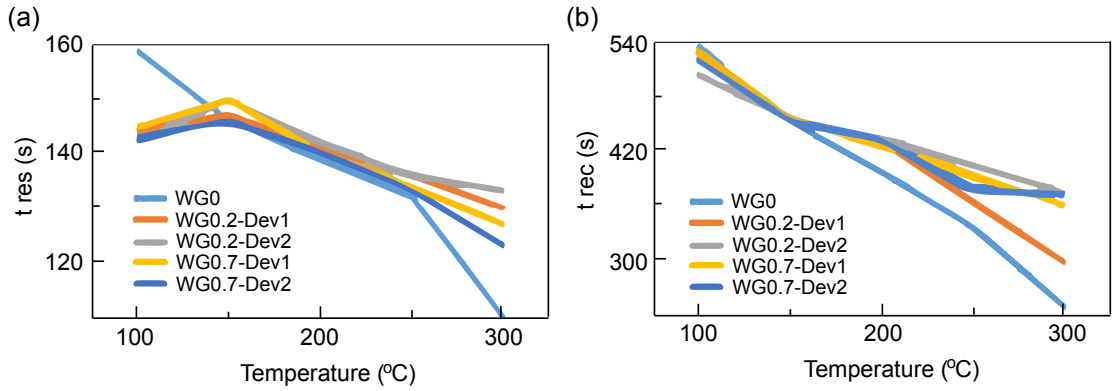

Fig. 7.5 (a) Response and (b) recovery time in ISO mode as function of temperature. The data is derived from Fig. 7.3.

The clearest trend is that both response time and recovery time falls as temperature increases. Temperature has the most impact on WG0 device. Devices with graphene generally has a shorter response time at low temperatures. At temperatures higher than 150 ˚C, WG0 device shows a faster response and recovery than those loaded with graphene. WG0.7 usually have a shorter response/recovery time than that of WG0.2.

The grounds for the observed behavior may be explained as follows. At low temperatures, the threshold of activation energy for chemisorption at WO_3 sites is not reached, therefore the adsorption process in WG0 devices is slow. Incorporation of graphene introduces adsorption sites at its edge defects, promoting physisorption of the acetone molecules. Therefore, WG0.2 and WG0.7 show faster response time than WG0 at lower temperatures. At higher temperatures, chemisorption at WO_3 sites dominates the receptor process. Compared to the ones with graphene loading, as the sites of the fast-reacting WO_3 is fewer, WG0 devices therefore show faster response time.

On the other hand, the desorption process at low temperature is likely to be more dependent on the physical mechanism. At low temperature, the acetone molecules do not attain sufficient energy to desorb. Therefore, graphene plays no role in recovery time. Whereas at high temperatures, the reaction rates are much higher at WO_3 sites. Therefore, WG0 devices also show faster response time.

There exists a small trade-off between responsivity and response/recovery time. As the optimal temperature for responsivity of all devices is at the higher range, the incorporation of graphene has a slightly negative effect on response/recovery time. Since the difference in responsivities among devices compared to that of time, it is reasonable to target responsivity.

7.3 Performances in TM mode

Typically, one can use pulse heating to promote desorption gas molecules from the sensing layer. It causes periodic changes in the resistance with a characteristic shape influenced by ambient temperature [252]. Fig. 7.6 show the processed responses of the representative devices in each material composite under TM mode. The concentration of acetone is tested in a pattern of 4, 3, 2, 1, 2, 3, 4, 3, 2, 1 ppm. The heating pulse is set to be 150 ˚C for 3 s and 300 ˚C for 1 s. The dataset is measured at 140/560 s acetone exposure/release cycles.

The responsivities show a similar trend towards the ones in ISO mode at comparable temperatures. WG0.7 devices have the best responsivity and WG0.2 devices perform the worst. Nevertheless, as compared to ISO mode, TM mode tends to give a more reliable result, with no apparent difference in responsivity between each cycle. The reason is that within the interval when acetone is off, TM mode allows more complete desorption of the

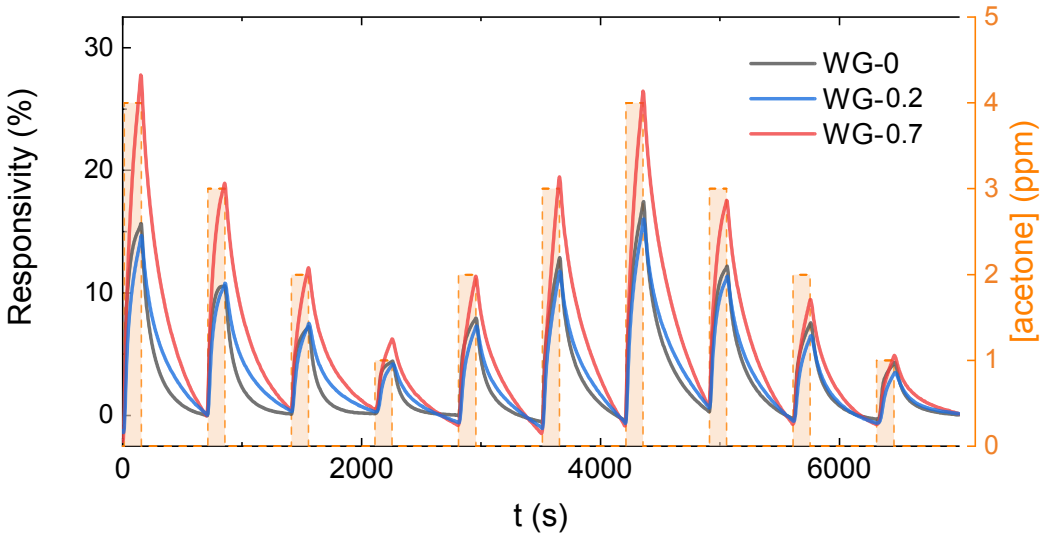

Fig. 7.6 Normalized response comparing various graphene loading varied at various concentrations. The devices are operated at TM 150/300 ˚C. See Appendix Fig. A.9 for raw data.

adsorbed gas molecules. Therefore, the previous cycle does not affect the later ones. With one pulse in a heating cycle having a higher temperature, it helps accelerate the desorption process as well as the electron transfer process (as discussed in Chapter 5 Section 6.3).

Response time comparisons

The response time for each concentration is calculated and plotted against temperature in Fig. 7.7(a). The response time for all 5 devices are plotted for two different modes for comparison. At 150/300 ˚C modulation, the behaviour of all 5 devices is consistent at different concentrations, with only a marginal difference between each device.

In Fig. 7.7(b), I compare the response time at 150/300 ˚C modulation with that at 150 and 300 ˚C at 1 ppm acetone. It is clearly seen that the response time across each device is significantly shorter than ISO mode at either temperature compared. This is a great advantage of TM scheme. Operating at a low temperature in ISO mode may lead to the accumulation of incompletely oxidized contaminant; whereas in TM mode, the sensors are regenerated efficiently by the periodical oscillations [253].

TM mode is highly desirable when response time is preferred over sensitivity. This mode allows the device to operate at a lower average temperature with a much improved response time. These characteristics are particularly useful for portable devices. In brief, TM 150/300 ˚C gives the best sensitivity and the best response time respectively. However, when com-

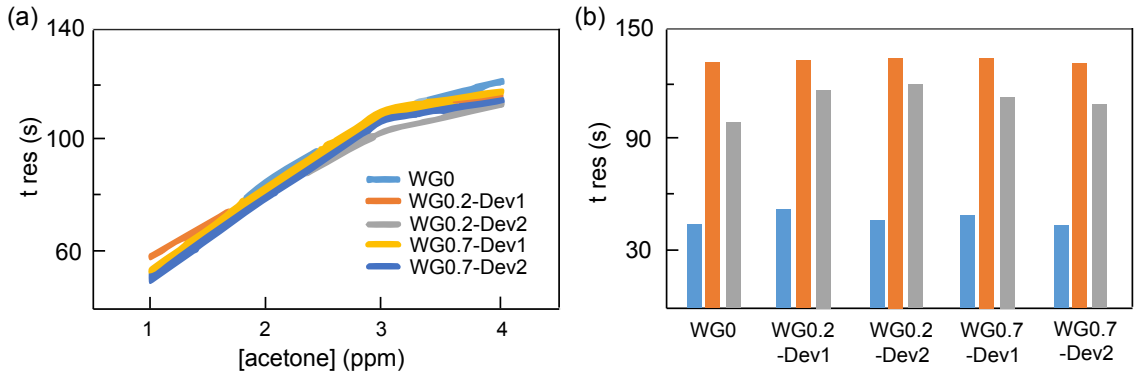

Fig. 7.7 (a) Response time at TM 150/300 ˚C (b) Response time for different mode at 150 ˚C. Blue, orange, and grey bars indicate TM at 150/300 ˚C, ISO at 150 ˚C, and ISO at 300 ˚C, respectively.

paring the optimal responsivity condition for ISO mode, it is noted that the responsivities at TM 150/300 ˚C are not as good.

Table 7.2 compares the power consumption for 250 ˚C ISO mode and 150/300 ˚C TM mode. For TM mode, The power is calculated according to the 75% duty cycle at 150 ˚C and 25% at 300 ˚C. The results show that the power consumption is 28% lower for 150/300 ˚C TM mode than the optimal ISO mode. TM is a preferred operation mode when the power consumption is limited.

Mode	Temperature (˚C)	Current (mA)	Voltage (V)	Power (mW)
ISO	250	21	1.1	23.1
TM	150/300	17/22.5	0.75/1.25	16.6

Table 7.2 Power consumption comparision between ISO and TM modes at their optimal conditions.

Performance in RH environment

Using the best performing WG0.7 sensors, I measure their performance in 40% RH environment. The sensors are operated at a train of heating pulse of 150/300 ˚C at 75% duty cycle. Acetone is injected for 10 cycles. The normalized reponses are shown in Fig. 7.8. The devices achieve 9.12% responsivity at 2 ppm of acetone in RH = 65% when operated at TM 150/300 ˚C. Well-alignment of device-to-device response and low cross-cycle variation are shown in Fig. 7.8. Although RH level causes a reduction in responsivity, the response curves remain similar to that in air environment.

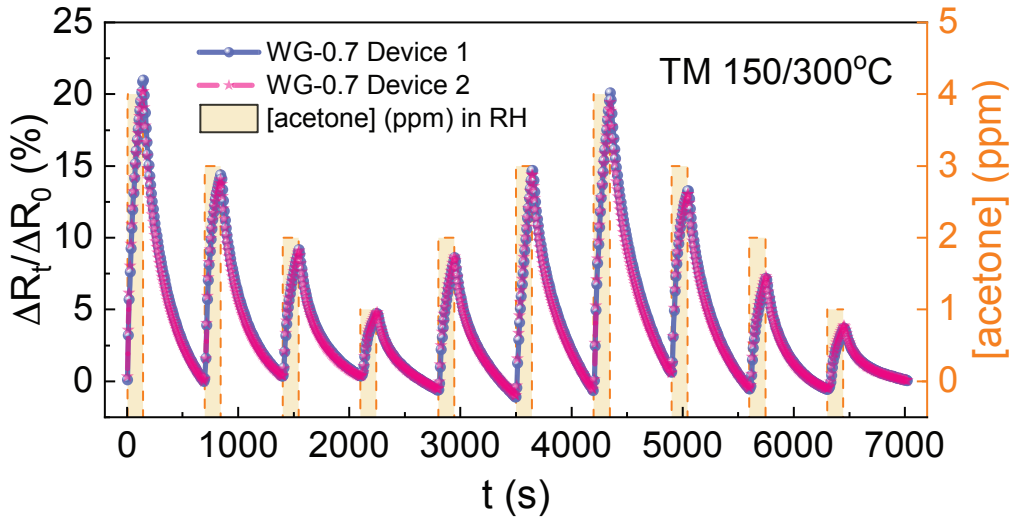

Fig. 7.8 Normalized response under RH for WG-0.7 at various concentrations.

7.4 Compensation of cross-analyte interference for disease diagnosis

WO_3 material exhibits high selectivity towards acetone. This is attributed to its high electric dipole moment which promotes strong interaction with acetone [111] (dipole moment of 2.91 D) as compared to NH_3 (1.46 D), H_2O (1.85 D), ethanol (1.69 D).

Following the discussions in Chapter 6 to compensate for the interference effects from acetone, I use WG-0.7 sensors in parallel to the graphene-ZnO sensors (ZG-3) developed in the previous Chapter. Harnessing the precise and uniform deposition of sensing films through the inkjet technology, a sensor array comprising a variety of graphene-MOx nanomaterials systems could be fabricated in a single multi-μHP CMOS die [254].

The WG-0.7 devices I fabricate achieve stable and linear responses with 9.12% responsivity at 2 ppm of acetone, a detection limit of 360 ppb, and sensitivity of 5.54%/ppm (Fig. 7.9(a)) when operated at TM 150/300 ˚C, under high RH conditions which simulate exhaled breath.

Fig. 7.9(b) maps tentative detection of kidney failure and diabetes (which associates with acetone level [7]) based upon plausible readouts from dual graphene-MOx sensors, ZG-3 and WG-0.7, as if presented in the breath. The orange-shaded area indicates potential kidney failure with a probability distribution; the green-shaded area indicates potential diabetes; whereas the intersection indicates both diseases. The responsivity boundary from the breath of a healthy person measured by ZG-3 device, S_{ZG-3} (healthy), is estimated to be 1.82%.

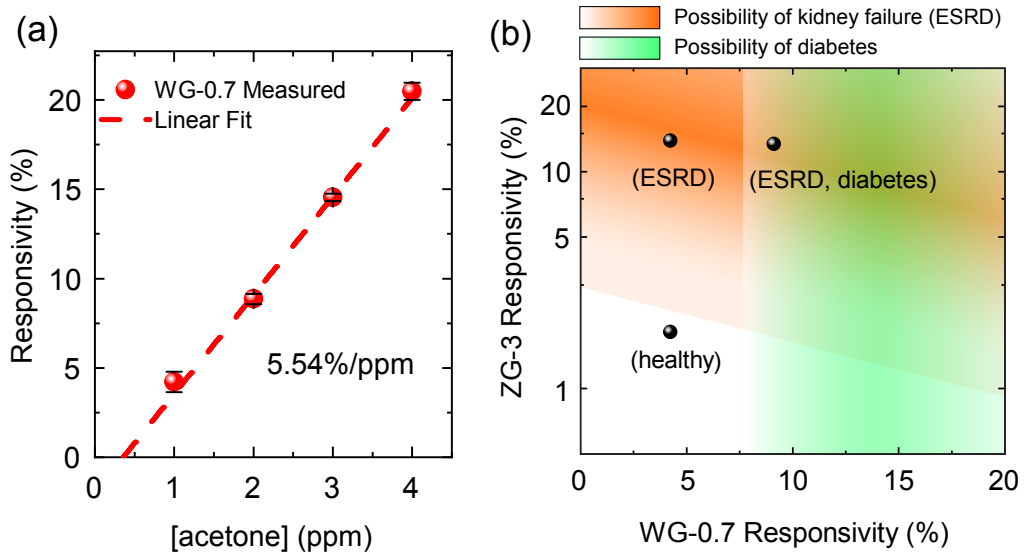

Fig. 7.9 (a) WG-0.7 responsivity as a function of acetone concentration. (b) Mapping for tentative detection of kidney failure and diabetes using dual graphene-MOx sensors: ZG-3 and WG-0.7. Responsivities indicated with respect to NH_3 and acetone using ZG-3 and WG-0.7 sensors, respectively. The responsivity data is derived from Fig. 6.19(a) and 7.8.

This readout is a result of combined contributions from 2 ppm NH_3 and 1 ppm VOC; whereas the readout point by WG-0.7, $S_{\mathrm{WG-0.7}}$ (healthy), is 4.23%. The tilt angle of the orange-shaded boundary is determined by cross-correlation with the compensating WG-0.7 sensor.

The typical responsivity from the breath of a patient with at least kidney failure (either with or without diabetes) measured by ZG-3 device, $S_{\mathrm{ZG-3}}$ (ESRD), is estimated to be 13.41-13.88%, which is contributed by 6 ppm NH_3 and acetone above 1 ppm. Note that patients with diabetes exhale 1.76-3.73 ppm of acetone [7]. The boundary for diabetes is thus determined at above 7.7% of WG-0.7 response. My work demonstrates a strong potential for multi-analyte breath diagnostics.

Calculations for disease diagnostics

(1) Boundary for healthy persons:
$S_{\mathrm{ZG-3}}$ (healthy bound) $= (4.7\% - 1.24\%) \times HF_{\mathrm{ZG-3}} = 1.82\%$, where humidity factor (HF) of ZG-3, $HF_{\mathrm{ZG-3}}$, is 52.6%; 4.7% and 1.24% are the responsivity contributions from 2 ppm NH_3 and 1 ppm acetone, respectively.
(2) For patients with ESRD but without diabetes:
Typical $S_{\mathrm{ZG-3}}$ (ESRD, $\overline{\text{diabetes}}$) $= (27.6\% - 1.24\%) \times HF_{\mathrm{ZG-3}} = 13.88\%$, where 27.6% and 1.24% are the responsivity contributions from 6 ppm NH_3 and 1 ppm acetone, respectively.

Typical $S_{\mathrm{WG-0.7}}$ (ESRD, $\overline{\text{diabetes}}$) = 4.23%.
(3) For patients with both ESRD and diabetes:
Typical $S_{\mathrm{ZG-3}}$ (ESRD, diabetes) = (27.6% − 2.12%) × $HF_{\mathrm{ZG-3}}$ = 13.41%, where 27.6% and 2.12% are the responsivity contributions from 6 ppm NH_3 and 2 ppm acetone, respectively.
Typical $S_{\mathrm{WG-0.7}}$ (ESRD, diabetes) = 9.12%.

7.5 Summary of results

In order to detect acetone in breath for early stage diagnosis, chemirisitive gas sensors have been made in this project. Devices are made using WO_3 nanoparticles for its selectivity towards acetone. Different graphene concentrations are mixed with WO_3 to improve performance. The ratio of graphene is selected to be 0, 0.2, and 0.7 wt%. The ink is deposited on a CMOS platform using inkjet printing. The response is measured quantitatively by the change in resistance. For isothermal operation, the optimal operating temperature for all devices is 250 ℃ and the 0.7 wt% ink has the largest response. The response and recovery time both decrease with temperature. Pure WO_3 ink appeared to have the shortest response and recovery time for temperature higher than 150 ℃.

Temperature modulation is an alternative to the isothermal mode. The largest improvements are that TM mode enables a shorter response time and produces repeatable responses, as compared to those of ISO mode. By comparing the responses at 150/300 ℃ modulation with that at 150 ℃ and 300 ℃ ISO mode, each device is able to respond faster. This mode also allows a 28% lower power consumption. However, TM mode does not give the best performance in terms of sensitivity.

TM mode is more practical as a gas sensor for breath due to its shorter response time and more reliable results. Since diabetes patients typically have an acetone concentration ranging between 1.76 and 3.73 ppm, WG0.7 devices are expected to deliver responsivities between 10-25% if 150/300 ℃ TM mode is used.

Furthermore, I deploy a parallel acetone-selective inkjet-printed WO_3-graphene sensor to compensate for the interference from acetone.

Chapter 8

Detection of Nitrogen Dioxide

Rapidly increasing environmental pollution has been recognized as a major concern for human health. In particular, nitrogen dioxide (NO_2) is a critical risk factor for asthma and respiratory infections. To establish new generational IoT-based air pollution heatmaps and real-time alert systems, ubiquitous deployment of low-powered embeddable devices emerges as an ideal solution. MOx chemiresistive sensing materials face critical challenges especially baseline drifts and cross-analyte interferences, compromising detection accuracies in real-world implementations.

Specifically, analyte selectivity is traditionally achieved by computational analysis of responses from cross-reactive arrays consisting of a variety of MOx materials [52], due to poor discrimination accuracies in using single MOx sensors [50, 51]. Despite reported discrimination of various chemical species qualitatively, the effects attributed to relative humidity (RH), a susceptible substance to most MOx materials [255], is not discriminated and quantified in such systems. Furthermore, literatures focusing on steady state training methods can be inaccurate in ambient environment due to non-linear baseline drifts and variations in interfering species [226, 227].

As a sensing material, MOx/rGO nanocomposites offer advantages such as improved responsivity [11] and lowered operating temperatures [95] over conventional MOx. rGO functionalized with MOx including SnO_2 [166], ZnO [55], Cu_2O [96], WO_3 [131], Fe_2O_3 [129] have been studied for NO_2 detection. In particular, α-Fe_2O_3/rGO, prepared by facile hydrothermal process, is capable of room temperature operation with 180 ppb detection limit [129]. Noteworthily, it exhibits good linearity and selectivity to NO_2 [129].

In this chapter, I fill the gap of analytical methodologies to further improve the selectivity and reliability for MOx/rGO composite in the ambient environment. My solution focuses on the development of machine learning (ML) approaches, including PCA and clustering, on a single α-Fe_2O_3/rGO nanocomposite platform. Coupled with training methods based

on transient responses, my approach achieves an overall discrimination accuracy of 96.4%, outperforming that of single MOx sensors [50, 51]. It is the first report to date that demonstrates humidity discrimination using single MOx/rGO CMOS-integrated sensor, representing a significant step towards reliable intelligent air quality monitoring systems.

Furthermore, in Section 8.6 I implement fully inkjet-printed room temperature NO_2 sensors integrated within the co-developed multi-sensory hub to carry out NO_2 detection in real-world environment. This is part of the InnovateUK project involving partnerships with Nanjing Tech University, University of Manchester, CPI, Novalia, NeuDrive, and KDX.

The contents of this Chapter have been submitted for publication [256]. The contents in Section 8.6.2 is submitted for review [181]. The contents of this Chapter are my original work, apart from Section 8.6 where the PCB board and the fully inkjet-printed devices are co-developed with Abdul Alzahrani and Guohua Hu, respectively. I thank Osarenkhoe Ogbeide for Raman characterizations. I thank Jay Dai (in Prof. Xiao Huang's group) for the development of material synthesis method and TEM characterizations.

8.1 Ink formulation and characterization

Formulation of α-Fe_2O_3/rGO ink

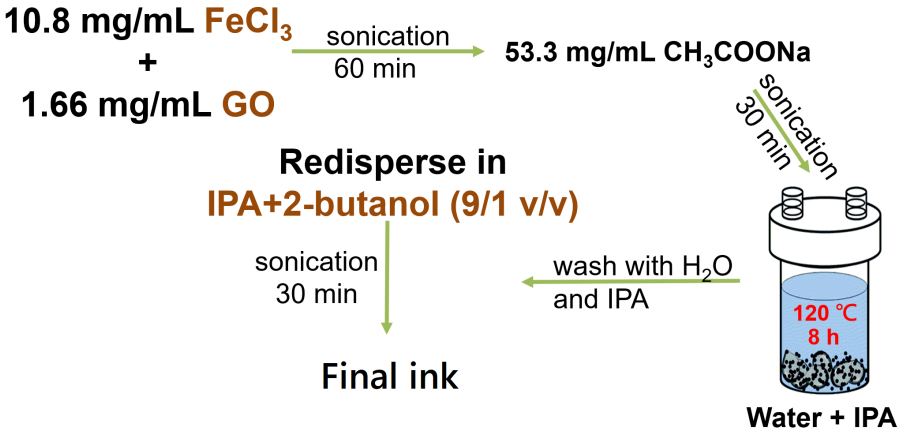

Fig. 8.1 A flowchart of α-Fe_2O_3/rGO ink formulation process.

Fig. 8.1 shows a flowchart of the Fe_2O_3/rGO ink formulation procedure. The sensing material is synthesized by an one-pot hydrothermal process. Unlike the previous formulations where polymer is used as a binder between the MOx NPs and graphene, hydrothermal process allows the formation of bondings between MOx and rGO, creating stable composites without the presence of polymer. The production of Fe_2O_3/rGO ink first involves formation

of a dispersion of GO in deionized (DI) water. 5.625 mg of GO is added to 11.25 ml of DI water and sonicated for 0.5 hour. Next, a mixture of 36.5 mg of iron(III) chloride ($FeCl_3$) is measured and added to 9 ml of DI water. The mixture of $FeCl_3$ and DI water is then added to sonicated mixture of GO and DI water, along with 180 mg of surfactant (sodium acetate) and 13.5 ml of IPA. The combined reagents are sonicated for 0.5 hour to ensure good mixing; afterwards the reagents are transferred to a hydrothermal autoclave reactor and baked at 120℃ for 8 hours.

After the sample is cooled down, it undergoes vacuum filtration using a hydrophobic polytetrafluoroethylene (PTFE) membrane filter with a pore size of 0.22 μm. Filtration is repeated for 3 times, rinsing the sample with DI water each time. The filtration process rinses off the residual surfactant presented. Next, the flakes from the filter paper are shaken off, in a vial containing a binary 9:1 solvent mixture of IPA and 2-butanol, and is sonicated for 0.5 hour. This completes the solvent exchange of the sample and, finally, the sample is centrifuged. The top 70% portion without aggregations is collected for inkjet printing. The final ink is shown in Fig. 8.2(a). The purpose of solvent exchange into a binary alcoholic solvent mixture is to suppress the ring-like deposition of suspended particles [190] through Marangoni-enhanced spreading and droplet deformation [58].

Characterization of formulated ink and printed film

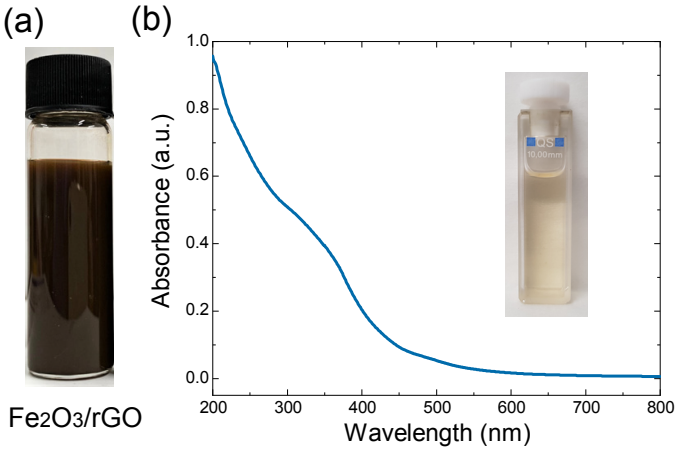

Fig. 8.2 (a) Photograph of formulated α-Fe_2O_3/rGO ink. (b) Optical absorption of diluted α-Fe_2O_3/rGO ink (inset).

Fig. 8.2(b) displays the optical absorption spectrum for the diluted α-Fe_2O_3/rGO ink. The spectra shows a shoulder at approximately 480 nm which is consistent with literature in identifying α-Fe_2O_3 [257]. The larger shoulder between 300-400 nm in the spectra is likely

due to red-shifted rGO from ≈275 nm [258], as attributed to the alteration of the bandgap of rGO [259].

Fig. 8.3(a) confirms the formation of a printable ink with stable jetting without appearance of secondary droplets during printing. This can be further supported with the calculation of the inverse Ohnesorge number, $Z = \sqrt{\gamma_{ink}\rho D}/\eta$ [63], where γ is surface tension, ρ is density, D is nozzle diameter, and η is ink viscosity. Using the measured values: $\gamma_{ink} = 29.6$ mN m^{-1}, $\rho = 0.8$ g cm^{-3}, $D = 22$ μm, and $\eta = 1.95$ mPa s, a Z value of 11.7 is calculated which lies within the optimal range for stable jetting [63]. Fig. 8.3(b) shows the evolution of contact angle of the ink over time. The angle initiates at around 12° and decreases rapidly over time, reaching below 4° in under 1 s. It continues to decrease beyond this point until it approaches 0, although the measurements are difficult to obtain due to errors from the glare, contrast, and viewing angles [260]. Despite this, the good wetting and high print definition is demonstrated by the printed Cambridge University crest in Fig. 8.3(c).

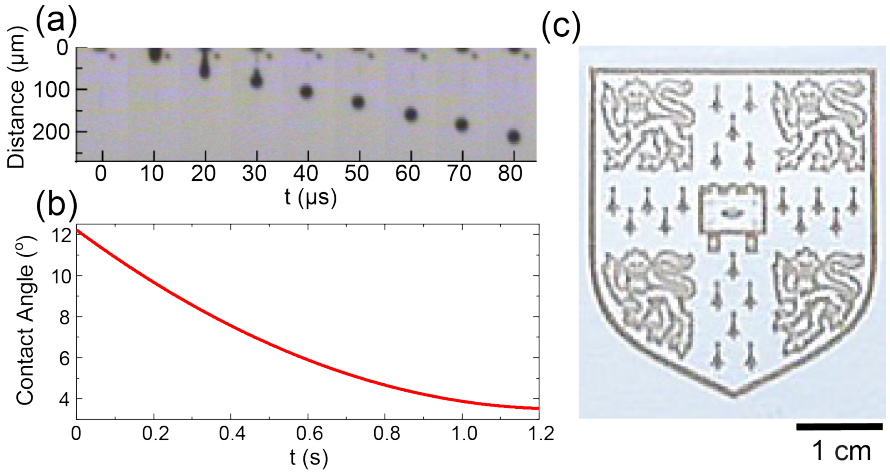

Fig. 8.3 (a) Jetting sequence of the ink. (b) Change in contact angle over drying process. (c) Inkjet-printed Cambridge University crest.

I inkjet-print 100 passes of α-Fe_2O_3/rGO layers onto the interdigitated electrodes (10 μm finger gap and width) above the Si_3N_4 membrane of the CMOS μHP platform. The fabricated device is shown optically in Fig. 8.4(a). From the enlarged microscope image, the α-Fe_2O_3 decorated rGO are uniformly distributed between and on top of the electrodes.

Fig. 8.4(b) displays the representative Raman spectrum (among 10 spectra measured) for printed α-Fe_2O_3/rGO films, showing D and G peaks at 1345 and 1607 cm^{-1} respectively [261]. The calculated I_D/I_G ratio is 0.95, indicating the presence of disorders or defects in rGO sheets which act as the active sites for gas adsorption [94]. I note that this ratio is higher than that of LPE-processed graphene (0.46). Pure hematite belongs to the R-3c crystal space group and can be identified with the A_{1g} and E_g phonon modes in Raman [262]. The inset

spectrum highlights the 200-650 cm^{-1} region, exhibiting the characteristic peaks at A_{1g}: 224 cm^{-1} and E_g: 294, 410, 611 cm^{-1} identified for α-Fe_2O_3 [262].

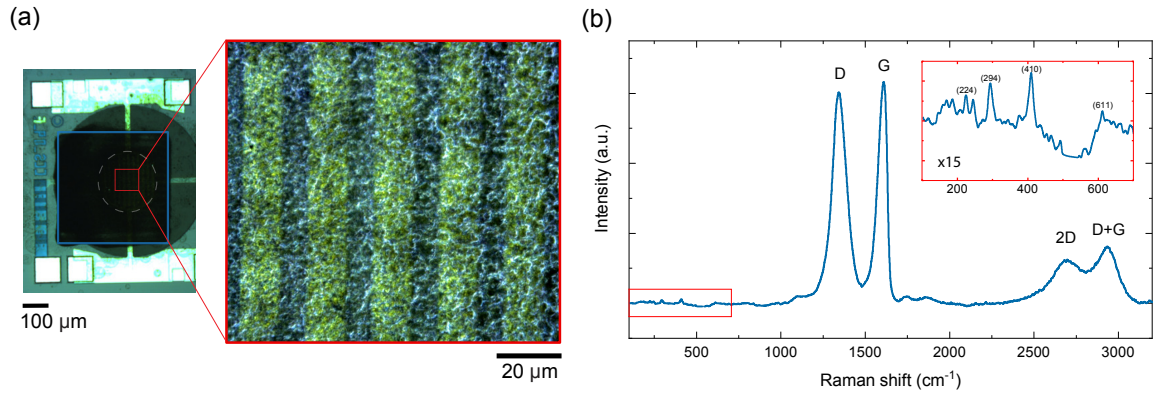

Fig. 8.4 (a) Microscopic image of the inkjet-deposited CMOS sensory device. (b) Raman spectra of α-Fe_2O_3/rGO printed films; (inset) zoomed-in spectra.

8.2 Sensing mechanism and performances

The sensing mechanism of NO_2 detection by the α-Fe_2O_3/rGO nanocomposite is depicted in Fig. 8.5(a). rGO is a typical p-type semiconductor, and NO_2 captures an electron from rGO to produce NO_2^- [263]. α-Fe_2O_3 is an n-type semiconductor and oxygen molecules in air act as electron acceptors. The molecular oxygen captures electrons from the conduction band of α-Fe_2O_3 and generates chemisorbed oxygen O_2^-. Then, NO_2 reacts with the O_2^- on the surface active sites of α-Fe_2O_3 and forms an intermediate complex NO_3^- [263]. Since rGO has a lower work function (≈5.2 eV) than α-Fe_2O_3 (≈5.9 eV) [264], the electrons transfer from rGO to α-Fe_2O_3 to equalize the Fermi level. This leads to an increase in hole density and thus reduction in electrical resistance during sensing events [264].

Transmission electron microscopy (TEM) in Fig. 8.5(b) captures the evenly-distributed Fe_2O_3 NPs grown on the rGO matrix (the semi-transparent layers bounded by wrinkles). Notably, the individual Fe_2O_3 NPs reveal microporous structures that may lead to an enhanced gas adsorption capacity. The selected area diffraction (SAED) pattern in the inset presents the crystallines of both restored aromatic graphene and Fe_2O_3 NPs, as seen by the diffraction rings and points, respectively.

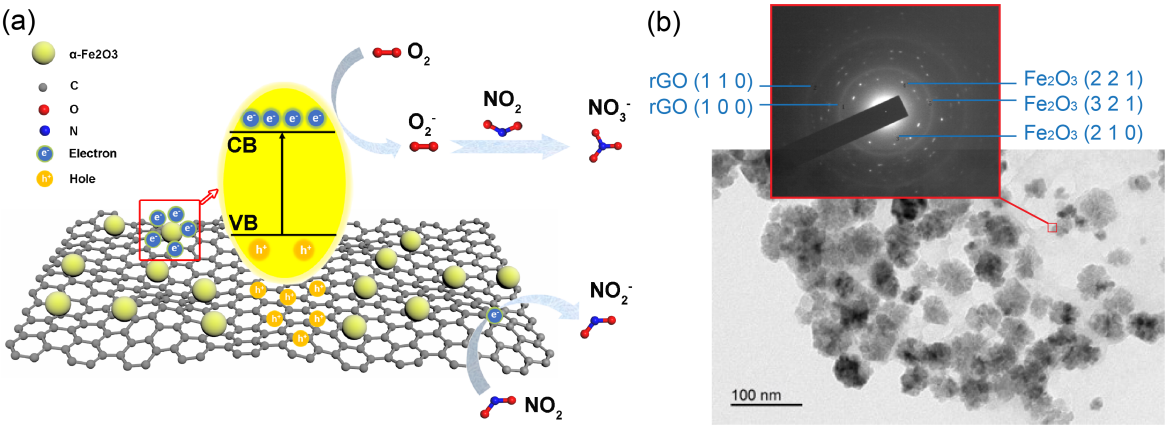

Fig. 8.5 (a) Illustration of sensing mechanism on detection of NO_2 in air with α-Fe_2O_3/rGO; (inset) band diagram at α-Fe_2O_3/rGO interfaces. (b) TEM image of α-Fe_2O_3/rGO composite; (inset) SAED at selected rectangular region.

Fig. 8.6 shows the responses under exposure of NO_2 at room temperature. It is suggested that due to the extended surface area and metal-semiconducting heterojunctions [94], the inkjet-printed sensors exhibit 1.48% responsivity as low as 100 ppb of NO_2, which satisfies the requirement (primary and secondary national standards of 100 ppb hourly average and 500 ppb 3-hour average, respectively [265]) for environmental NO_2 monitoring. However, the non-linear baseline drift reflects incomplete sensor recovery after individual sensing events. Therefore, I further optimize sensing performances through deployment of TM control algorithm.

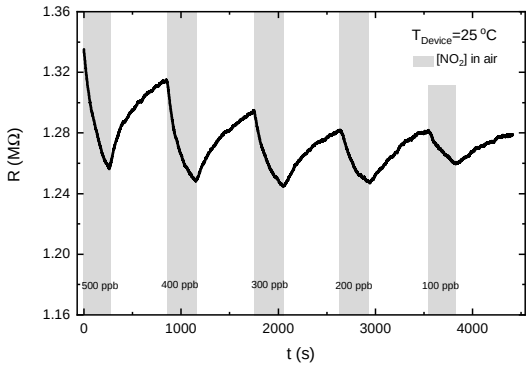

Fig. 8.6 Response under NO_2 exposure for inkjet-printed αFe_2O_3/graphene devices operated at room temperature.

8.3 Performance in TM mode

The control mechanism implements an application of 150°C pulse at every 5 s interval using the μHP platform. The mechanisms of TM scheme have been fully analyzed with surface adsorption, analyte diffusion, and carrier transport models in the previous chapters. Fig. 8.7(a) illustrates the response, deploying this protocol, after the sensor is stabilized. The electrical resistance R stabilizes to 1.2 MΩ at 25°C with a sharp drop to 0.34 MΩ at 150°C. The resistance drop due to increase in temperature aligns with the relationship:

$$\rho \propto \exp(\frac{\Delta V}{k_B T}) \tag{8.1}$$

where ρ is resistivity, ΔV is the potential barrier, k_B is the Boltzmann constant. The sharp reduction of R at 150°C pulse and its instant recovery to the 25°C plateau showcase the rapid dynamic heating/cooling operation offered.

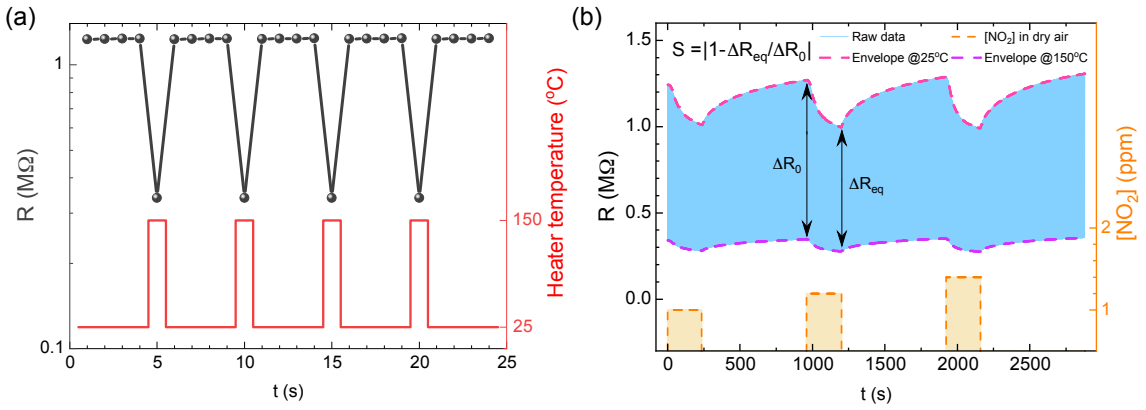

Fig. 8.7 (a) The control protocol (150°C pulse for every 5 s) and response at stabilization phase. (b) Data processing procedure for generating proceeding output curves.

The blue-shaded region in Fig. 8.7(b) shows the unprocessed response under exposure to various NO_2 concentrations in dry SA for 240 s every 960 s. I extract the respective envelopes at 25°C and 150°C pulses, and then employ a differential readout of the envelopes to generate an output curve S_t thereafter. The steady state responsivity S is defined as $|1 - \Delta R_{eq}/\Delta R_0|$, where ΔR_{eq} and ΔR_0 are the differential readouts at equilibrium in NO_2 and stabilization in SA, respectively. The lowered R present in the envelopes during exposure correspond to the reduction in ΔV from Equation 2.6 and mechanisms detailed in Chapter 5 Section 6.3.

Fig. 8.8(a) shows responses of 3 sensors under successive NO_2 injection, with concentrations varying at steps of 0.25 ppm. Moreover, individual responses show no hysteretic behavior and baseline drift, generating consistent responsivities at measured concentrations.

The well-alignment of responses (<2% variation) across devices showcases the consistency of the fabricated devices. Furthermore, the devices produce high SNR of > 5200 and consume 2 mW using the TM scheme, which is 97% more energy efficient than the latest commercial MEMS-based sensor (MiCS-6814) that consumes 73 mW. Fig. 8.8(b) assesses the long-term persistency of the sensor through comparison of transient responses before and after one month. The responsivity and linearity improve slightly with the ageing over a month's period.

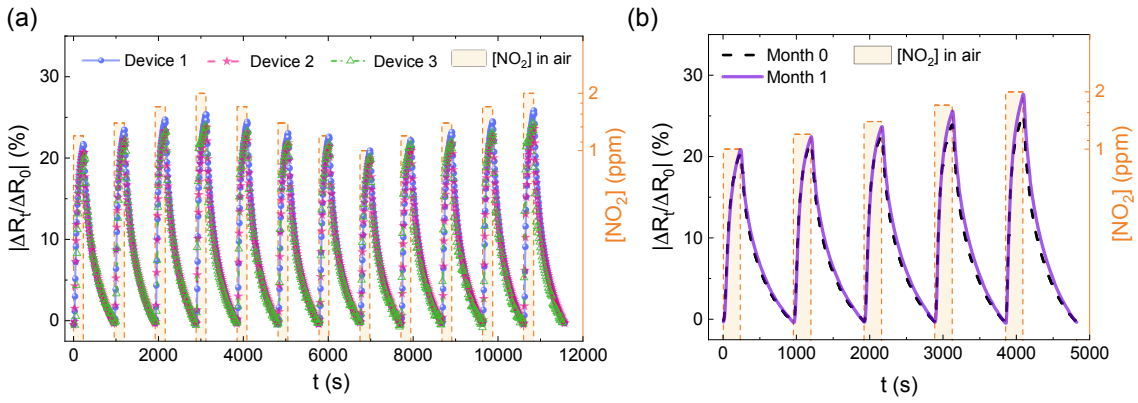

Fig. 8.8 (a) Multi-device response under successive NO_2 concentration steps. (b) Long term sensor response tested under successive NO_2 steps. See Appendix Fig. A.10 and A.11 for raw data.

8.4 Cross-selectivity measurements

The effects of interfering gas species are characterized and compensated. Four repeated measurements at 2 ppm of each interferant (see Appendix Fig. A.12) are carried for the cross-sensitivity characterization. The cross-selectivity measurements in Fig. 8.9(a) present negligible responsivity from 2 ppm of ethanol, acetone, and CO (0.48%, 0.23%, 0.14%, respectively) relative to NO_2, while the influence of humidity is significant (8.53% at 20% RH) which is common for MOx-based sensors. This is attributed to the interactions between water vapor and the adsorbed oxygen ions on the surface of MOx [255]. The responsivity in presence of analyte can be non-linear with respect to respective concentrations [266], and it can depend on other factors like surface morphology [266], building the complexity of modelling. In turn, I focus on a data-driven approach to compensate for the humidity effect in this work.

To examine the behaviors of humidity on NO_2 sensing, I measure the responses of NO_2 at 2 ppm within 20-60% RH levels of SA varying at 10% steps, as shown in Fig. 8.9(b). Despite

the hardly distinguishable steady state responsivities between various RH levels, I observe the disparities in their transient shapes which provides the grounds for further analysis.

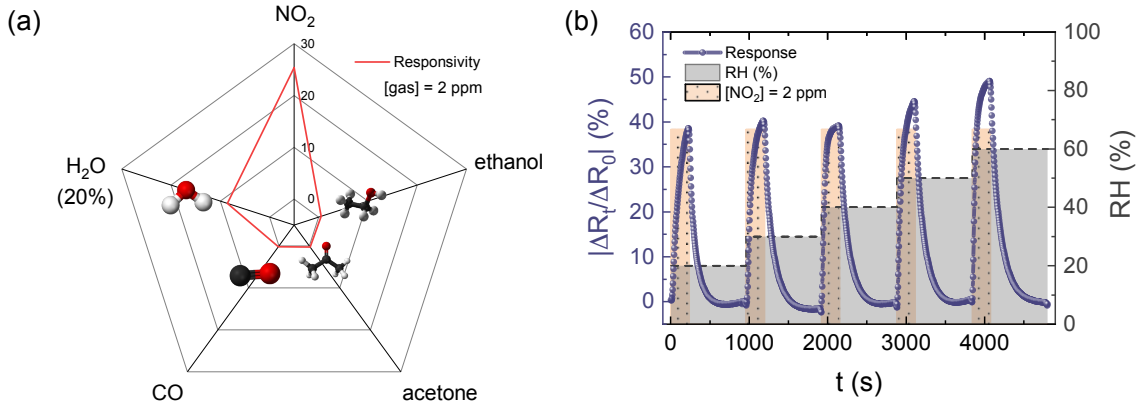

Fig. 8.9 (a) Cross-analyte selectivity among common interfering gas species. (b) Response NO_2 at 2 ppm under various RH levels. See Appendix Fig. A.12 for raw data.

8.5 Machine learning for selectivity improvement

I employ ML approaches to establish a predictive system to discriminate NO_2 concentrations in various RH conditions for compensation of interferences. First, I obtain signatures of the pre-processed transient responses S_t to create a pattern library for the dataset. Transient responses comprise comprehensive dynamic characteristics arising from gas adsorption/desorption processes, diffusion speed, and/or chemical reactions [50], offering many exploitable insights.

In this study, I extract 12 features for each curve. The methods are illustrated in Fig. 5.9. In brief, I obtain (i) response and recovery time constants τ_{resp}, τ_{recov} derived from exponential fitting (Equation 5.1) based on Langmuir model [267]; (ii) steady state information; (iii) area of response and recovery signal to incorporate baseline information; and (iv) features from differentiated curve which relate to reaction and diffusion dynamics.

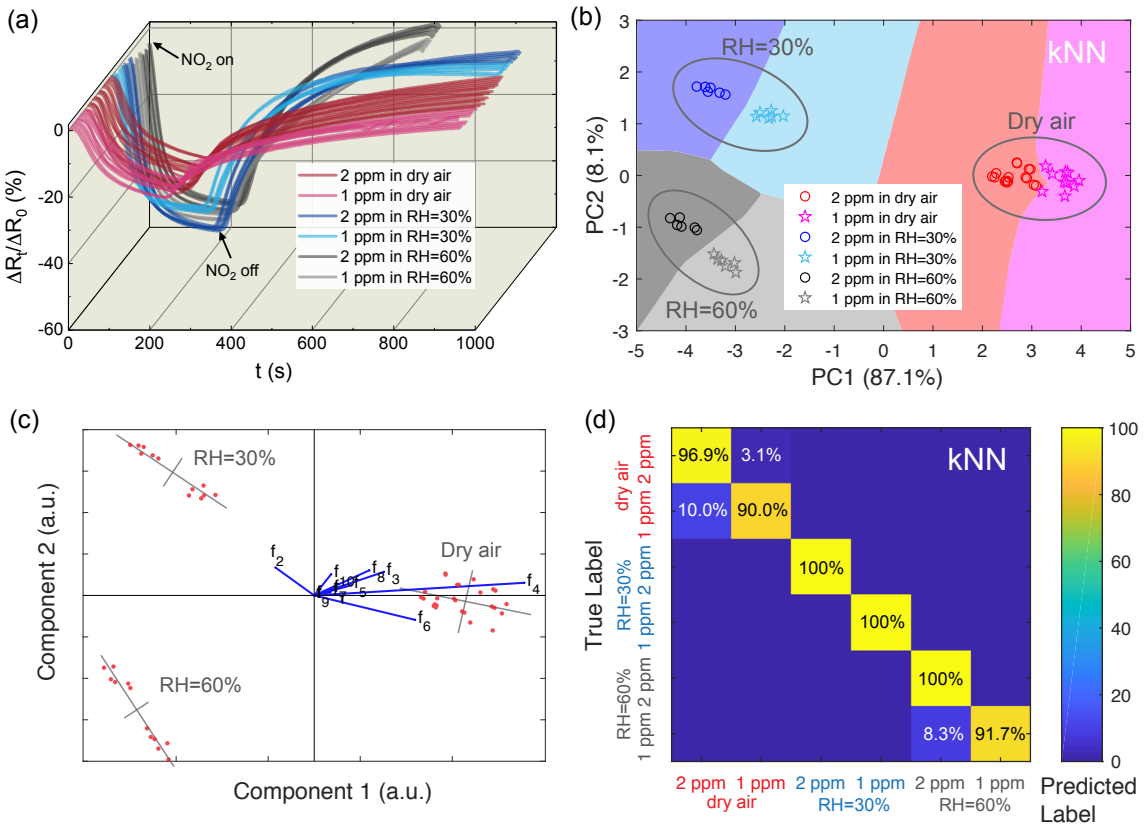

Fig. 8.10 (a) Sensor responses of 6 sets of ([NO_2], [RH]) paired groups. (b) PCA scores and classification with kNN. (c) PCA biplot, where f_k represents the loading attributed to k-*th* feature. (d) Confusion matrix of the predictive system.

PCA generates projections along the directions of maximum variances, selecting features important for class representation. PCA is then performed for dimensionality reduction of the computed features, and visualization of the clusters formed in low-dimensional projections. The input dataset comprises 6 sets of ([NO_2], [RH]) paired groups, in combinations of [NO_2] = 1, 2 ppm in [RH] = 0, 30, 60%. Figure 8.10(a) presents the input training set, containing 10-20 repeated measurements (50% of the total measured dataset) obtained for 3 fabricated α-Fe_2O_3/rGO devices simultaneously for each group.

Fig. 8.10(a) presents the input training set, containing 50% of the measured dataset. As noted, the excellent device-to-device consistency, cross-cycle reproducibility, and SNR offered by inkjet technology coupled with TM algorithms significantly suppress noisy information entering the training system. Fig. 8.10(b) shows the visual representation after PCA transformation. With only two most critical PCs, I can clearly separate the dataset into 3 widely distinct RH classes each composed of 2 distinct [NO_2] clusters, with 95.2% of variances explained. I then perform cluster analysis to segment transformed dataset into 6 classes. kNN is used for classification (background segments in Fig. 8.10(b)) due to its high discrimination accuracy [90].

To further analyze the contributions of individual features f_k towards separation of classes, I perform a PCA biplot as displayed in Fig. 8.10(c). Feature f_4 (t_{recov}) contributes most to PC1 (87% of variances); whereas f_2 (ΔR_{recov}) and f_6 (τ_{recov}) are the main features for separating different NO_2 concentrations within the same RH groups, indicating that the desorption behavior is the key identifier among different groups. My system is then evaluated with a confusion matrix (Fig. 8.10(d)) for prediction accuracy, using cross-validation dataset (50% of remaining dataset).

I successfully discriminate mixed concentrations of NO_2 and RH, with all labels being classified at above 90% accuracy, and particularly 4 classes at 96-100% accuracy, outperforming current literature on single-sensor chemical discrimination. The small portion of misclassification is attributed to the boundary between 1 and 2 ppm NO_2 in dry air. In summary, the comprehensive features I extract and the associated analysis leads to robust discrimination of ([NO_2], [RH]) groups, both qualitatively and quantitatively.

8.6 Field trial - the InnovateUK Project

This section describes the implementation of fully inkjet-printed room temperature NO_2 sensors I fabricate that are tested in field trials. This is part of the InnovateUK project involving collaborations with Nanjing Tech University, University of Manchester, CPI, Novalia, NeuDrive, and KDX.

8.6.1 Printed devices

Fig. 8.11 shows an array of fully-inkjet-printed rGO/α-Fe_2O_3 sensors. In each sensor, the inkjet-printed rGO/α-Fe_2O_3 onto silver interdigitated electrodes (Ag IDEs) acts as the active sensing layer. I use polyethylene terephthalate (PET) with a microporous coating that is specifically designed for silver printing, to avoid short-circuits of the Ag IDEs. Fig. 8.12 shows highly uniform deposition of rGO/α-Fe_2O_3 over the Ag IDEs.

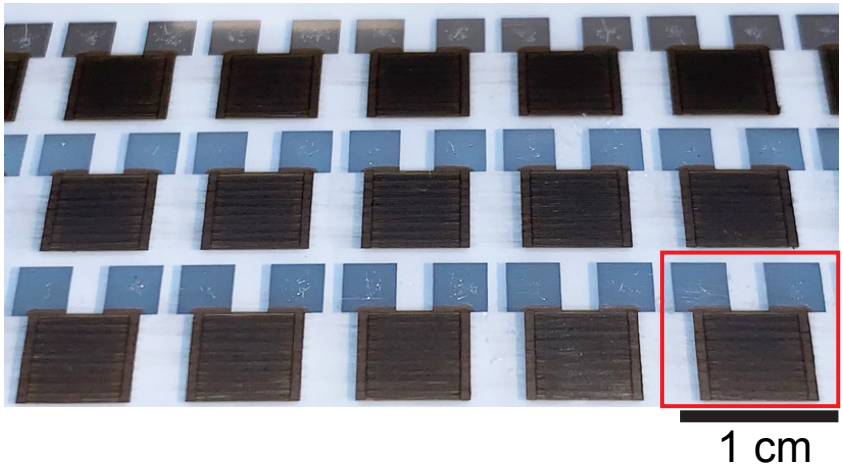

Fig. 8.11 Array of fully inkjet-printed rGO/α-Fe_2O_3 sensors.

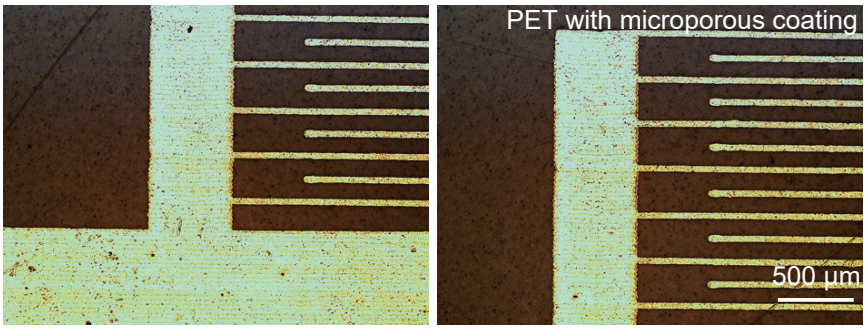

Fig. 8.12 Inkjet printed silver electrodes showing high printing resolution.

8.6.2 Measurement results in the laboratory

Fig. 8.13(a) presents the measured response following saturation under 1 ppm NO_2. To eliminate the influence from the residual gas and humidity absorbed by the sensors, I have done the following: (1) saturate the sensors under 1 ppm NO_2; (2) put the sensors under vacuum to allow complete desorption; (3) saturate the sensors under 1 ppm NO_2 and record the device resistance.

Fig. 8.13(b) is the extracted responsivity as a function of NO_2 concentration. As shown, after saturated in NO_2, the baseline drift issue is addressed, and the responsivity establishes a linear relationship with the NO_2 concentration. The inkjet-printed devices in RT shows the following performances: (1) 1% responsivity at 0.2 ppm NO_2; (2) ≈20% responsivity under 1ppm NO_2; (3) Sensitivity of 20.2%/ppm. The suppression of the baseline drift and the linear relationship suggest that the sensors are viable for room temperature, prolonged, multiple-cycle measurements for down to 0.2 ppm.

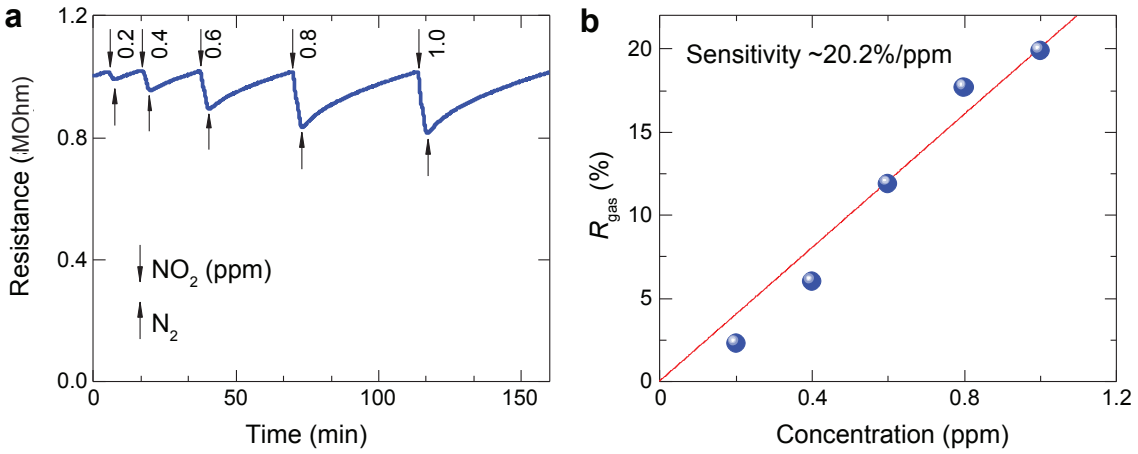

Fig. 8.13 (a) Response after saturated exposure to 1 ppm NO_2 for 30 min. (b) Responsivity as a function of NO_2 concentration.

To assess the device-to-device sensitivity variations across this sensor array, I measure the responsivity at 1ppm NO_2 of each individual device. Fig. 8.14(a) presents the measured responsivity map the sensor array. As shown here, all the sensors response identically with ≈90% responsivity. This is confirmed by its Gaussian distribution as presented in Fig. 8.14(b): all the devices are distributed in the $\mu \pm 3\sigma$ region. I find that the responsivities of 78% of sensors lie within 1σ (2.5% spread from their μ value). This demonstrates the viability of the fully-inkjet-printed sensors for manufacturing.

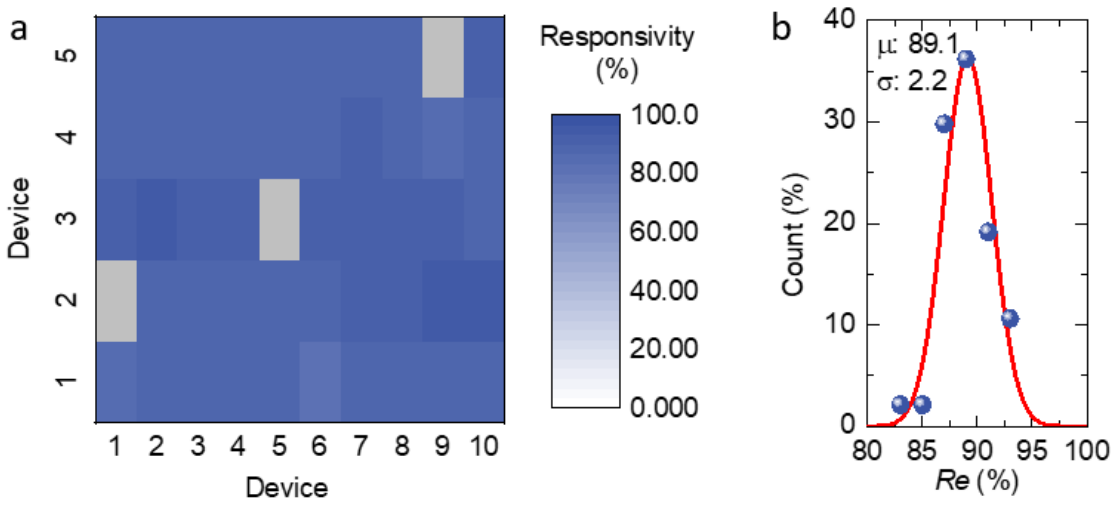

Fig. 8.14 (a) Measured responsivity map of the sensor array. The gray data points correspond to malfunctional devices. (b) The corresponding Gaussian fitting of measurement, showing that all devices are distributed within $\mu \pm 3\sigma$.

8.6.3 Compensation for RH levels

The responses of MOx based chemiresistive sensors often suffers from interference from other gas species. RH level is one of the major concerns for my sensor as the city where the field trial is conducted (Cambridge) is normally very humid, and the performance of the sensor may deteriorate due to the adsorption of OH^- group in water vapor. Hence, I need to calibrate the response of NO_2 under different RH level.

The testing is conducted in the gas testing rig where RH level can be controlled precisely with a dilution of synthetic air which is controlled by the flow rate passing through the mass flow controller. The measurement is conducted at an increasing step of 10% RH level, ranging from 0% to 80%. The RH level is set to hold for 10 min every cycle of testing. The resistance at various RH level at plotted in the scattered datasets in Fig. 8.15(a). As seen from the figure, the sensor response is barely dependent on humidity at below 30% RH level and drops by approximately 8% at 40% RH level. The response slightly drops linearly as RH level keeps increasing until 80% where the response starts to saturate.

My approach to compensate the effect of humidity is to compute R_0 as if RH is zero, based on the fitted equation and RH level readout from the humidity sensor which is integrated in the electronics on the PCB board. The concentration readout programmed in the microcontroller is computed by the linear relationships as a function of the concentration of NO_2 in dry air, as presented in Fig. 8.13(b).

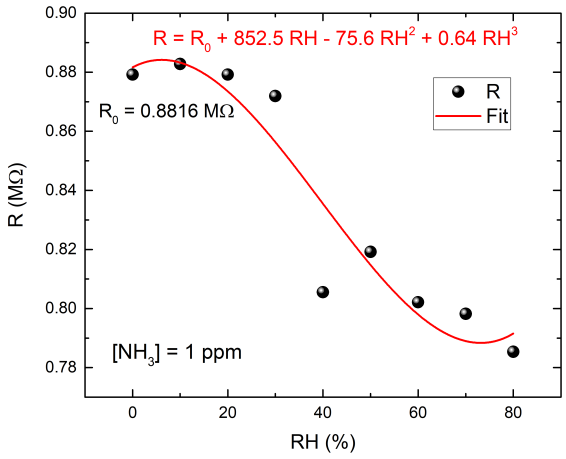

Fig. 8.15 Resistance of the inkjet-printed sensor characterized at 1 ppm of NO_2 under various RH conditions.

I have chosen a polynomial fit to better describe the behavior at low and high RH levels at which the resistance values are closer to saturation with a smaller variation with respect to the RH level. R_0 is then computed by the following equation as derived from the polynomial fit.

$$R_0 = R - 852.5RH + 75.6RH^2 - 0.64RH^3 \tag{8.2}$$

where R is the uncompensated resistance value from the sensor readout; RH is presented in percentage. R_0 in dry air for 1 ppm is confirmed to be 0.8816 MΩ which aligns with the measurement. The computed R_0 which has been compensated for the effect of humidity is then converted back to the linear relationships in a dry air environment.

8.6.4 Measurement system

Fig. 5.6 in Chapter 5 shows the housing and the PCB for the implementation of electronic measurements. The core circuitry (Fig. 5.7) to realize the measurement consists of a Wheatstone Bridge followed by a differential amplifier to deliver a readout with enhanced sensitivity in the range of 0.6 to 1 MΩ. The inkjet printed sensor on PET substrate is inserted into the zero insertion force (ZIF) socket. The concentration level is then computed and compensated against RH level by the microcontroller and displayed on the LCD connected to the PCB. The raw and processed data is then communicated through the UART protocol to the multi-sensory hub.

This NO_2 detection unit is put together with the other sensor units (polymer sensors developed by University of Manchester and commercial electrochemical sensor from Alphasense), along with other components (GPS, central pump, Raspberry Pi controller, and USB interface) in a large peli case, as shown in Fig. 8.16.

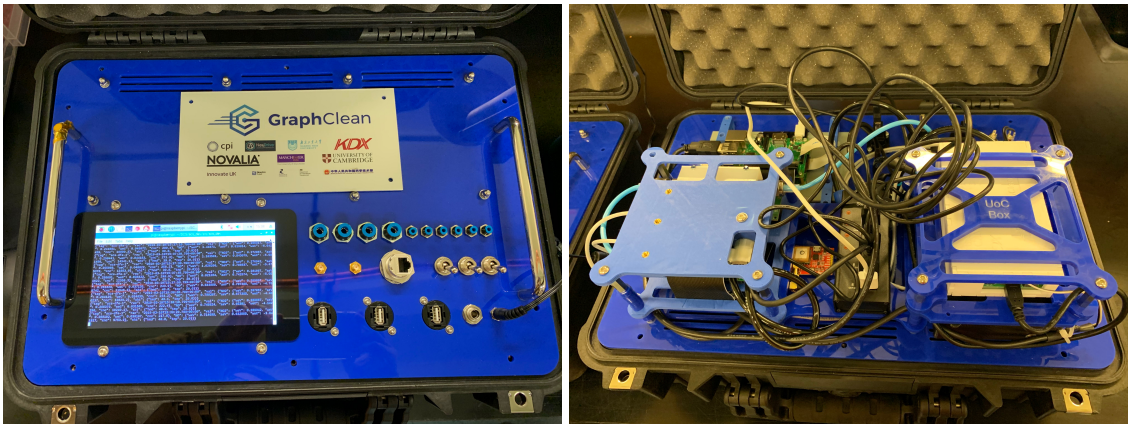

(a) Top view (b) Bottom view

Fig. 8.16 Integrated system for field trial.

8.6.5 Field trial results

The field trial is carried out outside our laboratory (at 52°12'37''N, 0°05'40''E). The test is conducted at 9:00 – 17:00 on Monday 18th March 2019. The system is placed inside an open storage room surrounded by a building construction site for continuous monitoring. The construction work is being carried out between approximately 10:00 to 16:00 on the day of the trial. I obtain the resistance value from the system (3 point average, with measurements taken every 60 seconds) and convert it into NO_2 concentrations based on the calibration curve shown in Fig. 8.17(a). Note that the humidity level used for compensation is between 45-55% as measured on the site.

The NO_2 concentration during the measurement period is shown in Fig. 8.17(b). The concentration initiates at 50 ppb which aligns with the average concentrations expected during a working day. The results show a clear rise from 50 ppb reaching 150 ppb within 1 hour, indicating the emission of NO_2 during the building construction. The concentration peaks at 200 ppb at 14:30 and drops afterward and more rapidly after construction is finished. The results demonstrate meaningful real-world implementation that aligns with the expected operation. I note that the Alphasense reference electrochemical sensor was unable to give any meaningful readings for comparison. This is likely due to the issue with the interface or data readout.

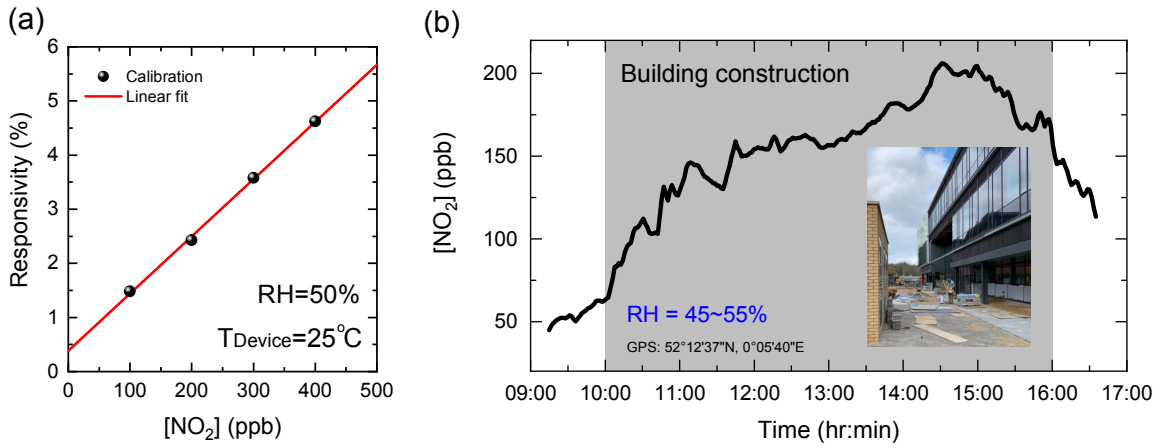

Fig. 8.17 (a) The calibration curve for the devices under the testing conditions during the field trial. (b) Field trial results. The grey shaded region shows the period when building construction takes place. See Appendix Fig. A.13 for raw data.

8.7 Summary of results

I have developed a machine-intelligent inkjet-printed α-Fe_2O_3/rGO integrated CMOS system to selectively measure NO_2 with high accuracy. Subsequently, I address the challenge of incomplete sensor regeneration through temperature modulation scheme, and achieve excellent SNR, repeatability/reversibility, device-to-device consistency, and long-term consistency that suppress noisy information. Interference from moisture is then addressed by machine learning approaches including PCA and clustering of transient features. The predictive system is capable of quantifying NO_2 concentrations under different RH conditions, with excellent separation between classes and all labels classified at above 90% accuracy (4 classes at 96-100% accuracy).

Furthermore, the fully inkjet-printed NO_2 room temperature sensors integrated within the developed multi-sensory hub have performed reliable continuous NO_2 detection in a real-world environment. The sensors are not susceptible to environmental noise, such as humidity variations, showing sub-10% variation at the highest humidity levels that can be compensated for algorithmically. The technologies could be ideal for IoT-based adaptive air quality monitoring systems.

Chapter 9

Conclusions

In this thesis, I have developed printable mobile-embeddable devices and intelligent sensory systems as integral parts of personal healthcare as well as air quality applications. The targets have been achieved through the development of novel sensing nanomaterials, scalable device fabrication technologies, as well as signal processing and machine learning algorithms for establishing intelligent systems.

9.1 Strategies and achievements

From the perspective of the material system, the synergistic advantages of various graphene-MOx nanocomposites are explored for the measurement of NH_3 and acetone levels for early disease diagnostics, and the quantification of NO_2 in ambient environments under various humidity levels for air pollution monitoring. The improved performance seen in these graphene-MOx hybrids is attributed to the formation of local metal-semiconductor heterojunctions and enhancements in gas adsorption capability at the active graphene sites. The production of high purity sensing nanocomposites is carried out with low cost and solution-processable hydrothermal synthesis.

From the perspective of device fabrication, UALPE coupled with inkjet printing of sensing materials is promising for the integration of the miniaturized CMOS-compatible devices. I optimize the ink formulations to achieve spatially uniform printed morphology for delivering device reproducibility. In particular, the optimization of solvent/polymer system enhances the dispersibility and rheological properties of inks; the employment of binary alcoholic solvent system suppresses the detrimental coffee-ring effect. Moreover, I develop a model to optimize the printed morphology based on droplet impact and spreading mechanisms, offering an additional tool for turning printing parameters.

In addition to improved material system and fabrication method, the challenges of sensor recovery, baseline drift, and cross-analyte interferences are further addressed from the perspective of computational approaches. The algorithms on temperature modulation scheme are developed based on temperature-dependent sensing mechanisms, which are analyzed quantitatively and qualitatively for graphene/MOx system from the aspects of analyte-interface interactions, electron transport based on band theory, and diffusion process. I further develop machine learning approaches including signal pre-processing and cluster analysis techniques to address the common issue of cross-analyte interference. For wireless connectivity, I establish a distributed wireless network of sensor platforms and generate visualization mappings of air quality index, and transmit timely alerts while the level of hazardous analyte is above a threshold.

In Chapter 6, I develop inkjet-printed graphene/ZnO integrated CMOS sensor for the measurement of NH_3 levels in the simulated breath. I have addressed the issue of incomplete sensor regeneration through the establishment of temperature-dependent sensing mechanisms and the associated algorithms, leading to enhanced sensing performances and reproducibility. Under both pure NH_3 and NH_3 in synthetic air, ultrahigh responsivity, sensitivity, and low response/recovery time are achieved. The devices are sustainable with significantly reduced baseline drift, extraordinary repeatability without hysteresis, and high device-to-device consistency.

In Chapter 7, I develop inkjet-printed graphene/WO_3 integrated CMOS sensor for the measurement of acetone levels. Functionalization using WO_3 nanoparticles offers selectivity towards acetone. Different graphene concentrations are investigated to improve performance. Temperature modulation mode is more practical as a gas sensor for breath due to its shorter response time and more reliable results. This mode also allows a significantly lower power consumption.

My strategy to combine the sensing material, inkjet printing onto CMOS platform and TM scheme promises a robust system that outperforms conventional devices in aspects of reproducibility, performance reliability, recovery time while enhancing responsivity. Additionally, my approach of using inkjet deposition offers excellent device-to-device consistency, overcoming a common drawback of the majority of the other studies. Furthermore, cross-selectivity is addressed by the parallel graphene/WO_3 sensor. My dual graphene-MOx strategy therefore allows tentative mapping of disease probability being constructed.

In Chapter 8, I develop a machine-intelligent inkjet-printed α-Fe_2O_3/rGO integrated system to selectively measure NO_2 in ambient environment. Interference from moisture is addressed by machine learning approaches including PCA and clustering of transient features. The predictive system is capable of quantifying NO_2 concentrations under different RH con-

ditions, with excellent separation between classes. The level of discrimination accuracy has not yet been reported using a single MOx/rGO composite sensor. Furthermore, the fully inkjet-printed room temperature NO_2 sensors assembled within the developed multi-sensory hub have performed reliable continuous NO_2 detection in a real-world environment. The sensors are minimally susceptible to humidity variations which can be compensated for algorithmically.

9.2 Future work and outlook

In order to achieve practical multi-analyte sensory systems for disease diagnosis and air quality monitoring systems, there is room for further research. From the material's perspective, the 2D material family (and their functionalization with MOx) with superior sensing properties are due to be explored for the establishment of cross-reactive arrays.

From the fabrication's perspective, further optimizations are required including accelerating the material deposition process, achieving wafer-scale device consistencies, as well as improving the integrability across inkjet and standard CMOS fabrication processes.

From the computational perspective, further developments of more sophisticated machine learning models such as neural networks are essential for more accurate classification of analytes.

My strategy to combine the sensing material, inkjet printing onto the CMOS platform, and temperature modulation / machine learning algorithms promises a robust system that outperforms conventional devices. The versatile technologies enable a multi-analyte sensor to be fabricated reliably and cost-effectively, offering more accurate disease diagnostics platforms.

The intelligent systems I develop also could be ideal for IoT-based adaptive air pollution monitoring systems. Ubiquitous deployment of a distributed network comprising these low-powered embeddable devices will promote the development of new generational IoT-enabled air pollution heatmaps and real-time alert systems in smart cities.

Therefore, I believe my technologies have great potentials to disrupt the field of disease diagnostics and air quality monitoring.

References

[1] S.Z. Ali, F. Udrea, W.I. Milne, and J.W. Gardner. Tungsten-Based SOI Microhotplates for Smart Gas Sensors. *Journal of Microelectromechanical Systems*, 17(6):1408–1417, dec 2008.

[2] Saving lives, averting costs: an analysis of the financial implications of achieving earlier diagnosis of colorectal, lung and ovarian cancers. Technical report, 2014.

[3] Thalakkotur Mathew, Prabhahari Pownraj, Sukhananazerin Abdulla, and Biji Pullithadathil. Technologies for Clinical Diagnosis Using Expired Human Breath Analysis. *Diagnostics*, 5(1):27–60, feb 2015.

[4] David J Kearney, Todd Hubbard, and David Putnam. Breath ammonia measurement in Helicobacter pylori infection. *Digestive diseases and sciences*, 47(11):2523–30, nov 2002.

[5] Zhennan Wang and Chuji Wang. Is breath acetone a biomarker of diabetes? A historical review on breath acetone measurements. *Journal of Breath Research*, 7(3):037109, aug 2013.

[6] Robert Beaglehole, Ruth Bonita, George Alleyne, Richard Horton, Liming Li, Paul Lincoln, Jean Claude Mbanya, Martin McKee, Rob Moodie, Sania Nishtar, Peter Piot, K Srinath Reddy, David Stuckler, and Lancet NCD Action Group. UN High-Level Meeting on Non-Communicable Diseases: addressing four questions. *Lancet (London, England)*, 378(9789):449–55, jul 2011.

[7] Chunhui Deng, Jie Zhang, Xiaofeng Yu, Wei Zhang, and Xiangmin Zhang. Determination of acetone in human breath by gas chromatography–mass spectrometry and solid-phase microextraction with on-fiber derivatization. *Journal of Chromatography B*, 810(2):269–275, oct 2004.

[8] Shinya Fujii, Toshio Maeda, Ichiro Noge, Yutaka Kitagawa, Kenichiro Todoroki, Koichi Inoue, Jun Zhe Min, and Toshimasa Toyo'oka. Determination of acetone in saliva by reversed-phase liquid chromatography with fluorescence detection and the monitoring of diabetes mellitus patients with ketoacidosis. *Clinica Chimica Acta*, 430:140–144, mar 2014.

[9] Chunhui Deng, Ning Li, Xiaochuan Wang, Xiangmin Zhang, and Jia Zeng. Rapid determination of acetone in human blood by derivatization with pentafluorobenzyl hydroxylamine followed by headspace liquid-phase microextraction and gas chromatography/mass spectrometry. *Rapid Communications in Mass Spectrometry*, 19(5):647–653, mar 2005.

[10] Chia-Chi Wang, Yu-Ching Weng, and Tse-Chuan Chou. An Amperometric Acetone Sensor by Using an Electro-Deposited Pb-Modified Electrode. Technical report, 2006.

[11] Zheng Meng, Robert M. Stolz, Lukasz Mendecki, and Katherine A. Mirica. Electrically-Transduced Chemical Sensors Based on Two-Dimensional Nanomaterials. *Chemical Reviews*, 119(1):478–598, jan 2019.

[12] Dieter Kohl. Function and applications of gas sensors. *Journal of Physics D: Applied Physics*, 34(19):R125–R149, oct 2001.

[13] Gonzalo Pajares Martinsanz (Ed.). *State-of-the-Art Sensors Technology*. MDPI (Multidisciplinary Digital Publishing Institute), 2017.

[14] Feng Yan, Meng Zhang, and Jinhua Li. Solution-Gated Graphene Transistors for Chemical and Biological Sensors. *Advanced Healthcare Materials*, 3(3):313–331, mar 2014.

[15] Frank Schwierz. Graphene transistors. *Nature Nanotechnology*, 5(7):487–496, jul 2010.

[16] Peng Lin and Feng Yan. Organic Thin-Film Transistors for Chemical and Biological Sensing. *Advanced Materials*, 24(1):34–51, jan 2012.

[17] Qiyuan He, Shixin Wu, Zongyou Yin, and Hua Zhang. Graphene-based electronic sensors. *Chemical Science*, 3(6):1764, may 2012.

[18] † T. O. Wehling, *, ‡ K. S. Novoselov, § S. V. Morozov, § E. E. Vdovin, ‖ M. I. Katsnelson, , ‡ A. K. Geim, and A. I. Lichtenstein†. Molecular Doping of Graphene. *Nano Letter*, 2007.

[19] Feng Yan and Hao Tang. Application of thin-film transistors in label-free DNA biosensors. *Expert Review of Molecular Diagnostics*, 10(5):547–549, jul 2010.

[20] Mahmood Aliofkhazraei, Nasar Ali, W. I. (William I.) Milne, Cengiz S. Ozkan, Stanislaw Mitura, and Juana L. Gervasoni. *Graphene science handbook. Size-dependent properties*. CRC Press, 2016.

[21] Sadanand Pandey. Highly sensitive and selective chemiresistor gas/vapor sensors based on polyaniline nanocomposite: A comprehensive review. *Journal of Science: Advanced Materials and Devices*, 1(4):431–453, dec 2016.

[22] Jiri Janata and Mira Josowicz. Conducting polymers in electronic chemical sensors. *Nature Materials*, 2(1):19–24, jan 2003.

[23] Syeda Erfana Zohora, A M Khan, A K Srivastava, and Nisar Hundewale. Electronic Noses Application to Food Analysis Using Metal Oxide Sensors: A Review. Technical Report 3, 2013.

[24] Oomman K. Varghese, Dawei Gong, Maggie Paulose, Keat G. Ong, and Craig A. Grimes. Hydrogen sensing using titania nanotubes. *Sensors and Actuators B: Chemical*, 93(1-3):338–344, aug 2003.

[25] Abu Samah Zuruzi, Noel C. MacDonald, Martin Moskovits, and Andrei Kolmakov. Metal Oxide "Nanosponges" as Chemical Sensors: Highly Sensitive Detection of Hydrogen with Nanosponge Titania. *Angewandte Chemie International Edition*, 46(23):4298–4301, jun 2007.

[26] Norman F. Sheppard, Robert C. Tucker, and Christine. Wu. Electrical conductivity measurements using microfabricated interdigitated electrodes. *Analytical Chemistry*, 65(9):1199–1202, may 1993.

[27] R. M. White and F. W. Voltmer. Direct Piezoelectric Coupling to Surface Elastic Waves. *Applied Physics Letters*, 7(12):314–316, dec 1965.

[28] Laura O. Péres, Rosamaria W.C. Li, Elaine Y. Yamauchi, Renata Lippi, and Jonas Gruber. Conductive polymer gas sensor for quantitative detection of methanol in Brazilian sugar-cane spirit. *Food Chemistry*, 130(4):1105–1107, feb 2012.

[29] Ilaria Fratoddi, Iole Venditti, Cesare Cametti, and Maria Vittoria Russo. Chemiresistive polyaniline-based gas sensors: A mini review. *Sensors and Actuators B: Chemical*, 220:534–548, dec 2015.

[30] Marion E. Franke, Tobias J. Koplin, and Ulrich Simon. Metal and Metal Oxide Nanoparticles in Chemiresistors: Does the Nanoscale Matter? *Small*, 2(1):36–50, jan 2006.

[31] Kun-Wei Kao, Ming-Che Hsu, Yuh-Hwa Chang, Shangjr Gwo, and J Andrew Yeh. A sub-ppm acetone gas sensor for diabetes detection using 10 nm thick ultrathin InN FETs. *Sensors (Basel, Switzerland)*, 12(6):7157–68, 2012.

[32] Teng Xiao, Xiu-Yue Wang, Zhi-Hua Zhao, Liu Li, Lin Zhang, Hong-Chang Yao, Jian-She Wang, and Zhong-Jun Li. Highly sensitive and selective acetone sensor based on C-doped WO_3 for potential diagnosis of diabetes mellitus. *Sensors and Actuators B: Chemical*, 199:210–219, aug 2014.

[33] L. Wang, A. Teleki, S. E. Pratsinis, and P. I. Gouma. Ferroelectric WO_3 Nanoparticles for Acetone Selective Detection. *Chemistry of Materials*, 2008.

[34] Jing Bai and Baoxue Zhou. Titanium Dioxide Nanomaterials for Sensor Applications. *Chemical Reviews*, 114(19):10131–10176, oct 2014.

[35] A. Nasehzadeh, M. Mohseni, K. Azizi, and K. Azizi. The effect of temperature on the Lennard-Jones (6-12) pair potential function. *Journal of Molecular Structure: THEOCHEM*, 589-590:329–335, 2002.

[36] M Damyanova, E Balabanova, and U Hohm. Temperature-dependent interaction potential between NF_3 molecules and thermophysical properties of gaseous NF_3. *Journal of Physics: Conference Series*, 514:012055, 2014.

[37] Soumen Das and V. Jayaraman. SnO_2: A comprehensive review on structures and gas sensors. *Progress in Materials Science*, 66:112–255, oct 2014.

[38] Koichi Suematsu, Wataru Harano, Tokiharu Oyama, Yuka Shin, Ken Watanabe, and Kengo Shimanoe. Pulse-Driven Semiconductor Gas Sensors Toward ppt Level Toluene Detection. *Analytical Chemistry*, 90(19):11219–11223, oct 2018.

[39] Yu-Feng Sun, Shao-Bo Liu, Fan-Li Meng, Jin-Yun Liu, Zhen Jin, Ling-Tao Kong, and Jin-Huai Liu. Metal oxide nanostructures and their gas sensing properties: a review. *Sensors (Basel, Switzerland)*, 12(3):2610–31, 2012.

[40] V.V. Sysoev, T. Schneider, J. Goschnick, I. Kiselev, W. Habicht, H. Hahn, E. Strelcov, and A. Kolmakov. Percolating SnO_2 nanowire network as a stable gas sensor: Direct comparison of long-term performance versus SnO_2 nanoparticle films. *Sensors and Actuators B: Chemical*, 139(2):699–703, jun 2009.

[41] John F. Fennell, Sophie F. Liu, Joseph M. Azzarelli, Jonathan G. Weis, Sébastien Rochat, Katherine A. Mirica, Jens B. Ravnsbaek, and Timothy M. Swager. Nanowire Chemical/Biological Sensors: Status and a Roadmap for the Future. *Angewandte Chemie International Edition*, 55(4):1266–1281, jan 2016.

[42] Florinel-Gabriel. Banica. *Chemical sensors and biosensors : fundamentals and applications*. John Wiley & Sons Inc, 2012.

[43] Kourosh Kalantar-Zadeh. *Sensors: an introductory course*. Springer Science & Business Media, 2013.

[44] Hans-Peter Loock and Peter D. Wentzell. Detection limits of chemical sensors: Applications and misapplications. *Sensors and Actuators B: Chemical*, 173:157–163, oct 2012.

[45] Martin Püntener, Tamás Vigassy, Ellen Baier, Alan Ceresa, and Ernö Pretsch. Improving the lower detection limit of potentiometric sensors by covalently binding the ionophore to a polymer backbone. *Analytica Chimica Acta*, 503(2):187–194, feb 2004.

[46] Daniel C Harris. *Quantitative chemical analysis*. Macmillan, 2010.

[47] John R Vig and Fred L Walls. A review of sensor sensitivity and stability. In *Proceedings of the 2000 IEEE/EIA International Frequency Control Symposium and Exhibition (Cat. No. 00CH37052)*, pages 30–33. IEEE, 2000.

[48] Brian C. Sisk and Nathan S. Lewis. Comparison of analytical methods and calibration methods for correction of detector response drift in arrays of carbon black-polymer composite vapor detectors. *Sensors and Actuators B: Chemical*, 104(2):249–268, jan 2005.

[49] A.A. Saaman and P. Bergveld. A note on the use of the word 'reversible'. *Sensors and Actuators*, 7(1):69–71, mar 1985.

[50] Chen Shi, Huixian Ye, Hui Wang, Dimitris E. Ioannou, and Qiliang Li. Precise gas discrimination with cross-reactive graphene and metal oxide sensor arrays. *Applied Physics Letters*, 113(22):222102, nov 2018.

[51] Vladimir Dobrokhotov, Alexander Larin, Dewayne Sowell, Vladimir Dobrokhotov, Alexander Larin, and Dewayne Sowell. Vapor Trace Recognition Using a Single Nonspecific Chemiresistor. *Sensors*, 13(7):9016–9028, jul 2013.

[52] P.C. Jurs, G. A. Bakken, and H. E. McClelland. Computational Methods for the Analysis of Chemical Sensor Array Data from Volatile Analytes. *Chemical Reviews*, 100(7):2649–2678, 2000.

[53] B. Renganathan, D. Sastikumar, G. Gobi, N. Rajeswari Yogamalar, and A. Chandra Bose. Nanocrystalline ZnO coated fiber optic sensor for ammonia gas detection. *Optics & Laser Technology*, 43(8):1398–1404, nov 2011.

[54] F. Shao, J.D. Fan, F. Hernández-Ramírez, C. Fàbrega, T. Andreu, A. Cabot, J.D. Prades, N. López, F. Udrea, A. De Luca, S.Z. Ali, and J.R. Morante. NH3 sensing with self-assembled ZnO-nanowire μHP sensors in isothermal and temperature-pulsed mode. *Sensors and Actuators B: Chemical*, 226:110–117, 2016.

[55] Sen Liu, Bo Yu, Hao Zhang, Teng Fei, and Tong Zhang. Enhancing NO_2 gas sensing performances at room temperature based on reduced graphene oxide-ZnO nanoparticles hybrids. *Sensors and Actuators B: Chemical*, 202:272–278, oct 2014.

[56] Gaurav Singh, Anshul Choudhary, D. Haranath, Amish G. Joshi, Nahar Singh, Sukhvir Singh, and Renu Pasricha. ZnO decorated luminescent graphene as a potential gas sensor at room temperature. *Carbon*, 50(2):385–394, feb 2012.

[57] Huiling Tai, Zhen Yuan, Weijian Zheng, Zongbiao Ye, Chunhua Liu, and Xiaosong Du. ZnO Nanoparticles/Reduced Graphene Oxide Bilayer Thin Films for Improved NH_3-Sensing Performances at Room Temperature. *Nanoscale Research Letters*, 11(1):130, dec 2016.

[58] Guohua Hu, Tom Albrow-Owen, Xinxin Jin, Ayaz Ali, Yuwei Hu, Richard C T Howe, Khurram Shehzad, Zongyin Yang, Xuekun Zhu, Robert I Woodward, Tien-Chun Wu, Henri Jussila, Jiang-Bin Wu, Peng Peng, Ping-Heng Tan, Zhipei Sun, Edmund J R Kelleher, Meng Zhang, Yang Xu, and Tawfique Hasan. Black phosphorus ink formulation for inkjet printing of optoelectronics and photonics. *Nature Communications*, 8(1):278, 2017.

[59] Tien Chun Wu, Andrea De Luca, Qinyu Zhong, Xiaoxi Zhu, Osarenkhoe Ogbeide, Doo Seung Um, Guohua Hu, Tom Albrow-Owen, Florin Udrea, and Tawfique Hasan. Inkjet-printed CMOS-integrated graphene–metal oxide sensors for breath analysis. *npj 2D Materials and Applications*, 3(42), dec 2019.

[60] Andrea C. Ferrari, Francesco Bonaccorso, Vladimir Fal'ko, Konstantin S. Novoselov, Stephan Roche, Peter Bøggild, Stefano Borini, Frank H. L. Koppens, Vincenzo Palermo, Nicola Pugno, José A. Garrido, Roman Sordan, Alberto Bianco, Laura Ballerini, Maurizio Prato, Elefterios Lidorikis, Jani Kivioja, Claudio Marinelli, Tapani Ryhänen, Alberto Morpurgo, Jonathan N. Coleman, Valeria Nicolosi, Luigi Colombo, Albert Fert, Mar Garcia-Hernandez, Adrian Bachtold, Grégory F. Schneider, Francisco Guinea, Cees Dekker, Matteo Barbone, Zhipei Sun, Costas Galiotis, Alexander N. Grigorenko, Gerasimos Konstantatos, Andras Kis, Mikhail Katsnelson, Lieven

Vandersypen, Annick Loiseau, Vittorio Morandi, Daniel Neumaier, Emanuele Treossi, Vittorio Pellegrini, Marco Polini, Alessandro Tredicucci, Gareth M. Williams, Byung Hee Hong, Jong-Hyun Ahn, Jong Min Kim, Herbert Zirath, Bart J. van Wees, Herre van der Zant, Luigi Occhipinti, Andrea Di Matteo, Ian A. Kinloch, Thomas Seyller, Etienne Quesnel, Xinliang Feng, Ken Teo, Nalin Rupesinghe, Pertti Hakonen, Simon R. T. Neil, Quentin Tannock, Tomas Löfwander, and Jari Kinaret. Science and technology roadmap for graphene, related two-dimensional crystals, and hybrid systems. *Nanoscale*, 7(11):4598–4810, mar 2015.

[61] Surajit Some, Yang Xu, Youngmin Kim, Yeoheung Yoon, Hongyi Qin, Atul Kulkarni, Taesung Kim, and Hyoyoung Lee. Highly Sensitive and Selective Gas Sensor Using Hydrophilic and Hydrophobic Graphenes. *Scientific Reports*, 3(1):1868, dec 2013.

[62] Yufeng Hao, M. S. Bharathi, Lei Wang, Yuanyue Liu, Hua Chen, Shu Nie, Xiaohan Wang, Harry Chou, Cheng Tan, Babak Fallahazad, H. Ramanarayan, Carl W. Magnuson, Emanuel Tutuc, Boris I. Yakobson, Kevin F. McCarty, Yong-Wei Zhang, Philip Kim, James Hone, Luigi Colombo, and Rodney S. Ruoff. The Role of Surface Oxygen in the Growth of Large Single-Crystal Graphene on Copper. *Science*, 342(6159):720–723, nov 2013.

[63] Felice Torrisi, Tawfique Hasan, Weiping Wu, Zhipei Sun, Antonio Lombardo, Tero S. Kulmala, Gen-Wen Hsieh, Sungjune Jung, Francesco Bonaccorso, Philip J. Paul, Daping Chu, and Andrea C. Ferrari. Inkjet-Printed Graphene Electronics. *ACS Nano*, 6(4):2992–3006, apr 2012.

[64] F. Schedin, A. K. Geim, S. V. Morozov, E. W. Hill, P. Blake, M. I. Katsnelson, and K. S. Novoselov. Detection of individual gas molecules adsorbed on graphene. *Nature Materials*, 6(9):652–655, sep 2007.

[65] Yaping Dan, Ye Lu, Nicholas J. Kybert, Zhengtang Luo, and A. T. Charlie Johnson. Intrinsic Response of Graphene Vapor Sensors. *Nano Letters*, 9(4):1472–1475, apr 2009.

[66] Shun Mao, Ganhua Lu, Kehan Yu, Zheng Bo, and Junhong Chen. Specific Protein Detection Using Thermally Reduced Graphene Oxide Sheet Decorated with Gold Nanoparticle-Antibody Conjugates. *Advanced Materials*, 22(32):3521–3526, aug 2010.

[67] Xiao Huang, Xiaoying Qi, Freddy Boey, and Hua Zhang. Graphene-based composites. *Chem. Soc. Rev.*, 41(2):666–686, jan 2012.

[68] Vasilios Georgakilas. *Functionalization of graphene*. Wiley, 2014.

[69] Fengnian Xia, Han Wang, Di Xiao, Madan Dubey, and Ashwin Ramasubramaniam. Two-dimensional material nanophotonics. *Nature Photonics*, 8(12):899–907, dec 2014.

[70] M Donarelli, L Ottaviano, L Giancaterini, G Fioravanti, F Perrozzi, and C Cantalini. Exfoliated black phosphorus gas sensing properties at room temperature. *2D Materials*, 3(2):025002, mar 2016.

[71] Xiaogan Li, Xiaoxin Li, Zhi Li, Jing Wang, and Jianwei Zhang. WS_2 nanoflakes based selective ammonia sensors at room temperature. *Sensors and Actuators B: Chemical*, 240:273–277, mar 2017.

[72] Kangho Lee, Riley Gatensby, Niall McEvoy, Toby Hallam, and Georg S. Duesberg. High-Performance Sensors Based on Molybdenum Disulfide Thin Films. *Advanced Materials*, 25(46):6699–6702, dec 2013.

[73] Bilu Liu, Liang Chen, Gang Liu, Ahmad N. Abbas, Mohammad Fathi, and Chongwu Zhou. High-Performance Chemical Sensing Using Schottky-Contacted Chemical Vapor Deposition Grown Monolayer MoS_2 Transistors. *ACS Nano*, 8(5):5304–5314, may 2014.

[74] Gianluca Fiori, Francesco Bonaccorso, Giuseppe Iannaccone, Tomás Palacios, Daniel Neumaier, Alan Seabaugh, Sanjay K. Banerjee, and Luigi Colombo. Electronics based on two-dimensional materials. *Nature Nanotechnology*, 9(10):768–779, oct 2014.

[75] Tianru Wu, Honglie Shen, Lei Sun, Bin Cheng, Bin Liu, and Jiancang Shen. Nitrogen and boron doped monolayer graphene by chemical vapor deposition using polystyrene, urea and boric acid. *New Journal of Chemistry*, 36(6):1385, jun 2012.

[76] Xuesong Li, Weiwei Cai, Jinho An, Seyoung Kim, Junghyo Nah, Dongxing Yang, Richard Piner, Aruna Velamakanni, Inhwa Jung, Emanuel Tutuc, Sanjay K Banerjee, Luigi Colombo, and Rodney S Ruoff. Large-area synthesis of high-quality and uniform graphene films on copper foils. *Science (New York, N.Y.)*, 324(5932):1312–4, jun 2009.

[77] Stephan Hofmann, Philipp Braeuninger-Weimer, and Robert S. Weatherup. CVD-Enabled Graphene Manufacture and Technology. *The Journal of Physical Chemistry Letters*, 6(14):2714–2721, jul 2015.

[78] Zhike Liu, Jinhua Li, and Feng Yan. Package-Free Flexible Organic Solar Cells with Graphene top Electrodes. *Advanced Materials*, 25(31):4296–4301, aug 2013.

[79] V. Nicolosi, M. Chhowalla, M. G. Kanatzidis, M. S. Strano, and J. N. Coleman. Liquid Exfoliation of Layered Materials. *Science*, 340(6139):1226419–1226419, jun 2013.

[80] Keith R. Paton, Eswaraiah Varrla, Claudia Backes, Ronan J. Smith, Umar Khan, Arlene O'Neill, Conor Boland, Mustafa Lotya, Oana M. Istrate, Paul King, Tom Higgins, Sebastian Barwich, Peter May, Pawel Puczkarski, Iftikhar Ahmed, Matthias Moebius, Henrik Pettersson, Edmund Long, João Coelho, Sean E. O'Brien, Eva K. McGuire, Beatriz Mendoza Sanchez, Georg S. Duesberg, Niall McEvoy, Timothy J. Pennycook, Clive Downing, Alison Crossley, Valeria Nicolosi, and Jonathan N. Coleman. Scalable production of large quantities of defect-free few-layer graphene by shear exfoliation in liquids. *Nature Materials*, 13(6):624–630, jun 2014.

[81] J. N. Coleman, M. Lotya, A. O'Neill, S. D. Bergin, P. J. King, U. Khan, K. Young, A. Gaucher, S. De, R. J. Smith, I. V. Shvets, S. K. Arora, G. Stanton, H.-Y. Kim, K. Lee, G. T. Kim, G. S. Duesberg, T. Hallam, J. J. Boland, J. J. Wang, J. F. Donegan, J. C. Grunlan, G. Moriarty, A. Shmeliov, R. J. Nicholls, J. M. Perkins, E. M.

Grieveson, K. Theuwissen, D. W. McComb, P. D. Nellist, and V. Nicolosi. Two-Dimensional Nanosheets Produced by Liquid Exfoliation of Layered Materials. *Science*, 331(6017):568–571, feb 2011.

[82] Yongchao Si and Edward T. Samulski. Synthesis of Water Soluble Graphene. *Nano Letters*, 8(6):1679–1682, jun 2008.

[83] Dan Li, Marc B. Müller, Scott Gilje, Richard B. Kaner, and Gordon G. Wallace. Processable aqueous dispersions of graphene nanosheets. *Nature Nanotechnology*, 3(2):101–105, feb 2008.

[84] Shun Mao, Kehan Yu, Ganhua Lu, and Junhong Chen. Highly sensitive protein sensor based on thermally-reduced graphene oxide field-effect transistor. *Nano Research*, 4(10):921–930, oct 2011.

[85] Yong-Hui Zhang, Ya-Bin Chen, Kai-Ge Zhou, Cai-Hong Liu, Jing Zeng, Hao-Li Zhang, and Yong Peng. Improving gas sensing properties of graphene by introducing dopants and defects: a first-principles study. *Nanotechnology*, 20(18):185504, may 2009.

[86] Rajat Kanti Paul, Sushmee Badhulika, Nuvia M. Saucedo, and Ashok Mulchandani. Graphene Nanomesh As Highly Sensitive Chemiresistor Gas Sensor. *Analytical Chemistry*, 84(19):8171–8178, oct 2012.

[87] Vineet Dua, Sumedh P. Surwade, Srikanth Ammu, Srikanth Rao Agnihotra, Sujit Jain, Kyle E. Roberts, Sungjin Park, Rodney S. Ruoff, and Sanjeev K. Manohar. All-Organic Vapor Sensor Using Inkjet-Printed Reduced Graphene Oxide. *Angewandte Chemie International Edition*, 49(12):2154–2157, mar 2010.

[88] Ganhua Lu, Kehan Yu, Leonidas E. Ocola, and Junhong Chen. Ultrafast room temperature NH_3 sensing with positively gated reduced graphene oxide field-effect transistors. *Chemical Communications*, 47(27):7761, jun 2011.

[89] Kehan Yu, Pengxiang Wang, Ganhua Lu, Ke-Hung Chen, Zheng Bo, and Junhong Chen. Patterning Vertically Oriented Graphene Sheets for Nanodevice Applications. *The Journal of Physical Chemistry Letters*, 2(6):537–542, mar 2011.

[90] Eric C. Nallon, Vincent P. Schnee, Collin Bright, Michael P. Polcha, and Qiliang Li. Chemical Discrimination with an Unmodified Graphene Chemical Sensor. *ACS Sensors*, 1(1):26–31, jan 2016.

[91] Stefano Borini, Richard White, Di Wei, Michael Astley, Samiul Haque, Elisabetta Spigone, Nadine Harris, Jani Kivioja, and Tapani Ryhänen. Ultrafast Graphene Oxide Humidity Sensors. *ACS Nano*, 7(12):11166–11173, dec 2013.

[92] Yao Yao, Xiangdong Chen, Jinfeng Zhu, Baoqing Zeng, Zuquan Wu, and Xiaoyu Li. The effect of ambient humidity on the electrical properties of graphene oxide films. *Nanoscale Research Letters*, 7(1):363, jul 2012.

[93] S. Santra, G. Hu, R. C. T. Howe, A. De Luca, S. Z. Ali, F. Udrea, J. W. Gardner, S. K. Ray, P. K. Guha, and T. Hasan. CMOS integration of inkjet-printed graphene for humidity sensing. *Scientific Reports*, 5(1):17374, dec 2015.

[94] Nantikan Tammanoon, Anurat Wisitsoraat, Chakrit Sriprachuabwong, Ditsayut Phokharatkul, Adisorn Tuantranont, Sukon Phanichphant, and Chaikarn Liewhiran. Ultrasensitive NO_2 Sensor Based on Ohmic Metal–Semiconductor Interfaces of Electrolytically Exfoliated Graphene/Flame-Spray-Made SnO_2 Nanoparticles Composite Operating at Low Temperatures. *ACS Applied Materials & Interfaces*, 7(43):24338–24352, nov 2015.

[95] Jun Zhang, Xianghong Liu, Giovanni Neri, and Nicola Pinna. Nanostructured Materials for Room-Temperature Gas Sensors. *Advanced Materials*, 28(5):795–831, feb 2016.

[96] Suzi Deng, Verawati Tjoa, Hai Ming Fan, Hui Ru Tan, Dean C. Sayle, Malini Olivo, Subodh Mhaisalkar, Jun Wei, and Chorng Haur Sow. Reduced Graphene Oxide Conjugated Cu_2O Nanowire Mesocrystals for High-Performance NO_2 Gas Sensor. *Journal of the American Chemical Society*, 134(10):4905–4917, mar 2012.

[97] Chengxiang Wang, Longwei Yin, Luyuan Zhang, Dong Xiang, and Rui Gao. Metal Oxide Gas Sensors: Sensitivity and Influencing Factors. *Sensors*, 10(3):2088–2106, mar 2010.

[98] Charles T. Campbell and Joachim Sauer. Introduction: Surface Chemistry of Oxides. *Chemical Reviews*, 113(6):3859–3862, jun 2013.

[99] Gianfranco Pacchioni and Hajo Freund. Electron Transfer at Oxide Surfaces. The MgO Paradigm: from Defects to Ultrathin Films. *Chemical Reviews*, 113(6):4035–4072, jun 2013.

[100] Helmut Kuhlenbeck, Shamil Shaikhutdinov, and Hans-Joachim Freund. Well-Ordered Transition Metal Oxide Layers in Model Catalysis – A Series of Case Studies. *Chemical Reviews*, 113(6):3986–4034, jun 2013.

[101] J Mannhart and D G Schlom. Oxide interfaces–an opportunity for electronics. *Science (New York, N.Y.)*, 327(5973):1607–11, mar 2010.

[102] M. G. Helander, Z. B. Wang, J. Qiu, and Z. H. Lu. Band alignment at metal/organic and metal/oxide/organic interfaces. *Applied Physics Letters*, 93(19):193310, nov 2008.

[103] H. Y. Hwang, Y. Iwasa, M. Kawasaki, B. Keimer, N. Nagaosa, and Y. Tokura. Emergent phenomena at oxide interfaces. *Nature Materials*, 11(2):103–113, feb 2012.

[104] A. Fioravanti, S. Morandi, and M.C. Carotta. Chemoresistive Gas Sensors for Sub-ppm Acetone Detection. *Procedia Engineering*, 168:485–488, jan 2016.

[105] F.I. Shaikh, L.P. Chikhale, J.Y. Patil, I.S. Mulla, and S.S. Suryavanshi. Enhanced acetone sensing performance of nanostructured Sm_2O_3 doped SnO_2 thick films. *Journal of Rare Earths*, 35(8):813–823, aug 2017.

[106] Shirshendu Chakraborty, Dibyajyoti Banerjee, Indrani Ray, and Amarnath Sen. Detection of biomarker in breath: A step towards noninvasive diabetes monitoring, 2008.

[107] Alberto Vomiero, Sebastiano Bianchi, Elisabetta Comini, Guido Faglia, Matteo Ferroni, and Giorgio Sberveglieri. Controlled Growth and Sensing Properties of In_2O_3 Nanowires. *Crystal Growth & Design*, 7(12):2500–2504, dec 2007.

[108] Nitul Kakati, Seung Hyun Jee, Su Hyun Kim, Jun Young Oh, and Young Soo Yoon. Thickness dependency of sol-gel derived ZnO thin films on gas sensing behaviors. *Thin Solid Films*, 519(1):494–498, oct 2010.

[109] P.A. Murade, V.S. Sangawar, G.N. Chaudhari, V.D. Kapse, and A.U. Bajpeyee. Acetone gas-sensing performance of Sr-doped nanostructured $LaFeO_3$ semiconductor prepared by citrate sol–gel route. *Current Applied Physics*, 11(3):451–456, may 2011.

[110] A. Teleki, S.E. Pratsinis, K. Kalyanasundaram, and P.I. Gouma. Sensing of organic vapors by flame-made TiO_2 nanoparticles. *Sensors and Actuators B: Chemical*, 119(2):683–690, dec 2006.

[111] Marco Righettoni, Antonio Tricoli, and Sotiris E. Pratsinis. Si:WO_3 Sensors for Highly Selective Detection of Acetone for Easy Diagnosis of Diabetes by Breath Analysis. *Analytical Chemistry*, 82(9):3581–3587, may 2010.

[112] Wei Li, Zhilin Feng, Enwen Dai, Jie Xu, and Gang Bai. Organic Vapour Sensing Properties of Area-Ordered and Size-Controlled Silicon Nanopillar. *Sensors (Basel, Switzerland)*, 16(11), nov 2016.

[113] Yu-Sheng Lin, Kung-Hsuan Lin, Yu-Ming Chang, and J. Andrew Yeh. Epitaxy of m-plane GaN on nanoscale patterned c-plane sapphire substrates. *Surface Science*, 606(1-2):L1–L4, jan 2012.

[114] Sunyong Hwang, Hyunah Kwon, Sameer Chhajed, Ji Won Byon, Jeong Min Baik, Jiseong Im, Sang Ho Oh, Ho Won Jang, Seok Jin Yoon, and Jong Kyu Kim. A near single crystalline TiO_2 nanohelix array: enhanced gas sensing performance and its application as a monolithically integrated electronic nose. *The Analyst*, 138(2):443–450, dec 2013.

[115] Avner Rothschild and Yigal Komem. The effect of grain size on the sensitivity of nanocrystalline metal-oxide gas sensors. *Journal of Applied Physics*, 95(11):6374–6380, jun 2004.

[116] Zain Ul Abideen, Akash Katoch, Jae-Hun Kim, Yong Jung Kwon, Hyoun Woo Kim, and Sang Sub Kim. Excellent gas detection of ZnO nanofibers by loading with reduced graphene oxide nanosheets. *Sensors and Actuators B: Chemical*, 221:1499–1507, dec 2015.

[117] Qianqian Lin, Yang Li, and Mujie Yang. Tin oxide/graphene composite fabricated via a hydrothermal method for gas sensors working at room temperature. *Sensors and Actuators B: Chemical*, 173:139–147, oct 2012.

[118] Y. Kajikawa. Effects of grain-boundary potential barrier height and its fluctuation on conductivity of polycrystalline semiconductors in the ionized-impurity-scattering dominated case. *Journal of Applied Physics*, 114(4):043719, jul 2013.

[119] Min-Hyun Seo, Masayoshi Yuasa, Tetsuya Kida, Jeung-Soo Huh, Noboru Yamazoe, and Kengo Shimanoe. Microstructure control of TiO_2 nanotubular films for improved VOC sensing. *Sensors and Actuators B: Chemical*, 154(2):251–256, jun 2011.

[120] Matt Law, Hannes Kind, Benjamin Messer, Franklin Kim, and Peidong Yang. Photochemical Sensing of NO_2 with SnO_2 Nanoribbon Nanosensors at Room Temperature. *Angewandte Chemie International Edition*, 41(13):2405, jul 2002.

[121] Nguyen Duc Hoa and Sherif A. El-Safty. Synthesis of Mesoporous NiO Nanosheets for the Detection of Toxic NO_2 Gas. *Chemistry - A European Journal*, 17(46):12896–12901, nov 2011.

[122] Mei Chen, Zhihua Wang, Dongmei Han, Fubo Gu, and Guangsheng Guo. Porous ZnO Polygonal Nanoflakes: Synthesis, Use in High-Sensitivity NO_2 Gas Sensor, and Proposed Mechanism of Gas Sensing. *The Journal of Physical Chemistry C*, 115(26):12763–12773, jul 2011.

[123] Qiuxia Feng, Xiaogan Li, Jing Wang, and Alexander M. Gaskov. Reduced graphene oxide (rGO) encapsulated Co_3O_4 composite nanofibers for highly selective ammonia sensors. *Sensors and Actuators B: Chemical*, 222:864–870, jan 2016.

[124] Xiaogan Li, Ning Chen, Shiwei Lin, Jing Wang, and Jianwei Zhang. NiO-wrapped mesoporous TiO_2 microspheres based selective ammonia sensor at room temperature. *Sensors and Actuators B: Chemical*, 209:729–734, mar 2015.

[125] Nicolae Barsan and Udo Weimar. Conduction Model of Metal Oxide Gas Sensors. *Journal of Electroceramics*, 7(3):143–167, 2001.

[126] M. Gardon and J. M. Guilemany. A review on fabrication, sensing mechanisms and performance of metal oxide gas sensors. *Journal of Materials Science: Materials in Electronics*, 24(5):1410–1421, may 2013.

[127] Ying Yang, Chungui Tian, Jingchao Wang, Li Sun, Keying Shi, Wei Zhou, and Honggang Fu. Facile synthesis of novel 3D nanoflower-like Cu_xO/multilayer graphene composites for room temperature NO_x gas sensor application. *Nanoscale*, 6(13):7369, jun 2014.

[128] Fubo Gu, Rui Nie, Dongmei Han, and Zhihua Wang. In_2O_3–graphene nanocomposite based gas sensor for selective detection of NO_2 at room temperature. *Sensors and Actuators B: Chemical*, 219:94–99, nov 2015.

[129] Ying-Li Dong, Xian-Fa Zhang, Xiao-Li Cheng, Ying-Ming Xu, Shan Gao, Hui Zhao, and Li-Hua Huo. Highly selective NO_2 sensor at room temperature based on nanocomposites of hierarchical nanosphere-like α-Fe_2O_3 and reduced graphene oxide. *RSC Advances*, 4:57493–57500, 2014.

[130] Hao Zhang, Jianchao Feng, Teng Fei, Sen Liu, and Tong Zhang. SnO_2 nanoparticles-reduced graphene oxide nanocomposites for NO_2 sensing at low operating temperature. *Sensors and Actuators B: Chemical*, 190:472–478, jan 2014.

[131] Xiaoqiang An, Jimmy C. Yu, Yu Wang, Yongming Hu, Xuelian Yu, and Guangjin Zhang. WO_3 nanorods/graphene nanocomposites for high-efficiency visible-light-driven photocatalysis and NO_2 gas sensing. *Journal of Materials Chemistry*, 22(17):8525, apr 2012.

[132] Huiling Tai, Zhen Yuan, Weijian Zheng, Zongbiao Ye, Chunhua Liu, and Xiaosong Du. ZnO Nanoparticles/Reduced Graphene Oxide Bilayer Thin Films for Improved NH_3-Sensing Performances at Room Temperature. *Nanoscale Research Letters*, 11(1):130, dec 2016.

[133] F. Perrozzi, S.M. Emamjomeh, V. Paolucci, G. Taglieri, L. Ottaviano, and C. Cantalini. Thermal stability of WS_2 flakes and gas sensing properties of WS_2/WO_3 composite to H_2, NH_3 and NO_2. *Sensors and Actuators B: Chemical*, 243:812–822, may 2017.

[134] Sridhar Komarneni. Nanophase materials by hydrothermal, microwave-hydrothermal and microwave-solvothermal methods, 2003.

[135] Mujeeb Khan, Muhammad Nawaz Tahir, Syed Farooq Adil, Hadayat Ullah Khan, M. Rafiq H. Siddiqui, Abdulrahman A. Al-warthan, and Wolfgang Tremel. Graphene based metal and metal oxide nanocomposites: synthesis, properties and their applications. *Journal of Materials Chemistry A*, 3(37):18753–18808, sep 2015.

[136] Yong Zhou, Qiaoliang Bao, Lena Ai Ling Tang, Yulin Zhong, and Kian Ping Loh. Hydrothermal Dehydration for the "Green" Reduction of Exfoliated Graphene Oxide to Graphene and Demonstration of Tunable Optical Limiting Properties. *Chemistry of Materials*, 21(13):2950–2956, jul 2009.

[137] Zanyong Zhuang, Jing Zhang, Feng Huang, Yonghao Wang, and Zhang Lin. Pure multistep oriented attachment growth kinetics of surfactant-free SnO_2 nanocrystals. *Physical Chemistry Chemical Physics*, 11(38):8516, sep 2009.

[138] Qing Li, Nasir Mahmood, Jinghan Zhu, Yanglong Hou, and Shouheng Sun. Graphene and its composites with nanoparticles for electrochemical energy applications. *Nano Today*, 9(5):668–683, oct 2014.

[139] Tao Li, Jonas Rahlf Hauptmann, Zhongming Wei, Søren Petersen, Nicolas Bovet, Tom Vosch, Jesper Nygård, Wenping Hu, Yunqi Liu, Thomas Bjørnholm, Kasper Nørgaard, and Bo W. Laursen. Solution-Processed Ultrathin Chemically Derived Graphene Films as Soft Top Contacts for Solid-State Molecular Electronic Junctions. *Advanced Materials*, 24(10):1333–1339, mar 2012.

[140] Jianfeng Shen, Min Shi, Bo Yan, Hongwei Ma, Na Li, and Mingxin Ye. Ionic liquid-assisted one-step hydrothermal synthesis of TiO_2-reduced graphene oxide composites. *Nano Research*, 4(8):795–806, aug 2011.

[141] Le Thuy Hoa, Huynh Ngoc Tien, Van Hoang Luan, Jin Suk Chung, and Seung Hyun Hur. Fabrication of a novel 2D-graphene/2D-NiO nanosheet-based hybrid nanostructure and its use in highly sensitive NO_2 sensors. *Sensors and Actuators B: Chemical*, 185:701–705, aug 2013.

[142] Lingmin Yu, Fen Guo, Sheng Liu, Bing Yang, Yanxing Jiang, Lijun Qi, and Xinhui Fan. Both oxygen vacancies defects and porosity facilitated NO2 gas sensing response in 2D ZnO nanowalls at room temperature. *Journal of Alloys and Compounds*, 682:352–356, oct 2016.

[143] Michael J. McAllister, Je-Luen Li, Douglas H. Adamson, Hannes C. Schniepp, Ahmed A. Abdala, Jun Liu, Margarita Herrera-Alonso, David L. Milius, Roberto Car, Robert K. Prud'homme, and Ilhan A. Aksay. Single Sheet Functionalized Graphene by Oxidation and Thermal Expansion of Graphite. *Chemistry of Materials*, 19(18):4396–4404, sep 2007.

[144] Konstantin N. Kudin, Bulent Ozbas, Hannes C. Schniepp, Robert K. Prud'homme, Ilhan A. Aksay, and Roberto Car. Raman Spectra of Graphite Oxide and Functionalized Graphene Sheets. *Nano Letters*, 8(1):36–41, jan 2008.

[145] Ziqi Sun, Ting Liao, Yuhai Dou, Soo Min Hwang, Min-Sik Park, Lei Jiang, Jung Ho Kim, and Shi Xue Dou. Generalized self-assembly of scalable two-dimensional transition metal oxide nanosheets. *Nature Communications*, 5(1):3813, sep 2014.

[146] Xu Xiao, Huaibing Song, Shizhe Lin, Ying Zhou, Xiaojun Zhan, Zhimi Hu, Qi Zhang, Jiyu Sun, Bo Yang, Tianqi Li, Liying Jiao, Jun Zhou, Jiang Tang, and Yury Gogotsi. Scalable salt-templated synthesis of two-dimensional transition metal oxides. *Nature Communications*, 7(1):11296, sep 2016.

[147] Edward J. W. Crossland, Nakita Noel, Varun Sivaram, Tomas Leijtens, Jack A. Alexander-Webber, and Henry J. Snaith. Mesoporous TiO_2 single crystals delivering enhanced mobility and optoelectronic device performance. *Nature*, 495(7440):215–219, mar 2013.

[148] Gugang Chen, Tereza M. Paronyan, and Avetik R. Harutyunyan. Sub-ppt gas detection with pristine graphene. *Applied Physics Letters*, 101(5):053119, jul 2012.

[149] Nantao Hu, Zhi Yang, Yanyan Wang, Liling Zhang, Ying Wang, Xiaolu Huang, Hao Wei, Liangmin Wei, and Yafei Zhang. Ultrafast and sensitive room temperature NH_3 gas sensors based on chemically reduced graphene oxide. *Nanotechnology*, 25(2):025502, jan 2014.

[150] Ji-yan Leng, Xiu-juan Xu, Ning Lv, Hui-tao Fan, and Tong Zhang. Synthesis and gas-sensing characteristics of WO_3 nanofibers via electrospinning. *Journal of Colloid and Interface Science*, 356(1):54–57, apr 2011.

[151] Chandra Sekhar Rout, Manu Hegde, A Govindaraj, and C N R Rao. Ammonia sensors based on metal oxide nanostructures. *Nanotechnology*, 18(20):205504, may 2007.

[152] Jiao Zhou, Muhammad Ikram, Afrasiab Ur Rehman, Jing Wang, Yiming Zhao, Kan Kan, Weijun Zhang, Fazal Raziq, Li Li, and Keying Shi. Highly selective detection of NH_3 and H_2S using the pristine CuO and mesoporous In_2O_3@CuO multijunctions nanofibers at room temperature. *Sensors and Actuators B: Chemical*, 255:1819–1830, feb 2018.

[153] Ching-Feng Li, Chia-Yen Hsu, and Yuan-Yao Li. NH_3 sensing properties of ZnO thin films prepared via sol–gel method. *Journal of Alloys and Compounds*, 606:27–31, sep 2014.

[154] P. Dhivya, Arun K. Prasad, and M. Sridharan. Nanostructured TiO_2 films: Enhanced NH_3 detection at room temperature. *Ceramics International*, 40(1):409–415, jan 2014.

[155] Dongzhi Zhang, Chuanxing Jiang, and Yan'e Sun. Room-temperature high-performance ammonia gas sensor based on layer-by-layer self-assembled molybdenum disulfide/zinc oxide nanocomposite film. *Journal of Alloys and Compounds*, 698:476–483, mar 2017.

[156] Dongzhi Zhang, Chuanxing Jiang, Peng Li, and Yan'e Sun. Layer-by-Layer Self-assembly of Co_3O_4 Nanorod-Decorated MoS_2 Nanosheet-Based Nanocomposite toward High-Performance Ammonia Detection. *ACS Applied Materials & Interfaces*, 9(7):6462–6471, feb 2017.

[157] Keng Xu, Neng Li, Dawen Zeng, Shouqin Tian, Shasha Zhang, Die Hu, and Changsheng Xie. Interface Bonds Determined Gas-Sensing of SnO_2 –SnS_2 Hybrids to Ammonia at Room Temperature. *ACS Applied Materials & Interfaces*, 7(21):11359–11368, jun 2015.

[158] Ming-Shui Yao, Xiao-Jing Lv, Zhi-Hua Fu, Wen-Hua Li, Wei-Hua Deng, Guo-Dong Wu, and Gang Xu. Layer-by-Layer Assembled Conductive Metal-Organic Framework Nanofilms for Room-Temperature Chemiresistive Sensing. *Angewandte Chemie International Edition*, 56(52):16510–16514, dec 2017.

[159] Michael G. Campbell, Dennis Sheberla, Sophie F. Liu, Timothy M. Swager, and Mircea Dincă. Cu_3 (hexaiminotriphenylene)$_2$: An Electrically Conductive 2D Metal-Organic Framework for Chemiresistive Sensing. *Angewandte Chemie International Edition*, 54(14):4349–4352, mar 2015.

[160] Merry K. Smith, Kennedy E. Jensen, Polina A. Pivak, and Katherine A. Mirica. Direct Self-Assembly of Conductive Nanorods of Metal–Organic Frameworks into Chemiresistive Devices on Shrinkable Polymer Films. *Chemistry of Materials*, 28(15):5264–5268, aug 2016.

[161] Douglas C. Meier, Steve Semancik, Bradley Button, Evgheni Strelcov, and Andrei Kolmakov. Coupling nanowire chemiresistors with MEMS microhotplate gas sensing platforms. *Applied Physics Letters*, 91(6):063118, aug 2007.

[162] Bappaditya Chatterjee and Amitava Bandyopadhyay. Development of Zinc Oxide Sensors for Detecting Ammonia Gas in the Ambient Air: A Critical Short Review. *Environmental Quality Management*, 26(1):89–105, dec 2016.

[163] Vardan Galstyan, Elisabetta Comini, Iskandar Kholmanov, Guido Faglia, and Giorgio Sberveglieri. Reduced graphene oxide/ZnO nanocomposite for application in chemical gas sensors. *RSC Advances*, 6(41):34225–34232, apr 2016.

[164] Shumao Cui, Zhenhai Wen, Eric C. Mattson, Shun Mao, Jingbo Chang, Michael Weinert, Carol J. Hirschmugl, Marija Gajdardziska-Josifovska, and Junhong Chen. Indium-doped SnO_2 nanoparticle–graphene nanohybrids: simple one-pot synthesis and their selective detection of NO_2. *Journal of Materials Chemistry A*, 1(14):4462, mar 2013.

[165] Jae-Hyoung Lee, Akash Katoch, Sun-Woo Choi, Jae-Hun Kim, Hyoun Woo Kim, and Sang Sub Kim. Extraordinary Improvement of Gas-Sensing Performances in SnO_2 Nanofibers. *ACS Applied Materials & Interfaces*, 7(5):3101–3109, feb 2015.

[166] Giovanni Neri, Salvatore Gianluca Leonardi, Mariangela Latino, Nicola Donato, Seunghwan Baek, Donato E. Conte, Patrícia A. Russo, and Nicola Pinna. Sensing behavior of SnO_2/reduced graphene oxide nanocomposites toward NO_2. *Sensors and Actuators B: Chemical*, 179:61–68, mar 2013.

[167] D. H. Wang, Y. Hu, J. J. Zhao, L. L. Zeng, X. M. Tao, and W. Chen. Holey reduced graphene oxide nanosheets for high performance room temperature gas sensing. *J. Mater. Chem. A*, 2(41):17415–17420, aug 2014.

[168] N. Barsan, D. Koziej, and U. Weimar. Metal oxide-based gas sensor research: How to? *Sensors and Actuators B: Chemical*, 121(1):18–35, jan 2007.

[169] Wei Yang, Peng Wan, Xiaodong Zhou, Jiming Hu, Yafeng Guan, and Liang Feng. Additive-Free Synthesis of In_2O_3 Cubes Embedded into Graphene Sheets and Their Enhanced NO ₂ Sensing Performance at Room Temperature. *ACS Applied Materials & Interfaces*, 6(23):21093–21100, dec 2014.

[170] Ganhua Lu, Sungjin Park, Kehan Yu, Rodney S. Ruoff, Leonidas E. Ocola, Daniel Rosenmann, and Junhong Chen. Toward Practical Gas Sensing with Highly Reduced Graphene Oxide: A New Signal Processing Method To Circumvent Run-to-Run and Device-to-Device Variations. *ACS Nano*, 5(2):1154–1164, feb 2011.

[171] Qingwu Huang, Dawen Zeng, Huayao Li, and Changsheng Xie. Room temperature formaldehyde sensors with enhanced performance, fast response and recovery based on zinc oxide quantum dots/graphene nanocomposites. *Nanoscale*, 4(18):5651, aug 2012.

[172] A. De Luca, S. Santra, R. Ghosh, S. Z. Ali, J. W. Gardner, P. K. Guha, and F. Udrea. Temperature-modulated graphene oxide resistive humidity sensor for indoor air quality monitoring. *Nanoscale*, 8(8):4565–4572, feb 2016.

[173] Phillip H. Rogers, Kurt D. Benkstein, and Steve Semancik. Machine Learning Applied to Chemical Analysis: Sensing Multiple Biomarkers in Simulated Breath Using a Temperature-Pulsed Electronic-Nose. *Analytical Chemistry*, 84(22):9774–9781, nov 2012.

[174] Faramarz Hossein-Babaei and Amir Amini. A breakthrough in gas diagnosis with a temperature-modulated generic metal oxide gas sensor. *Sensors and Actuators B: Chemical*, 166-167:419–425, may 2012.

[175] Jiang-Bin Wu, Miao-Ling Lin, Xin Cong, He-Nan Liu, and Ping-Heng Tan. Raman spectroscopy of graphene-based materials and its applications in related devices. *Chemical Society Reviews*, 47(5):1822–1873, mar 2018.

[176] Andrea C. Ferrari and Denis M. Basko. Raman spectroscopy as a versatile tool for studying the properties of graphene. *Nature Nanotechnology*, 8(4):235–246, apr 2013.

[177] Peter Vandenabeele. *Practical Raman Spectroscopy - An Introduction*. John Wiley & Sons, Ltd, Chichester, UK, jul 2013.

[178] R. Saito, M. Hofmann, G. Dresselhaus, A. Jorio, and M. S. Dresselhaus. Raman spectroscopy of graphene and carbon nanotubes. *Advances in Physics*, 60(3):413–550, jun 2011.

[179] Yenny Hernandez, Valeria Nicolosi, Mustafa Lotya, Fiona M. Blighe, Zhenyu Sun, Sukanta De, I. T. McGovern, Brendan Holland, Michele Byrne, Yurii K. Gun'Ko, John J. Boland, Peter Niraj, Georg Duesberg, Satheesh Krishnamurthy, Robbie Goodhue, John Hutchison, Vittorio Scardaci, Andrea C. Ferrari, and Jonathan N. Coleman. High-yield production of graphene by liquid-phase exfoliation of graphite. *Nature Nanotechnology*, 3(9):563–568, sep 2008.

[180] Yang Leng. *Materials characterization : introduction to microscopic and spectroscopic methods*. Wiley-VCH Verlag GmbH & Co. KGaA, Weinheim, Germany, sep 2013.

[181] Guohua Hu, Lisong Yang, Zongyin Yang, Yubo Wang, Xinxin Jin, Jie Dai, Qing Wu, Shouhu Liu, Xiaoxi Zhu, Xiaoshan Wang, Tien-Chun Wu, Richard Howe, Tom Albrow-Owen, Leonard Ng, Qing Yang, Luigi Occhipinti, Robert Woodward, Edmund Kelleher, Zhipei Sun, Xiao Huang, Meng Zhang, Colin Bain, and Tawfique Hasan. A general ink formulation of 2d crystals for wafer-scale inkjet printing. *Nature*, 2019.

[182] Leonard W. T. Ng, Guohua Hu, Richard C. T. Howe, Xiaoxi Zhu, Zongyin Yang, Christopher G. Jones, and Tawfique Hasan. 2D Material Production Methods. In *Printing of Graphene and Related 2D Materials*, chapter 3, pages 53–101. Springer International Publishing, Cham, 2019.

[183] Helmut Kipphan. Print Media and Electronic Media. In *Handbook of Print Media*, pages 1005–1026. Springer Berlin Heidelberg, Berlin, Heidelberg, 2001.

[184] R. H. Leach. *The printing ink manual.* Blueprint, 1993.

[185] Woo Jin Hyun, Ethan B. Secor, Mark C. Hersam, C. Daniel Frisbie, and Lorraine F. Francis. High-Resolution Patterning of Graphene by Screen Printing with a Silicon Stencil for Highly Flexible Printed Electronics. *Advanced Materials*, 27(1):109–115, jan 2015.

[186] Guohua Hu, Joohoon Kang, Leonard W T Ng, Xiaoxi Zhu, Richard C T Howe, Christopher G Jones, Mark C Hersam, and Tawfique Hasan. Functional inks and printing of two-dimensional materials. *Chem. Soc. Rev.*, 47(9):3265–3300, 2018.

[187] Madhusudan Singh, Hanna M. Haverinen, Parul Dhagat, and Ghassan E. Jabbour. Inkjet Printing-Process and Its Applications. *Advanced Materials*, 22(6):673–685, feb 2010.

[188] Koji Abe, Koji Suzuki, and Daniel Citterio. Inkjet-Printed Microfluidic Multianalyte Chemical Sensing Paper. *Analytical Chemistry*, 80(18):6928–6934, sep 2008.

[189] Frederik C. Krebs. Fabrication and processing of polymer solar cells: A review of printing and coating techniques. *Solar Energy Materials and Solar Cells*, 93(4):394–412, apr 2009.

[190] Robert D. Deegan, Olgica Bakajin, Todd F. Dupont, Greb Huber, Sidney R. Nagel, and Thomas A. Witten. Capillary flow as the cause of ring stains from dried liquid drops. *Nature*, 389(6653):827–829, oct 1997.

[191] Jonathan N Coleman. Liquid Exfoliation of Defect-Free Graphene. *Accounts of Chemical Research*, 46(1):14–22, jan 2013.

[192] Jacob N. Israelachvili. *Intermolecular and surface forces*. Academic Press, 2011.

[193] Francesco Bonaccorso, Antonio Lombardo, Tawfique Hasan, Zhipei Sun, Luigi Colombo, and Andrea C. Ferrari. Production and processing of graphene and 2d crystals. *Materials Today*, 15(12):564–589, dec 2012.

[194] Umar Khan, Arlene O'Neill, Harshit Porwal, Peter May, Khalid Nawaz, and Jonathan N. Coleman. Size selection of dispersed, exfoliated graphene flakes by controlled centrifugation. *Carbon*, 50(2):470–475, feb 2012.

[195] Francesco Bonaccorso, Antonino Bartolotta, Jonathan N. Coleman, and Claudia Backes. 2D-Crystal-Based Functional Inks. *Advanced Materials*, 28(29):6136–6166, aug 2016.

[196] David J. Finn, Mustafa Lotya, Graeme Cunningham, Ronan J. Smith, David McCloskey, John F. Donegan, and Jonathan N. Coleman. Inkjet deposition of liquid-exfoliated graphene and MoS_2 nanosheets for printed device applications. *J. Mater. Chem. C*, 2(5):925–932, jan 2014.

[197] Mustafa Lotya, Yenny Hernandez, Paul J. King, Ronan J. Smith, Valeria Nicolosi, Lisa S. Karlsson, Fiona M. Blighe, Sukanta De, Zhiming Wang, I. T. McGovern, Georg S. Duesberg, and Jonathan N. Coleman. Liquid Phase Production of Graphene by Exfoliation of Graphite in Surfactant/Water Solutions. *Journal of the American Chemical Society*, 131(10):3611–3620, mar 2009.

[198] Claudia Backes, Thomas M Higgins, Adam Kelly, Conor Boland, Andrew Harvey, Damien Hanlon, and Jonathan N Coleman. Guidelines for Exfoliation, Characterization and Processing of Layered Materials Produced by Liquid Exfoliation. *Chemistry of Materials*, 29(1):243–255, jan 2017.

[199] Yenny Hernandez, Mustafa Lotya, David Rickard, Shane D. Bergin, and Jonathan N. Coleman. Measurement of Multicomponent Solubility Parameters for Graphene Facilitates Solvent Discovery. *Langmuir*, 26(5):3208–3213, mar 2010.

[200] Shane D. Bergin, Zhenyu Sun, David Rickard, Philip V. Streich, James P. Hamilton, and Jonathan N. Coleman. Multicomponent Solubility Parameters for Single-Walled Carbon Nanotube-Solvent Mixtures. *ACS Nano*, 3(8):2340–2350, aug 2009.

[201] Daryl McManus, Sandra Vranic, Freddie Withers, Veronica Sanchez-Romaguera, Massimo Macucci, Huafeng Yang, Roberto Sorrentino, Khaled Parvez, Seok-Kyun Son, Giuseppe Iannaccone, Kostas Kostarelos, Gianluca Fiori, and Cinzia Casiraghi. Water-based and biocompatible 2D crystal inks for all-inkjet-printed heterostructures. *Nature Nanotechnology*, 12(4):343–350, apr 2017.

[202] Ethan B. Secor, Bok Y. Ahn, Theodore Z. Gao, Jennifer A. Lewis, and Mark C. Hersam. Rapid and Versatile Photonic Annealing of Graphene Inks for Flexible Printed Electronics. *Advanced Materials*, 27(42):6683–6688, nov 2015.

[203] Yu Teng Liang and Mark C. Hersam. Highly Concentrated Graphene Solutions via Polymer Enhanced Solvent Exfoliation and Iterative Solvent Exchange. *Journal of the American Chemical Society*, 132(50):17661–17663, dec 2010.

[204] Dennis Bolten and Michael Turk. Experimental Study on the Surface Tension, Density, and Viscosity of Aqueous Poly(vinylpyrrolidone) Solutions. *Journal of Chemical & Engineering Data*, 56(3):582–588, mar 2011.

[205] Liying Cui, Junhu Zhang, Xuemin Zhang, Long Huang, Zhanhua Wang, Yunfeng Li, Hainan Gao, Shoujun Zhu, Tieqiang Wang, and Bai Yang. Suppression of the Coffee Ring Effect by Hydrosoluble Polymer Additives. *ACS Applied Materials & Interfaces*, 4(5):2775–2780, may 2012.

[206] Michael J. O'Connell, Peter Boul, Lars M. Ericson, Chad Huffman, Yuhuang Wang, Erik Haroz, Cynthia Kuper, Jim Tour, Kevin D. Ausman, and Richard E. Smalley. Reversible water-solubilization of single-walled carbon nanotubes by polymer wrapping. *Chemical Physics Letters*, 342(3-4):265–271, jul 2001.

[207] Athanasios B. Bourlinos, Vasilios Georgakilas, Radek Zboril, Theodore A. Steriotis, Athanasios K. Stubos, and Christos Trapalis. Aqueous-phase exfoliation of graphite in the presence of polyvinylpyrrolidone for the production of water-soluble graphenes. *Solid State Communications*, 149(47-48):2172–2176, dec 2009.

[208] Tawfique Hasan, Vittorio Scardaci, PingHeng Tan, Aleksey G Rozhin, William I Milne, and Andrea C Ferrari. Stabilization and "Debundling" of Single-Wall Carbon Nanotube Dispersions in N-Methyl-2-pyrrolidone (NMP) by Polyvinylpyrrolidone (PVP). *The Journal of Physical Chemistry C*, 111(34):12594–12602, aug 2007.

[209] David Dodoo-Arhin, Richard C T Howe, Guohua Hu, Yinghe Zhang, Pritesh Hiralal, Abdulhakeem Bello, Gehan Amaratunga, and Tawfique Hasan. Inkjet-printed graphene electrodes for dye-sensitized solar cells. *Carbon*, 105:33–41, 2016.

[210] Artur Ciesielski and Paolo Samorì. Grapheneviasonication assisted liquid-phase exfoliation. *Chem. Soc. Rev.*, 43(1):381–398, dec 2014.

[211] Bertrand Faure, German Salazar-Alvarez, Anwar Ahniyaz, Irune Villaluenga, Gemma Berriozabal, Yolanda R De Miguel, and Lennart Bergström. Dispersion and surface functionalization of oxide nanoparticles for transparent photocatalytic and UV-protecting coatings and sunscreens. *Science and Technology of Advanced Materials*, 14(2):023001, mar 2013.

[212] Lin Guo, Shihe Yang, Chunlei Yang, Ping Yu, Jiannong Wang, Weikun Ge, and George K. L. Wong. Highly monodisperse polymer-capped ZnO nanoparticles: Preparation and optical properties. *Applied Physics Letters*, 76(20):2901, may 2000.

[213] Kirill Arapov, Eric Rubingh, Robert Abbel, Jozua Laven, Gijsbertus de With, and Heiner Friedrich. Conductive Screen Printing Inks by Gelation of Graphene Dispersions. *Advanced Functional Materials*, 26(4):586–593, jan 2016.

[214] Ethan B. Secor, Pradyumna L. Prabhumirashi, Kanan Puntambekar, Michael L. Geier, and Mark C. Hersam. Inkjet Printing of High Conductivity, Flexible Graphene Patterns. *The Journal of Physical Chemistry Letters*, 4(8):1347–1351, apr 2013.

[215] Naif Mohammed Al-Hada, Elias B. Saion, Abdul Halim Shaari, Mazliana A. Kamarudin, Moayad Husein Flaifel, Sahrim Hj Ahmad, and Salahudeen A. Gene. A Facile Thermal-Treatment Route to Synthesize ZnO Nanosheets and Effect of Calcination Temperature. *PLoS ONE*, 9(8):e103134, aug 2014.

[216] Brian Derby. Inkjet Printing of Functional and Structural Materials: Fluid Property Requirements, Feature Stability, and Resolution. *Annual Review of Materials Research*, 40(1):395–414, jun 2010.

[217] Daehwan Jang, Dongjo Kim, and Jooho Moon. Influence of Fluid Physical Properties on Ink-Jet Printability. *Langmuir*, 25(5):2629–2635, mar 2009.

[218] Robert D. Deegan, Olgica Bakajin, Todd F. Dupont, Greg Huber, Sidney R. Nagel, and Thomas A. Witten. Contact line deposits in an evaporating drop. *Physical Review E*, 62(1):756–765, jul 2000.

[219] Shijian Luo, T. Harris, and C.P. Wong. Study on surface tension and adhesion for flip chip packaging. In *Proceedings International Symposium on Advanced Packaging Materials Processes, Properties and Interfaces (IEEE Cat. No.01TH8562)*, pages 299–304, 2001.

[220] Huimin Liu, Wei Xu, Wanyi Tan, Xuhui Zhu, Jian Wang, Junbiao Peng, and Yong Cao. Line printing solution-processable small molecules with uniform surface profile via ink-jet printer. *Journal of Colloid and Interface Science*, 465:106–111, mar 2016.

[221] J. A. Lim, W. H. Lee, H. S. Lee, J. H. Lee, Y. D. Park, and K. Cho. Self-Organization of Ink-jet-Printed Triisopropylsilylethynyl Pentacene via Evaporation-Induced Flows in a Drying Droplet. *Advanced Functional Materials*, 18(2):229–234, jan 2008.

[222] Hua Hu and Ronald G. Larson. Marangoni Effect Reverses Coffee-Ring Depositions. *J. Phys. Chem. B*, 110(14):7090–7094, 2006.

[223] Hua Hu and Ronald G. Larson. Analysis of the Effects of Marangoni Stresses on the Microflow in an Evaporating Sessile Droplet. *Langmuir*, 21(9):3972–3980, 2005.

[224] Dan Soltman and Vivek Subramanian. Inkjet-Printed Line Morphologies and Temperature Control of the Coffee Ring Effect. *Langmuir*, 2007.

[225] Vincent Quemener, Lasse Vines, Edouard V. Monakhov, and Bengt G. Svensson. Electrical Characterization of Hydrothermally Grown ZnO Annealed in Different Atmospheres. *International Journal of Applied Ceramic Technology*, 8(5):1017–1022, sep 2011.

[226] Alphus D Wilson and Manuela Baietto. Applications and advances in electronic-nose technologies. *Sensors (Basel, Switzerland)*, 9(7):5099–148, 2009.

[227] Denise M. Wilson and Stephen P. DeWeerth. Odor discrimination using steady-state and transient characteristics of tin-oxide sensors. *Sensors and Actuators B: Chemical*, 28(2):123–128, aug 1995.

[228] E.L. Hines, E. Llobet, and J.W. Gardner. Electronic noses: a review of signal processing techniques. *IEE Proceedings - Circuits, Devices and Systems*, 146(6):297, 1999.

[229] Morad K Nakhleh, Haitham Amal, Raneen Jeries, Yoav Y Broza, Manal Aboud, Alaa Gharra, Hodaya Ivgi, Salam Khatib, Shifaa Badarneh, Lior Har-Shai, Lea Glass-Marmor, Izabella Lejbkowicz, Ariel Miller, Samih Badarny, Raz Winer, John Finberg, Sylvia Cohen-Kaminsky, ric Perros, David Montani, Barbara Girerd, Gilles Garcia, rald Simonneau, Farid Nakhoul, Shira Baram, Raed Salim, Marwan Hakim, Maayan Gruber, Ohad Ronen, Tal Marshak, Ilana Doweck, Ofer Nativ, Zaher Bahouth, Da-you Shi, Wei Zhang, Qing-ling Hua, Yue-yin Pan, Li Tao, Hu Liu, Amir Karban, Eduard Koifman, Tova Rainis, Roberts Skapars, Armands Sivins, Douglas Johnson, Stuart Z Millstone, Jennifer Fulton, John W Wells, Larry H Wilf, Marc Humbert, Marcis Leja, Nir Peled, and Hossam Haick. Diagnosis and Classification of 17 Diseases from 1404 Subjects via Pattern Analysis of Exhaled Molecules. *ACS Nano*, 11, 2017.

[230] Lisa A Spacek, Arthur Strzepka, Saurabh Saha, Jonathan Kotula, Jeffrey Gelb, Sarah Guilmain, Terence Risby, and Steven F Solga. Repeated Measures of Blood and Breath Ammonia in Response to Control, Moderate and High Protein Dose in Healthy Men. *Scientific Reports*, 8(1):2554, 2018.

[231] E G Goh, X Xu, and P G McCormick. Effect of particle size on the UV absorbance of zinc oxide nanoparticles. *Scripta Materialia*, 78-79:49–52, 2014.

[232] Konstantinos Kouroupis-Agalou, Andrea Liscio, Emanuele Treossi, Luca Ortolani, Vittorio Morandi, Nicola Maria Pugno, and Vincenzo Palermo. Fragmentation and exfoliation of 2-dimensional materials: a statistical approach. *Nanoscale*, 6(11):5926–5933, may 2014.

[233] Henri Jussila, Tom Albrow-Owen, He Yang, Guohua Hu, Sinan Aksimsek, Niko Granqvist, Harri Lipsanen, Richard C. T. Howe, Zhipei Sun, and Tawfique Hasan. New Approach for Thickness Determination of Solution-Deposited Graphene Thin Films. *ACS Omega*, 2(6):2630–2638, jun 2017.

[234] Taneli Juntunen, Henri Jussila, Mikko Ruoho, Shouhu Liu, Guohua Hu, Tom Albrow-Owen, Leonard W. T. Ng, Richard C. T. Howe, Tawfique Hasan, Zhipei Sun, and Ilkka Tittonen. Inkjet Printed Large-Area Flexible Few-Layer Graphene Thermoelectrics. *Advanced Functional Materials*, 28(22):1800480, may 2018.

[235] S. J. Chen, Y. C. Liu, C. L. Shao, R. Mu, Y. M. Lu, J. Y. Zhang, D. Z. Shen, and X. W. Fan. Structural and Optical Properties of Uniform ZnO Nanosheets. *Advanced Materials*, 17(5):586–590, mar 2005.

[236] In-yeal Lee, Hyung-Youl Park, Jin-hyung Park, Gwangwe Yoo, Myung-Hoon Lim, Junsung Park, Servin Rathi, Woo-Shik Jung, Jeehwan Kim, Sang-Woo Kim, Yonghan Roh, Gil-Ho Kim, and Jin-Hong Park. Poly-4-vinylphenol and poly(melamine-co-formaldehyde)-based graphene passivation method for flexible, wearable and transparent electronics. *Nanoscale*, 6(7):3830, mar 2014.

[237] A. Das, S. Pisana, B. Chakraborty, S. Piscanec, S. K. Saha, U. V. Waghmare, K. S. Novoselov, H. R. Krishnamurthy, A. K. Geim, A. C. Ferrari, and A. K. Sood. Monitoring dopants by Raman scattering in an electrochemically top-gated graphene transistor. *Nature Nanotechnology*, 3(4):210–215, apr 2008.

[238] Zhaoyong Guan, Shuang Ni, and Shuanglin Hu. Band gap opening of graphene by forming a graphene/$PtSe_2$ van der Waals heterojunction. *RSC Advances*, 7(72):45393–45399, 2017.

[239] Hyoun Woo Kim, Yong Jung Kwon, Ali Mirzaei, Sung Yong Kang, Myung Sik Choi, Jae Hoon Bang, and Sang Sub Kim. Synthesis of zinc oxide semiconductors-graphene nanocomposites by microwave irradiation for application to gas sensors. *Sensors and Actuators B: Chemical*, 249:590–601, 2017.

[240] Oleg Lupan, Fabian Schütt, Vasile Postica, Daria Smazna, Yogendra Kumar Mishra, and Rainer Adelung. Sensing performances of pure and hybridized carbon nanotubes-ZnO nanowire networks: A detailed study. *Scientific Reports*, 7(1):14715, dec 2017.

[241] M. V. Bracamonte, G. I. Lacconi, S. E. Urreta, and L. E. F. Foa Torres. On the Nature of Defects in Liquid-Phase Exfoliated Graphene. *The Journal of Physical Chemistry C*, 118(28):15455–15459, jul 2014.

[242] R. Gutierrez-Osuna, A. Gutierrez-Galvez, and N. Powar. Transient response analysis for temperature-modulated chemoresistors. *Sensors and Actuators B: Chemical*, 93(1-3):57–66, aug 2003.

[243] P.K. Guha, S.Z. Ali, C.C.C. Lee, F. Udrea, W.I. Milne, T. Iwaki, J.A. Covington, and J.W. Gardner. Novel design and characterisation of SOI CMOS micro-hotplates for high temperature gas sensors. *Sensors and Actuators B: Chemical*, 127(1):260–266, oct 2007.

[244] G. H. Mhlongo, D. E. Motaung, F. R. Cummings, H. C. Swart, and S. S. Ray. A highly responsive NH_3 sensor based on Pd-loaded ZnO nanoparticles prepared via a chemical precipitation approach. *Scientific Reports*, 9(1):9881, dec 2019.

[245] Hua-Yao Li, Chul-Soon Lee, Do Hong Kim, and Jong-Heun Lee. Flexible Room-Temperature NH_3 Sensor for Ultrasensitive, Selective, and Humidity-Independent Gas Detection. *ACS Applied Materials & Interfaces*, 10(33):27858–27867, aug 2018.

[246] F M Schmidt, O Vaittinen, M Metsälä, M Lehto, C Forsblom, P-H Groop, and L Halonen. Ammonia in breath and emitted from skin. *Journal of Breath Research*, 7(1):017109, feb 2013.

[247] Troy Hibbard and Anthony J. Killard. Breath Ammonia Analysis: Clinical Application and Measurement. *Critical Reviews in Analytical Chemistry*, 41(1):21–35, jan 2011.

[248] W. Lindinger and A. Jordan. Proton-transfer-reaction mass spectrometry (PTR–MS): on-line monitoring of volatile organic compounds at pptv levels. *Chemical Society Reviews*, 27(5):347, jan 1998.

[249] Luís F. da Silva, Ariadne C. Catto, Waldir Avansi, Laécio S. Cavalcante, Valmor R. Mastelaro, Juan Andrés, Khalifa Aguir, and Elson Longo. Acetone gas sensor based on α-Ag_2WO_4 nanorods obtained via a microwave-assisted hydrothermal route. *Journal of Alloys and Compounds*, 683:186–190, oct 2016.

[250] Seon-Jin Choi, Bong-Hoon Jang, Seo-Jin Lee, Byoung Koun Min, Avner Rothschild, and Il-Doo Kim. Selective Detection of Acetone and Hydrogen Sulfide for the Diagnosis of Diabetes and Halitosis Using SnO_2 Nanofibers Functionalized with Reduced Graphene Oxide Nanosheets. *ACS Applied Materials & Interfaces*, 6(4):2588–2597, feb 2014.

[251] Shouli Bai, Kewei Zhang, Liangshi Wang, Jianhua Sun, Ruixian Luo, Dianqing Li, and Aifan Chen. Synthesis mechanism and gas-sensing application of nanosheet-assembled tungsten oxide microspheres. *J. Mater. Chem. A*, 2(21):7927–7934, may 2014.

[252] Janusz Marek Smulko, Maciej Trawka, Claes Goran Granqvist, Radu Ionescu, Fatima Annanouch, Eduard Llobet, and Laszlo Bela Kish. New approaches for improving selectivity and sensitivity of resistive gas sensors: a review. *Sensor Review*, 35(4):340–347, sep 2015.

[253] Anindita Bora and Kanak Chandra Sarma. A Temperature Modulation Circuit for Metal Oxide Semiconductor Gas Sensor. *Indian Journal of Science and Technology*, 8(13), jul 2015.

[254] F. Udrea, S.Z. Ali, and J.W. Gardner. CMOS micro-hotplate array design for nanomaterial-based gas sensors. In *2008 International Semiconductor Conference*, pages 143–146. IEEE, 2008.

[255] Dorota Koziej, Nicolae Bârsan, Udo Weimar, Jacek Szuber, Kengo Shimanoe, and Noboru Yamazoe. Water–oxygen interplay on tin dioxide surface: Implication on gas sensing. *Chemical Physics Letters*, 410(4-6):321–323, jul 2005.

[256] Tien-Chun Wu, Jie Dai, Guohua Hu, Wen-Bei Yu, Osarenkhone Ogbeide, Andrea De Luca, Xiao Huang, Florin Udrea, and Tawfique Hasan. Machine-intelligent inkjet-printed α-Fe_2O_3/rGO towards NO_2 detection in ambient humidity. *Submitted*, 2020.

[257] Jianxing Liu, He Yang, and Xiangxin Xue. Preparation of different shaped α-Fe_2O_3 nanoparticles with large particles of iron oxide red. *CrystEngComm*, 21(7):1097–1101, feb 2019.

[258] Abid, Poonam Sehrawat, S. S. Islam, Prabhash Mishra, and Shahab Ahmad. Reduced graphene oxide (rGO) based wideband optical sensor and the role of Temperature, Defect States and Quantum Efficiency. *Scientific Reports*, 8(1):3537, dec 2018.

[259] Nagi M El-Shafai, Mohamed E El-Khouly, Maged El-Kemary, Mohamed S Ramadan, and Mamdouh S Masoud. Graphene oxide-metal oxide nanocomposites: fabrication, characterization and removal of cationic rhodamine B dye. *RSC Advances*, 8:13323–13332, 2018.

[260] Zero Degree Contact Angle Measurements.

[261] T. Gokus, R. R. Nair, A. Bonetti, M. Böhmler, A. Lombardo, K. S. Novoselov, A. K. Geim, A. C. Ferrari, and A. Hartschuh. Making Graphene Luminescent by Oxygen Plasma Treatment. *ACS Nano*, 3(12):3963–3968, dec 2009.

[262] Abdelmajid Lassoued, Brahim Dkhil, Abdellatif Gadri, and Salah Ammar. Control of the shape and size of iron oxide (α-Fe_2O_3) nanoparticles synthesized through the chemical precipitation method. *Results in Physics*, 7:3007–3015, jan 2017.

[263] Bo Zhang, Guannan Liu, Ming Cheng, Yuan Gao, Lianjing Zhao, Shan Li, Fangmeng Liu, Xu Yan, Tong Zhang, Peng Sun, and Geyu Lu. The preparation of reduced graphene oxide-encapsulated α-Fe_2O_3 hybrid and its outstanding NO_2 gas sensing properties at room temperature. *Sensors and Actuators, B: Chemical*, 261:252–263, may 2018.

[264] Haojie Song, Linxuan Xia, Xiaohua Jia, and Wenming Yang. Polyhedral α-Fe_2O_3 crystals@rGO nanocomposites: Synthesis, characterization, and application in gas sensing. *Journal of Alloys and Compounds*, 732:191–200, jan 2018.

[265] OAR US EPA. Nitrogen Dioxide (NO_2) Primary Air Quality Standards.

[266] Konrad Maier, Andreas Helwig, Gerhard Müller, Pascal Hille, and Martin Eickhoff. Effect of Water Vapor and Surface Morphology on the Low Temperature Response of Metal Oxide Semiconductor Gas Sensors. *Materials (Basel, Switzerland)*, 8(9):6570–6588, sep 2015.

[267] Stephen Brunauer, Lola S. Deming, W. Edwards Deming, and Edward Teller. On a Theory of the van der Waals Adsorption of Gases. *Journal of the American Chemical Society*, 62(7):1723–1732, jul 1940.

Appendix A

Raw data for Chapter 5

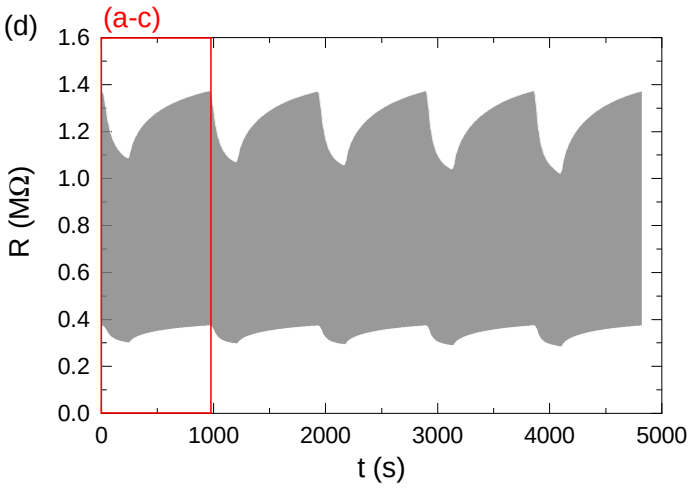

Fig. A.1 Raw resistance data for Fig. 5.9

Optimization of print repetitions

Fig. A.2 shows that 20 passes of print produces interconnected film (as compared to 10 passes), as well as producing uniformly distributed particles. The electrical resistance is ≈5 MΩ in the ambient environment which lies within the measurable boundary of 10 M□. On the other hand, localized aggregation (see also Fig A.3) is observed in the printed films with 40 passes. Excessive print repetition is not desirable for manufacturability either, as it increases fabrication time and material consumption. Therefore, 20 print repetitions are chosen throughout the project.

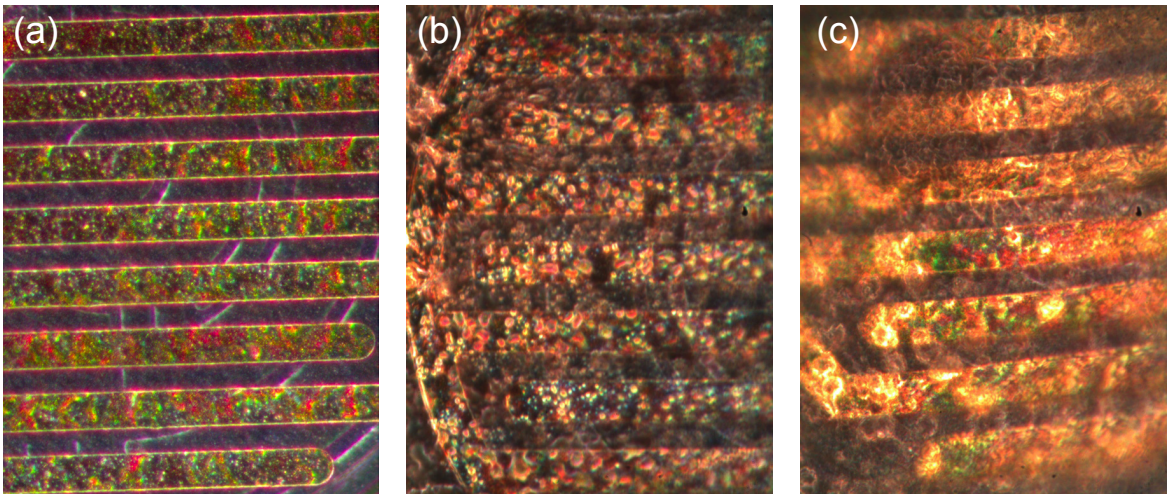

Fig. A.2 Microscopic dark field images of the printed ZnO/graphene film with (a) 10 print repetitions (b) 20 print repetitions (c) 40 print repetitions. Optical magnification of 50x.

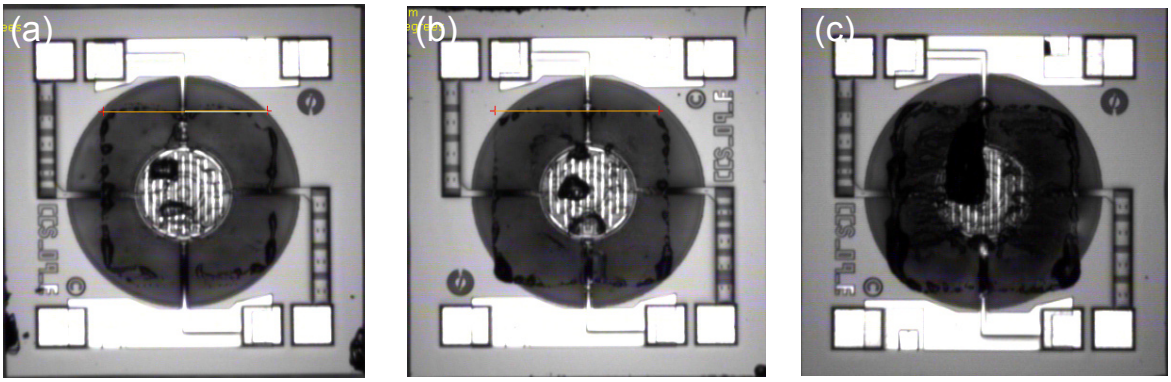

Fig. A.3 Images of the printed ZnO/graphene film with (a) 10 print repetitions (b) 20 print repetitions (c) 40 print repetitions. Image captured from the printer camera prior to drying and annealing.

Raw data for Chapter 6

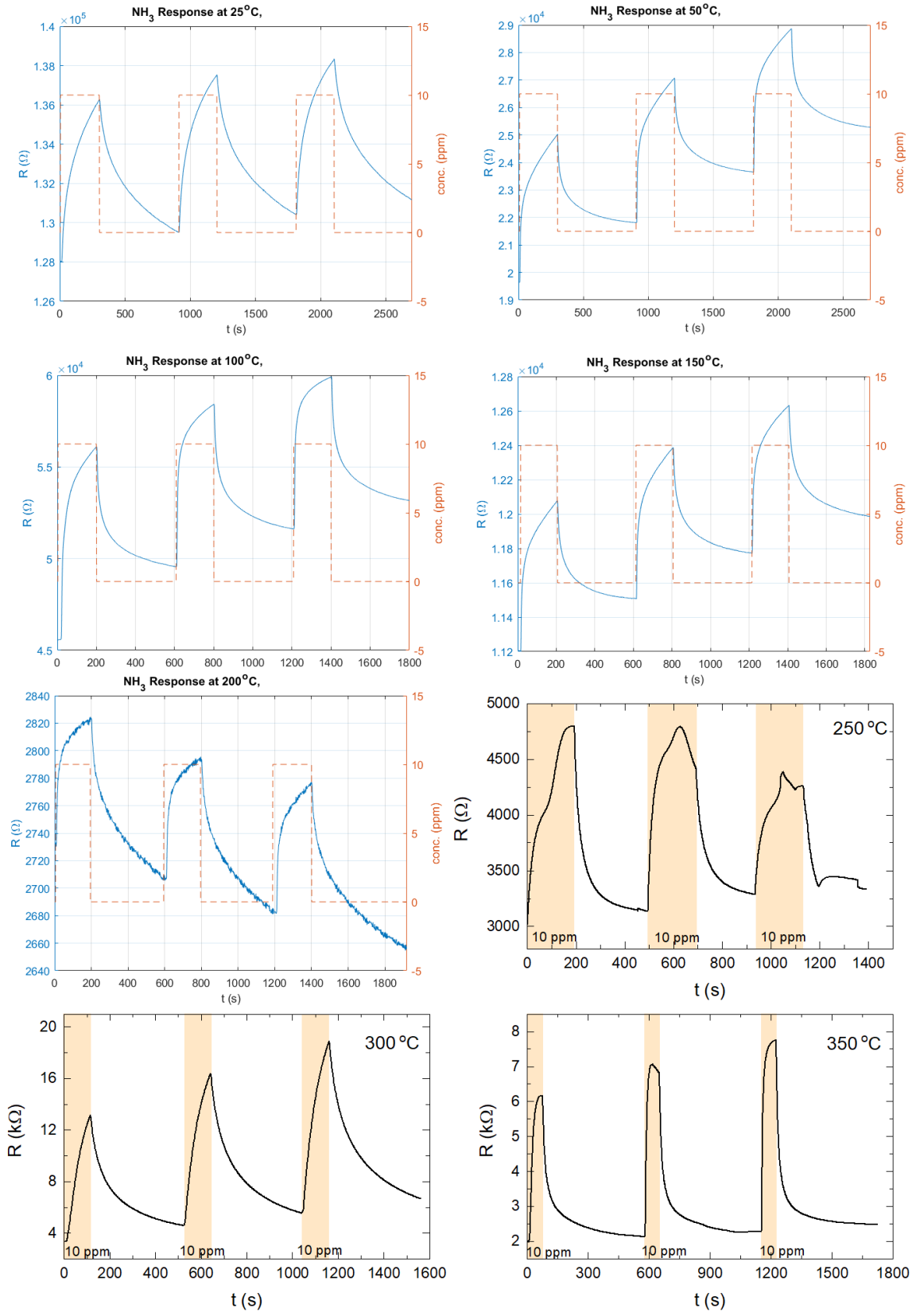

Fig. A.4 Raw resistance data for Fig. 6.9

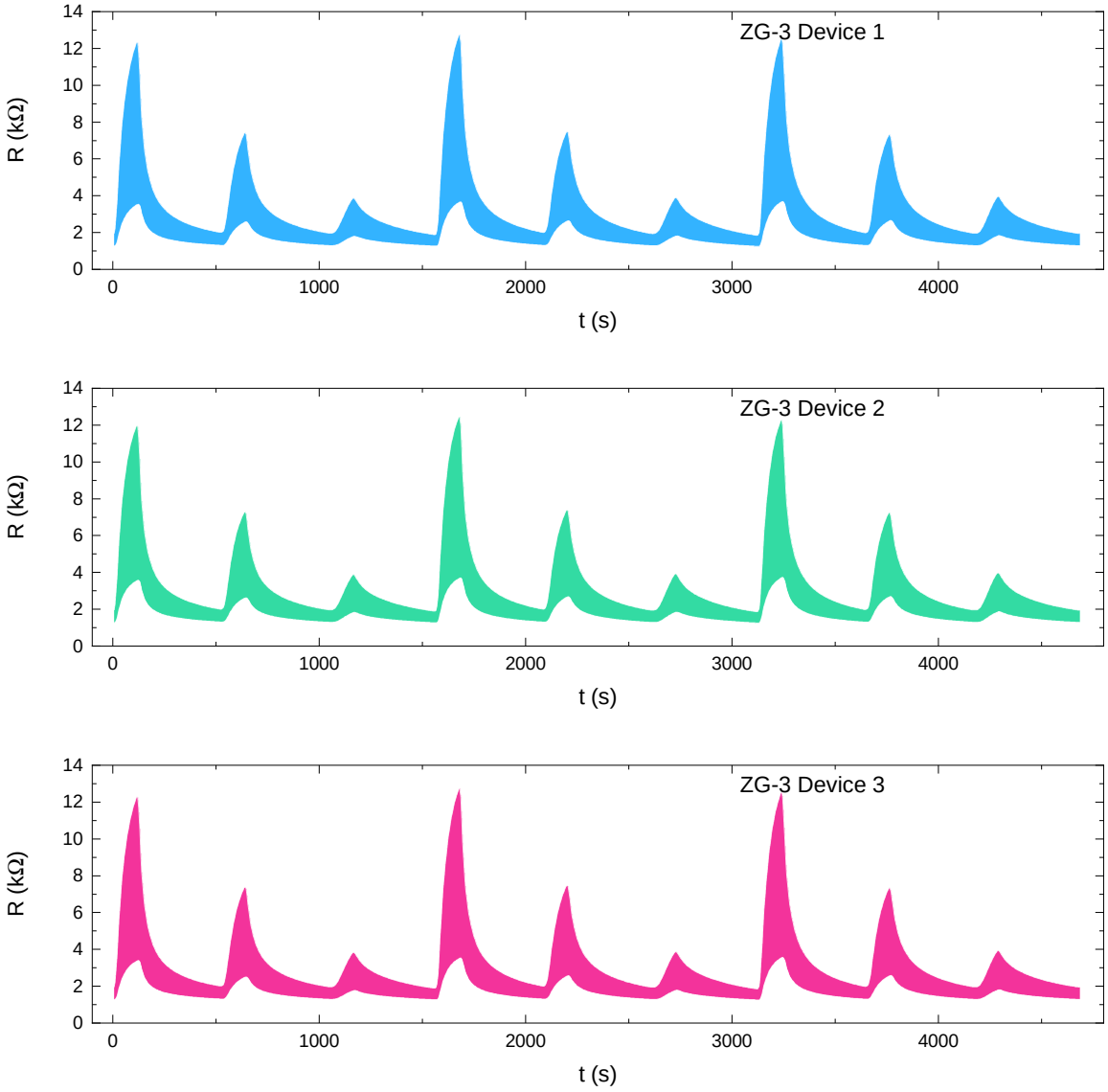

Fig. A.5 Raw resistance data for Fig. 6.15

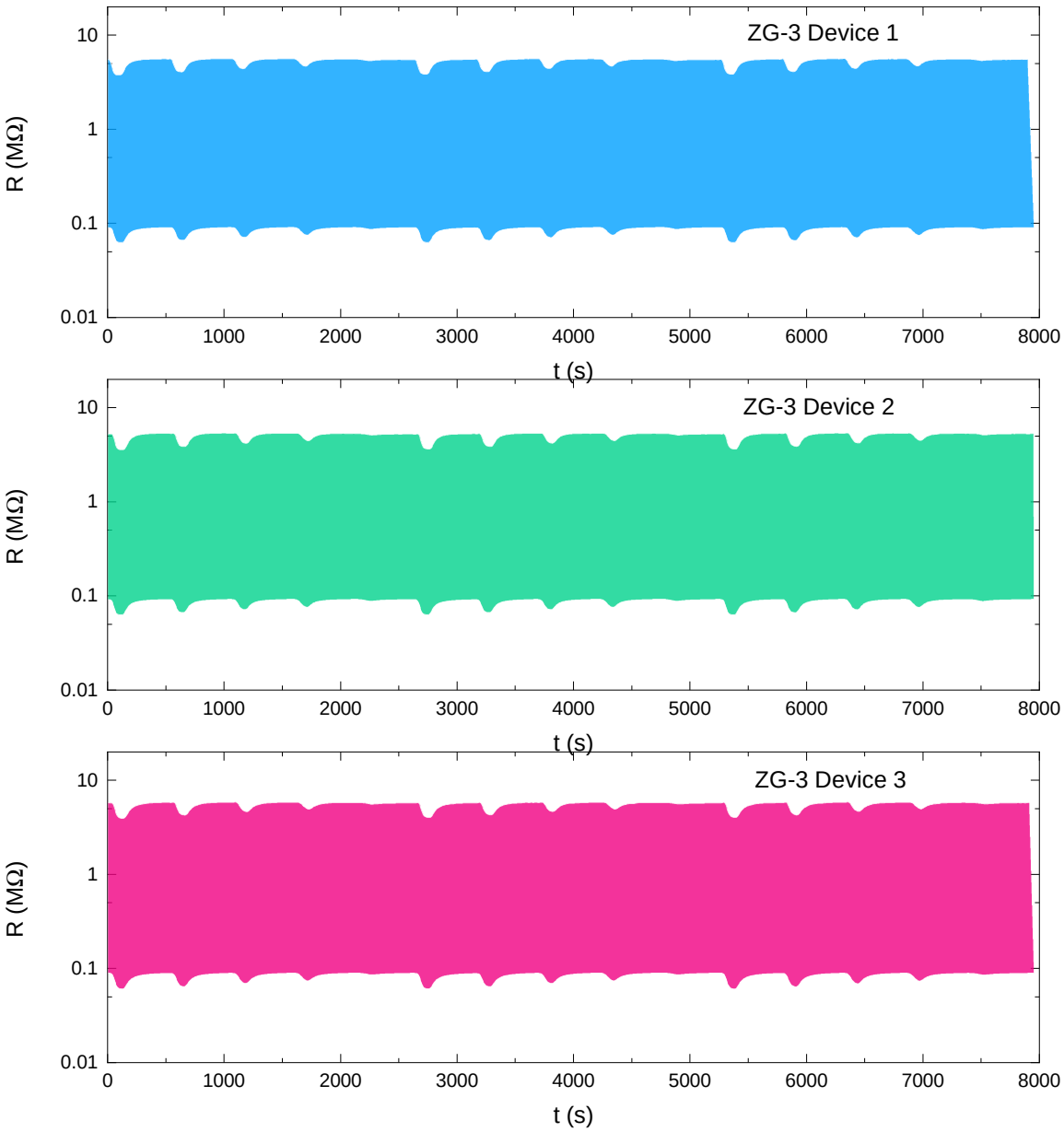

Fig. A.6 Raw resistance data for Fig. 6.17

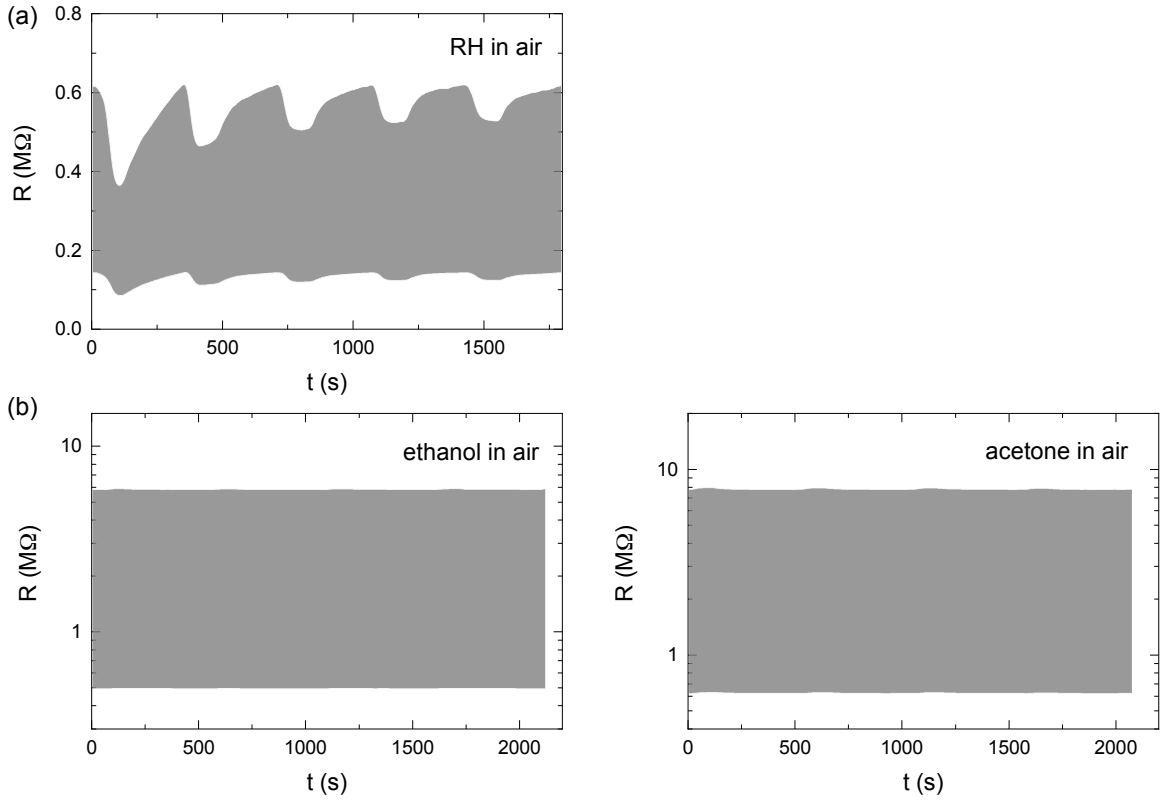

Fig. A.7 Raw resistance data for Fig. 6.19

Raw data for Chapter 7

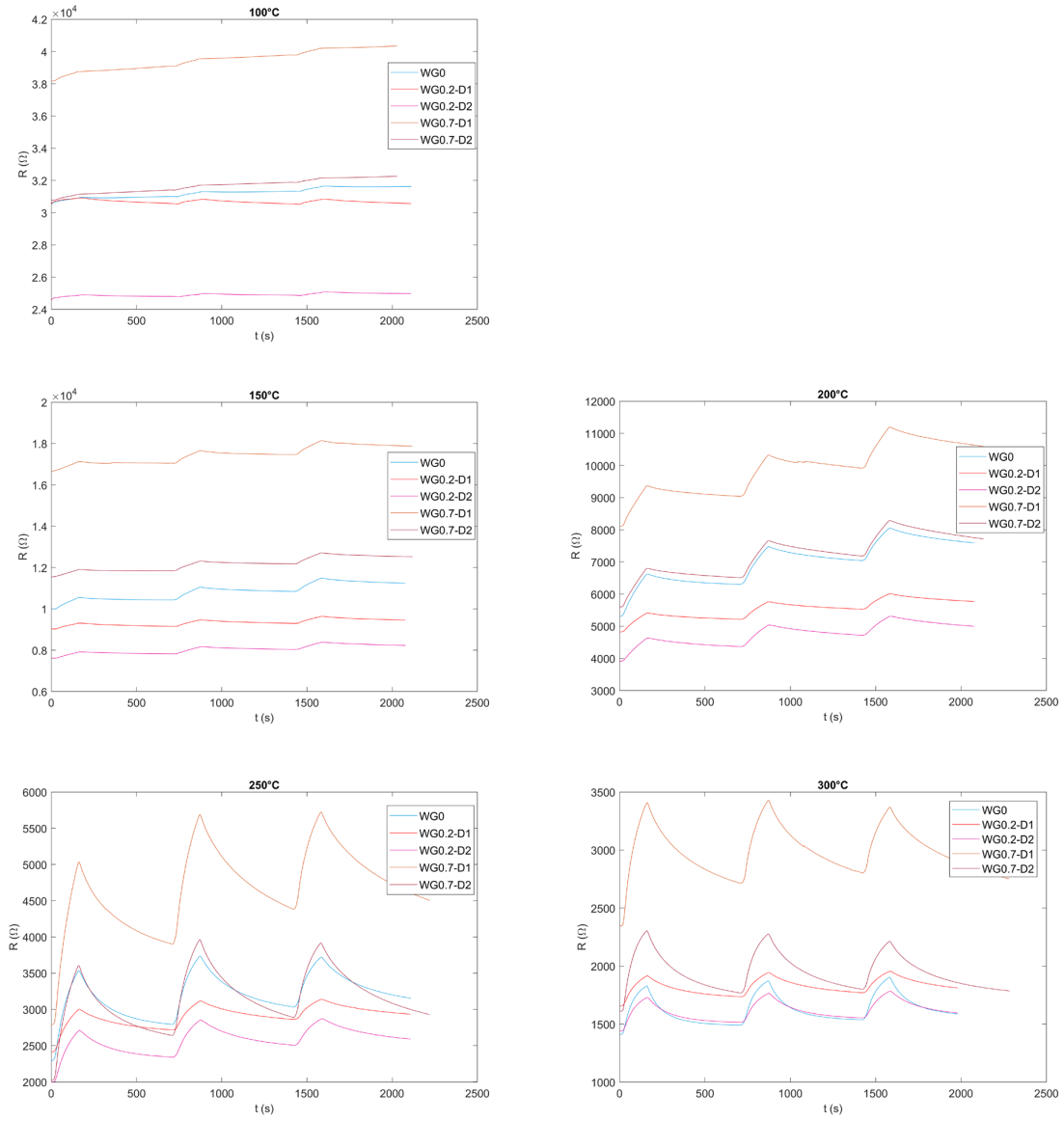

Fig. A.8 Raw resistance data for Fig. 7.3

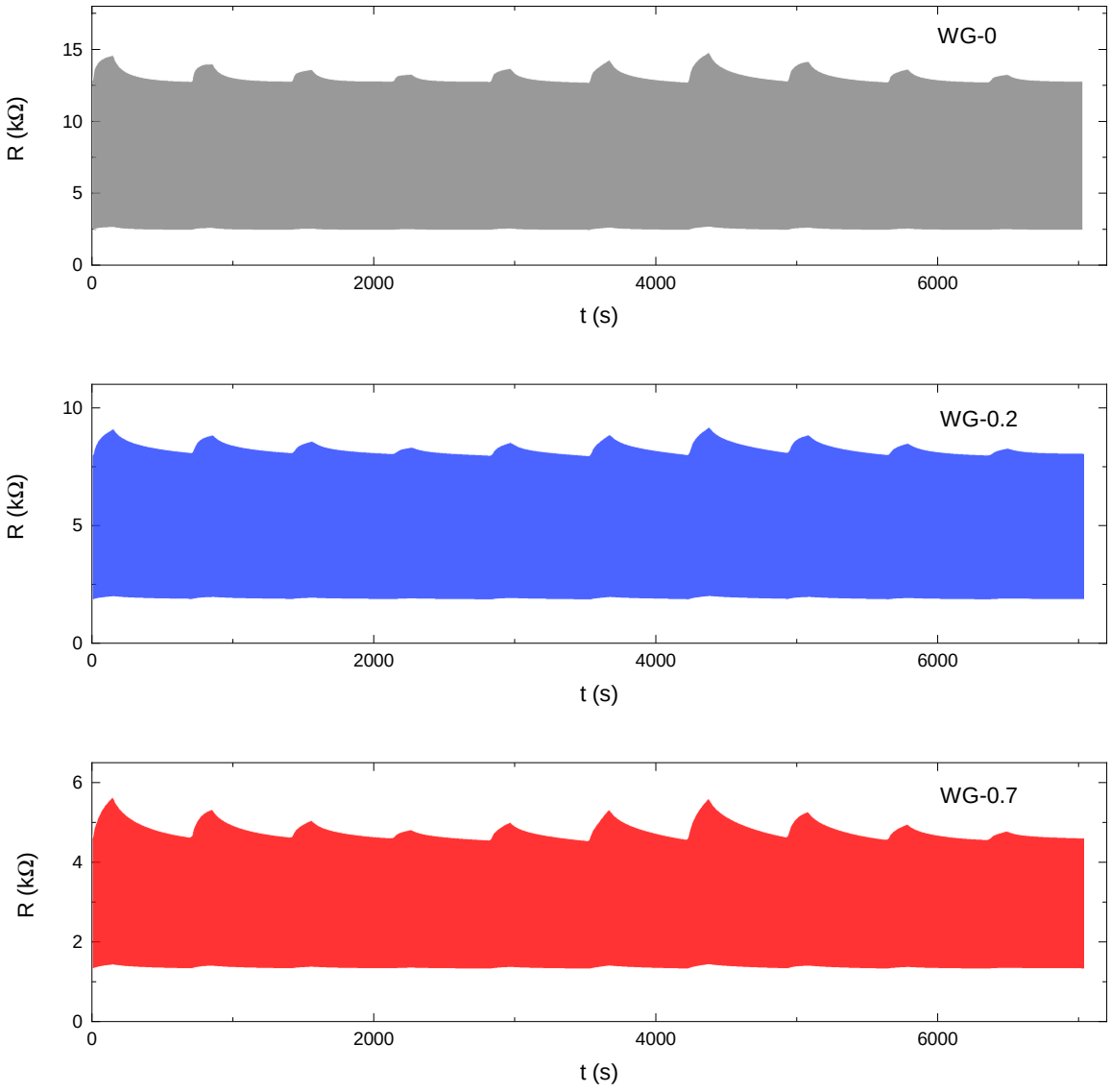

Fig. A.9 Raw resistance data for Fig. 7.6

Raw data for Chapter 8

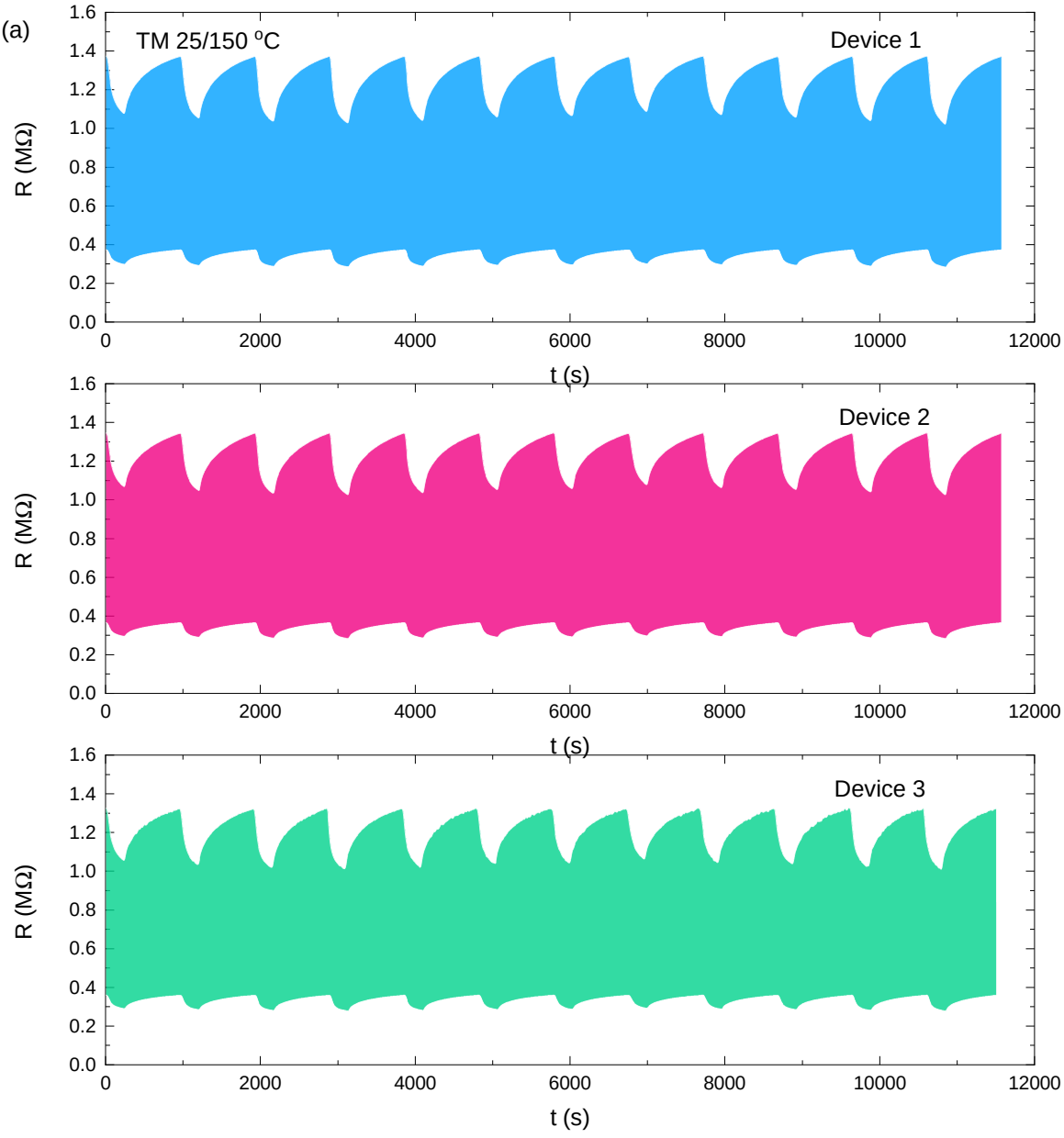

Fig. A.10 Raw resistance data for Fig. 8.8(a).

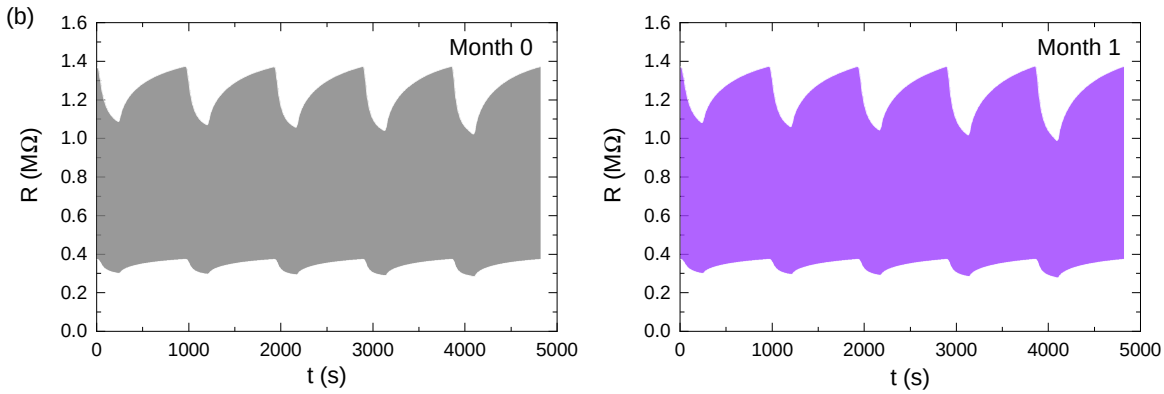

Fig. A.11 Raw resistance data for Fig. 8.8(b).

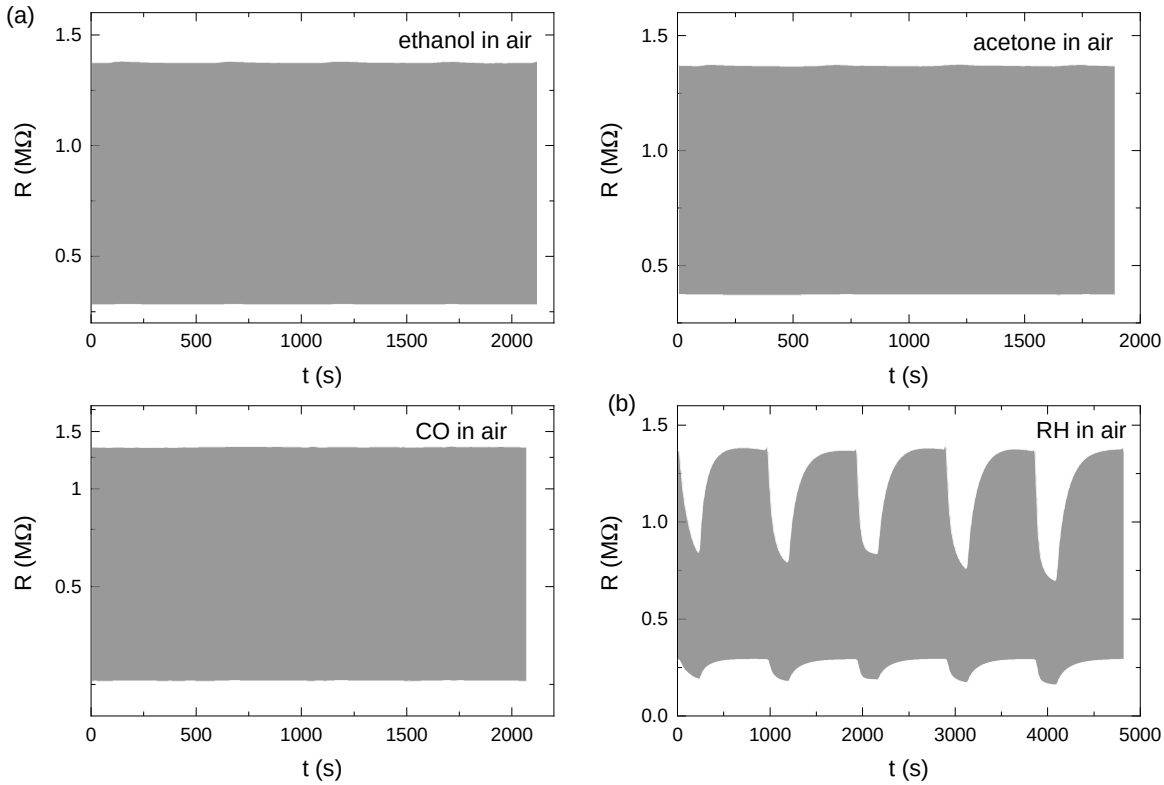

Fig. A.12 Raw resistance data for Fig. 8.9.

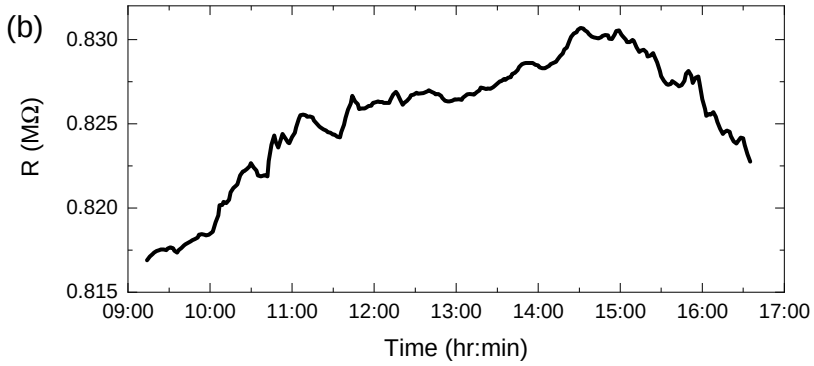

Fig. A.13 Raw resistance data for Fig. 8.17.